

DISSERTATION

PART I — ACCESS TO UV PHOTOCURED NANOSTRUCTURES VIA
SELECTIVE MORPHOLOGICAL TRAPPING OF BLOCK COPOLYMER
MELTS

PART II — MORPHOLOGICAL PHASE BEHAVIOR OF POLY(RTIL)
CONTAINING BLOCK COPOLYMER MELTS

Submitted by

Vincent F. Scalfani

Department of Chemistry

In partial fulfillment of the requirements

For the Degree of Doctor of Philosophy

Colorado State University

Fort Collins, Colorado

Spring 2012

Doctoral Committee:

Advisor: Travis S. Bailey

Richard G. Finke

Charles S. Henry

Matt J. Kipper

Amy L. Prieto

Copyright by Vincent F. Scalfani 2012

All Rights Reserved

ABSTRACT

PART I — ACCESS TO UV PHOTOCURED NANOSTRUCTURES VIA SELECTIVE MORPHOLOGICAL TRAPPING OF BLOCK COPOLYMER MELTS

PART II — MORPHOLOGICAL PHASE BEHAVIOR OF POLY(RTIL)- BASED BLOCK COPOLYMER MELTS

A thermally stable photocuring system was developed for high fidelity translation of block copolymer based melt-state morphologies into their equivalent solid analogs. Cationic photoacids were combined with partially epoxidized polyisoprene-*b*-poly(ethylene oxide) (PI-PEO) block copolymers, forming composite blends that allow for extended thermal processing prior to cure, in addition to precise trapping of selected morphologies, a consequence of the temperature independent UV curing mechanism. The parent PI-PEO block copolymer exhibited multiple melt-state morphologies including crystalline lamellae (L_c), hexagonally packed cylinders (C), bicontinuous gyroid (G), and an isotropic disordered state (Dis). Modification of the PI-PEO backbone with epoxy groups and addition of a UV cationic photoacid acted only to shift transition temperatures quantitatively, leaving the overall morphological behavior completely unmodified. UV irradiation exposure of the composite blends directly in the melt-phase at selected temperatures resulted in permanent trapping of both the cylinder and gyroid morphologies from a single block copolymer sample.

The studied photocuring chemistry was extended to produce spherical nanostructured

hydrogel networks. Fabricated hydrogel networks are built from a pre-structured lattice of body-centered cubic spheres (S_{BCC}), produced via melt-state self-assembly of blended AB diblock and ABA triblock copolymers. Added ABA triblock serves to produce active tethered junction points between the AB diblock spherical micelles. The integrated thermally stable photocuring chemistry allows for *in situ* trapping of these spherical domains directly in the melt phase, independent from the required thermal processing necessary to achieve the tethered BCC lattice. Specifically, the hydrogel networks were fabricated from partially epoxidized blends of polybutadiene-*b*-poly(ethylene oxide) diblock (PB-PEO) and PB-PEO-PB triblock copolymers. UV cured samples of composite copolymer disks containing an added amount of UV activated cationic photoinitiator samples retained the S_{BCC} structure with high fidelity, which serves to pre-structure the hydrogel network prior to swelling. Photocured disks preserved their original shape when swollen in water or organic media, were highly elastic and had excellent mechanical properties. Control experiments with uncured samples immediately dissolved or dispersed when swollen. Simple photopatterning of the cross-linked hydrogel system is also explored.

The developed pre-structured hydrogel network was then adapted to incorporate light sensitive anthracene groups into the spherical forming AB diblock copolymer for *in situ* generation of tethering ABA triblock. Pressed disks of anthracene terminated poly(styrene)-*b*-poly(ethylene oxide) diblock (PS-PEO-An) were photocoupled with UV 365 nm filtered light directly in the melt-phase, post the necessary thermal self-assembly process. Photocoupled disks swelled in water, were highly elastic, had tunable mechanical properties (based on UV irradiation time), and showed complete preservation of initial shape. Swollen photocoupled disks were found to exhibit similar properties to pre-blended PS-PEO/PS-PEO-PS hydrogels with slight differences likely resulting from an asymmetric distribution of triblock in the photocoupled gels. The PS-PEO-An based hydrogels are proposed to be possible future candidates for the development of new asymmetric hydrogels because of their simple fabrication and excellent mechanical properties.

A new poly(room temperature ionic liquid) (RTIL) BCP platform was developed based on

the sequential, living ring-opening metathesis polymerization (ROMP) of a hydrophobic non-charged dodecyl ester norbornene monomer followed by a cationic imidazolium norbornene ionic liquid (RTIL) monomer. The synthesized BCPs were found to exhibit surfactant behavior in solution and form highly periodic nanoscale melt morphologies. Extensive control experiments with homopolymer blends do not show any surfactant behavior in solution nor micro-phase separation in the neat melt phase. After an initial study optimizing the synthesis and verifying the block architecture, a series of 16 poly(RTIL)-based BCP samples were synthesized with varying compositions of 0.42–0.96 vol% poly(norbornene dodecyl ester). A phase diagram was developed through a combination of small-angle X-ray scattering and dynamic rheology. Morphologies identified and assigned within the phase space studied include lamellae (Lam), hexagonally packed cylinders (Hex), a coexistence of Hex and Lam domains in place of the gyroid region, spheres on a body-centered cubic lattice (S_{BCC}), and a “liquid like” packing of spheres (LLP). Annealing samples containing a coexistence of Lam and Hex domains suggest extremely slow ordering kinetics disposing one of the morphologies. The studied poly(RTIL)-based BCPs containing highly charged species are very strongly segregated (large χ parameter), resulting in limited if any access to the disordered and gyroid regime.

Finally, in Appendix I a supramolecular polymer system comprised of benzene-1,3,5-tricarboxamide (BTA) and 2-ureido-4[1H]-pyrimidinone (UPy) functional hydrogenated polybutadiene was developed that forms two unique and independent nanorod motif assemblies. When the two supramolecular motifs are end-capped to different homopolymers, the motifs self-assemble independent of each other into separate nanorod stacked structures. However, when a telechelic polymer is introduced into the system containing both supramolecular motifs (one on each end), a network is formed between the nanorod assemblies. Without the telechelic polymer, the supramolecular material is a viscous liquid with little mechanical integrity. In contrast, addition of the telechelic polymer acts as a cross-linker and results in a networked material that is highly elastic with excellent mechanical properties.

For my daughter, Mia

TABLE OF CONTENTS

PART I — ACCESS TO UV PHOTOCURED NANOSTRUCTURES VIA SELECTIVE MORPHOLOGICAL TRAPPING OF BLOCK COPOLYMER MELTS

CHAPTER 1	2
INTRODUCTION AND PERSPECTIVE OF DISSERTATION	
1.1 COMMON ABBREVIATIONS AND CHEMICAL STRUCTURES USED WITHIN DISSERTATION	3
1.2 BRIEF OVERVIEW OF DISSERTATION	5
1.3 PHOTOCURING CHEMISTRY FOR SELECTIVE CURING OF BLOCK COPOLYMER MELTS (CHAPTER 3)	6
1.4 NANOSTRUCTURED HYDROGEL NETWORKS (CHAPTERS 4 AND 5) .	8
1.5 SYNTHESIS AND PHASE BEHAVIOR OF POLY(RTIL)-BASED BLOCK COPOLYMERS (CHAPTERS 7 AND 8)	9
1.6 ORTHOGONAL SUPRAMOLECULAR POLYMER MOTIF NETWORKS (APPENDIX I)	11
1.7 FINAL REMARKS BEFORE DISSERTATION MAIN TEXT	12
CHAPTER 2	13
INTRODUCTION TO BLOCK COPOLYMER THERMODYNAMICS AND EXPERIMENTAL CHARACTERIZATION TECHNIQUES USED WITHIN DISSERTATION	
2.1 CONSPECTUS	14
2.2 BLOCK COPOLYMER THERMODYNAMICS AND MELT-STATE PHASE BEHAVIOR	14
2.3 EXPERIMENTAL CHARACTERIZATION TECHNIQUES FOR BCPs . .	18

2.3.1 Nuclear Magnetic Resonance (NMR)	18
2.3.2 End-group Analysis.	19
2.3.3 Volume Fraction Determination	20
2.3.4 Percent Epoxidation Determination	22
2.3.5 Size Exclusion Chromatography (SEC).....	25
2.3.6 Dynamic Mechanical Spectroscopy (Rheology).....	27
2.3.7 Small-angle X-ray Scattering (SAXS)	29
2.3.8 Indexing of BCP Morphologies.	32
2.4 REFERENCES	36
CHAPTER 3	39
THERMALLY STABLE PHOTOCURING CHEMISTRY FOR SELECTIVE MORPHOLOGICAL TRAPPING IN BLOCK COPOLYMER MELT SYSTEMS	
3.1 CONSPECTUS	40
3.2 INTRODUCTION	40
3.3 RESULTS AND DISCUSSION	44
3.3.1 Synthesis	44
3.3.2 Melt State Phase Behavior of PI-PEO.....	46
3.3.3 Melt State Phase Behavior of ePI-PEO.....	48
3.3.4 Melt State Phase Behavior of ePI-PEO with IPDPST Photoacid	49
3.3.5 Cylindrical Trapping Curing Experiment	51
3.3.6 Gyroid Trapping Curing Experiment.....	53
3.4 CONCLUSIONS	54
3.5 EXPERIMENTAL	55
3.5.1 Materials and Methods.....	55
3.5.2 Physical and Analytical Measurements.....	56

3.5.3	<i>Dynamic Mechanical Spectroscopy</i>	56
3.5.4	<i>Small Angle X-ray Scattering (SAXS)</i>	57
3.5.5	<i>ω-hydroxy-polyisoprene (PI)</i>	57
3.5.6	<i>ω-hydroxy-polyisoprene-<i>b</i>-poly(ethylene oxide) (PI-PEO)</i>	57
3.5.7	<i>Epoxidized Polyisoprene-<i>b</i>-poly(ethylene oxide) (ePI-PEO)</i>	58
3.5.8	<i>Photocuring of ePI_{16.8}-PEO-1</i>	58
3.6	ACKNOWLEDGEMENTS	59
3.7	SUPPORTING INFORMATION AVAILABLE.	59
3.8	REFERENCES	59
CHAPTER 4		61
ACCESS TO NANOSTRUCTURED HYDROGEL NETWORKS THROUGH PHOTOCURED BODY-CENTERED CUBIC BLOCK COPOLYMER MELTS		
4.1	CONSPECTUS	62
4.2	INTRODUCTION	62
4.3	RESULTS AND DISCUSSION	68
4.3.1	<i>Synthesis</i>	68
4.3.2	<i>Melt State Phase Behavior</i>	70
4.3.3	<i>Trapping of the S_{BCC} Morphology in ePB_{19.6}-PEO-11.5-0.5</i>	77
4.3.4	<i>Swelling Behavior of Cured ePB_{19.6}-PEO-11.5-0.5</i>	80
4.3.5	<i>Photopatterning of ePB_{19.6}-PEO-11.5-0.5</i>	83
4.4	CONCLUSIONS	84
4.5	EXPERIMENTAL	85
4.5.1	<i>Materials and Methods</i>	85
4.5.2	<i>Measurements</i>	86
4.5.3	<i>ω-hydroxy-polybutadiene (PB)</i>	87
4.5.4	<i>ω-hydroxy-polybutadiene-<i>b</i>-poly(ethylene oxide) (PB-PEO)</i>	87

4.5.5 Polybutadiene- <i>b</i> -poly(ethylene oxide)- <i>b</i> -polybutadiene (PB-PEO-PB) . . .	88
4.5.6 Epoxidation of PB-PEO/PB-PEO-PB Blends (<i>ePB</i> _{19.6} -PEO-11.5)	88
4.5.7 Photocuring of <i>ePB</i> _{19.6} -PEO-11.5-0.5.	89
4.6 ACKNOWLEDGEMENTS	90
4.7 SUPPORTING INFORMATION AVAILABLE	90
4.8 REFERENCES	90
CHAPTER 5	92
TUNABLE MECHANICAL PERFORMANCE OF BLOCK COPOLYMER HYDROGEL NETWORKS VIA UV PHOTOCOUPLING OF ANTHRACENE END-GROUPS	
5.1 CONSPECTUS	93
5.2 INTRODUCTION	93
5.3 RESULTS AND DISCUSSION	96
5.3.1 Synthesis and Physical Characterization.	96
5.3.2 Melt-State Morphological Characterization	97
5.3.3 UV Photocoupling of PS-PEO-An in the Melt-State	99
5.3.4 Swelling Behavior of UV Photocoupled PS-PEO-An Hydrogels.	100
5.3.5 Mechanical Performance of UV Photocoupled PS-PEO-An Hydrogels.	103
5.3.6 Preliminary Photoreversibility Experiment.	106
5.4 CONCLUSIONS	107
5.5 EXPERIMENTAL	108
5.5.1 Materials and Methods	108
5.5.2 Measurements	109
5.5.3 Synthesis of PS-PEO and PS-PEO-PS	110
5.5.4 Synthesis of PS-PEO-An	110
5.5.5 UV Photocoupling PS-PEO-Anthracene in the Melt Phase	111

5.6 ACKNOWLEDGEMENTS	111
5.7 REFERENCES	111
CHAPTER 6	114
SUMMARY — PART I — ACCESS TO UV PHOTOCURED NANOSTRUCTURES VIA SELECTIVE MORPHOLOGICAL TRAPPING OF BLOCK COPOLYMER MELTS	
6.1 MAJOR RESULTS	115
6.2 BROAD IMPACTS TO THE SCIENTIFIC COMMUNITY	116
PART II — MORPHOLOGICAL PHASE BEHAVIOR OF POLY(RTIL)- BASED BLOCK COPOLYMER MELTS	
CHAPTER 7	119
SYNTHESIS AND ORDERED PHASE SEPARATION OF IMIDAZOLIUM- BASED AKYL-IONIC DIBLOCK COPOLYMERS MADE VIA ROMP	
7.1 CONSPECTUS	120
7.2 INTRODUCTION	120
7.3 RESULTS AND DISCUSSION	122
7.3.1 <i>Synthesis</i>	122
7.3.2 <i>Solution-State Phase Behavior</i>	124
7.3.3 <i>Melt-State Phase Behavior</i>	125
7.4 CONCLUSIONS	128
7.5 ACKNOWLEDGEMENTS	129
7.6 SUPPORTING INFORMATION AVAILABLE	129
7.7 REFERENCES	129
CHAPTER 8	132
MORPHOLOGICAL PHASE BEHAVIOR OF POLY(RTIL) CONTAINING DIBLOCK COPOLYMER MELTS	

8.1	CONSPECTUS	133
8.2	INTRODUCTION	134
8.3	RESULTS AND DISCUSSION	137
	8.3.1 <i>Overview of Melt-State Phase Behavior.</i>	139
	8.3.2 <i>Lamellae</i>	142
	8.3.3 <i>Hexagonally Packed Cylinders.</i>	146
	8.3.4 <i>Coexistence of Lamellae and Hexagonally Packed Cylinders.</i>	149
	8.3.5 <i>Spherical</i>	157
8.4	CONCLUSIONS	160
8.5	EXPERIMENTAL	162
	8.5.1 <i>Materials and Methods.</i>	162
	8.5.2 <i>General Synthetic Procedures for the synthesis of poly(alkyl)-Ionic BCPs</i>	162
	8.5.3 <i>Representative Synthesis of Diblock Copolymer 1P</i>	163
	8.5.4 <i>Physical Measurements.</i>	164
	8.5.5 <i>Dynamic Mechanical Spectroscopy</i>	164
	8.5.6 <i>Small Angle X-ray Scattering (SAXS)</i>	164
	8.5.7 <i>Synchrotron SAXS Characterization</i>	165
8.6	ACKNOWLEDGMENTS	165
8.7	SUPPORTING INFORMATION AVAILABLE	165
8.8	REFERENCES	166
CHAPTER 9		170
SUMMARY — PART II — MORPHOLOGICAL PHASE BEHAVIOR OF POLY(RTIL) CONTAINING BLOCK COPOLYMER MELTS		
9.1	MAJOR RESULTS	171
9.2	BROAD IMPACTS TO THE SCIENTIFIC COMMUNITY	172

APPENDIX I	173
NETWORK FORMATION IN AN ORTHOGONALLY SELF-ASSEMBLING SYSTEM	

AI.1 CONSPECTUS	174
AI.2 INTRODUCTION	174
AI.3 RESULTS AND DISCUSSION	176
<i>AI.3.1 Synthesis</i>	176
<i>AI.3.2 Solution-State Phase Behavior</i>	177
<i>AI.3.2 Solid-State Phase Behavior</i>	177
<i>AI.3.3 Mechanical Performance</i>	180
AI.4 CONCLUSIONS	182
AI.5 SUPPORTING INFORMATION AVAILABLE	182
AI. 6 ACKNOWLEDGEMENTS	183
AI. 7 REFERENCES	183

APPENDIX II	185
-----------------------	-----

SUPPLEMENTARY INFORMATION

CHAPTER 3 — SUPPLEMENTARY INFORMATION— THERMALLY STABLE PHOTOCURING CHEMISTRY FOR SELECTIVE MORPHOLOGICAL TRAPPING IN BLOCK COPOLYMER MELT SYSTEMS	186
CHAPTER 4 — SUPPLEMENTARY INFORMATION— ACCESS TO NANOSTRUCTURED HYDROGEL NETWORKS THROUGH PHOTOCURED BODY-CENTERED CUBIC BLOCK COPOLYMER MELTS	188
CHAPTER 7 — SUPPLEMENTARY INFORMATION— SYNTHESIS AND ORDERED PHASE SEPARATION OF IMIDAZOLIUM-BASED ALKYL- IONIC DIBLOCK COPOLYMERS MADE VIA ROMP	192
CHAPTER 8 — SUPPLEMENTARY INFORMATION— MORPHOLOGICAL PHASE BEHAVIOR OF POLY(RTIL) CONTAINING DIBLOCK COPOLYMER MELTS	210
APPENDIX I — SUPPLEMENTARY INFORMATION— NETWORK FORMATION IN AN ORTHOGONALLY SELF-ASSEMBLING SYSTEM	244

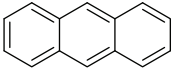
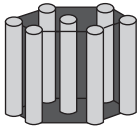
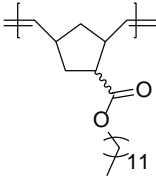
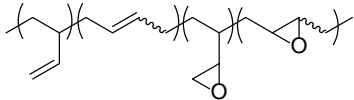
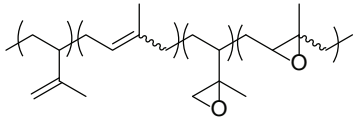

PART I — ACCESS TO UV PHOTOCURED NANOSTRUCTURES VIA
SELECTIVE MORPHOLOGICAL TRAPPING OF BLOCK COPOLYMER
MELTS

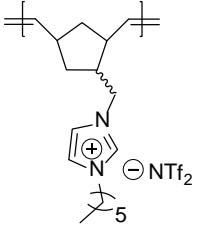
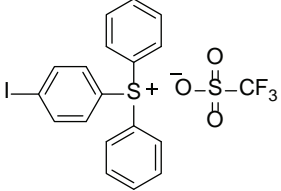
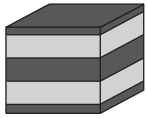

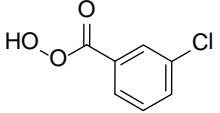
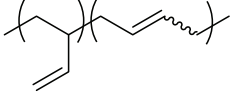
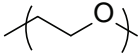
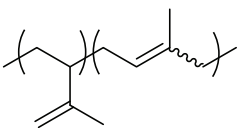
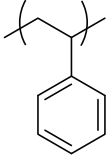
CHAPTER 1

INTRODUCTION AND PERSPECTIVE OF DISSERTATION

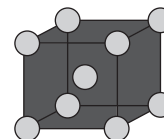
The contents of this dissertation chapter were written by Vincent F. Scalfani.

1.1 COMMON ABBREVIATIONS AND CHEMICAL STRUCTURES USED WITHIN DISSERTATION

Abbreviation	Full Name	Chemical Structure/ Cartoon (Where Applicable)
An	Anthracene	
BCC	Body-centered cubic	
BCP	Block copolymer	
C/Hex	Hexagonally packed cylinders	
χ	Flory interaction parameter	
Dis	Disordered	
DOD	Poly(norbornene dodecyl ester)	
DOSY	Diffusion ordered spectroscopy	
DSC	Differential scanning calorimetry	
ePB	Partially epoxidized polybutadiene	
ePI	Partially epoxidized polyisoprene	
G/Gyr	Gyroid	
G'	Storage (elastic) modulus	
G''	Loss (viscous) modulus	
GPC	Gel permeation chromatography	
IL	Ionic liquid	

IMD	Poly(norbornene imidazolium)	
IPDPST	(4-Iodophenyl)diphenylsulfonium triflate photoinitiator	
L/Lam	Lamellae	
L _C	Crystalline Lamellae	
LLP	Liquid-like packing	
MCPBA	3-chloroperoxybenzoic acid	
MW	Molecular weight	
NMR	Nuclear Magnetic Resonance	
ODT	Order-disorder transition	
OOT	Order-order transition	
PB	Polybutadiene	
PEO	Poly(ethylene oxide)	
PI	Polyisoprene	
PS	Polystyrene	

ROMP	Ring-opening metathesis polymerization
RTIL	Room temperature ionic liquid
SAXS	Small-angle X-ray scattering
S_{BCC}	Spheres on a body-centered cubic lattice
SEC	Size exclusion chromatography



1.2 BRIEF OVERVIEW OF DISSERTATION

The purpose of this introductory chapter is to provide context and perspective for the research involved in completing this dissertation. There are four main studies within parts I and II of the dissertation: a) Development of photocuring chemistry for selective trapping of block copolymer (BCP) melt nanostructures (Chapter 3), b) Nanostructured hydrogel networks (Chapters 4 and 5), c) Synthesis and phase behavior of poly(RTIL)-based block copolymers (Chapters 7 and 8), and d) Orthogonal supramolecular polymer motif networks (Appendix I). The following sections describe the project history and a brief account of each project individually. Introduction to chemical details and a literature review specific to each goal is reserved for the individual chapters; the majority of chapters contained in this dissertation have been adapted from published work (*accepted format according to the Colorado State University Graduate School*) containing comprehensive introductions specific to each desired goal. Citations of published work that is contained in this dissertation are listed below, and are also noted at the beginning of the corresponding chapter title page.

Chapter 3 — Scalfani, V. F.; Bailey, T. S. Thermally Stable Photocuring Chemistry for Selective Morphological Trapping in Block Copolymer Melt Systems. *Chem. Mater.* **2010**, *22*, 5992–6000.

Chapter 4 — Scalfani, V. F.; Bailey, T. S. Access to Nanostructured Hydrogel Networks Through Photocured Body-Centered Cubic Block Copolymer Melts. *Macromolecules* **2011**, *44*, 6557–6567.

Chapter 7 — Wiesenauer, E. F.; Edwards, J. P.; Scalfani, V. F.; Bailey, T. S.; Gin, D. L. Synthesis and Ordered Phase Separation of Imidazolium–Based Alkyl–Ionic Diblock Copolymers Made via ROMP. *Macromolecules* **2011**, *44*, 5075–5078.

Chapter 8 — Scalfani, V. F.; Wiesenauer, E. F.; Ekblad, J. R.; Edwards, J. P.; Gin, D. L.; Bailey, T. S. Morphological Phase Behavior of Poly(RTIL) Containing Diblock Copolymer Melts. *Macromolecules* **2012**, submitted.

Appendix I — Mes, T.; Koenigs, M. M. E.; Scalfani, V. F.; Bailey, T.S.; Meijer, E.W.; Palmans, A. R. A. Network Formation in an Orthogonally Self-Assembling System *ACS Macro Lett.* **2011**, *1*, 105.

1.3 PHOTOCURING CHEMISTRY FOR SELECTIVE CURING OF BLOCK COPOLYMER MELTS (CHAPTER 3)

In chapter 3, a thermally stable UV cationic photoinitiator system was developed for selective curing of block copolymer melt nanostructures. The developed photocuring system was comprised of partially epoxidized polydiene-based block copolymer and UV cationic photoinitiator composite blends. After melt-processing the composite blends to obtain the targeted nanoscale structure, UV irradiation was used to permanently translate the melt-state structure to the solid analogue with high fidelity. The curing mechanism is completely independent of the required thermal melt-processing, which is particularly useful for solidifying specific melt morphologies in block copolymer systems exhibiting multiple thermally accessible phase-separated nanostructures.

Unfortunately, much of the preliminary research towards the photocuring of block copolymer melts did not become part of this dissertation. The original project was aimed at developing a nanostructured hydrogel system based on spherical forming poly(siloxane)-*b*-poly(ethylene oxide) BCPs where the polysiloxane block could be cross-linked independent of any thermal processing (necessary for the BCP self-assembly process). However, developing a cross-linkable poly(siloxane)-*b*-poly(ethylene oxide) BCP proved to be synthetically challenging within the available time frame of this dissertation. In fact, many months of research went into developing new cyclic epoxy monomers and epoxy functional polysiloxane homopolymers. The biggest

challenge in synthesizing a cross-linkable epoxidized polysiloxane-*b*-poly(ethylene oxide) BCP is avoiding a silyl ether bond linkage (formed through sequential polymerization, and easily cleavable with acid or base) between the polysiloxane and poly(ethylene oxide) block. Several coupling strategies were explored that utilized protected initiator or terminating agents on the polysiloxane block, which would eliminate the silyl ether linkage between the polysiloxane and poly(ethylene oxide) block. Deprotecting the initiator and/or terminating agents, most often relying on basic conditions, repeatedly led to severe degradation of the polysiloxane block. In hindsight, strategies using terminating agents that can be readily deprotected in mild acidic conditions such as silyl protected amines would, perhaps, have been more successful. In addition, strategies where the epoxy modified polysiloxane is end-functionalized with a macroinitiator (e.g. for controlled free-radical polymerization) may also have been an excellent alternative to produce a cross-linkable polysiloxane with a hydrophilic block (notably, a hydrophilic monomer compatible with the initiation method would have to be selected). Ultimately, it was realized that the desired goal of fabricating a cross-linked nanostructured BCP hydrogel could be more easily achieved with a polydiene-*b*-poly(ethylene oxide) BCP system, which is synthetically straightforward. I look forward to future students revisiting the polysiloxane BCP project; in fact, polysiloxane-based BCPs are still very appealing alternative materials for much of the work accomplished in this dissertation.

After synthesizing several partially epoxidized polyisoprene-*b*-poly(ethylene oxide) BCPs and exploring some of the thermal properties of the cationic photocuring chemistry, we realized that the system would have implications beyond fabricating nanostructured spherical hydrogels. The composite materials were found to exhibit excellent thermal stability and have curing conditions completely independent of any melt processing below ~200 °C in the epoxidized polyisoprene-*b*-poly(ethylene oxide) system. We hypothesized that having a curing mechanism solely triggered with UV light and independent of temperature could be extremely useful in selectively trapping different morphologies from a single block copolymer containing multiple thermally accessible nanostructures. Chapter 3 is the product and research support-

ing the aforementioned hypothesis. To our knowledge, this was the first example of selectively trapping two different temperature-dependent morphologies from one BCP sample.

1.4 NANOSTRUCTURED HYDROGEL NETWORKS (CHAPTERS 4 AND 5)

The developed photocuring system in Chapter 3 was then utilized to fabricate pre-structured hydrogels in Chapter 4. The hydrogel networks were based on a spherical tethered system of AB diblock and ABA triblock comprised of hydrophobic junction points (A domains) and hydrophilic (B) domains which are selectively swollen in compatible media. Specifically, the hydrogels were built from UV cross-linked partially epoxidized polybutadiene-*b*-poly(ethylene oxide)/polybutadiene-*b*-poly(ethylene oxide)-*b*-polybutadiene ePB-PEO/ePB-PEO-ePB copolymer blends with an added amount of cationic photoacid initiator. The composite blends were pressed as disks and photocured directly in the melt, permanently locking in the pre-structured tethered BCC spherical morphology. After swelling disks in aqueous or organic media, gels preserved their original shape, had excellent mechanical properties and were highly elastic.

Chapter 4 fulfilled the original proposed goals of fabricating a chemically cross-linked BCP hydrogel that self-assembled in the melt independent of the curing kinetics. In fact, the vast majority of proposed research for this dissertation was fulfilled in Chapter 4. Notably, the fabricated hydrogel networks represent *one of many* possible applications of the thermally stable photocuring chemistry initially developed in Chapter 3.

The chemically cross-linked ePB/ePB-PEO-ePB hydrogels were researched in parallel to a similar physically cross-linked hydrogel system based on polystyrene-*b*-poly(ethylene oxide) AB and ABA blends studied in the Bailey research group and experimentally led by Chen Guo (Colorado State University). Pre-structured hydrogels built from PS-PEO/PS-PEO-PS blends were found to have excellent properties such as preservation of shape, good mechanical properties, and adjustable swelling. The chemically cross-linked hydrogels developed in this dissertation overcame several limitations of the vitrified physically cross-linked PS-PEO/PS-PEO-PS hydrogels including: 1) access to lower molecular weights resulting in highly ordered melt structures, 2) organic solvent compatibility, and 3) greater accessibility of smaller mesh

sizes and swelling ratios.

In Chapter 5, a nanostructured hydrogel system based on pre-structured anthracene end-tagged PS-PEO melts was developed. This eliminated the necessity to pre-blend a set amount of triblock tethers, in the original PS-PEO/PS-PEO-PS system. Pressed disks of anthracene functional PS-PEO were photocoupled directly in the melt-phase, forming a concentration of triblock *in situ* which is controlled directly by adjusting the amount of UV light exposure. Swollen disks were found to be highly elastic with tunable mechanical properties and swelling simply by controlling the amount of UV irradiation time.

Originally, we sought to fabricate anthracene functional ePB-PEO hydrogels, as this would have been a direct extension to the ePB-PEO hydrogels developed in Chapter 4; however complications separating the photocuring chemistry from the anthracene coupling precluded further exploration of the system within this dissertation. It was quickly discovered that the required curing step (also based on UV light) photocoupled a significant amount of anthracene groups (20 mol %), allowing for little control over subsequent anthracene photocoupling (maximum achieved photocoupling efficiency was about 50 mol %). The use of narrow bandpass filters such as 254 nm to prevent anthracene coupling, did not allow for efficient photo cross-linking, likely a result of the reduced filtered light intensity. It made sense, for the initial development of anthracene functional gels, to completely eliminate the photocuring chemistry by developing a physically cross-linked system first and then returning to the chemically cross-linked system in a future study. PS-PEO, which did not require chemically cross-linking, was a better suited material for an initial development of self-assembled anthracene functional hydrogels, and proved to be quite successful in Chapter 5. Future researchers may achieve the separation of the photocuring and photocoupling steps in anthracene functional ePB-PEO melts by using selective filters containing a broad transmission wavelength range (e.g. 200–300 nm) that can efficiently cross-link the epoxy groups independent of anthracene (or alternative photodimerizing species) coupling.

1.5 SYNTHESIS AND PHASE BEHAVIOR OF POLY(RTIL)-BASED BLOCK COPOLYMERS (CHAPTERS 7 AND 8)

In Chapter 7, a new highly charged BCP was synthesized by the sequential ring-opening metathesis polymerization (ROMP) of a dodecyl ester norbornene and charged imidazolium norbornene monomer. Some nanoscale morphological analysis is also presented in Chapter 7 which helped to confirm the block architecture. In Chapter 8, a total of 16 poly(RTIL)-based block copolymers were synthesized for a complete melt-state morphological analysis. A phase diagram was developed through a systematic characterization of the morphological behavior through a combination of small-angle X-ray scattering (SAXS) and dynamic rheology.

The poly(RTIL)-based block copolymer project began in the Douglas L. Gin group at Colorado University Boulder, Boulder, CO. Erin F. Wiesenauer and Julian P. Edwards were synthesizing these unique BCPs, and already had some convincing evidence, such as solubility and NMR DOSY studies, suggesting the materials were indeed block copolymers. Unfortunately, direct evidence confirming the BCP architecture could still not be achieved with straightforward experiments such as GPC and dynamic light scattering due to complications of the highly charged nature of the polymers. We ran some rheological and SAXS experiments at Colorado State University on the charged BCP samples which led to conclusive confirmation of the block architecture (Chapter 7). The collaboration continued into Chapter 8, where Erin and Julian synthesized the BCPs and we developed the phase diagram of the poly(RTIL)-based block copolymer system. These are very exciting materials for two reasons: 1) the ionic block is polymerized directly from a charged monomer, which is atypical in synthesizing charged BCPs, often the ionic block is introduced as a post-polymerization modification in other charged BCP systems and 2) nearly all of the BCPs synthesized self-assemble into very well-defined nanoscale melt morphologies, potentially useful for many new materials requiring incorporation of an ionic liquid polymer such as separation membranes. This project could not have been completed without the hard work of every member of the research team; I very much look forward to the future development of similar charged BCP systems and, better yet, the develop-

ment and morphological characterization of triblock installments.

1.6 ORTHOGONAL SUPRAMOLECULAR POLYMER MOTIF NETWORKS (APPENDIX I)

In Appendix I, a supramolecular polymer system was studied that contains two unique nanorod forming supramolecular functional group motifs. The two motifs self-assemble independently to form two separate nanorods, which produces a material lacking in mechanical properties. However when a telechelic polymer containing both unique motifs is introduced into the system a cross-linked network is formed. The resulting supramolecular material with the cross-linker exhibits excellent elastomeric and mechanical properties.

This project began in the E.W. (Bert) Meijer group (Eindhoven University of Technology, The Netherlands) with Tristan Mes, Marcel M. E. Koenigs, and Anja R.A. Palmans. The proposed research required a narrow molecular weight telechelic hydrogenated polybutadiene homopolymer, which we had some experience with in our lab. Interestingly, it looked very straightforward on paper to synthesize a difunctional polybutadiene through the use of a protected anionic initiator with subsequent ethylene oxide quenching. It took us quite a bit longer than expected to synthesize the difunctional homopolymer due to complications of unwanted deprotection of the initiator during the end-functionalization with ethylene oxide step. It turns out that by simply quenching the oxanion within about an hour (classically ethylene oxide is allowed to react overnight with polymer carbanion end-chain alcohol functionalization), a near perfect (~98%) telechelic homopolymer was synthesized. The Meijer group was then able to functionalize the homopolymer with the supramolecular motifs for use in the orthogonally self-assembling nanorod network study. We also performed the rheological melt analysis of the supramolecular materials here at Colorado State University which greatly aided in the confirmation of network formation and increased mechanical properties upon introduction of the difunctional cross-linker motif. Collaborating on this project with the Meijer group was a fantastic experience and opportunity to work with some unique polymeric materials that were very different compared to the majority of polymeric materials studied in this dissertation. I

hope that our collaborative contribution facilitates future studies with cross-linked polymer networks based on supramolecular self-assembly.

1.7 FINAL REMARKS BEFORE DISSERTATION MAIN TEXT

There are several chapters not mentioned in this introduction including chapters 2, 6, 9, and Appendix II. Chapter 2 is an overview of the main experimental characterization techniques used throughout the dissertation, which should also be useful for other researchers studying BCPs. Chapters 6 and 9 contain a summary of the major results and impacts to the scientific community for parts I and II of the dissertation, respectively. Appendix II is a compilation of the supporting information noted throughout the dissertation. Much of the work in this dissertation was highly collaborative, some of which was described and acknowledged above; delineation of all research within this dissertation can be found at the beginning of each chapter.

CHAPTER 2

INTRODUCTION TO BLOCK COPOLYMER THERMODYNAMICS AND EXPERIMENTAL CHARACTERIZATION TECHNIQUES USED WITHIN DISSERTATION

The contents of this dissertation chapter were written by Vincent F. Scalfani.

2.1 CONSPECTUS

The purpose of this chapter is to present a brief introduction to block copolymer phase behavior (linear AB diblocks) and an overview of the main experimental characterization techniques used throughout the dissertation for the characterization of block copolymer based materials. Discussion of characterization methods including NMR, size-exclusion chromatography (SEC), dynamic mechanical spectroscopy (rheology), and small-angle X-ray scattering (SAXS) will be limited to the experiments and data analysis procedures used within the context of the completed thesis research. Detailed background, discussion of instrumental components, and other experiments with the aforementioned techniques are reserved for the references cited. The general data collection practices are presented along with a worked example of data analysis where applicable.

2.2 BLOCK COPOLYMER THERMODYNAMICS AND MELT-STATE PHASE BEHAVIOR

Block copolymers (BCPs)¹⁻⁴ have continued to be of current interest to researchers over the past several decades as a result of their inherent ability to self-assemble on the nanometer length scale (typically 10–100 nm). Past comprehensive research performed both theoretically⁵⁻⁸ and experimentally⁹⁻¹¹ has built a strong foundation for future researchers seeking to exploit the self-assembled phase behavior of block copolymer nanostructures for use in a variety of applications such as electronics, fuel cells, nanolithography and templating.¹²⁻¹⁶ In the most simplistic BCP, two chemically distinct homopolymers are joined together covalently, forming a linear AB diblock copolymer. Microphase separation on the nanometer length scale in BCPs is driven by the degree of incompatibility of the constituent blocks which can be characterized by the product χN , where χ is the Flory–Huggins interaction parameter and N is the segmental volume of a chosen repeat unit. If the product χN is large enough, and exceeds a critical point, it becomes energetically more favorable to microphase separate into an ordered morphology than to form an isotropic mixture (disordered state). The adopted equilibrium geometry of

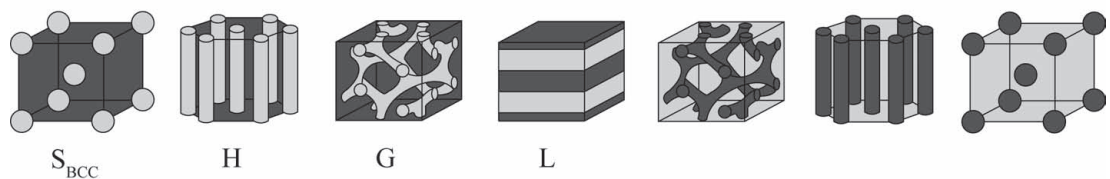
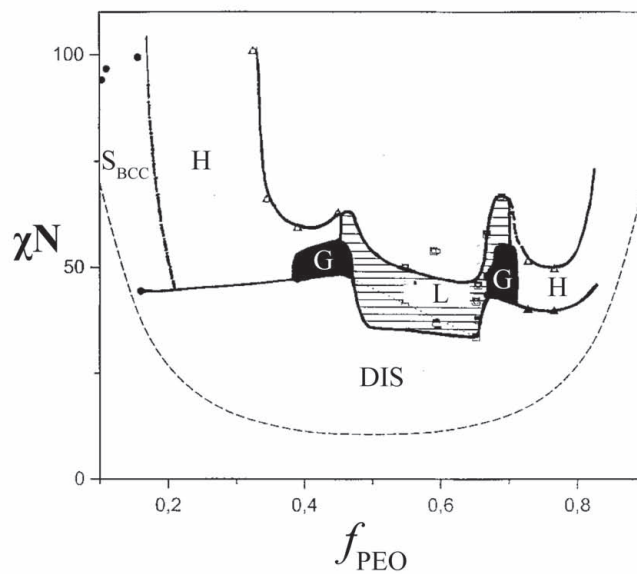
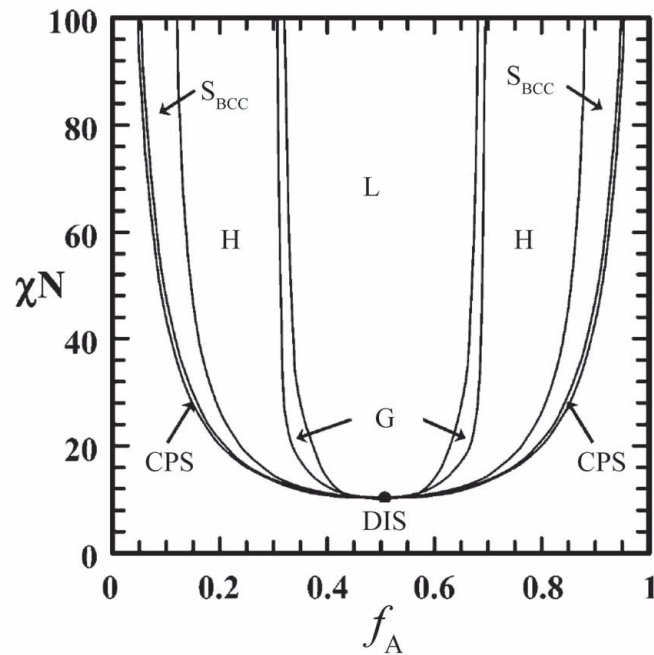


Figure 2-1. Calculated self-consistent field theory (SCFT) phase diagram for a linear AB diblock copolymer. Reproduced with permission from ref 8 (top). Experimental phase diagram for a linear polyisoprene-*b*-poly(ethylene oxide) block copolymer, reproduced with permission from ref 9 (bottom). The theoretical and experimental phase diagrams are remarkably similar, particularly with the location of compositional morphological phase boundaries. The asymmetric nature of the experimental PI-PEO phase diagram is attributed to the conformational asymmetry of the constituent block segments.

the phase separated state is then determined by the sensitive balance of entropic chain stretching and enthalpic interfacial surface contact energy; both parameters can be finely tuned through judicious choice of monomers, architecture, length, and relative volume fraction of the blocks.^{1,2,5} In linear AB diblock copolymer systems, four primary self-assembled morphologies are adopted which include spheres on a body-centered cubic lattice (S_{BCC}), hexagonally packed cylinders (H), bicontinuous gyroid (G), and lamellae (L) (Figure 2-1).

As demonstrated qualitatively in Figure 2-2, the thermodynamics of BCP phase separation can be envisioned as a pseudo two-step process; that is, first and foremost, is it energetically favorable to mix or phase separate? And second, if it is energetically favorable to phase separate, which ordered morphology provides a structure that balances the interfacial surface contact and chain stretching penalties to produce the lowest free energy? Importantly, there is a substantial difference in the free energy of a disordered state (G_{DIS}) compared to a phase separated ordered state in the strong segregation limit (SSL, lower temperatures). However, the relative energy differences of the ordered morphological states (G_{BCC} , G_{H} , G_{G} , G_{L}) are less drastic, but differ significantly enough to be highly selective at equilibrium. In the weak segregation limit (WSL, higher temperatures), the free energy of the ordered states and disordered state are of similar magnitude and eventually converge at an order-to-disorder (ODT) boundary where the ordered state energies become greater than the disordered state free energy.

Hypothetical free energy profiles of the disordered (G_{DIS}) and phase separated ordered states (G_{BCC} , G_{H} , G_{G} , G_{L}) of two AB diblock copolymers with differing relative block fractions are shown in Figure 2-2. At equilibrium, the BCPs will self-assemble into the morphology (including an ordered state or disordered state) with the lowest free energy, denoted by the bolded paths in Figure 2-2. In the first example (Figure 2-2 top), a BCP with a symmetric volume fraction ($f_{\text{A}} \approx 0.5$) self-assembles into the lamellar morphology (lowest energy) along the thermal trajectory until becoming disordered at higher temperatures. The morphological behavior of this symmetric BCP example is fairly simplistic along its entire thermal trajectory; there exists one ordered lamellar state and a disordered state after an ODT transition. In the

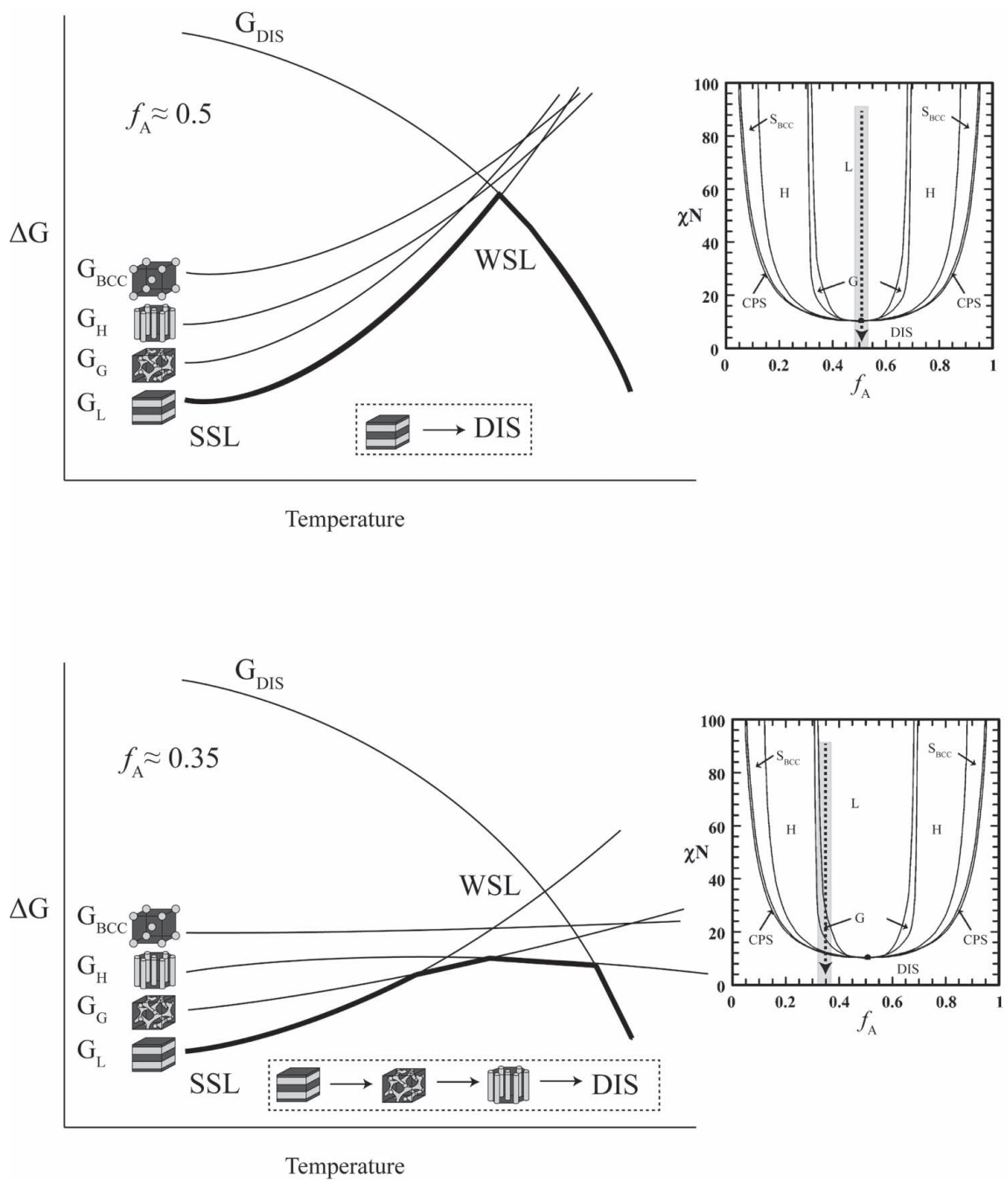


Figure 2-2. Qualitative depictions of the free energy of the disordered (G_{DIS}) and ordered states (G_{BCC} , G_H , G_G , G_L) of a linear AB diblock copolymer. The adopted morphology with the lowest free energy ($f_A \approx 0.5$ top, and $f_A \approx 0.35$, bottom) is represented by the bold line. Inset figures are SCFT calculated phase diagrams, adapted from ref 8, which show the plotted qualitative thermal trajectories (outlined in grey).

second example (Figure 2-2 bottom), a BCP with some asymmetry ($f_A \approx 0.35$) was chosen, where the self-assembled morphology becomes much more complex and extremely dependent on the chosen temperature. Analogous to the first example, there is a clear distinction between the free energy of the mixed state (G_{DIS}) and ordered states (G_{BCC} , G_{H} , G_{G} , G_{L}) at low temperatures (SSL). In addition, the lamellar morphology with the lowest free energy is also adopted in the SSL. However, following the path with the lowest free energy reveals several locations where the free energies of the morphological states cross, resulting in several order-to-order transitions (OOT) before disordering at higher temperature. Following the bolded line representing the path with the lowest free energy shows the BCP would transform from lamellae to gyroid, and then from gyroid to hexagonally packed cylinders, and then finally disordered. Importantly, many experimental BCP systems exhibit complex phase behavior similar to the aforementioned hypothetical example; that is, adoption of multiple temperature dependent morphologies. An example of an experimental BCP system (PI-PEO) that exhibits similar complex behavior is discussed in Chapter 3.

Notably, only simple AB diblock copolymers have been considered here for the introduction to block copolymer thermodynamics. Increasing complexity of the block copolymer will alter the adopted morphology, for example addition of just one more block, C, forming a linear ABC triblock copolymer results in an array of exquisite and complex spatially periodic morphologies; a product of the added incompatibility of not only A-B, but also A-C and C-B block interactions.¹⁷ Modern synthetic techniques¹⁸⁻²² allow for precise tuning of chemical composition, block sequence and numerous architectures such as rigid rod-coil, cyclic, and star, which can, of course, further increase the complexity of the adopted nanoscale phase separated geometries.^{4, 23, 24}

2.3 EXPERIMENTAL CHARACTERIZATION TECHNIQUES FOR BCPs

2.3.1 Nuclear Magnetic Resonance (NMR)

NMR is an extremely powerful characterization technique available to distinguish the chemical

structures of species. While there are a multitude of available experiments and techniques based on the principles of NMR,²⁵⁻²⁷ proton (¹H) NMR was the most relevant and useful NMR experiment in this dissertation work for the physical characterization of polymers. In contrast to most small molecules where line widths are fairly narrow and well-resolved, typical ¹H NMR spectra of polymers often have much broader line widths.^{26, 28} The broad nature of the line width in polymer spectra is generally a result of a combination of: (1) long correlation times (slow molecular movement) resulting in more efficient spin-spin relaxation (T_2) of nuclei,^{26, 28} and (2) presence of multiple similar nuclei (i.e., chain backbone) absorbing a range of frequencies, rather than a single frequency.²⁸ Shorter T_2 relaxation times and absorptions of a band of frequencies both produce broader lines.^{25, 26, 28} Despite the broad nature of line-width inherent to ¹H NMR polymer characterization, in general integrations are still relatively accurate (~5%) and amenable to several critical calculations such as end-group analysis and relative block fractions. In fact, sometimes the broad nature of the line width is advantageous to polymer end-group analysis, as most often the line width of end-group protons are broadened compared to its analogues freely unbound molecule. The broad nature of bound end-group fragment protons is often useful in determining if end-tagging was successful and/or if there is residual free end-group molecules contaminating the sample.

In a typical ¹H NMR experiment for the polymers studied herein, 20–40 mg of sample is dissolved in 1.0 mL CDCl₃. A larger amount of sample is utilized compared to small molecule analysis, as the concentration of end-groups is small compared to the polymer chain. In addition to using a larger amount of sample, a time delay (20–60 s) is typically added between trials (32–128) to ensure complete relaxation of end-group nuclei in an effort to obtain greater intensity.

2.3.2 End-group Analysis

End-group analysis^{29, 30} allows for the determination of the number average molecular weight of polymers, providing there is a sufficient concentration of end-groups (> 1% relative to polymer

chain²⁹) and they are resolved from the protons associated with the backbone repeat units. An example ¹H NMR of alcohol terminated polybutadiene (PB-OH) is depicted in Figure 2-3. A typical procedure for end-group analysis is to normalize the integrations relative to the number of initiator protons (i.e. 6 for *sec*-butyllithium initiated butadiene). Then, two equations can be extracted, where *A* and *B* are the integral values and *x* and *y* are the number of repeat units:

$$A = x + 2y \quad \text{Equation 2-1}$$

$$B = 2x \quad \text{Equation 2-2}$$

After solving the former two equations, the M_n value can be determined by multiplying the total repeat units (*x* + *y*) by the MW of a butadiene repeat unit. The relative amount of 1,4 addition to 1,2 addition can be calculated with:

$$\%1,4 = \frac{y}{y+x} \times 100 \quad ; \quad \%1,2 = \frac{x}{y+x} \times 100 \quad \text{Equation 2-3}$$

Lastly, the efficiency of chain termination can be determined from the relative ratio of the initiator to end-group fragment. In the particular example of PB-OH depicted in Figure 2-3, the relative ratio for quantitative functionality would be $CH_3-CH_2-C(R)H-CH_3$ (initiator): $-CH_2-OH$ (end-group) = 6 : 2. All polymer samples in this dissertation contained near quantitative (within 5% NMR error) functionality of terminating agent or post-polymerization end-tagging (also confirmed with SEC, *vide infra*).

2.3.3 Volume Fraction Determination

The volume fraction of the polydiene based BCPs synthesized in this work were determined from relative NMR integrations, similarly to the previous end-group analysis discussion where:

$$A = x + 2y \quad \text{Equation 2-4}$$

$$B = 2x \quad \text{Equation 2-5}$$

$$C = 4z \quad \text{Equation 2-6}$$

A, B, and C are the integral values and x , y , and z represent the individual repeat units (Figure 2-4). Again, the M_n value can be determined by multiplying the repeat units ($x + y, z$) by the corresponding MW of the repeat unit. The volume fraction of the PB-PEO BCP example can then be calculated with:

$$f_{PB} = \frac{\frac{M_{nPB}}{\rho_{PB}}}{\frac{M_{nPB}}{\rho_{PB}} + \frac{M_{nPEO}}{\rho_{PEO}}} \quad \text{Equation 2-7}$$

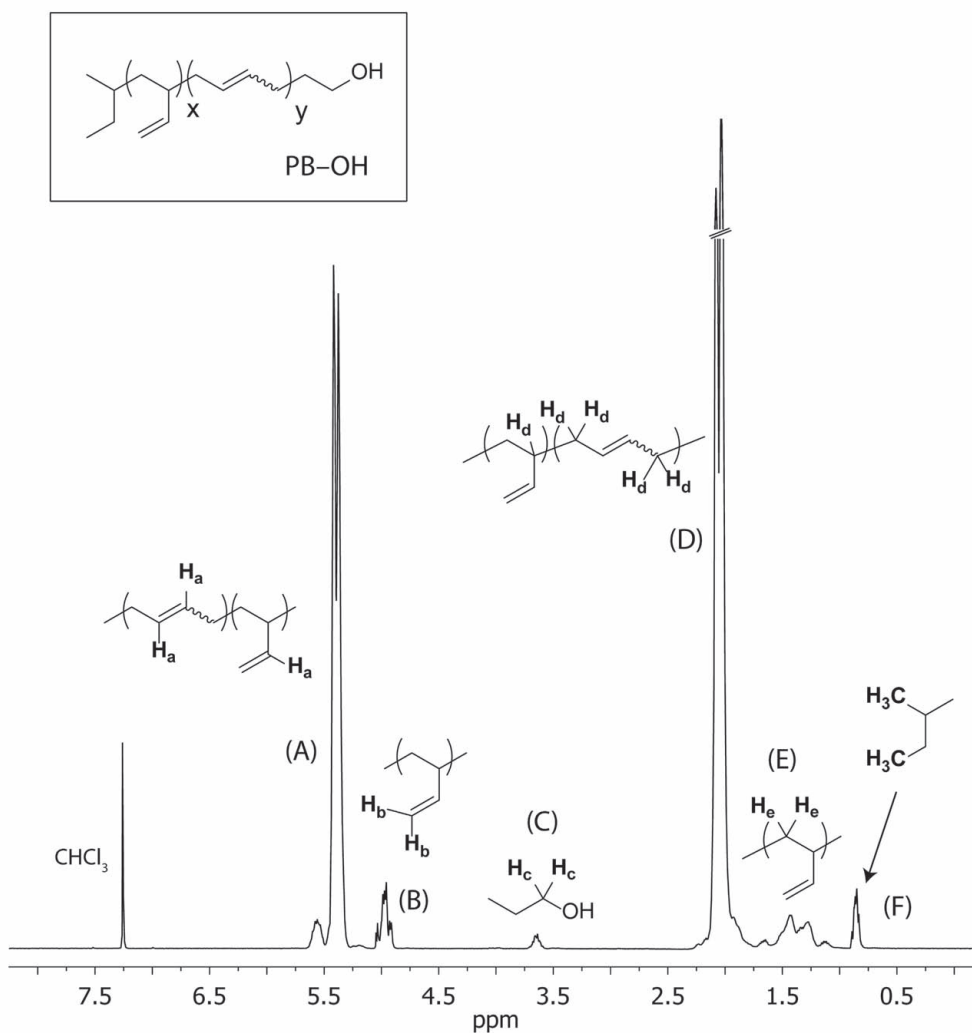


Figure 2-3. 1H NMR of a hydroxyl terminated polybutadiene homopolymer. End-group analysis and determination of relative amount of *cis* to *trans* units can be calculated with Equations 2-1 through 2-3. Further characterization can be found in Chapter 4.

The densities used for PB/PI and PEO in this work were taken from tabulated literature values compiled by Fetters et al.³¹

2.3.4 Percent Epoxidation Determination

A partially epoxidized PB/PB-PEO-PB blend ¹H NMR is shown in Figure 2-5. The relative amount of epoxidized units to diene units can be calculated as follows:

$$A = 2P + Q ; P = \frac{A}{2} - \frac{B}{4} \quad \text{Equation 2-8}$$

$$B = 2Q ; Q = \frac{B}{2} \quad \text{Equation 2-9}$$

$$C = 2R + S ; R = \frac{C}{2} - \frac{E}{4} \quad \text{Equation 2-10}$$

$$E = 2S ; S = \frac{E}{2} \quad \text{Equation 2-11}$$

$$D = 2T ; T = \frac{D}{2} \quad \text{Equation 2-12}$$

Where *A-E* are the integral values and *P-T* are the unique repeat units. Combining the above equations, an expression for the total % epoxidation (*E*) can be derived, as well as % epoxidation of the various units including 1,2, 1,4 cis and 1, 4 trans:

$$\%E = \frac{R + S + T}{P + Q + R + S + T} \times 100 \quad \text{Equation 2-13}$$

$$\%1,2E = \frac{S}{P + Q + R + S + T} \times 100 \quad \text{Equation 2-14}$$

$$\%1,4Trans E = \frac{T}{P + Q + R + S + T} \times 100 \quad \text{Equation 2-15}$$

$$\%1,4\text{Cis } E = \frac{R}{P+Q+R+S+T} \times 100$$

Equation 2-16

Notably in the example provided in Figure 2-5, epoxidation of 1,2 units is ~0 but equations were provided regardless for reference.

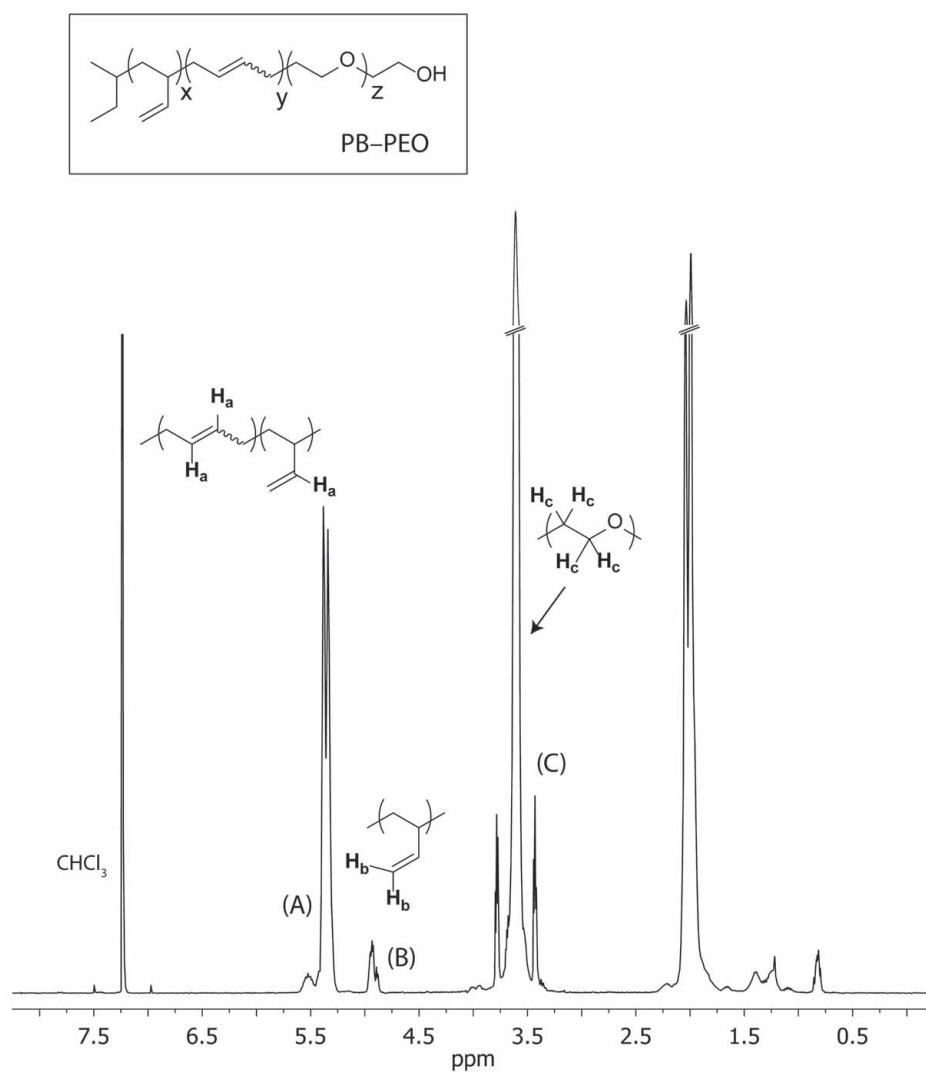


Figure 2-4. ¹H NMR of a hydroxyl terminated polybutadiene-*b*-poly(ethylene oxide) PB-PEO BCP. The relative volume fraction of the block can be calculated with Equations 2-7. Further characterization can be found in Chapter 4.

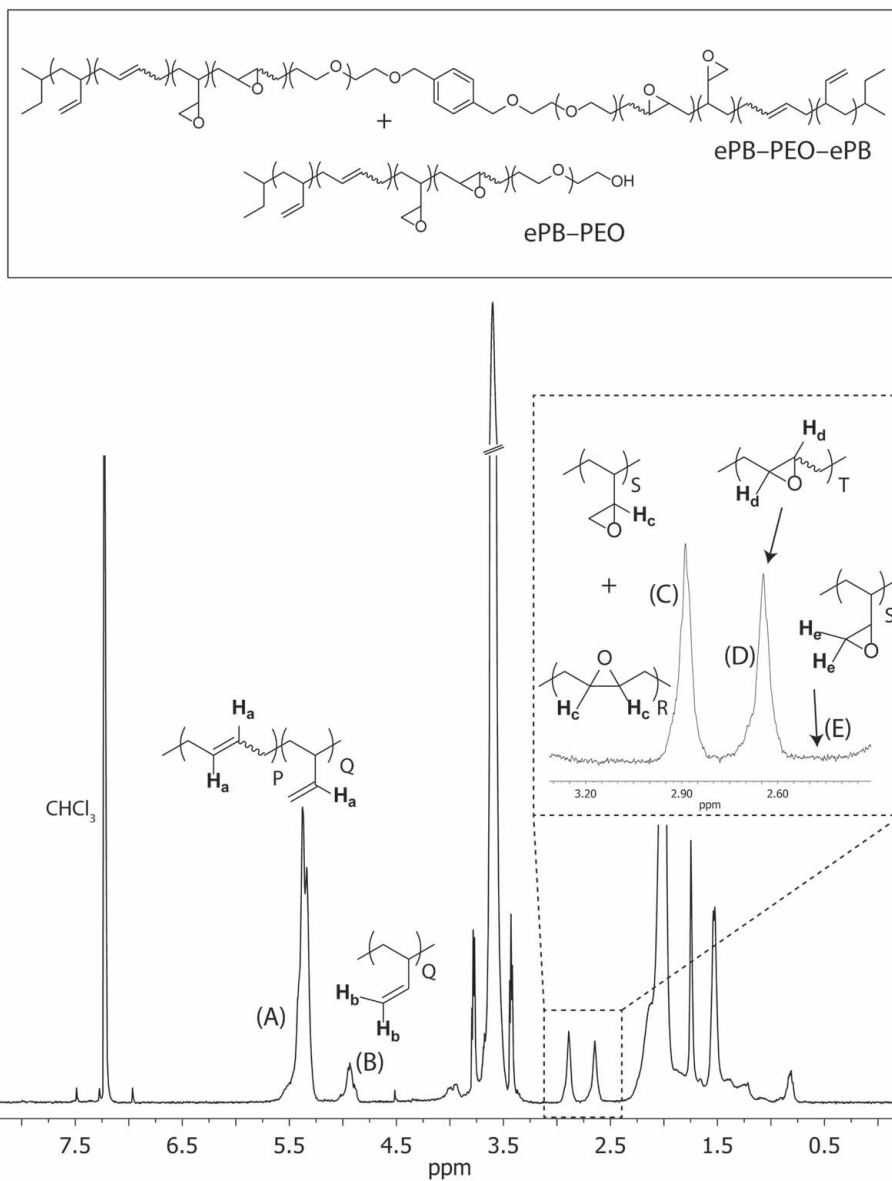


Figure 2-5. ¹H NMR of a blend of diblock and triblock epoxidized PB-PEO BCP. Epoxidation analysis including total amount relative to original diene units, and ratio of epoxidized cis and trans units can be calculated with Equations 2-8 through 2-16. Further characterization can be found in Chapter 4.

2.3.5 Size Exclusion Chromatography (SEC)

SEC is a liquid chromatography technique commonly employed in polymer science to separate macromolecules of different sizes. This separation technique can provide information about molecular weight, molecular weight distribution, chemical composition, and architecture. Data that can be readily acquired from the separation process is dependent upon the efficiency of column separation, method of calibration, and type(s) of detection used.^{29,30} The SEC system in this dissertation exclusively utilized a refractive index (RI) detector with a calibration method based on known homopolymer standards (PS or PEO).

In a typical experiment, 5–10 mg of polymer sample(s) are dissolved in THF (eluting solvent), filtered and injected into the SEC/RI detector instrument. The calibration standards (usually 5–8 different molecular weights) were also run shortly after, following injection of the sample(s). Characterization information that could be easily obtained from the resulting chromatograms included molecular weight distribution, chemical composition (e.g. triblock vs. diblock content), and some architectural characteristics (e.g. connectivity of polymer blocks). Figure 2–6 depicts a series of polymer samples starting from a parent PB–OH functional homopolymer. It is clearly evident that after the addition of the PEO block, the chromatogram peak shifts to a shorter elution time, consistent with a larger molecule. Importantly, SEC in contrast to NMR can distinguish the architecture (connectivity) of the two blocks. For example, a sample containing a mixture of PEO and PB would look nearly identical in ¹H NMR as a PB–PEO block copolymer, whereas SEC could readily discern between the two samples since molecules would be separated based on size. It is also noted that there is an absence of residual PB–OH homopolymer in the SEC trace for PB–PEO, suggesting the initiation of PB–OH was quantitative. Coupling of PB–PEO to form triblock, PB–PEO–11.5 (11.5 mol % TB) shows an SEC trace with a bimodal distribution, as expected for a mixture of polymeric species with vastly different molecular weights. The relative amount of triblock (TB) was determined by integrating the individual peaks as the relative area is dependent upon mass concentration (g/ml) in the RI detector response (Figure 2–6, top) and subsequently converted to mol % with

the number average molecular weights determined from ^1H NMR. Lastly, SEC was utilized to monitor if any chain degradation was observed after post-polymerization chain modification. For example, epoxidation of PB-PEO-11.5 to 19.6% shows a nearly identical molecular weight distribution, indicating no chain degradation or coupling took place during the reaction.

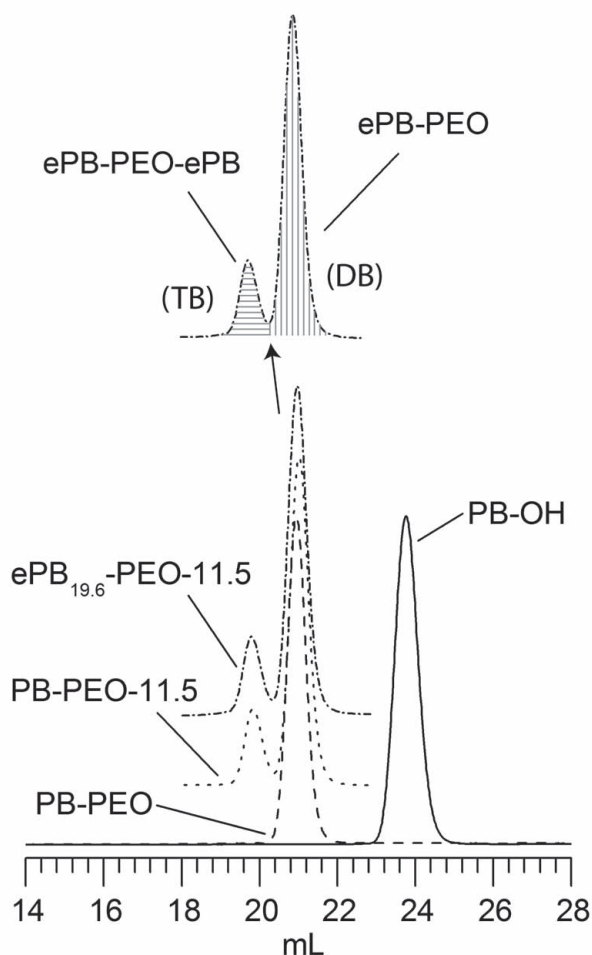


Figure 2-6. SEC of a series of BCPs including PB, PB-PEO, PB-PEO with 11.5 mol% triblock and a partially epoxidized (19.6%) PB-PEO with 11.5 mol% triblock. The SEC traces clearly show the absence of homopolymer in the PB-PEO block copolymer suggesting a quantitative initiation step. The copolymer mixtures (PB-PEO-11.5 and ePB_{19.6}-PEO-11.5) have well-resolved chromatogram peaks of relative triblock to diblock polymer. In addition, the partial epoxidation shows no indication of chain degradation (bottom). Pictorial representation of individual integration of relative triblock (horizontal lines) to diblock (vertical lines) percent in an SEC trace (top). This figure has been adapted from reference 20. Further characterization can be found in Chapter 4.

2.3.6 Dynamic Mechanical Spectroscopy (Rheology)

Rheology is an invaluable tool for studying the flow and deformation response of materials and has become tremendously useful in the characterization of polymer and copolymer melts and solutions.^{4, 29, 32} Polymers and block copolymers possess viscoelastic properties; they are therefore characterized by a combination of their liquid-like (viscous) and solid-like properties (elastic) within a rheological experiment. The rheological characterization of block copolymer materials is most commonly performed by observing the response of the complex modulus (ratio of stress to strain) while applying a dynamic sinusoidal (oscillating) strain.^{29, 32} Briefly, a small strain and frequency of oscillation is applied to the sample, and the resulting torque required to produce the chosen strain is then measured as a stress wave. The stress wave is then divided by the strain input and then mathematically decomposed into two modulus components: one in-phase (G' , storage modulus) with the applied strain input, and one 90° out of phase (G'' , loss modulus) with the applied strain. The storage modulus (G') is a measure of the solid elastic properties of the material, and the loss modulus is a measure of the viscous liquid properties of the material. Block copolymers typically have a considerable component of each G' and G'' , confirming their inherent viscoelastic behavior. Importantly, actual measurements on polymer systems are customarily made in what is referred to as the linear viscoelastic regime, where the moduli are independent of the strain and where the strain varies linearly with stress (Figure 2-7).^{29, 32}

Direct morphological structural interpretation of BCPs cannot be determined with rheology alone; instead rheology becomes extremely powerful when combined with other techniques such as SAXS or TEM. The rheological response of block copolymers to a dynamic sinusoidal oscillating strain widely varies with structure (or lack thereof); particularly there is a substantial difference between the rheological response of an ordered morphological state and disordered isotropic liquid state.^{4, 33, 34} Thermally and kinetically (providing the transition takes place on the time scale of the rheology experiment) induced morphological changes such as order to order transitions (OOT) and order to disorder transitions (ODT) in a block copolymer can be readily

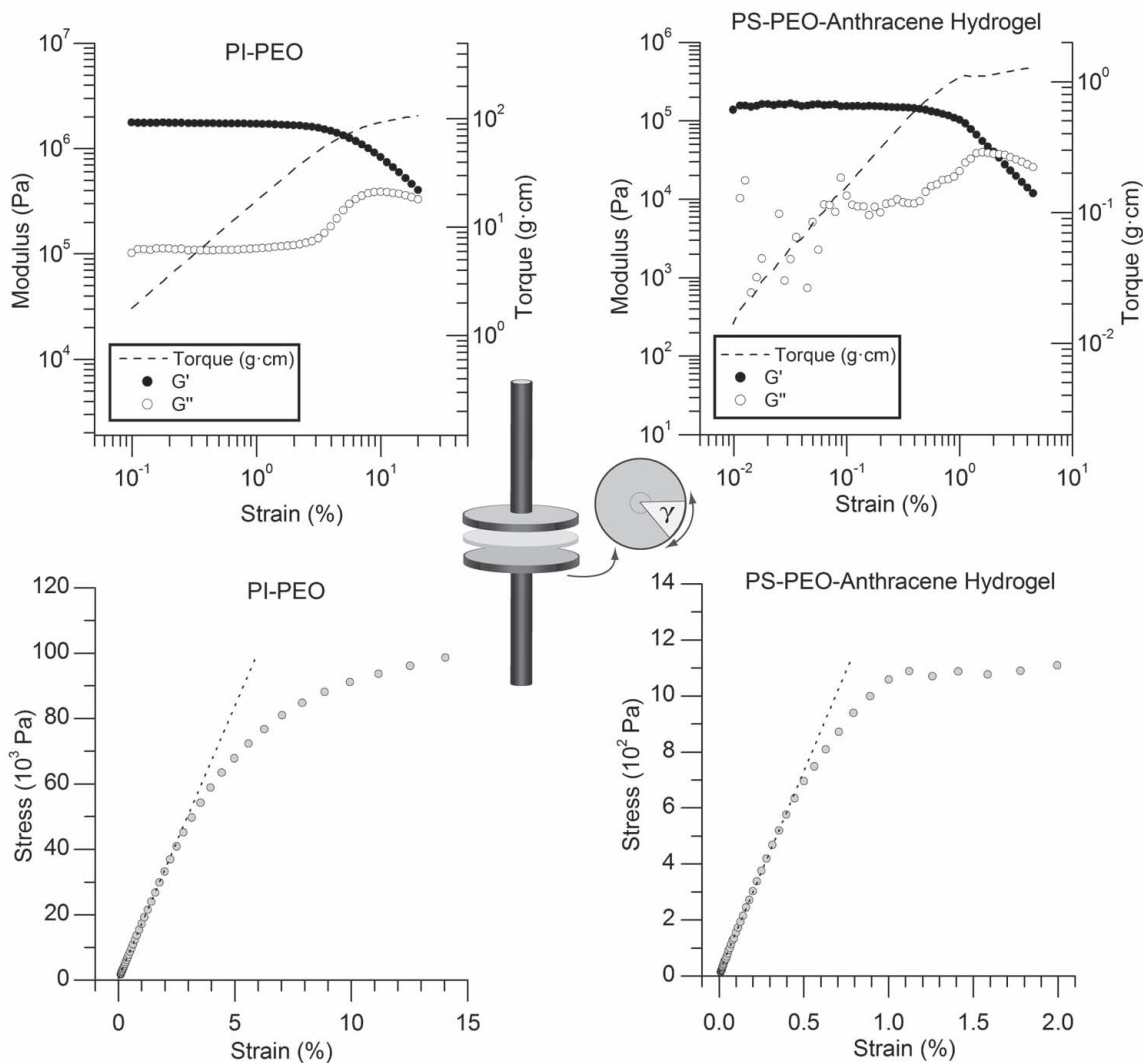


Figure 2–7. Determination of a suitable strain rate in the linear viscoelastic regime under dynamic oscillatory shear. The PI–PEO BCP melt sample exhibits a linear viscoelastic regime in the range of 0.1–4 % strain at a frequency of 1 rad s^{-1} , evident by the plateau behavior of the modulus (G' , G'') and the linear response of the stress vs. strain curve. Any strain rate in the range of 0.1–4 % is a suitable choice for further rheological experiments since all strain values in the range of 0.1–4 % produce torque measurements above the ARES rheometer limit of detection of 0.01 g·cm (left). The PS–PEO Anthracene coupled hydrogel exhibits a linear viscoelastic response from 0.01–0.5 % strain at a frequency of 1 rad s^{-1} . Torque values are much lower compared to the PI–PEO BCP melt sample, as a result data collected below 0.01 g·cm torque does not produce an acceptable signal-to-noise ratio. Therefore, a suitable strain rate for further rheology experiments must be above 0.01 g·cm torque and within the linear viscoelastic regime, a range that meets these requirements is 0.2–0.5 % strain. Inset depicts the parallel plate tool geometry. Further characterization of the PI–PEO BCP melt and PS–PEO hydrogel can be found in Chapters 3 and 5, respectively.

detected with rheology as the nanostructure directly affects the materials response to dynamic shear.^{9, 10, 33-43} In addition, there are also rheological trends that accompany block copolymer morphologies which can aid in the assignment of structure, for example cubic systems (e.g. spheres, gyroid) typically have moduli with a plateau-like response independent of temperature,^{40, 41, 43, 44} while lamellar BCPs often exhibit a steady decrease in moduli upon heating.^{10, 33, 36, 45-47}

Several different rheological experiments were performed in this dissertation on polymer melt samples including dynamic temperature ramp (e.g. locate OOTs and ODT, Chapters 3, 4, and 8) and dynamic frequency sweep tests (e.g. comparison of cross-linked vs. non cross-linked supramolecular polymeric materials, Appendix I). For swollen hydrogel samples, dynamic frequency sweep and compression tests were used for the characterization of the materials (e.g. confirmation of highly elastic response, chapters 4 and 5). The detailed analysis of the individual experiments is sample dependent and has been reserved for the designated chapters above. However, common to all rheological experiments performed in this thesis is the parallel plate tool configuration and determination of the linear viscoelastic regime. For melt samples, 8 mm upper and lower parallel plates were used, and for hydrogel samples an 8 mm upper tool was used along with a covered water bath lower tool to prevent evaporation of absorbed water. An appropriate strain rate for each of the aforementioned experiments was determined independently for each sample by locating the linear viscoelastic regime where the modulus is independent of strain. In addition, a strain rate was carefully chosen such that the torque measurements were well above the instrument detection limit of (0.01 g-cm) when possible. Two examples of such dynamic strain sweep test measurements are presented in Figure 2-7, for a melt polymer and swollen hydrogel studied herein.

2.3.7 Small-angle X-ray Scattering (SAXS)

The investigation of block copolymer nanoscale morphology (10s of nanometers) including those which are highly periodic, weakly-ordered, or amorphous (disordered) in structure

can often be readily characterized with small-angle X-ray scattering (SAXS).⁴⁸⁻⁵⁰ Similarly to conventional X-ray scattering of molecular crystals or powders, BCP melts that exhibit highly periodic structures can typically be characterized by their unique set of relative diffraction planes dependent of the inherent symmetry of the crystallographic planes in the periodic structure.^{51,52} Diffraction from BCP melts occur at very small angles (θ_B), compared to molecular crystals or powders, as a result of the large interplanar domain spacings (d). This relationship is consistent with the definition of the Bragg law, where the Bragg angle (θ_B) varies inversely with d (with constant wavelength of radiation, λ):

$$n\lambda = 2d \sin \theta_B \quad \text{Equation 2-17}$$

Notably, SAXS data is most often presented as a function of the scattering wave vector, q and not $2\theta_B$ which is commonly used for small molecule X-ray diffraction. The magnitude of q is defined as the difference between the incident (k_i) and scattering (k_s) wave vectors for elastic scattering. The scattering wave vector, q , is dependent of the Bragg angle and quantifies the change in momentum of the waves resulting from the scattering of radiation. The relationship between the Bragg angle and q is shown below and depicted in Figure 2-8.

$$q = \frac{4\pi}{\lambda} \sin\left(\frac{2\theta_B}{2}\right) \quad \text{Equation 2-18}$$

A simplified SAXS diagram is presented in Figure 2-8. In a representative SAXS experiment conducted in this work, the BCP sample is typically comprised of many small crystallographic grains, similarly to a powder XRD sample. The resulting diffraction patterns appear as a series of Debye-Scherrer rings, a product of an infinite number of individual spots diffracted from the many orientations of the crystalline grains. Pseudo-single crystalline BCP samples can be formed with pre-shear techniques⁵³⁻⁵⁶ resulting in a series of diffraction spots; however such techniques were not studied to any significant extent in this work. After a suitable data collection time that provides a sufficient signal-to-noise ratio (typically 10-30 min with the Rigaku S-Max 3000 system at Colorado State University), the 2D scattering pattern is transformed

from polar coordinates to a Cartesian coordinate system (it is not a requirement to change coordinate systems, but doing so simplifies data analysis). The scattering data is then azimuthally integrated resulting in a 1D plot of intensity vs. the scattering wave, q . If the integrated data produced numerous well-resolved diffraction reflections, the BCP melt structure can generally be indexed through analysis of the diffraction pattern; one example is shown in the following section. In addition, past comprehensive research performed both theoretically^{1, 2, 4, 6, 8} and experimentally^{4, 9-11} aids in the identification of morphology. For example, in AB diblock^{1, 2, 6} and ABA triblock^{57, 58} systems, only a select number of phases have been shown to exist and therefore analysis of the structure is greatly simplified.

BCP morphologies that exhibit multiple reflections that cannot be identified readily with diffraction techniques, such as some of the more elaborate morphologies formed by ABC triblock copolymers¹⁷ typically utilize other characterization techniques in combination, such as TEM or AFM.⁵⁹⁻⁶¹ Such alternative techniques were not utilized in this dissertation as all BCP melt samples studied that exhibited well-resolved peaks were conclusively indexed to four morphologies including spheres on a BCC lattice (S_{BCC}), hexagonally packed cylinders (H), lamellae (L), a coexistence of lamellar and hexagonal domains (H + L), and bicontinuous gyroid (G).

BCP Morphological states that do not exhibit well-resolved diffraction patterns include weakly-ordered samples (e.g. liquid-like packing) or disordered samples. Both morphologies are usually characterized by very broad scattering coupled with low intensity.^{33, 34, 43, 62-64} Rigorous morphological characterization is more complex and is performed by modeling a mathematical function combining the form factor (particle) and structure factor (lattice) of the scattering. No such efforts of mathematical modeling were performed in this thesis, as this was outside of the scope of the desired goals. A far less rigorous method of comparison to past research was sufficient for the morphological analysis of the limited amount of BCP samples that contained weak-order studied in this thesis. Additionally, the majority of samples studied quickly (minutes to hours) transformed from weakly-ordered to highly-ordered with annealing, effectively eliminating the necessity to model the non-equilibrium weakly-ordered state. Lastly,

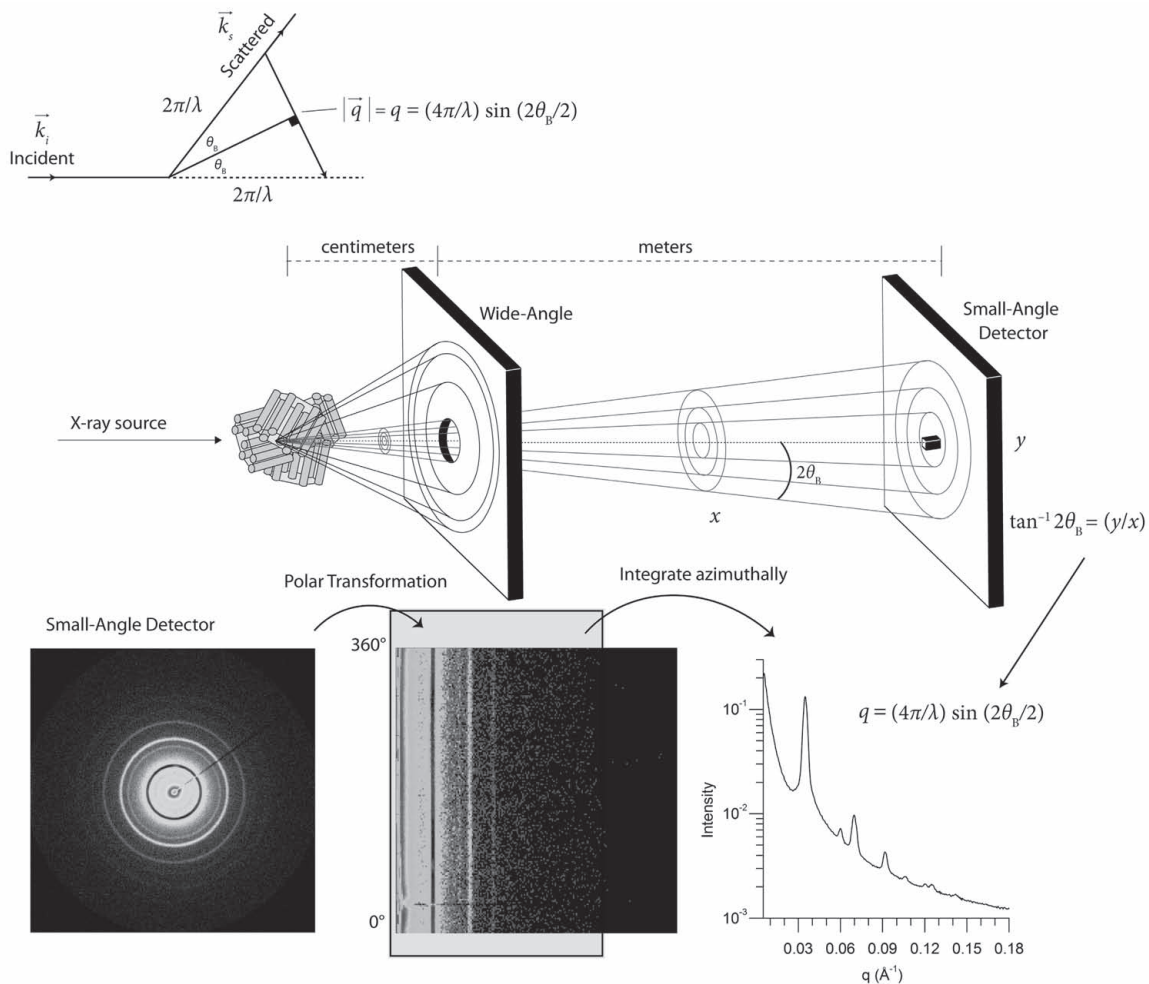


Figure 2–8. Geometric relationship between the Bragg angle and the scattering wave vector, q (top). Schematic of a “poly-crystalline” BCP sample diffracting x-rays with an ordered hexagonally packed cylindrical morphology. The wide-angle detector is located fairly close to the sample (centimeters) and is similar to the proximity of a detector in a powder XRD instrument utilized for small molecule scattering. The small-angle detector is located much further away from the sample (meters) and allows for suitable resolution of scattering resulting from large domain spacings, occurring at very small angles. After data collection, the 2D plot is converted to a 1D plot of intensity vs. q . The unique diffraction pattern can then be indexed similarly to a powder XRD pattern.

samples having a disordered state were characterized by the disappearance of the diffraction reflections, before appearance of the well-known correlation hole scattering, characterized by a low intensity hump in the 1D broad scattering profile.^{62, 63}

2.3.8 Indexing of BCP Morphologies

Identification of symmetry in the primary four BCP morphologies including spheres on a BCC

lattice, hexagonally packed cylinders, bicontinuous gyroid and lamellae is greatly simplified for three main reasons: (1) relatively high symmetry morphologies (e.g. cubic BCC spheres and gyroid) reducing the number of allowed reflections and (2) an assumption of one or more lattice parameters approaching an infinite length scale, which simplifies the lattice geometry (e.g. lamellae and cylinders) (3) comprehensive past research on BCP morphologies^{1, 2, 6, 8-11, 57, 58} documenting the assignment of morphology for a particular space group. In addition, diffraction intensity predictions that adjust the structure factor to aid in the determination of symmetry are typically unnecessary in the assignment of the classic BCP morphologies.^{51, 52} However the suppression or absence of a particular allowed reflection of an indexed morphology can sometimes be used to determine the relative densities and thus volume fractions of the constituent blocks in and block copolymer.⁶⁵⁻⁶⁷ Two special cases are discussed in Chapter 8.

As a result of the aforementioned simplifications, all four primary BCP morphologies produce diffraction patterns that are independent of the unit cell dimensions. Combining equations 2-17 and 2-18 gives a relationship of q to the domain spacing, d :

$$q_{hkl} = \frac{2\pi}{d_{hkl}} \quad \text{Equation 2-19}$$

The inverse relationship of the scattering wave vector, q , and the interplanar spacing, d , of a particular set of crystallographic planes, d_{hkl} , is very convenient for the symmetry analysis of small-angle x-ray diffraction patterns. As an example, in a BCP sample exhibiting spheres on a BCC lattice (S_{BCC}), the distance between crystallographic planes, d , and the corresponding miller indices is represented by the plane spacing equation 2-20 for cubic systems.^{50, 51}

$$\frac{1}{d_{hkl}^2} = \frac{h^2 + k^2 + l^2}{a^2} \quad \text{Equation 2-20}$$

Combining Equation 2-19 and 2-20, and simplifying in terms of a relative ratio to a reference reflection, q_{hkl}^p produces equation 2-21.

$$\frac{q_{h'k'l'}}{q_{hkl}} = \frac{\sqrt{h'^2 + k'^2 + l'^2}}{\sqrt{h^2 + k^2 + l^2}} \quad \text{Equation 2-21}$$

Equation 2-21 confirms the aforementioned statement that the relative $q_{h'k'l'}/q_{hkl}$ values for a cubic morphology are independent of the unit cell size (a) and can be readily calculated with only the Miller indices. Before calculating the relative diffraction ratios, it is important to consider any systematic absences arising from the lattice centering and symmetry elements of the particular unit cell. In this example, the S_{BCC} morphology belongs to the space group $Im\bar{3}m$. The systematic absences can be identified through calculation of the structure factor of the unit cell. The structure factor calculations have already been compiled in the *International Tables for Crystallography* as reflection conditions, which essentially quantify the Miller indices, h , k and l required in order to produce a diffracted intensity. The reflection conditions for the $Im\bar{3}m$ space group are listed below, where h , k and l are permutable and n is any integer.

$$hkl : h + k + l = 2n \quad \text{Equation 2-22}$$

$$0kl : k + l = 2n \quad \text{Equation 2-23}$$

$$hhl : l = 2n \quad \text{Equation 2-24}$$

$$h00 : h = 2n \quad \text{Equation 2-25}$$

A typical procedure to calculate the allowed reflections would be to tabulate a list of relative q ratios with equation 2-21 and various hkl miller indices. The reflection conditions are then applied removing any forbidden reflections to produce a series of ratios consistent for the $Im\bar{3}m$ space group as summarized in Table 2-1 and depicted in Figure 2-9.

The discussion of morphological assignments from SAXS has been limited to the primary AB diblock copolymer morphologies where the crystallographic analysis is greatly simplified due to either very high symmetry, or by assuming a lattice with only one identifiable finite lattice parameter. In addition, there is a wealth of past research performed both theoretically and experimentally on AB diblock copolymer melt equilibrium morphologies to aid in com-

parison and identification.^{1, 2, 6, 8-11, 57, 58} Indexing for other more elaborate BCP morphologies can be accomplished similarly to the previously described procedure by calculating the relative ratios and applying the appropriate reflection conditions. However, for direct assignment of morphology by SAXS alone, scattering patterns for a block copolymer must contain a convincing number of higher order reflections, which can be unambiguously resolved. If that is not the case, additional methods such as AFM or TEM must be applied.

Table 2-1. Allowed and forbidden reflections for the $Im\bar{3}m$ space group tabulated with the relative q ratios of the allowed reflections.

hkl	q_{hkl}/q_{100}	Reflection Condition	hkl	q_{hkl}/q_{100}	Reflection Condition
100	absent	$hkl: h+k+l \neq 2n$	511	absent	$hkl: h+k+l \neq 2n$
110	$\sqrt{2}$		333	absent	$hkl: h+k+l \neq 2n$
111	absent	$hkl: h+k+l \neq 2n$	234	absent	$hkl: h+k+l \neq 2n$
200	$\sqrt{4}$		520	absent	$hkl: h+k+l \neq 2n$
210	absent	$hkl: h+k+l \neq 2n$	521	$\sqrt{30}$	
211	$\sqrt{6}$		440	$\sqrt{32}$	
220	$\sqrt{8}$		522	absent	$hkl: h+k+l \neq 2n$
212	absent	$hkl: h+k+l \neq 2n$	441	absent	$hkl: h+k+l \neq 2n$
300	absent	$hkl: h+k+l \neq 2n$	530	$\sqrt{34}$	
301	$\sqrt{10}$		531	absent	$hkl: h+k+l \neq 2n$
311	absent	$hkl: h+k+l \neq 2n$	600	$\sqrt{36}$	
222	$\sqrt{12}$		601	absent	$hkl: h+k+l \neq 2n$
320	absent	$hkl: h+k+l \neq 2n$	532	$\sqrt{38}$	
123	$\sqrt{14}$		620	$\sqrt{40}$	
400	$\sqrt{16}$		621	absent	$hkl: h+k+l \neq 2n$
410	absent	$hkl: h+k+l \neq 2n$	443	absent	$hkl: h+k+l \neq 2n$
322	absent	$hkl: h+k+l \neq 2n$	541	$\sqrt{42}$	
411	$\sqrt{18}$		533	absent	$hkl: h+k+l \neq 2n$
313	absent	$hkl: h+k+l \neq 2n$	622	$\sqrt{44}$	
420	$\sqrt{20}$		630	absent	$hkl: h+k+l \neq 2n$
214	absent	$hkl: h+k+l \neq 2n$	542	absent	$hkl: h+k+l \neq 2n$
233	$\sqrt{22}$		631	$\sqrt{46}$	
422	$\sqrt{24}$		444	$\sqrt{48}$	
500	absent	$hkl: h+k+l \neq 2n$	700	absent	$hkl: h+k+l \neq 2n$
430	absent	$hkl: h+k+l \neq 2n$	632	absent	$hkl: h+k+l \neq 2n$
431	$\sqrt{26}$		534	$\sqrt{50}$	

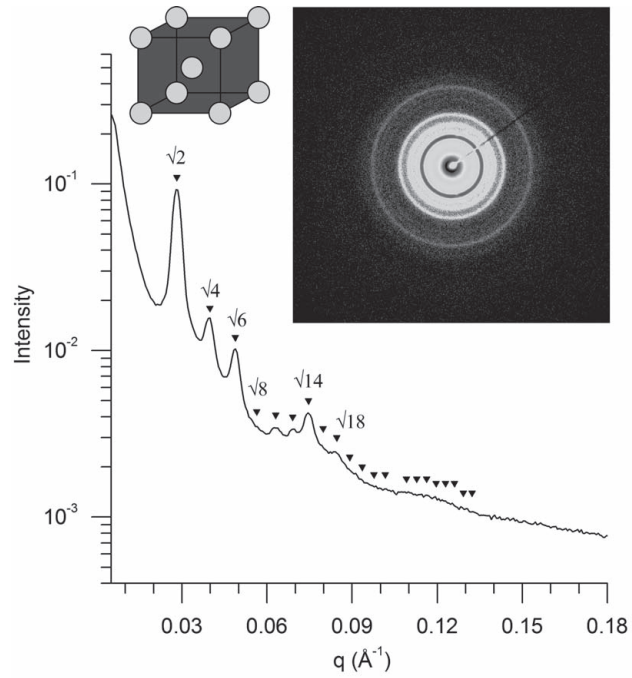


Figure 2–9. SAXS data of a PB–PEO BCP melt sample at 100 °C. The sample is consistent with the S_{BCC} morphology which belongs to the $Im\bar{3}m$ space group. The inverted triangles represent the calculated relative q ratios of allowed reflections as tabulated in table 2–1. Further characterization can be found in Chapter 4.

2.4 REFERENCES

1. Bates, F. S. *Science* **1991**, *251*, 898-905.
2. Bates, F. S.; Fredrickson, G. H. *Phys.Today* **1999**, *52*, 32-38.
3. Ruzette, A.-V.; Leibler, L. *Nat Mater* **2005**, *4*, 19-31.
4. Hadjichristidis, N., *Block copolymers synthetic strategies, physical properties, and applications*. Wiley-Interscience: Hoboken, N.J., 2003.
5. Matsen, M. W. *J. Phys.-Condes. Matter* **2002**, *14*, R21-R47.
6. Matsen, M. W.; Bates, F. S. *Macromolecules* **1996**, *29*, 1091-1098.
7. Matsen, M. W.; Bates, F. S. *J. Chem. Phys.* **1997**, *106*, 2436-2448.
8. Cochran, E. W.; Garcia-Cervera, C. J.; Fredrickson, G. H. *Macromolecules* **2006**, *39*, 2449-2451.
9. Floudas, G.; Vazaiou, B.; Schipper, F.; Ulrich, R.; Wiesner, U.; Iatrou, H.; Hadjichristidis, N. *Macromolecules* **2001**, *34*, 2947-2957.
10. Khandpur, A. K.; Foerster, S.; Bates, F. S.; Hamley, I. W.; Ryan, A. J.; Bras, W.; Almdal, K.; Mortensen, K. *Macromolecules* **1995**, *28*, 8796-8806.
11. Castelletto, V.; Hamley, I. W. *Curr. Opin. Solid State Mat. Sci.* **2004**, *8*, 426-438.
12. Kim, H.-C.; Park, S.-M.; Hinsberg, W. D. *Chemical Reviews* **2009**, *110*, 146-177.
13. Olson, D. A.; Chen, L.; Hillmyer, M. A. *Chemistry of Materials* **2008**, *20*, 869-890.
14. Phillip, W. A.; O'Neill, B.; Rodwogin, M.; Hillmyer, M. A.; Cussler, E. L. *ACS Appl. Mater. Interfaces* **2010**, *2*, 847-853.
15. Segalman, R. A.; McCulloch, B.; Kirmayer, S.; Urban, J. J. *Macromolecules* **2009**, *42*, 9205-9216.
16. Smart, T.; Lomas, H.; Massignani, M.; Flores-Merino, M. V.; Perez, L. R.; Battaglia, G. *Nano Today* **2008**, *3*, 38-46.
17. Zheng, W.; Wang, Z. G. *Macromolecules* **1995**, *28*, 7215-7223.
18. Aoshima, S.; Kanaoka, S. *Chemical Reviews* **2009**, *109*, 5245-5287.
19. Gibson, V. C. *Advanced Materials* **1994**, *6*, 37-42.
20. Hadjichristidis, N.; Pitsikalis, M.; Pispas, S.; Iatrou, H. *Chemical Reviews* **2001**, *101*, 3747-3792.
21. Hawker, C. J.; Bosman, A. W.; Harth, E. *Chemical Reviews* **2001**, *101*, 3661-3688.
22. Matyjaszewski, K.; Xia, J. *Chemical Reviews* **2001**, *101*, 2921-2990.
23. Lee, M.; Cho, B.-K.; Zin, W.-C. *Chemical Reviews* **2001**, *101*, 3869-3892.
24. Abetz, V.; Simon, P. F. W., Phase behaviour and morphologies of block copolymers. In *Block Copolymers I*, Abetz, V., Ed. Springer-Verlag Berlin: Berlin, 2005; Vol. 189, pp 125-212.
25. Drago, R. S., *Physical Methods for Chemists*. 2 ed.; Surfside Scientific Publishers: Gainesville, FL, 1977.
26. James, T. L., *Fundamentals of NMR*. Thomas L. James: San Francisco, CA, 1998.
27. Macomber, R. S., *A complete introduction to modern NMR spectroscopy*. Wiley: New York, 1998.
28. Skoog, D. A., *Principles of instrumental analysis*. Harcourt Brace College Publishers: Philadelphia, 1998.
29. Hiemenz, P. C.; Lodge, T. P., *Polymer chemistry*. CRC Press: Boca Raton, 2007.
30. Painter, P. C., *Fundamentals of polymer science an introductory text*. Technomic Pub. Co.: Lancaster, Pa., 1997.
31. Fetters, L. J.; Lohse, D. J.; Richter, D.; Witten, T. A.; Zirkel, A. *Macromolecules* **1994**, *27*,

- 4639-4647.
32. Macosko, C. W., *Rheology principles, measurements, and applications*. VCH: New York, 1994.
 33. Rosedale, J. H.; Bates, F. S.; Almdal, K.; Mortensen, K.; Wignall, G. D. *Macromolecules* **1995**, *28*, 1429-1443.
 34. Lee, S.-H.; Char, K.; Kim, G. *Macromolecules* **2000**, *33*, 7072-7083.
 35. Cavicchi, K. A.; Lodge, T. P. *Macromolecules* **2003**, *36*, 7158-7164.
 36. Foerster, S.; Khandpur, A. K.; Zhao, J.; Bates, F. S.; Hamley, I. W.; Ryan, A. J.; Bras, W. *Macromolecules* **1994**, *27*, 6922-6935.
 37. Hamersky, M. W.; Hillmyer, M. A.; Tirrell, M.; Bates, F. S.; Lodge, T. P.; von Meerwall, E. D. *Macromolecules* **1998**, *31*, 5363-5370.
 38. Hamley, I. W.; Castelletto, V.; Floudas, G.; Schipper, F. *Macromolecules* **2002**, *35*, 8839-8845.
 39. Rosedale, J. H.; Bates, F. S. *Macromolecules* **1990**, *23*, 2329-2338.
 40. Scalfani, V. F.; Bailey, T. S. *Chemistry of Materials* **2010**, *22*, 5992-6000.
 41. Scalfani, V. F.; Bailey, T. S. *Macromolecules* **2011**, *44*, 6557-6567.
 42. Vigild, M. E.; Almdal, K.; Mortensen, K.; Hamley, I. W.; Fairclough, J. P. A.; Ryan, A. J. *Macromolecules* **1998**, *31*, 5702-5716.
 43. Wang, X.; Dormidontova, E. E.; Lodge, T. P. *Macromolecules* **2002**, *35*, 9687-9697.
 44. Kossuth, M. B.; Morse, D. C.; Bates, F. S. *J. Rheol.* **1999**, *43*, 167-196.
 45. Riise, B. L.; Fredrickson, G. H.; Larson, R. G.; Pearson, D. S. *Macromolecules* **1995**, *28*, (23), 7653-7659.
 46. Wiesenauer, E. F.; Edwards, J. P.; Scalfani, V. F.; Bailey, T. S.; Gin, D. L. *Macromolecules* **2011**, *44*, 5075-5078.
 47. Zhao, J.; Majumdar, B.; Schulz, M. F.; Bates, F. S.; Almdal, K.; Mortensen, K.; Hajduk, D. A.; Gruner, S. M. *Macromolecules* **1996**, *29*, 1204-1215.
 48. Chu, B.; Hsiao, B. S. *Chemical Reviews* **2001**, *101*, 1727-1762.
 49. Hamley, I. W.; Castelletto, V. *Progress in Polymer Science* **2004**, *29*, 909-948.
 50. Roe, R. J., *Methods of X-ray and neutron scattering in polymer science*. Oxford University Press: New York, 2000.
 51. Cullity, B. D., *Elements of x-ray diffraction*. Addison-Wesley Pub. Co.: Reading, Mass., 1978.
 52. De Graef, M.; McHenry, M. E., *Structure of Materials: An Introduction to Crystallography, Diffraction, and Symmetry*. Cambridge University Press: New York, 2007.
 53. Almdal, K.; Koppi, K. A.; Bates, F. S. *Macromolecules* **1993**, *26*, 4058-4060.
 54. Kleppinger, R.; Mischenko, N.; Theunissen, E.; Reynaers, H. L.; Koch, M. H. J.; Almdal, K.; Mortensen, K. *Macromolecules* **1997**, *30*, 7012-7014.
 55. Mortensen, K.; Theunissen, E.; Kleppinger, R.; Almdal, K.; Reynaers, H. *Macromolecules* **2002**, *35*, 7773-7781.
 56. Park, M. J.; Bang, J.; Harada, T.; Char, K.; Lodge, T. P. *Macromolecules* **2004**, *37*, 9064-9075.
 57. Matsen, M. W. *J. Chem. Phys.* **2000**, *113*, 5539-5544.
 58. Matsen, M. W.; Thompson, R. B. *J. Chem. Phys.* **1999**, *111*, 7139-7146.
 59. Bailey, T. S.; Pham, H. D.; Bates, F. S. *Macromolecules* **2001**, *34*, 6994-7008.
 60. Stadler, R.; Auschra, C.; Beckmann, J.; Krappe, U.; Voight-Martin, I.; Leibler, L. *Macromolecules* **1995**, *28*, 3080-3097.
 61. Stocker, W.; Beckmann, J.; Stadler, R.; Rabe, J. P. *Macromolecules* **1996**, *29*, 7502-7507.

62. Bates, F. S. *Macromolecules* **1985**, *18*, 525-528.
63. Floudas, G.; Ulrich, R.; Wiesner, U. *J. Chem. Phys.* **1999**, *110*, 652-663.
64. Kinning, D. J.; Thomas, E. L. *Macromolecules* **1984**, *17*, 1712-1718.
65. Hashimoto, T.; Kawamura, T.; Harada, M.; Tanaka, H. *Macromolecules* **1994**, *27*, 3063-3072.
66. Hasegawa, H.; Hashimoto, T.; Kawai, H.; Lodge, T. P.; Amis, E. J.; Glinka, C. J.; Han, C. C. *Macromolecules* **1985**, *18*, 67-78.
67. Hashimoto, T.; Nagatoshi, K.; Todo, A.; Hasegawa, H.; Kawai, H. *Macromolecules* **1974**, *7*, 364-373.

CHAPTER 3

THERMALLY STABLE PHOTOCURING CHEMISTRY FOR SELECTIVE MORPHOLOGICAL TRAPPING IN BLOCK COPOLYMER MELT SYSTEMS

The contents of this dissertation chapter have been adapted from a manuscript published in *ACS Chemistry of Materials*: Scalfani, V. F.; Bailey, T. S. *Chem. Mater.* **2010**, *22*, 5992-6000. Vincent F. Scalfani and Travis S. Bailey developed and designed the experiments. Vincent F. Scalfani performed the experiments. The manuscript and dissertation chapter were written by Vincent F. Scalfani with editing by Travis S. Bailey.

3.1 CONSPECTUS

In this work we report the novel application of thermally stable photocuring chemistry towards high fidelity translation of block copolymer based melt-state morphologies into their equivalent solid analogs. The thermal stability of the cationic photocuring chemistry allows for both extended thermal processing prior to cure, as well as precise trapping of selected morphologies afforded by the temperature independent initiation mechanism. We demonstrate this powerful approach using a model polyisoprene-*b*-poly(ethylene oxide) (PI-PEO, $f_{\text{PEO}} = 0.39$, $M_n = 10120 \text{ g mol}^{-1}$) block copolymer, prepared by two-step anionic polymerization and subsequent partial epoxidation (7.3–16.8 mol% relative to diene repeat units) with 3-chloroperoxybenzoic acid. Small-angle X-ray scattering (SAXS) and dynamic rheology were used to determine morphological behavior of the block copolymers synthesized. The targeted PI-PEO parent block copolymer exhibited multiple melt-state morphologies including crystalline lamellae (L_c), hexagonally packed cylinders (C), bicontinuous gyroid (G), and a final isotropic disordered state (Dis). The partial epoxidation and the addition of the UV-activated cationic photoinitiator (4-iodophenyl)diphenylsulfonium triflate (1.0–1.25 mol%) acted only to shift transition temperatures between phases, without disturbing the overall morphological sequence present in the neat, unmodified PI-PEO block copolymer. Exposure of the photoacid/block copolymer blends to UV radiation at selected temperatures permitted successful permanent trapping of both the cylinder and gyroid morphologies from a single block copolymer sample, as verified by pre- and post-cure SAXS measurements. Importantly, this approach should be applicable to any block copolymer in which cationically polymerizable functional groups can be incorporated.

3.2 INTRODUCTION

The nanoscale structuring of material through block copolymer (BCP) self-assembly^{1,2} continues to populate current technological development strategies; the variety of highly ordered morphologies produced both in solution and melt-state environments has already led to promising advances in nanolithography,^{3,4} separations,^{5–8} high surface area catalyst supports,^{9,10} hydrogel-

based materials,¹¹ organic electronics,^{12,13} ultra-low dielectric materials,¹⁴ templating,¹⁵ fuel cells,^{16,17} and magnetic storage media.¹⁸ Interestingly, in the most developed areas of use, the block copolymer species are used predominately as a sacrificial structuring tool, with the polymeric blocks being removed physically or chemically once the structure produced is fixed through subsequent processing steps (e.g. metal deposition¹⁹). However, in a growing number of proposed applications, such as porous membrane substrates²⁰⁻²² or organic photovoltaic active layers, the BCP species are occupying non-sacrificial roles and are being relied upon to persist as functional components in the end product. In such applications, the high fidelity translation of the structured melt-state (or solution-state) morphology into its equivalent solid analog stands as one of the most crucial processing steps. The integrity and facility of this translation process, coupled with the resulting mechanical and chemical robustness of the solidified analog, stand as the greatest barriers hindering the efficacy of structured BCPs as primary design materials.

Two principal strategies have been historically utilized to solidify melt-state morphologies in BCP systems: either (1) cooling induced vitrification of, or (2) melt-state cross-linking of, one or more of the constituent polymer blocks; the exact strategy used is very system specific (*vide infra*). Taken together, however, the collection of these established strategies share a common fundamental limitation; the mechanisms for the solidification techniques used have been highly temperature dependent; that is, the temperature at which the solidification mechanism can be triggered is largely fixed by the chemistry or the physical properties of the system. This presents a significant challenge for the generalization of solidification strategies to other BCP samples, since it is commonplace for BCPs to exhibit multiple thermally induced changes in morphological state,²³⁻²⁵ the temperatures at which of those changes take place being a strong function of the chemical nature, size, and relative composition of the constituent blocks. In fact, we believe the capability to selectively trap multiple, temperature-dependent morphologies from the same sample, by either of these classical strategies, has yet to be demonstrated.

For example, simple vitrification strategies, while generally effective at producing solids of a desired morphology with little to no loss in melt-state organization, are constrained by the

inability to preserve any morphology except that directly superior to the highest glass transition. Highly ordered BCP systems tend to also come from lower molecular weight materials, where there is limited kinetic resistance to ordering. Since these molecular weights routinely fall below those necessary to produce high entanglement densities, vitrification in these samples tends to yield very brittle mechanical characteristics with little resistance to solvation. Classical crosslinking strategies have been proposed as a means to overcome some of these limitations; unfortunately, effective and efficient solutions based on thermally independent cure mechanisms, permitting selective morphological trapping, still remain scarce, if not non-existent.

Examples of such classical cross-linking strategies applied to BCP systems include: (1) condensation²⁶ or coupling^{27,28} reactions, (2) thermally^{29,30} initiated free-radical polymerizations, and (3) integration of reactive (post-polymerization) repeat units.^{31,32} Self-initiated condensation and coupling based mechanisms in BCPs compete directly with the time scales of the self-assembly process and effectively preclude any significant application of thermal processing. Catalytic coupling reactions, such as hydrosilation reactions^{27,28} likewise occur upon introduction of the catalytic agent and therefore prohibit any thermal treatment. The general disadvantage of these approaches is their reliance on small molecules (catalysts, free radical initiators, coupling agents) that must be pre-integrated with the self-assembled system to evoke a homogeneous cure. Several more interesting systems, in which the cross-linking molecules are introduced through vapors such as sulfur monochloride³³ or 1,4-diiodobutane,^{34,35} seem to circumvent this problem; however, the cross-linking reaction is slow, taking up to two weeks for a full cure. As such, these methods have only been applied to pre-solidified (through vitrification of another block) samples. The feasibility of their application to melts is suspect given the required exposure times; thermal processing under these conditions is impractical in most cases. Cross-linking systems that utilize thermally^{29,30} initiated free radical mechanisms can be effective, but require the initiator to be selected in a system-specific manner, such that cure is activated in the desired thermal window. Of course, if the desired morphological window is small, the curing event will initiate during the approach to the phase boundary, which can result in mixed-phase solids.

At the very least, thermally induced free radical initiators prohibit extended pre-cure processing in the thermal window of interest, and are therefore particularly unsuitable for systems exhibiting more complex phase behavior. At the other end of the spectrum, several groups have focused on the development of novel monomer molecules that retain latent reactive functionality post-polymerization, which can then be employed to crosslink the system. However, the two prominent examples, benzocyclobutene^{31,32} and 2,3-dimethylenebicyclo[2.2.1]-heptane³⁶ both rely on thermally induced cycloaddition reactions activated at high temperatures. As such, these systems are constrained to high temperature cures and preclude selective morphological trapping at lower temperatures.

In contrast to these traditional approaches, we have focused our attention on the integration of UV activated curing chemistries, developed by Crivello and coworkers³⁷, into various BCPs, based on their successful application to a wide array of homopolymers and homopolymer composites over the last several decades.³⁷ As with more classical approaches, any light-triggered curing mechanism applied to BCPs must also be tolerant of pre-cure thermal processing. Photo-induced free-radical initiators notoriously suffer from poor thermal stability, with the exception of acylphosphineoxides that are stable up to 180 °C.^{38,39} Unfortunately, they are sensitive to visible light, which makes it difficult to avoid premature curing in the system without special handling.³⁹ We have instead focused our attention on photoinitiated cationic crosslinking reactions with onium salt photoacids, which have been shown to possess great thermal stability (reported to 150 °C) in epoxy functional curing systems³⁷ with no indication of premature curing under extended thermal processing conditions. As such, BCP systems incorporating this rapid cationically based curing chemistry should afford a powerful means of selectively trapping of any expressed morphology over a wide range of temperatures; the incorporation of sulfonium salts and cationically polymerizable functional groups (oxiranes, vinyl ethers, thiiranes, etc.) allows for the separation of thermal processing from the curing event. Interestingly, the potential utility of these photoacids towards non-cationic curing in BCP systems has been recently demonstrated by the work of Ober and coworkers.^{40,41} Using tri-

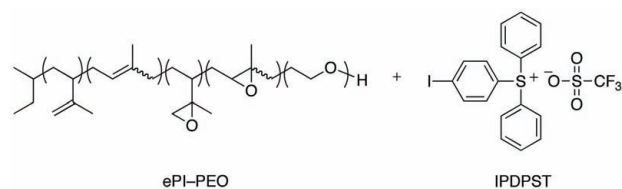


Figure 3–1. Thermally stable sulfonium salts, such as IPDPST are highly soluble in partially epoxidized polyisoprene-*b*-poly(ethylene oxide) BCPs, and enable rapid UV curing over a wide range of temperatures.

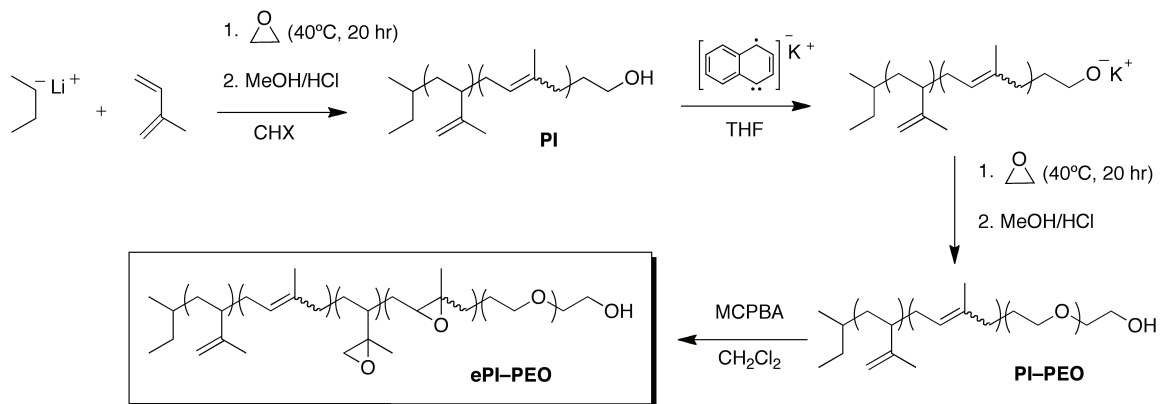
phenylsulfonium triflate, they were able to activate condensation-based crosslinking of blends of poly(α -methylstyrene)-*b*-poly(4-hydroxystyrene) with tetramethoxy-functional small molecule additives.⁴¹ Using solvent exposure to induce changes in thin film morphology, the UV activated photoacids were used to selectively cure morphology in these four-component blends. The use of temperature to induce changes in morphology, however, was not a focus of their work, as all curing was done at room temperature.

Herein we report, as one possible approach, the use of UV activated (4-iodophenyl)di-phenylsulfonium triflate (IPDPST) to selectively trap multiple melt-state morphologies from a single polyisoprene-*b*-poly(ethylene oxide) block copolymer (PI-PEO), which has been modified through the introduction of a small fraction of epoxide groups within the PI block (ePI-PEO) (Figure 3–1). PI-PEO was chosen as a model BCP candidate because of its well-developed phase diagram⁴² and its tendency to exhibit complex phase behavior over a wide range of volume fractions.

3.3 RESULTS AND DISCUSSION

3.3.1 Synthesis

The synthesis of ePI-PEO was accomplished in three steps using a combination of anionic polymerization followed by partial modification of the olefin repeat units in the PI backbone (Scheme 3–1). The PI-PEO BCP ($M_n = 10\,120\text{ g mol}^{-1}$, polydispersity index (PDI) = 1.05) used was synthesized according to previously reported two step anionic polymerization of isoprene and ethylene oxide monomer.⁴³ The targeted volume fraction of PEO ($f_{\text{PEO}} = 0.39$)



Scheme 3-1. Synthesis of Epoxidized Polyisoprene-*b*-poly(ethylene oxide) (ePI-PEO)

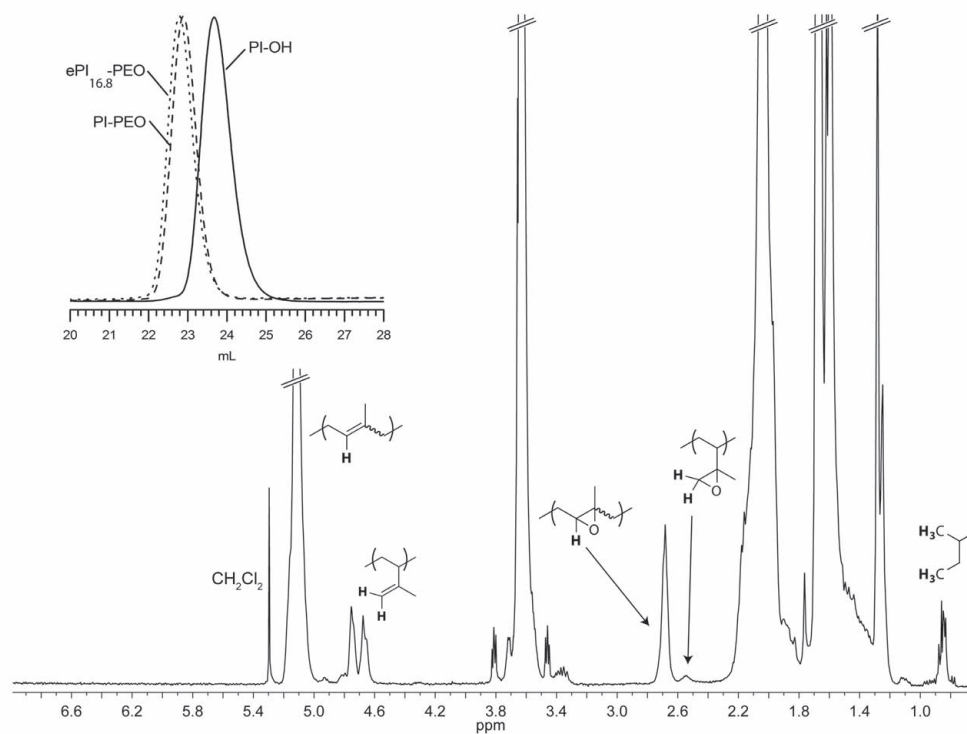


Figure 3-2. ¹H NMR of ePI_{16.8}-PEO. The percent epoxidation is calculated based on the integration of epoxy protons relative to olefin repeat units. Inset, Size Exclusion Chromatography (SEC) for PI-OH, PI-PEO, and ePI_{16.8}-PEO. SEC confirms the absence of PI-OH homopolymer in the PI-PEO diblock copolymer. Subsequent partial epoxidation of the PI-PEO diblock copolymer has no significant effect on the original molecular weight distribution.

was confirmed by ^1H NMR spectroscopy. 3-chloroperoxybenzoic acid (MCPBA) was used to carry out controlled partial epoxidation of the isoprene monomer units (Figure 3–2). No side reactions or chain degradation were observed during the epoxidation step, with post reaction molecular weight distributions (e.g., 16.8% of isoprene repeat units epoxidized, PDI = 1.05) being identical to the pre-epoxidized product (Figure 3–2, inset).

3.3.2 Melt State Phase Behavior of PI–PEO

The synthesized PI–PEO BCP was targeted for its anticipated complex phase behavior, with thermally induced phase transitions expected between lamellae (L_C , coinciding with crystalline PEO), hexagonally packed cylinders (C), bicontinuous gyroid (G), and a final isotropic disordered state (Dis). Complementary analysis using dynamic rheology and small-angle X-ray scattering (SAXS) of the native PI–PEO block copolymer confirmed the targeted behavior, which is illustrated in detail in Figure 3–3. Below 53 °C, the PEO domains are partially crystalline, which gives rise to a higher modulus and forces the molecules into a distorted lamellar-like morphology (L_C). Notably, the transition to this distorted lamellar structure is purely crystallization induced and not a melt-state equilibrium structure. The distortion in the lattice clearly evident in the SAXS data is the product of the rapid crystallization kinetics that prevents full development of a highly periodic structure. Upon heating, the partially crystalline PEO domains melt (53 °C), which is accompanied by a simultaneous drop in modulus associated with the direct transition to cylinders (C). Continued heating produces a step increase in modulus at a second transition (155 °C) to the gyroid phase (G) which persists until the sample finally disorders at 277 °C. The gyroid phase (G) is recovered with little hysteresis upon cooling from this disordered state; however, the system fails to reversibly transition to the cylindrical phase as the sample is cooled further. Instead, the gyroid phase persists until the re-crystallization of PEO occurring in the vicinity of 35 °C. As the scattering data suggests, the rapid crystallization event produces a distorted lamellar morphology, similar to that observed in a previous report by Floudas.⁴² Importantly, when the sample is then subjected to subsequent thermal cycles identical to the

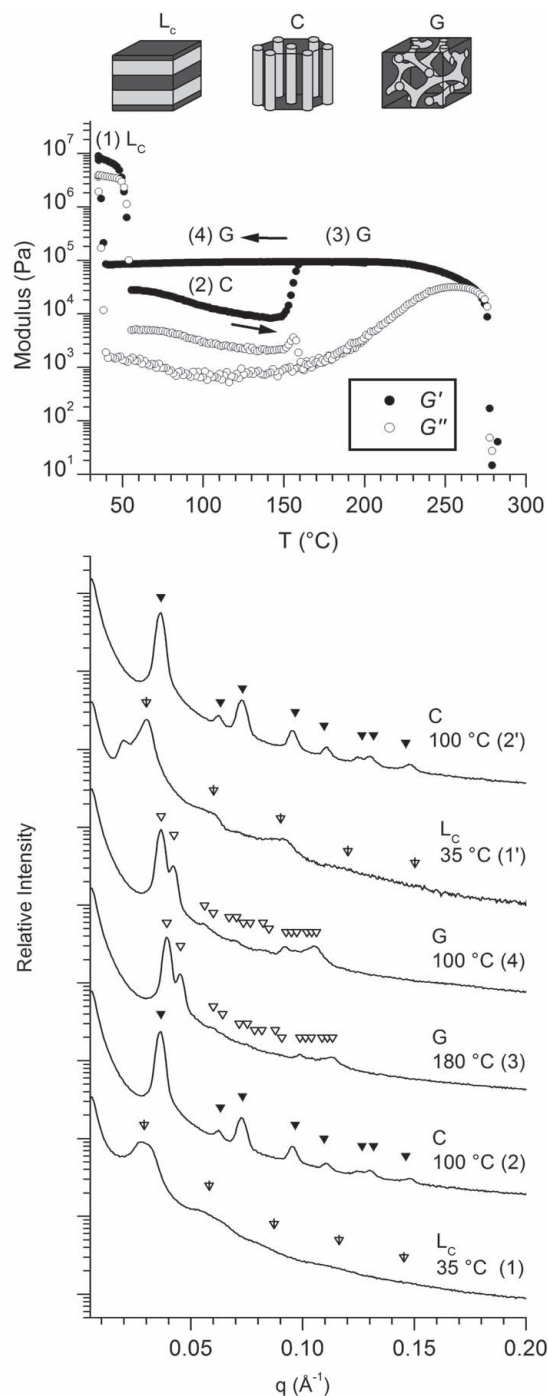


Figure 3-3. Thermal dependence of phase behavior for native PI-PEO ($f_{\text{PEO}} = 0.39$). Elastic and loss moduli as a function of heating and cooling at $1\text{ }^\circ\text{C min}^{-1}$ (1 rad s^{-1} and 1.0% strain). Arrows indicate the heating and cooling directions (top). SAXS data collected at positions (1)–(4) of the depicted thermal cycle. Primed locations represent data from the second cycle. Inverted triangles represent location of allowed reflections for the morphology designated at the right, based on the principal scattering wave vector q^* : (L_c) q/q^* at $\sqrt{1}, \sqrt{4}, \sqrt{9}, \sqrt{16}, \sqrt{25}, \text{etc.}$; (C) q/q^* at $\sqrt{1}, \sqrt{3}, \sqrt{4}, \sqrt{7}, \sqrt{9}, \sqrt{12}, \sqrt{13}, \sqrt{16}, \text{etc.}$; (G) q/q^* at $\sqrt{6}, \sqrt{8}, \sqrt{14}, \sqrt{16}, \sqrt{20}, \sqrt{22}, \sqrt{24}, \sqrt{26}, \sqrt{30}, \sqrt{32}, \sqrt{38}, \sqrt{40}, \sqrt{42}, \sqrt{46}, \sqrt{48}, \sqrt{50}, \text{etc.}$ (bottom)

first, all of the original scattering character observed in the first cycle is reproduced. That is, the cylindrical phase reappears upon melting of the crystalline PEO domains, with the complete absence of any mixed (gyroid) character (Figure 3–3).

3.3.3 Melt State Phase Behavior of ePI-PEO

Partial epoxidation of the PI-PEO block copolymer produces only minor quantitative changes in the phase behavior of the system, with the qualitative progression of morphologies (verified by SAXS, not shown) being identical to those exhibited by the native PI-PEO BCP (Figure 3–3).

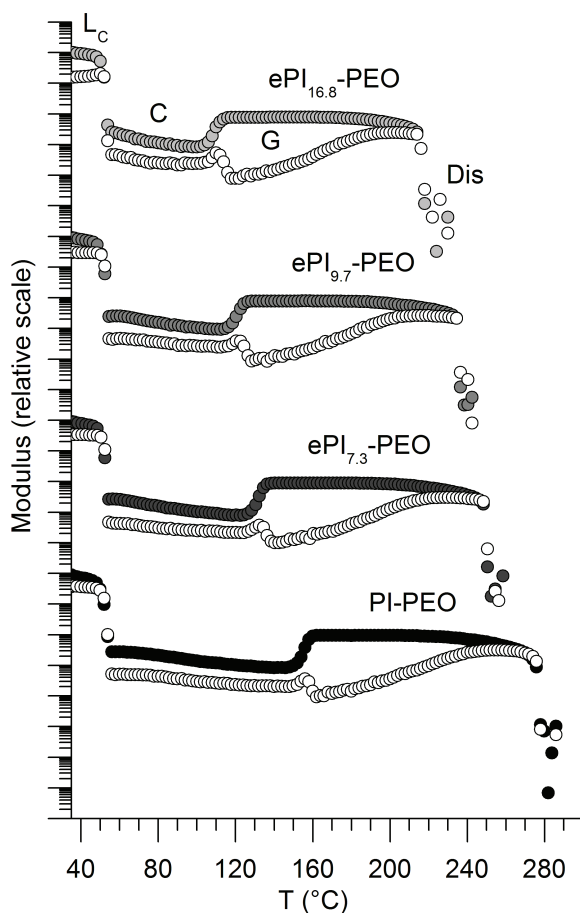


Figure 3–4. Dynamic temperature ramps for ePI-PEO samples with differing epoxide content (0 mol%, 7.3 mol%, 9.7 mol%, and 16.8 mol%, relative to PI repeat units). All samples progress through the same series of morphologies: crystalline lamellar (L_C), hexagonally packed cylinders (C), gyroid (G), and disordered (Dis). Increasing epoxide content leaves the qualitative phase behavior intact, but shifts the transitions to the gyroid and disordered phases to lower temperatures. The initial transition from L_C to C is correlated to the melting of PEO crystallites and is unaffected by the epoxide content.

Notably, increasing epoxide content has no effect on the position of the transition from lamellae to cylinders (53 °C), confirming its correlation with the melting transition of crystalline PEO domains. In contrast, increasing the epoxide content produces a reduction in the temperatures at which the samples transition to both the gyroid phase and the disordered state (Figure 4). For this report, we have chosen to focus on a single sample in which 16.8% of the isoprene repeat units in the PI block have been epoxidized (ePI_{16.8}-PEO). At this level of epoxidation, the decrease in temperatures at which the transitions to the gyroid and disordered phases occur (during heating) is the most significant, dropping from 155 °C to 110 °C and from 277 °C to 215 °C (Figure 3–4), respectively. It is apparent that the introduction of additional oxygen into the PI block acts to reduce the Flory interaction parameter, χ , weakening the degree of segregation in the system. Despite this trend, the continued presence of each of the morphologies over a broad range of epoxide content (we examined up to 16.8%) is encouraging; not only does it suggest facile tuning of the crosslink density may be possible, but that the epoxidation approach is mild enough to find success when applied to other BCP systems. Importantly, the epoxidized BCPs also exhibit the same behavior under thermal cycling (from 35 °C to disorder and back) as the native PI–PEO samples (Figure 3–4); that is, the cylinder phase is deposited by the gyroid phase upon cooling through the onset of PEO crystallization, but is immediately restored upon re-melting of the PEO crystals during subsequent heating.

3.3.4 Melt State Phase Behavior of ePI–PEO with IPDPST Photoacid

Small quantities (1.0–1.25 mol%, relative to the original number of unmodified isoprene repeat units) of IPDPST were codissolved with the ePI–PEO samples and subsequently freeze dried overnight. The sulfonium salt/ePI–PEO blends were universally malleable, with a paste-like consistency. Similar to the epoxidation step, the addition of the sulfonium salt had no effect on the qualitative progression of morphologies (verified by SAXS, not shown) previously exhibited by the native PI–PEO and ePI–PEO samples. As before, the position of the transition from lamellae to cylinders (53 °C) remained tied to the melting of the PEO crystallites; however,

unlike epoxidation, the temperatures at which the samples transitioned to the gyroid phase increased with increasing IPDPST content (Figure 3–S1, Appendix II). As shown in Figure 3–5, the addition of just 1 mol% IPDPST to the $ePI_{16.8}$ -PEO sample ($ePI_{16.8}$ -PEO-1) increases the transition to the gyroid morphology from 110 °C up to 127 °C. Disorder transitions were not measured in IPDPST containing samples as the sulfonium salt begins to degrade when heated above 200 °C. Again, the behavior during thermal cycling (from 35 °C to 165 °C and back) mimics that exhibited by the PI-PEO and ePI -PEO samples, with the retention of the gyroid phase upon cooling and subsequent recovery of the cylinder phase upon reheating from the crystalline state. The systematic influence of the IPDPST on the gyroid transition temperature

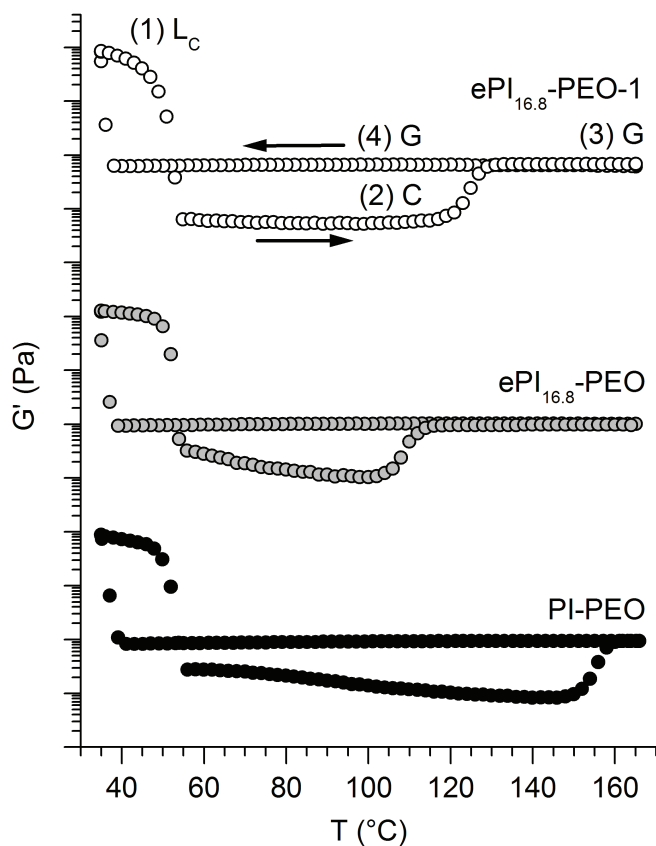


Figure 3–5. Rheological comparison of the thermally dependent phase behavior of PI-PEO, $ePI_{16.8}$ -PEO, and $ePI_{16.8}$ -PEO-1. Elastic moduli as a function of heating and cooling at 1 °C min⁻¹ (1 rad s⁻¹ and 0.5 – 2.0 % strain). Locations (1)–(4) indicate specific positions in the thermal cycle used during curing experiments discussed in the main text. Arrows indicate the heating and cooling directions.

is consistent with the homogenous dispersion of the sulfonium salt within the BCP sample. Differential scanning calorimetry data (Figure 3-S2, Appendix II) supports these conclusions, as the melting transition for crystalline IPDPST is no longer present in the blend. Whether there is any preferential segregation to the ePI domains is unclear at this point, although the retention of PEO crystallinity at lower temperatures suggests that may be the case. As discussed below, the application of UV radiation does activate the cationic polymerization of the epoxidized PI repeat units, which fails to occur in the absence of the sulfonium salt (control experiment). As such, the distribution of the IPDPST is at the very least sufficient to initiate cure in the ePI domains.

3.3.5 Cylindrical Trapping Curing Experiment

To demonstrate the ability of these photocurable BCP systems to enable selective morphological trapping, two curing experiments are presented for the ePI_{16.8}-PEO-1 sample. In the first experiment (Figure 3-6) 0.1 mm thin films of the ePI_{16.8}-PEO-1 paste were placed between two mica sheets and slowly heated to 100 °C (location (2) in Figure 3-5, cylinder morphology). Samples were then exposed to broad spectrum UV radiation (xenon lamp, 45 mW cm⁻²) for 10 min, and then cooled over several minutes to room temperature. Following exposure, the samples were mechanically rigid, insoluble in organic solvents, and light amber in color. SAXS data were collected while subjecting the cured samples to the same thermal cycle used to characterize the paste (from 35 °C to 165 °C and back). The sample was too rigid to perform melt-state rheological analysis. Representative SAXS data on a cured ePI_{16.8}-PEO-1 sample at both 100 °C and 160 °C are given in Figure 3-6, together with data collected at the same temperatures on the uncured ePI_{16.8}-PEO-1 paste. At 100°C, the cured sample exhibits hexagonal symmetry indicative of the cylinder morphology, consistent with that expected in the sample prior to cure. Clearly the curing kinetics and cationic propagation mechanism itself are sufficient to translate the pre-cure morphology to the solid state with high fidelity, given the number of higher order reflections in the post-cure SAXS. Some enlargement of the structure during

cure was observed, however, as the inter-cylinder spacing at 100 °C increased from about 20 nm to 22 nm based on a comparison of pre- and post-cure SAXS measurements. It is possible that the slightly increased lattice spacing is a product of local heating during cure, which could arise due to both the incident radiation and the reaction exotherm itself. Curing configurations in which greater thermal control is possible may be necessary in thermally sensitive systems. Slight broadening of the peak widths is also apparent, and suggests a correlated broadening of the distribution of lattice spacings present in the cured sample. Again, a small degree of heterogeneity in temperature across the sample is the likely culprit. At temperatures above 127 °C, the uncured $ePI_{16.8}$ -PEO-1 samples adopt the gyroid morphology. The cured $ePI_{16.8}$ -PEO-1 solid, however, clearly retains the hexagonal symmetry of the cylinder morphology and no longer undergoes the gyroid phase transition. Detailed SAXS characterization confirmed the cylindri-

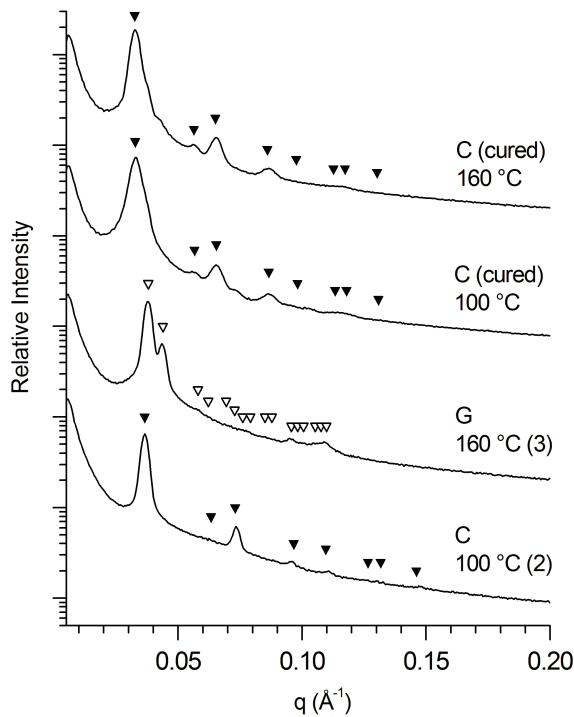


Figure 3-6. Comparison of SAXS data collected on cured (at 100 °C, location (2) (Figure 3-5), cylinder morphology) and uncured $ePI_{16.8}$ -PEO-1. Following cure, the $ePI_{16.8}$ -PEO-1 solid is prevented from transitioning to the gyroid phase typical of the uncured paste above 127 °C. The cylinder phase was present at all temperatures in the thermal cycle following cure at location (2).

cal morphology is retained throughout the applied thermal cycle, although crystallization of the PEO domains still appears to readily distort the lattice at lower temperatures. Even so, the highly organized, cured cylindrical phase is recovered upon melting of the PEO crystallites, suggesting no permanent rearrangement is occurring; likely, the rubbery nature of the cured ePI domains allows local elastic distortion of the hexagonal lattice during the crystallization event.

3.3.6 Gyroid Trapping Curing Experiment

In the second, similarly conducted experiment (Figure 3-7), thin films of the ePI_{16.8}-PEO-1 paste were first preheated to 160 °C (location (3) in Figure 3-5, gyroid morphology) before being slowly cooled back to 100 °C (location (4) in Figure 3-5, gyroid morphology). As before, the samples were exposed to broad spectrum UV radiation for 10 min, and then cooled over several minutes to room temperature. Following exposure, samples had similar mechanical rigidity, solvent resistance, and coloration as those from the first experiment. The morphology of the cured sample as a function of temperature was again characterized by collecting SAXS data throughout the same thermal cycle. In this case, the sample retained the gyroid morphology throughout the entire thermal cycle, consistent with the morphology present during cure. This is illustrated in Figure 3-7, where SAXS data collected on the cured ePI_{16.8}-PEO-1 solid at 100 °C, following direct heating from room temperature, is presented, together with data from the uncured ePI_{16.8}-PEO-1 paste at both 100 °C (location (2) in Figure 3-5, cylinder morphology) and 160 °C (location (4) in Figure 3-5, gyroid morphology). During the initial heating to 100°C, the cured sample now exhibits the diffraction pattern consistent with the gyroid morphology, instead of the cylinder morphology always present (in uncured samples) upon melting of the PEO crystallites. Again, the pre-cure morphology is effectively translated to the solid with high fidelity, with obvious higher order reflections in the post-cure SAXS. As with the sample cured in experiment one, scattering peak widths are broadened, significantly enough to blur the first two principle reflections (211 and 220) so characteristic of the gyroid

structure. In contrast to that observed in the curing of the cylinder phase, no significant change in the lattice spacing was detected upon cure. Both the pre-cure and post-cure lattice constants, as determined from SAXS, were 43 nm. Again, crystallization of the PEO domains still appears to readily distort the lattice at lower temperatures (SAXS not shown); however, like the cured cylinder phase described above, the distortion is highly elastic, with complete recovery of the underlying gyroid morphology upon melting of the PEO crystallites (Figure 3–7).

3.4 CONCLUSIONS

In both the gyroid and cylindrical curing experiments, curing was triggered at 100 °C, although at two distinctly different locations in the applied thermal cycle (locations (2) and (4) in Figure 3–5). The inherent thermal stability of the IPDPST enables its use as a robust cationic photo-

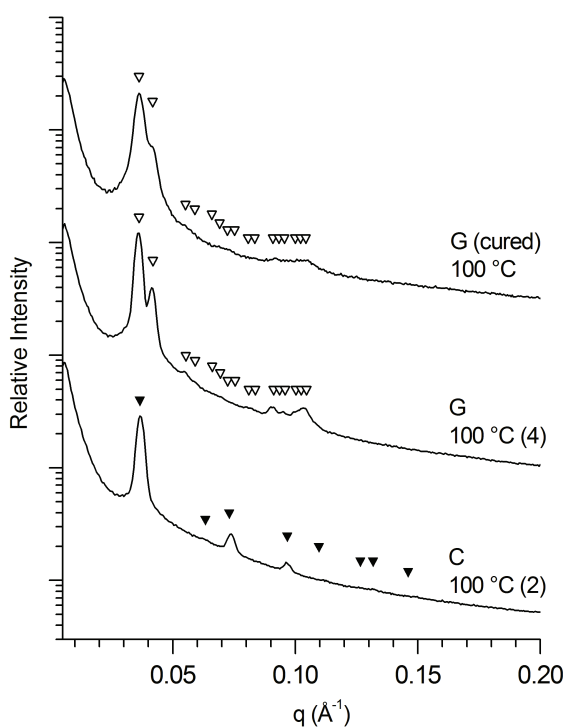


Figure 3–7. Comparison of SAXS data collected on cured (at 100 °C, location (4) (Figure 3–5), gyroid morphology) and uncured ePI_{16.8}-PEO-1. Following cure, the ePI_{16.8}-PEO-1 solid is prevented from transitioning to the cylinder phase upon heating from room temperature, typical of the uncured paste below 127 °C. The gyroid phase was present at all temperatures in the thermal cycle following cure at location (4).

initiator in systems that require extended thermal processing prior to cure. In this report we emphasize their value as curing agents in BCP systems exhibiting complex phase behavior, where multiple morphologies can be selectively trapped as a result of the temperature independent curing trigger. We think this approach will be particularly useful in the selective curing of morphologies bound to very narrow regions of phase space, such as those found in more complex ABC triblock copolymer systems, or of A/B/AB homopolymer/diblock copolymer blends. The introduction of both epoxide groups and low concentrations of sulfonium salts produced systems with qualitatively similar phase behavior as the native PI-PEO system of study. We believe this result accentuates the potential for facile transfer to other BCP systems in which mild concentrations of cationically polymerizable functional groups (e.g., oxiranes, vinyl ethers, and thiiranes) can be introduced. Detailed investigations evaluating the influence of epoxide and sulfonium salt concentrations on curing kinetics, translation fidelity, and resulting mechanical properties are now in progress.

3.5 EXPERIMENTAL

3.5.1 Materials and Methods

Isoprene (99%, 100 ppm *p*-tert-butylcatechol inhibitor, Aldrich) was purified by successive static vacuum (15-30 mTorr) distillations from *n*-butyllithium (1.6 M in hexanes, Aldrich). Ethylene oxide (99.5+%, compressed gas, Aldrich) was purified by successive distillations from di-*n*-butylmagnesium (1.0 M in heptane, Aldrich). *sec*-butyllithium (1.3 M in cyclohexane/hexane, Fisher) was used as received. 3-chloroperoxybenzoic acid (MCPBA, 70-75%, Acros Organics) was dissolved in methylene chloride and dried twice over anhydrous sodium sulfate. Naphthalene (Fisher) was recrystallized twice from diethyl ether. Potassium metal (98 %, Fisher) was cut into pieces under light mineral oil and fresh non-oxidized metal surfaces were obtained by washing in a hexane: ethanol (200: 1) mixture for 30 s. Potassium naphthalenide solution was prepared by dissolving excess (1.1 x) recrystallized naphthalene and freshly cut potassium in tetrahydrofuran (THF) under argon. The dark green solution was allowed to stir overnight with

a glass spinbar before use. (4-iodophenyl)diphenylsulfonium triflate (IPDPST) photoinitiator was purchased from Aldrich and used as received. All other common chemicals were used as received unless otherwise stated. THF was degassed by sparging with argon (10 psi) for a period of 45 minutes and then purified over two molecular sieve columns of neutral alumina (Glass Contour, Inc.) Cyclohexane (CHX) was degassed with argon and purified through a column of neutral alumina followed by a column of Q5 copper (II) oxide catalyst (Glass Contour, Inc.). Ultra high purity argon (99.998% Airgas) was passed through a column of 5 Å molecular sieves with drierite (Agilent) and an oxygen absorbing purifier column (Matheson Tri-gas). All glassware and polymerization reactors were flamed under vacuum and backfilled with argon (3x).

3.5.2 Physical and Analytical Measurements

NMR spectra were recorded on a Varian Inova 400 MHz spectrometer with a pulse delay of 20 s to ensure complete relaxation of end groups. The spectra were referenced to the residual protio solvent (CHCl_3 or CH_2Cl_2). Gel permeation chromatography (GPC) was performed on a Viscotek GPC-Max chromatography system outfitted with three 7.5 x 340 mm Polypore (Polymer Laboratories) columns in series. The columns were maintained at 40 °C in an Alltech column oven. The GPC system was attached to a Viscotek differential refractive index (RI) detector. All polymer samples were run in THF (mobile phase, 1 mL min⁻¹).

3.5.3 Dynamic Mechanical Spectroscopy

Rheological experiments were run on a TA Instruments ARES rheometer. Samples were roughly formed as discs and put between two parallel plates (8 mm). The plates were then heated to 75 °C and the gap was adjusted to ensure even distribution of the sample. Typical gaps were 0.3–0.5 mm. Dynamic temperature ramp tests were performed while heating and cooling at 1 °C min⁻¹ at angular frequency of 1 rad s⁻¹ and a strain of 0.5 – 2.0% (depending on the linear viscoelastic regime).

3.5.4 Small Angle X-ray Scattering (SAXS)

Scattering data was collected on a Rigaku S-Max 3000 High Brilliance three pinhole SAXS system outfitted with a MicroMax-007HFM rotating anode (CuK α), Confocal Max-Flux Optics, Gabriel multiwire area detector, and a Linkam thermal stage. Polymer samples were sandwiched between either Kapton discs or mica discs. Exposure times for uncured samples were typically on the order of 1200–3600 s. Cured sample exposure times varied between 3600–10800 s.

3.5.5 ω -hydroxy-polyisoprene (PI).

Anionic polymerization of isoprene (37.5 g, 8h) was initiated with sec-butyllithium (6.01 mL, 1.3 M) in 1L of cyclohexane at 40°C under a positive argon pressure of 1 psi. Ethylene oxide (7.8g, 20 h) was added as an end-capping agent. The terminal alkoxide was quenched with acidic methanol (35 mL, 70:1 MeOH:HCl (conc.)), and the cyclohexane polymer solution was reduced to 500 mL on a roto-evaporator. The product precipitated from 4:1 MeOH: EtOH (2.5 L). The polymeric alcohol was dissolved in benzene and freeze-dried in vacuo (25 °C, 24 h). Recovered sticky clear viscous liquid, 34.9 g (93%). GPC (Polystyrene standards): $M_w/M_n = 1.07$. $^1\text{H NMR}$ (400 MHz, CDCl_3 , δ): 4.9–5.4 (b, $-\text{CH}_2-\text{CH}=\text{C}(\text{CH}_3)-\text{CH}_2-$), 4.6–4.8 (b, $\text{CH}_2=\text{C}(\text{CH}_3)-$), 3.5–3.7 (m, $-\text{CH}_2-\text{OH}$), 1.7–2.3 (b, $-\text{CH}_2-\text{C}(\text{CH}_3)=\text{CH}-\text{CH}_2-$ and $-\text{CH}_2-\text{C}(\text{R})-\text{H}-\text{C}(\text{CH}_3)=\text{CH}_2$), 1.5–1.7 (b, $-\text{CH}_2-\text{C}(\text{CH}_3)=\text{CH}-\text{CH}_2-$ and $-\text{CH}_2-\text{C}(\text{R})\text{H}-\text{C}(\text{CH}_3)=\text{CH}_2$), 1.0–1.5 (b, $-\text{CH}_2-\text{C}(\text{R})\text{H}-\text{C}(\text{CH}_3)=\text{CH}_2$), 0.9 (m, $\text{CH}_3-\text{CH}_2-\text{C}(\text{R})\text{H}-\text{CH}_3$, initiator fragment). M_n (calc. From $^1\text{H NMR}$ integrations) = 5352 g mol $^{-1}$. 4,3 content= 6.8%

3.5.6 ω -hydroxy-polyisoprene-*b*-poly(ethylene oxide) (PI-PEO)

PI (8.05 g) was dissolved in 500 mL dry THF. The solution was titrated with potassium naphthalenide until a light green color remained for at least 5 min at 40 °C. Ethylene oxide (6.4g, 24h) was added to the reactor under a slight positive pressure of argon (1 psi), the solution immediately went from light green to clear. The terminal alkoxide was quenched with acidic methanol (25 mL, 50:1 MeOH:HCl (conc.)), the polymer solution changed color from smokey

rose red to milky orange. The solution was reduced to 200 mL on a roto-evaporator. The block copolymer alcohol product precipitated from $-20\text{ }^{\circ}\text{C}$ acetone (1 L). Filtration and drying in vacuo ($25\text{ }^{\circ}\text{C}$, 24 h) gave the block copolymer as a waxy light tan paste. Yield= 13.09 g (91 %). GPC (Polystyrene standards): $M_w/M_n = 1.05$. $^1\text{H NMR}$ (400 MHz, CDCl_3 , δ): 4.9–5.4 (b, $-\text{CH}_2-\text{CH}=\text{C}(\text{CH}_3)-\text{CH}_2-$), 4.6–4.8 (b, $\text{CH}_2=\text{C}(\text{CH}_3)-$), 3.3–3.8 (b, $-\text{CH}_2-\text{CH}_2-\text{O}-$), 1.7–2.3 (b, $-\text{CH}_2-\text{C}(\text{CH}_3)=\text{CH}-\text{CH}_2-$ and $-\text{CH}_2-\text{C}(\text{R})\text{H}-\text{C}(\text{CH}_3)=\text{CH}_2$), 1.5–1.7 (b, $-\text{CH}_2-\text{C}(\text{CH}_3)=\text{CH}-\text{CH}_2-$ and $-\text{CH}_2-\text{C}(\text{R})\text{H}-\text{C}(\text{CH}_3)=\text{CH}_2$), 1.0–1.5 (b, $-\text{CH}_2-\text{C}(\text{R})\text{H}-\text{C}(\text{CH}_3)=\text{CH}_2$), 0.9 (m, $\text{CH}_3-\text{CH}_2-\text{C}(\text{R})\text{H}-\text{CH}_3$, initiator fragment). $f_{\text{PEO}} = 0.39$, $M_n = 10\ 120\ \text{g mol}^{-1}$, calc. from $^1\text{H NMR}$ integrations).

3.5.7 Epoxidized Polyisoprene-*b*-poly(ethylene oxide) (ePI-PEO)

PI-PEO (3.5 g) was dissolved in 75 mL methylene chloride. MCPBA (1.05 g) was dissolved in 75 mL methylene chloride and dried twice with anhydrous Na_2SO_4 . The filtered MCPBA solution was then added to the PI-PEO solution under argon. After 2h the reaction was washed (3x) with DI water, and dried with anhydrous Na_2SO_4 . Removal of solvent and drying in vacuo (25°C , 24 h) gave the epoxidized block copolymer as a waxy light yellow paste. Yield= 3.2 g, 91%. GPC (Polystyrene standards): $M_w/M_n = 1.05$. $^1\text{H NMR}$ (400 MHz, CDCl_3 , δ): 4.9–5.4 (b, $-\text{CH}_2-\text{CH}=\text{C}(\text{CH}_3)-\text{CH}_2-$), 4.6–4.8 (b, $\text{CH}_2=\text{C}(\text{CH}_3)-$), 3.3–3.8 (b, $-\text{CH}_2-\text{CH}_2-\text{O}-$), 2.6–2.8 (b, $-\text{CH}_2-\text{CH}(\text{O})\text{C}(\text{CH}_3)-\text{CH}_2-$, epoxidized 4,1 units), 2.3–2.6 (b, $\text{CH}_2(\text{O})\text{C}(\text{CH}_3)$, epoxidized 4,3 units), 1.7–2.3 (b, $-\text{CH}_2-\text{C}(\text{CH}_3)=\text{CH}-\text{CH}_2-$, $-\text{CH}_2-\text{C}(\text{CH}_3)(\text{O})-\text{CH}-\text{CH}_2-$, $-\text{CH}_2-\text{C}(\text{R})\text{H}-\text{C}(\text{CH}_3)=\text{CH}_2$), and $-\text{CH}_2-\text{C}(\text{R})\text{H}-\text{C}(\text{CH}_3)(\text{O})\text{CH}_2$), 1.5–1.7 (b, $-\text{CH}_2-\text{C}(\text{CH}_3)=\text{CH}-\text{CH}_2-$, $-\text{CH}_2-\text{C}(\text{CH}_3)(\text{O})-\text{CH}-\text{CH}_2-$, $-\text{CH}_2-\text{C}(\text{R})\text{H}-\text{C}(\text{CH}_3)=\text{CH}_2$), and $\text{CH}_2-\text{C}(\text{R})\text{H}-\text{C}(\text{CH}_3)(\text{O})\text{CH}_2$), 1.0–1.5 (b, $-\text{CH}_2-\text{C}(\text{R})\text{H}-\text{C}(\text{CH}_3)=\text{CH}_2$ and $-\text{CH}_2-\text{C}(\text{R})\text{H}-\text{C}(\text{CH}_3)(\text{O})\text{CH}_2$), 0.9 (m, $\text{CH}_3-\text{CH}_2-\text{C}(\text{R})\text{H}-\text{CH}_3$, initiator fragment). Epoxidized units (calc. From $^1\text{H NMR}$) = 16.8%.

3.5.8 Photocuring of ePI_{16.8}-PEO-1

ePI_{16.8}-PEO samples were codissolved with 1 mol % (relative to PI repeat units) (4-iodophenyl) diphenylsulfonium triflate in a 1:1 benzene: chloroform mixture and freeze-dried overnight.

The resulting blends, ePI_{16.8}-PEO-1 were then heated to 75 °C and pressed between two mica discs (10mm dia., 0.1 mm thickness). Sample thicknesses were ~ 0.1 mm. The mica sandwich was then placed in home built flood enclosure containing a Hoenle (Gräfelfing, Germany) UV xenon lamp. The intensity at the cure site was ~ 45 mW cm⁻² (measured in the range of 230–410 nm with a Con-Trol-Cure Silver Line UV-Radiometer). The sample was heated to the desired temperature on an IKA stir plate, and then exposed to the UV light for a period of 10 min. After curing the block copolymers became mechanically rigid, insoluble, and light amber in color.

3.6 ACKNOWLEDGEMENTS

The authors would like to thank R. Wickramasinghe for generous access to the UV light source. This work was supported by the National Science Foundation (DMR-0645781) and the Colorado State University.

3.7 SUPPORTING INFORMATION AVAILABLE.

Figures 3–S1 and 3–S2 located in Appendix II.

3.8 REFERENCES

1. Bates, F. S. *Science* **1991**, 251 (4996), 898-905.
2. Bates, F. S.; Fredrickson, G. H. *Phys. Today* **1999**, 52, 32-38.
3. Melde, B. J.; Burkett, S. L.; Xu, T.; Goldbach, J. T.; Russell, T. P. *Chem. Mater.* **2005**, 17, (18), 4743-4749.
4. Zhang, Q. L.; Xu, T.; Butterfield, D.; Misner, M. J.; Ryu, D. Y.; Emrick, T.; Russell, T. P. *Nano Lett.* **2005**, 5 (2), 357-361.
5. Akthakul, A.; Salinaro, R. F.; Mayes, A. M. *Macromolecules* **2004**, 37, (20), 7663-7668.
6. Gabashvili, A.; Medina, D. D.; Gedanken, A.; Mastai, Y. *J. Phys. Chem. B* **2007**, 111 (38), 11105-11110.
7. Phillip, W. A.; O'Neill, B.; Rodwogin, M.; Hillmyer, M. A.; Cussler, E. L. *ACS Appl. Mater. Interfaces* **2010**, 2 (3), 847-853.
8. Yang, S. Y.; Ryu, I.; Kim, H. Y.; Kim, J. K.; Jang, S. K.; Russell, T. P. *Adv. Mater.* **2006**, 18 (6), 709-712.
9. Durkee, D. A.; Eitouni, H. B.; Gomez, E. D.; Ellsworth, M. W.; Bell, A. T.; Balsara, N. P. *Adv. Mater.* **2005**, 17 (16), 2003-2006.
10. Mayavan, S.; Choudhury, N. R.; Dutta, N. K. *Adv. Mater.* **2008**, 20 (10), 1819-1824.
11. Guo, C.; Bailey, T. S. *Soft Matter* **2010**, 6 (19), 4807-4818.
12. Kim, H.-C.; Park, S.-M.; Hinsberg, W. D. *Chem. Rev.* **2009**, 110 (1), 146-177.
13. Segalman, R. A.; McCulloch, B.; Kirmayer, S.; Urban, J. J. *Macromolecules* **2009**, 42 (23), 9205-9216.
14. Fu, G. D.; Yuan, Z. L.; Kang, E. T.; Neoh, K. G.; Lai, D. M.; Huan, A. C. H. *Adv. Funct. Mater.* **2005**, 15 (2), 315-322.
15. Olson, D. A.; Chen, L.; Hillmyer, M. A. *Chem. Mater.* **2008**, 20 (3), 869-890.
16. Cho, C. G.; Kim, S. H.; Park, Y. C.; Kim, H.; Park, J. W. *J. Membr. Sci.* **2008**, 308 (1-2), 96-106.
17. Perrin, R.; Elomaa, M.; Jannasch, P. *Macromolecules* **2009**, 42 (14), 5146-5154.
18. Darling, S. B.; Yufa, N. A.; Cisse, A. L.; Bader, S. D.; Sibener, S. J. *Adv. Mater.* **2005**, 17 (20), 2446-2450.
19. Crossland, E. J. W.; Kamperman, M.; Nedelcu, M.; Ducati, C.; Wiesner, U.; Smilgies, D. M.; Toombes, G. E. S.; Hillmyer, M. A.; Ludwigs, S.; Steiner, U.; Snaith, H. J. *Nano Lett.* **2009**, 9 (8), 2807-2812.
20. Bailey, T. S.; Rzaev, J.; Hillmyer, M. A. *Macromolecules* **2006**, 39 (25), 8772-8781.
21. Hillmyer, M. A. *Adv. Polym. Sci.* **2005**, 190, 137-181.
22. Rzaev, J.; Hillmyer, M. A. *J. Am. Chem. Soc.* **2005**, 127, (38), 13373-13379.
23. Foerster, S.; Khandpur, A. K.; Zhao, J.; Bates, F. S.; Hamley, I. W.; Ryan, A. J.; Bras, W. *Macromolecules* **1994**, 27 (23), 6922-6935.
24. Hamersky, M. W.; Hillmyer, M. A.; Tirrell, M.; Bates, F. S.; Lodge, T. P.; von Meerwall, E. D. *Macromolecules* **1998**, 31 (16), 5363-5370.
25. Hillmyer, M. A.; Bates, F. S.; Almdal, K.; Mortensen, K.; Ryan, A. J.; Fairclough, J. P. A. *Science* **1996**, 271 (5251), 976-978.
26. Matmour, R.; Joncheray, T. J.; Gnanou, Y.; Duran, R. S. *Langmuir* **2007**, 23 (2), 649-658.
27. Wang, X.-S.; Arsenault, A.; Ozin, G. A.; Winnik, M. A.; Manners, I. *J. Am. Chem. Soc.* **2003**, 125 (42), 12686-12687.
28. Wang, X.; Liu, K.; Arsenault, A. C.; Rider, D. A.; Ozin, G. A.; Winnik, M. A.; Manners, I. *J. Am. Chem. Soc.* **2007**, 129 (17), 5630-5639.

29. Cavicchi, K. A.; Zalusky, A. S.; Hillmyer, M. A.; Lodge, T. P. *Macromol. Rapid Commun.* **2004**, *25* (6), 704-709.
30. Guo, F.; Andreasen, J. W.; Vigild, M. E.; Ndoni, S. *Macromolecules* **2007**, *40* (10), 3669-3675.
31. Leiston-Belanger, J. M.; Russell, T. P.; Drockenmuller, E.; Hawker, C. J. *Macromolecules* **2005**, *38* (18), 7676-7683.
32. Drockenmuller, E.; Li, L. Y. T.; Ryu, D. Y.; Harth, E.; Russell, T. P.; Kim, H.-C.; Hawker, C. *J. J. Polym. Sci., Part A: Polym. Chem.* **2005**, *43* (5), 1028-1037.
33. Zhou, N.; Bates, F. S.; Lodge, T. P. *Nano Lett.* **2006**, *6* (10), 2354-2357.
34. Okumura, A.; Nishikawa, Y.; Hashimoto, T. *Polymer* **2006**, *47* (22), 7805-7812.
35. Hayward, R. C.; Chmelka, B. F.; Kramer, E. J. *Macromolecules* **2005**, *38* (18), 7768-7783.
36. Luo, K.; Rzaev, J. *Macromolecules* **2009**, *42* (23), 9268-9274.
37. Crivello, J. V. *Ann. Rev. Mater. Sci.* **1983**, *13*, 173-190.
38. Won, J.; Park, H. H.; Kim, Y. J.; Choi, S. W.; Ha, H. Y.; Oh, I.-H.; Kim, H. S.; Kang, Y. S.; Ihn, K. J. *Macromolecules* **2003**, *36* (9), 3228-3234.
39. Gruber, H. F. *Prog. Polym. Sci.* **1992**, *17*, 953-1044.
40. Li, M. Q.; Douki, K.; Goto, K.; Li, X. F.; Coenjarts, C.; Smilgies, D. M.; Ober, C. K. *Chem. Mater.* **2004**, *16* (20), 3800-3808.
41. Bosworth, J. K.; Black, C. T.; Ober, C. K. *ACS Nano* **2009**, *3* (7), 1761-1766.
42. Floudas, G.; Vazaiou, B.; Schipper, F.; Ulrich, R.; Wiesner, U.; Iatrou, H.; Hadjichristidis, N. *Macromolecules* **2001**, *34* (9), 2947-2957.
43. Hillmyer, M. A.; Bates, F. S. *Macromolecules* **1996**, *29* (22), 6994-7002.

CHAPTER 4

ACCESS TO NANOSTRUCTURED HYDROGEL NETWORKS THROUGH PHOTOCURED BODY-CENTERED CUBIC BLOCK COPOLYMER MELTS

The contents of this dissertation chapter have been adapted from a manuscript published in *ACS Macromolecules*: Scalfani, V. F.; Bailey, T. S. *Macromolecules* **2011**, *44*, 6557-6567. Vincent F. Scalfani and Travis S. Bailey developed and designed the experiments. Vincent F. Scalfani performed the experiments. The manuscript and dissertation chapter were written by Vincent F. Scalfani with editing by Travis S. Bailey.

4.1 CONSPECTUS

In this report, direct access to nanostructured hydrogel networks through high fidelity photocuring of sphere-forming block copolymer melts is demonstrated. Hydrophobic junction points within the hydrogel network are based on an underlying lattice of body-centered cubic spheres (S_{BCC}), produced via melt-state self-assembly of blended AB diblock and ABA triblock copolymer amphiphiles. Integrated thermally stable photocuring chemistry allows for in situ trapping of these spherical domains, independent from the required melt processing necessary to achieve the highly ordered BCC lattice. Swelling of the photocured solids in aqueous (and organic) media afforded highly elastic gels exhibiting excellent mechanical properties ($G' \sim 10^3$ Pa) and complete preservation of the cured solid shape. The hydrogels fabricated in this study were produced from partially epoxidized (19.6 %, relative to diene repeat units) blends of polybutadiene-*b*-poly(ethylene oxide) diblock (PB-PEO, $f_{\text{PB}} = 0.13$, $M_n = 29\,500$ g mol⁻¹, 88.5 mol%) and PB-PEO-PB triblock ($f_{\text{PB}} = 0.13$, $M_n = 59\,000$ g mol⁻¹, 11.5 mol%) copolymers synthesized via anionic polymerization. Addition of UV activated cationic photoinitiator (4-iodophenyl)diphenylsulfonium triflate (0.5 mol%) produced composite samples exhibiting a highly ordered S_{BCC} morphology after annealing at moderate temperatures (4 hr at 80 °C or 60 s at 140 °C) above the PEO melting transition. Composite films (0.33 mm thickness) were then photocured directly from the melt-state, post-anneal. Cured samples retained the S_{BCC} structure with extremely high fidelity, effectively pre-structuring the network of junction points prior to swelling. The photopatterning potential of these uniquely designed hydrogels is also demonstrated.

4.2 INTRODUCTION

Hydrogel networks¹⁻⁵ are attractive materials in a range of biomedical and biotechnological applications as a result of their potential to provide both mechanical support and sustained permeability (and compatibility) in biologically relevant media.⁶ Example applications include intervertebral disc implants, tissue scaffolds,⁷⁻¹¹ cell¹² or molecular¹³ encapsulation media,

chemical and drug delivery agents,^{14,15} and separation membranes.¹⁶⁻¹⁸ Effective performance in these applications, however, is dependent on accurate control over a range of hydrogel characteristics, including: elasticity, modulus, mesh size (pore size), mass transfer properties, equilibrium water content, micro- and macroscopic structure (shape preservation), and ease of functional group incorporation.¹⁹ The classic hydrogel frameworks, formed predominately from random physically or chemically cross-linked networks of hydrophilic polymers, are severely limited in this respect, providing limited control over the aforementioned parameters. In these simple systems, the inherently random nature of the cross-linking event produces spatially heterogeneous network connectivity with wide distributions of mesh sizes across the sample. Such heterogeneity is manifested through spatial inconsistencies in mechanical properties, swelling response and mass transport behavior within the hydrogel.² Furthermore, functionalization of the hydrogel can be challenging, as it requires the presence of free reactive sites independent of the exploited cross-linking chemistry. Our group is interested in developing synthetic strategies that overcome these limitations, and provide access to spatially homogeneous hydrogel networks with integrated functional group assemblies that can be easily and efficiently modified.

Critical to this mission are hydrogel formation mechanisms that permit active control over the uniformity in the network architecture. In this regard, block copolymers (BCPs) are prime candidates for producing structured hydrogels due to their unique ability to phase separate on the nanometer length scale.^{20,21} Of course, the use of ABA block copolymers as solution gelators has been a commonly explored motif in both solvogel and hydrogel research over the last decade or two, particularly in regard to the development of injectable delivery systems. These approaches are based on the formation of micellar networks where hydrophobic A blocks aggregate in solution to form micellar cores and the hydrophilic B mid-blocks act as tethering elements which span different micelle units. Gelation efficacy in such systems is highly concentration dependent, requiring ABA triblock copolymers to be present in amounts that statistically favor bridging of ABA chains across micelles; dilute solutions favor looping into the same micelle and the formation of flower type structures that are unable to contribute to network

formation.

Such strategies dramatically improve uniformity in average distance between junction points (micellar cores), but have been used primarily to produce gels systems that are readily deformable with limited elastic character.^{6,19,22–24} Such characteristics are consistent with the design constraints for injectable delivery systems, but are not particularly useful for more mechanically demanding applications such as membrane separations or biomedical implant technologies. However, this same tethered micelle network motif can be used to form more mechanically robust systems, but requires fabrication conditions that produce micelle cores resistant to permanent deformation or failure under load. Ultimately, this amounts to the generation of micelle cores that are sufficiently glassy or rubbery to resist chain pullout under an applied force. Highly entangled, glassy cores can be challenging to produce under solution-based assembly conditions, due to plasticization by residually trapped solvents or co-solvents required to temporarily compatibilize the hydrophobic blocks. Post-assembly chain extension²⁵ and crosslinking²⁶ within the core has been used to enhance elasticity in solution-assembled micelle systems, but does require initiation chemistry compatible with the solvating media (typically water), and chain mobility (in the core) consistent with the specific cross-linking mechanism employed.

Recently, our group has developed a new strategy for hydrogel formation using BCPs and tethered micelle networks that is based on pre-structuring the gel network in the absence of solvent.²⁷ The strategy employs blends of sphere-forming AB diblock and ABA triblock copolymers that are melt-processed and subsequently vitrified to preserve their nano- and macroscale structure after cooling. Self-assembly into densely packed spherical aggregates while in the melt-state produces a highly regular lattice of spherical junction points, similar to that shown in Figure 4–1. In aqueous media, the majority component B is selectively solvated, while the minority sphere component A is hydrophobic and remains solid under the solvating conditions. The added ABA triblock, which can be as little as 3 mol percent,²⁷ serves to physically cross-link the spheres in an extended periodic network. Ultimately, the equilibrium swelling di-

mensions are determined by a balance among solvent induced osmotic swelling forces, entropic resistance provided by the tethering midblocks, and topologically constrained entanglements among the tether population. This strategy allows precise control over nanoscale structuring prior to swelling, taking advantage of the near equilibrium conditions produced by annealing in the melt state. In contrast, network morphologies and tethering configurations produced by solution-based assembly are often kinetically determined, and are therefore susceptible to variations in processing conditions, such as co-solvent removal rates, for example. Pre-structuring in the melt state also avoids the inherent concentration dependence of solution-based network formation, and eliminates potential trapping of organic co-solvents during the gelation process. The original systems studied by our group were comprised of poly(styrene)-*b*-poly(ethylene oxide) (PS-PEO) diblock and poly(styrene)-*b*-poly(ethylene oxide)-*b*-poly(styrene) (PS-PEO-PS) triblock copolymers. These model PS-PEO hydrogels validated the ability of our melt blending strategy to provide tunable mechanical properties (through adjustment of triblock copolymer ratio), adjustable pore sizes (length of bridging block), long-term preservation of macroscopic shape, and high-density incorporation of free hydroxyl groups within the hydrogel interior.

Only a few examples exist of using melt-state self-assembly of BCPs to pre-structured hydrogel systems.²⁷⁻²⁹ Interestingly, in each of these, including our own previous work,²⁷ vitrified PS was utilized to physically cross-link the system. While the use of vitrification as a physical cross-linking mechanism presents many advantages (simplicity, re-processability, etc.), reliance on vitrification has significant limitations as well. Glass transition temperatures are extremely sensitive to both domain size and molecular weights below the entanglement limit, which places a lower molecular weight bound on the minority, core forming, blocks. For example, in our previous studies, we found the use of 8 kDa PS²⁷ with a bulk glass transition of approximately 80 °C, still resulted in hydrogel softening in the 60 °C range. Thus the use of vitrified core blocks to physically crosslink the system can limit the usage temperatures for the hydrogel formed. Given the significant asymmetry in the block volume fractions required to form sphere-based systems

in the melt, such a lower bound on core block molecular weight translates into hydrogel systems with on overall block copolymer molecular weights that are very large, that is, on the order of 70 kDa and higher. This in turn, constrains the hydrogel swelling ratios to large equilibrium values, limiting access to materials with smaller degrees of swelling, often desirable for particular biomedical and drug encapsulation technologies.

Commonly used vitreous core polymers such as PS and polylactide also offer little to no resistance to non-aqueous solvents, limiting the compositional flexibility of swelling media that can be employed. This is particularly problematic when post-swelling functionalization chemistries are considered (for example, the addition of small organic moieties, peptide sequences, growth factors, etc.), as the solvent conditions (even aqueous) that can be readily employed without plasticizing the vitrified domains can be highly restrictive. Considering one of the very promising advantages of incorporating AB diblock copolymer into these tethered micelle networks is the natural presentation of readily functionalizable, free chain ends within the hydrogel interior and surface, the exclusive use of vitrified core strategies in tethered micelle-based hydrogels is extremely limiting.

These disadvantages can be overcome through the use of non-vitreous, lower molecular weight BCP systems, in which the core domains can be chemically cross-linked into fixed, rubbery domains. The cross-linking of the core domains removes the lower molecular weight bound on the minority component of the block copolymer, giving access to the full range of possible swelling ratios in these materials, and produces network structures that are resilient in both aqueous and non-aqueous solvent systems. Significant challenges must be met, however, with respect to the cross-linking chemistry adopted. Introduction of any cross-linking agents or functionality to the system must be delicate enough to not disturb the self-assembled structure. The curing chemistry itself must also be able to withstand thermal annealing of the BCP system to moderately high temperature (up to ~ 200 °C, commonly necessary to generate highly ordered structures). Finally, the curing event must be rapid enough to translate the melt-state morphology to the cured form without disturbing the delicate balance of forces defining the

domain geometry established through self-assembly.

Our group has recently demonstrated the use of thermally stable photocuring chemistry that allows BCPs to be thermally processed for extended periods prior to cure, while simultaneously providing high fidelity translation of the melt-state morphology into the post-cure solid.³⁰ We have shown successful selective trapping of multiple morphological states from a single BCP that exhibits thermally dependent order-to-order transitions (OOT). Partially epoxidized polyisoprene-*b*-poly(ethylene oxide) (PI-PEO) BCPs were blended with a thermally stable UV cationic photoinitiator^{31,32} (1 mol % (4-iodophenyl)diphenylsulfonium triflate, IPDPST) and photocured in the melt via UV irradiation as either hexagonally packed cylinders or bicontinuous gyroid. Importantly, the thermal stability of the cationic photoinitiator provides ample melt-state processing time, without any thermally induced, premature initiation of cure. Classic methods for cross-linking BCPs such as thermal free-radical initiated mechanisms or coupling

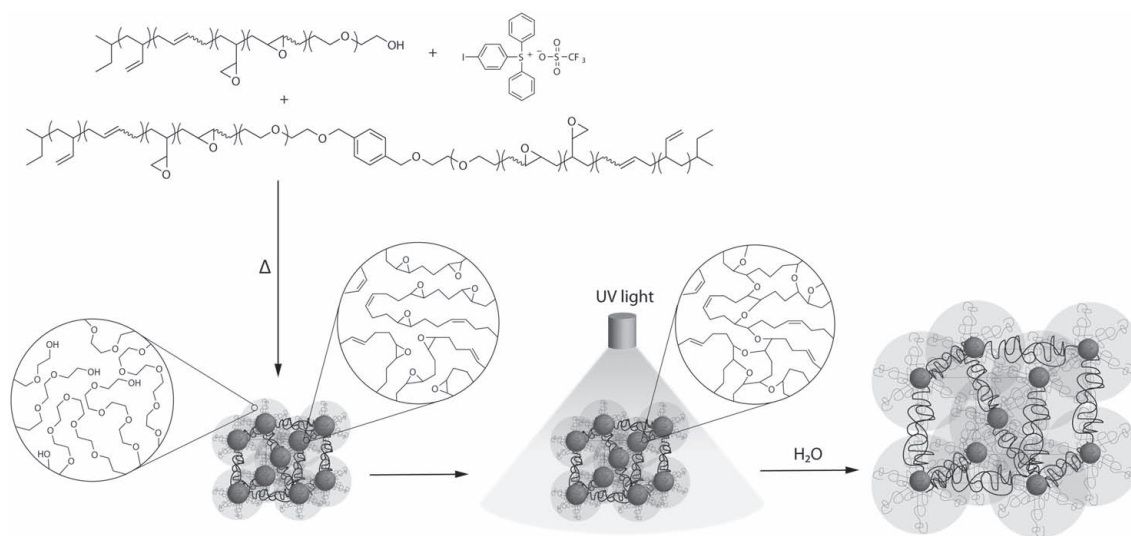


Figure 4–1. Pre-structured hydrogel formation based on spherical forming AB diblock and ABA triblock copolymer melts. Majority component, poly(ethylene oxide), surrounds partially epoxidized polybutadiene spheres, and also serves to tether (highlighted in bold) the spherical domains. After melt processing, UV initiated cross-linking of the epoxide groups with IPDPST cationic photoinitiator solidifies the spheres resulting in direct trapping of the melt phase morphology. Upon addition of selective solvent for the majority component, an equilibrium swollen elastic network is created, while preserving the pre-formed structure and shape. The osmotic swelling forces of the selected solvent and the entropic restoring force in the tethering midblock determine the equilibrium swelling dimensions. Magnification circles portray simplified views of the copolymers utilized in this report.

reactions are extremely system dependent and most often do not allow for extended pre-cure processing.³³ These newly developed polydiene-based BCP systems are low molecular weight, highly ordered (pre- and post-cure), and chemically cross-linkable. Thus, these systems are ideal candidates for non-vitrified forms of our pre-structured hydrogels.

In this report, we demonstrate the versatility of combining this thermally stable photocuring chemistry³⁰ with AB diblock and ABA triblock copolymer blend-based hydrogels²⁷ to produce highly elastic, nanostructured, solvent tolerant, and potentially photopatternable hydrogels systems. The hydrogels described herein are comprised of partially epoxidized polybutadiene-*b*-poly(ethylene oxide) (ePB-PEO) BCPs amenable to curing through cationic ring-opening polymerization of the epoxide functionality. The general approach, depicted in Figure 4-1, requires melt processing blends of ePB-PEO diblock, ePB-PEO-ePB triblock (11.5 mol %), and small amounts of photoinitiator (0.5 mol % IPDPST relative to diene repeat units) into small disks, which are then annealed above the PEO melt transition (65 °C) to facilitate assembly of the targeted body-centered cubic sphere morphology (S_{BCC}). The ordered structure is then exposed to UV light while being held at 100 °C, triggering the curing event and translating the S_{BCC} melt morphology to the cured solid. After curing, pressed discs swell isotropically in solution, with complete preservation of the pre-swollen shape. Analysis of rheological properties, and the demonstration of simple, large-scale photopatterning conclude this report.

4.3 RESULTS AND DISCUSSION

4.3.1 Synthesis

A parent PB-PEO diblock copolymer ($M_n = 29\,500\text{ g mol}^{-1}$, polydispersity index (PDI) = 1.03) was synthesized according to a previously reported procedure^{30,34} using two-step anionic polymerization of butadiene and ethylene oxide monomer. The targeted volume fraction ($f_{\text{PB}} = 0.13$) of PB was confirmed with ¹H NMR spectroscopy. PB-PEO-PB triblock copolymer was synthesized by titrating the alcohol end-groups on PB-PEO with potassium naphthalenide to form active alkoxides and then slowly adding the coupling agent³⁵ α,α -Dibromo-*p*-xylene (1 eq.

PB-PEO: 0.5 eq. α,α -Dibromo-*p*-xylene). The resulting copolymer mixture was determined to be 89.6 mass % triblock copolymer by size exclusion chromatography peak integrations, which is consistent with typical coupling yields using this agent in other polymer systems.³⁵ Mixed triblock copolymer product was then codissolved with pure PB-PEO diblock copolymer such that the overall triblock copolymer content of the blend (PB-PEO-11.5) was 11.5 mol %. This value was selected based on experience with our PS-based hydrogels, as a composition that would produce materials with reasonably high swelling ratios and excellent handling characteristics.²⁷ Notably, at these blend compositions the hydrogels ultimately produced (vide infra) contain a high concentration of hydroxyl-functional free chain ends, providing a convenient route towards future hydrogel modification. While the latter is not the subject of this report, the efficient introduction of cross-linking chemistry described directly enables such modifications

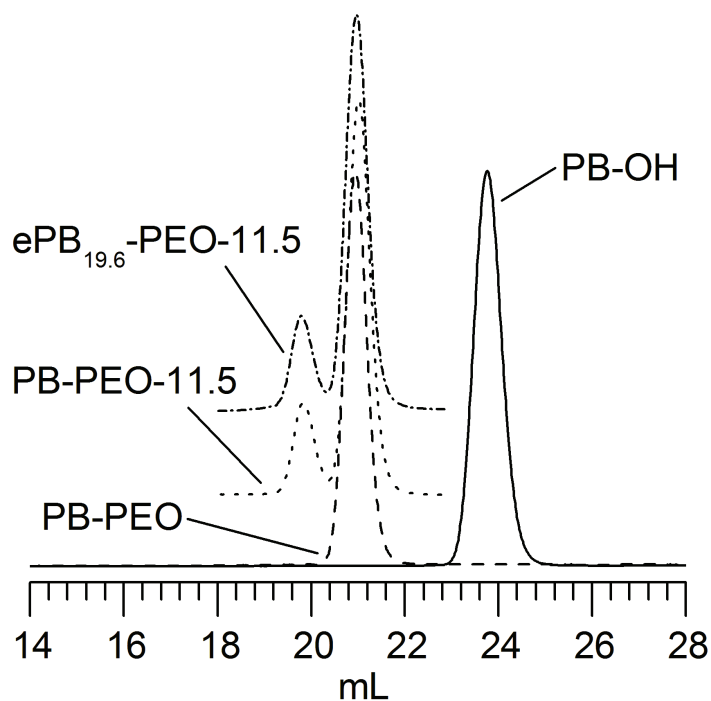


Figure 4-2. Size exclusion chromatography (SEC) of PB-OH, PB-PEO, PB-PEO-11.5, and ePB_{19.6}-PEO-11.5. SEC confirms the absence of PB homopolymer in the PB-PEO diblock. Partial epoxidation is selective without any indication of chain degradation. Near identical molecular weight distributions were observed. The data for ePB_{19.6}-PEO-11.5 and PB-PEO-11.5 have been shifted vertically for clarity.

to be performed in organic environments, if necessary (the demonstration of such modification is the subject of future reports). The olefin repeat units in the PB-PEO-11.5 samples were partially epoxidized (ePB_{19.6}-PEO-11.5, 19.6 % of butadiene repeat units epoxidized, calcd. from ¹H NMR integrations) with 3-chloroperoxybenzoic acid (MCPBA), a mild epoxidizing agent. No chain degradation from the MCPBA oxidation was observed as the pre- and post-epoxidized products showed identical molecular weight distributions (Figure 4-2).

4.3.2 Melt State Phase Behavior

The parent PB-PEO ($f_{\text{PB}} = 0.13$) BCP was targeted for its anticipated S_{BCC} morphology,^{20,21} which was subsequently confirmed through complementary analysis with small-angle X-ray scattering (SAXS) and dynamic rheology. Melt samples exhibited numerous higher order SAXS diffraction peaks consistent with the S_{BCC} assignment (Figure 4-3), while dynamic temperature ramp tests exhibited the classic plateau behavior in both the elastic and loss modulus prototypical of cubic (S_{BCC}) BCP phases (Figure 4-4).³⁶ The addition of 11.5 mol % triblock, PB-PEO-11.5, had minimal effect on the high degree of order exhibited by the PB-PEO diblock copolymer system; only quantitative changes in the phase behavior were observed with no qualitative differences in the morphology (Figures 4-5 and 4-S1 in Appendix II show complete SAXS thermal cycle data). Comparing the (110) interplanar spacing determined from the primary scattering wave vector of PB-PEO and PB-PEO-11.5 at 100 °C reveals a slight increase in magnitude from 22.4 to 23.1 nm. The increase in domain spacing with addition of triblock is consistent with previous work from Mai et al.³⁷ (experimental) and Matsen et al.³⁸ (mean-field calculations), who found small increases in domain spacing in ordered triblock copolymer melts when compared with compositionally equivalent diblock copolymers of half the molecular weight. The phenomenon is attributed to an increase in the elastic properties of the bridging block domains (PEO, here) afforded by the triblock copolymer, although a direct explanation of why this is so remains unanswered, currently.³⁸ Interestingly, Matsen's previous work predicts that the fraction of triblock copolymers that bridge separate spherical domains (in contrast to

looping into the same domain) in pure S_{BCC} forming ABA systems falls impressively in the 75 to 80% range, although no discussion of the underlying driving force for such high bridging fractions is presented.³⁸ This is by far the highest value for all the classic morphologies, with lamellar phases being closer to half of that value ($\sim 40\%$). Notably, bridging fractions in blends of ABA triblock and AB diblock copolymer systems, such as those used in this report, have not

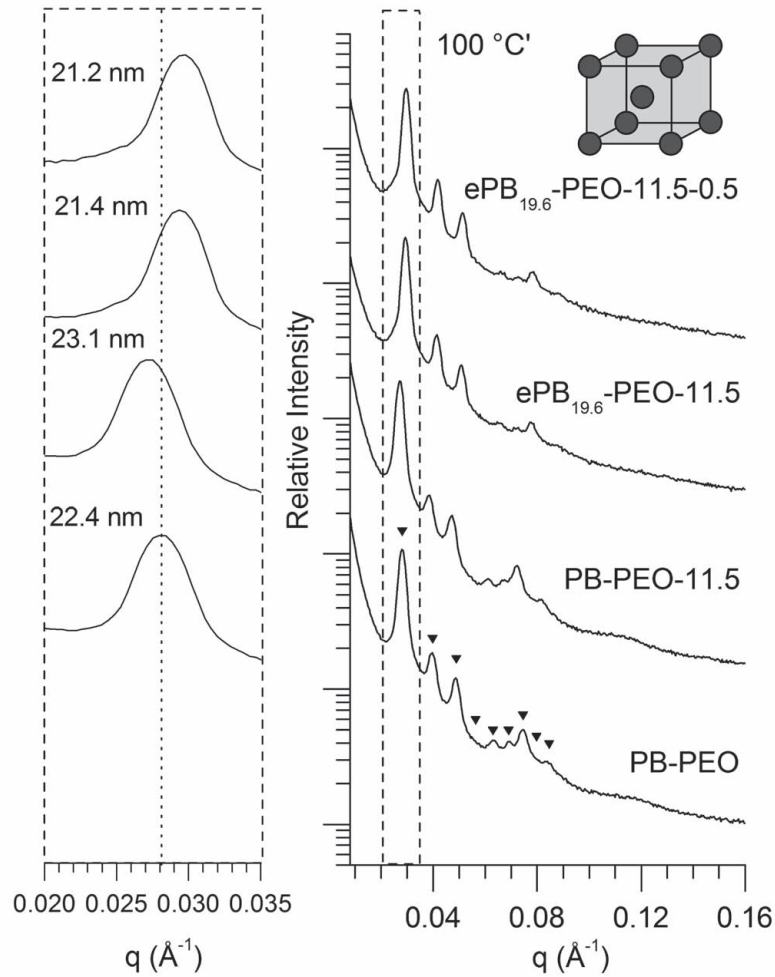


Figure 4-3. Dependence of d-spacing (d_{110}) on the addition of triblock (PB-PEO-11.5), partial epoxidation ($e\text{PB}_{19.6}\text{-PEO-11.5}$), and incorporation of 0.5 mol % IPDPST cationic photoinitiator ($e\text{PB}_{19.6}\text{-PEO-11.5-0.5}$) to the parent PB-PEO, all at 100 °C (from cooling). Addition of triblock copolymer increases the plane spacing, while subsequent epoxidation decreases the plane spacing. Incorporation of IPDPST has a negligible effect. All copolymer samples exhibit a highly ordered body centered cubic spherical S_{BCC} morphology. Inverted triangles represent the location of the allowed reflections for S_{BCC} morphology, based on the position of the primary scattering wave vector $q^*=q_{100}$ (absent for S_{BCC}): q/q^* at $\sqrt{2}$, $\sqrt{4}$, $\sqrt{6}$, $\sqrt{8}$, $\sqrt{10}$, $\sqrt{12}$, $\sqrt{14}$, $\sqrt{16}$, $\sqrt{18}$, etc.

yet been investigated, experimentally or theoretically, to the best of our knowledge. However, simple comparisons of the unperturbed root mean square (RMS) end-to-end distance for a PEO chain in the melt, and that which is necessarily imposed on a bridging (or looping) PEO chain through the intersphere distances in the S_{BCC} morphology, reveals the inherent compatibility of bridging (vs. looping) and justifies the result of the more elaborate mean field calculations. For example, at 140 °C, an unperturbed PEO chain equivalent in molecular weight to that used in the PB-PEO-PB triblock copolymer blended here (52 400 g mol⁻¹), would have a RMS end-to-end distance of 20.5 nm.³⁹ A spherical domain in the S_{BCC} structure has two unique sets of nearest-neighbors, both of which are proximal enough to accommodate the other end of a bridging molecule. Analysis of the SAXS data for PB-PEO-11.5 at 140 °C reveals an S_{BCC} structure in which spheres of 15 nm diameters are set on a cubic unit cell of lattice constant $a = 30$ nm. This produces geometries in which the eight nearest-neighbor spherical domains provide a range of surface-to-surface distances covering 11 to 41 nm, while the additional six second-nearest neighbors provide a range of surface-to-surface distances from 15 to 45 nm. In combination the surrounding spherical domains offer tethering chains a broad range of possible end-to-end distances spanning the preferred RMS value for PEO. Note that looping offers a chain end-to-end distances from 0 to 15 nm (the full diameter if insertion occurs on the exact opposite side of the sphere), although the average value sits at around 10.6 nm, much smaller (nearly half) than the preferred RMS end-to-end value for PEO. Notably, the spheres themselves occupy non-accessible (excluded) volume and further constrain the conformational freedom of the tethered triblock copolymers, but this simple analysis appears to support the high degrees of bridging predicted by SCFT calculations) and apparent in our system. In our system, each sphere contains approximately 260 ePB chains, and therefore 11.5 mol % triblock would yield ~30 triblock chains per spheres capable of producing active tethers between neighboring spheres. That is, we find only 11.5% triblock copolymer is easily sufficient to achieve full network connectivity in our cured samples.

Both PB-PEO and PB-PEO-11.5 do not exhibit an experimentally accessible (< 300 °C)

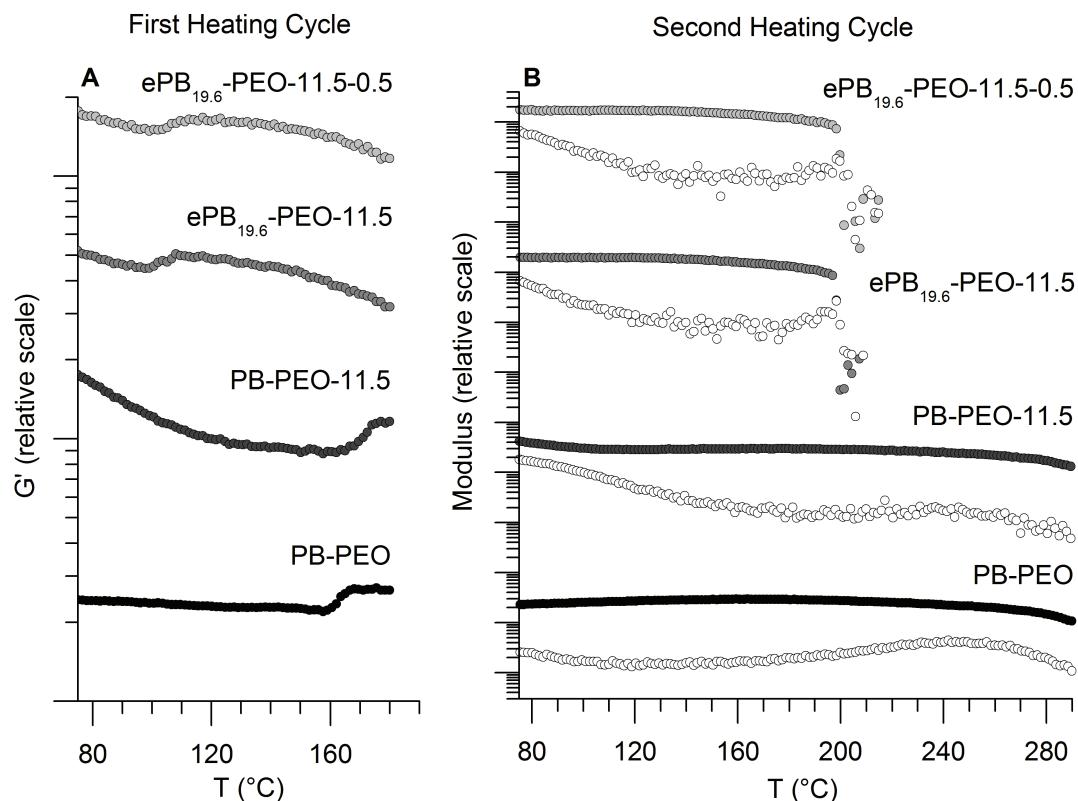


Figure 4-4. Dynamic temperature ramps of PB-PEO, PB-PEO-11.5, ePB_{19.6}-PEO-11.5, and ePB_{19.6}-PEO-11.5-0.5 at 1 °C min⁻¹ (1 rad s⁻¹ and 1% strain). (A) All samples exhibit an initial melt ordered phase consisting of a mixture of the original distorted lamellar-like morphology (PEO crystallization induced) and spherical domains before ordering into pure S_{BCC}. Epoxidation has the greatest effect on the temperature at which this phase transition occurs. (B) Second heating cycles (without allowing PEO to crystallize) do not exhibit the distorted L_C phase; only the S_{BCC} morphology is observed for all copolymer samples. Epoxidation drastically lowers the ODT; in contrast, the incorporation of 0.5 mol % IPDPST photoacid (ePB_{19.6}-PEO-11.5-0.5) increases the ODT a few degrees.

order-disorder transitions (ODTs) as shown in Figure 4-4B. Partial epoxidation (19.6%) of the PB-PEO-11.5 also produces only quantitative changes in the morphology (Figure 4-S2, complete thermal cycle SAXS data, Appendix II), with the highly ordered S_{BCC} phase preserved despite modification of the PB backbone. A drastic lowering of the ODT is observed with epoxidation, decreasing from greater than 300 °C in PB-PEO-11.5 to 201 °C in ePB_{19.6}-PEO-11.5 (Figure 4-4B). Comparable behavior was observed in more symmetric PI-PEO BCPs ($f_{PI} = 0.61$) previously studied by our group, where partial epoxidation lowered transition temperatures from both the cylindrical to gyroid phase (order-order transition) and the gyroid phase

to the final disordered state (ODT).³⁰ At the highest level of epoxidation studied in the PI-PEO system (16.8 mol %), both the OOT and ODT were lowered on the order of 50 °C. Here, epoxidation of spherical forming PB-PEO-11.5 to 19.6% appears to have a much greater influence on the position of the ODT (~100 °C +), perhaps a consequence of the greater compositional asymmetry in combination with the chemical differences between PB and PI. In both PI-PEO and PB-PEO systems, clearly the addition of oxygen into the polydiene domain serves to reduce the Flory-like interaction parameter, χ , without disrupting the qualitative morphological behavior. Epoxidation of the system also reduces the (110) interplanar spacing from 23.1 nm in PB-PEO-11.5 to 21.4 nm in ePB_{19.6}-PEO-11.5 (Figure 4-3). This could be a result of changes in either density or conformational asymmetry of the PB chain upon partial epoxidation, which can directly influence chain aggregation numbers associated with each spherical domain. The addition of 0.5 mol % IPDPST photoacid (ePB_{19.6}-PEO-11.5-0.5), in contrast to epoxidation, increases the ODT slightly from 201 °C to 204 °C. This increase is marginal, but is consistent with our previous results, in which the addition of the IPDPST photoacid to epoxidized PI-PEO also resulted in slight increases in OOTs.³⁰ Again, no qualitative changes were observed in the dynamic rheology or SAXS (Figures 4-3 and 4-4) upon addition of the photoacid. The (110) interplanar spacing of ePB_{19.6}-PEO-11.5 and ePB_{19.6}-PEO-11.5-0.5 were nearly identical at 21.4 nm and 21.2 nm, respectively.

SAXS data collected for the original diblock copolymer, PB-PEO, and the final cure-ready blend, ePB_{19.6}-PEO-11.5-0.5, at multiple temperatures between 25 °C and 180 °C are depicted in Figure 4-5. Below the melting point of PEO, the crystalline PEO domains force the structure into a distorted lamellar-like morphology (L_C)^{40,41} Upon heating PB-PEO and ePB_{19.6}-PEO-11.5-0.5, above the melt transition, the adoption of a true BCC lattice of spherical domains is far from immediate. Instead, the block copolymer samples appear to retain some memory of the original distorted lamellar-like morphology, with an eventual progression to what appears to be a “liquid-like packing” (LLP) of spherical domains.⁴²⁻⁴⁵ After heating past a subtle rheological transition ending at 170 °C for PB-PEO and 110 °C for ePB_{19.6}-PEO-11.5-0.5

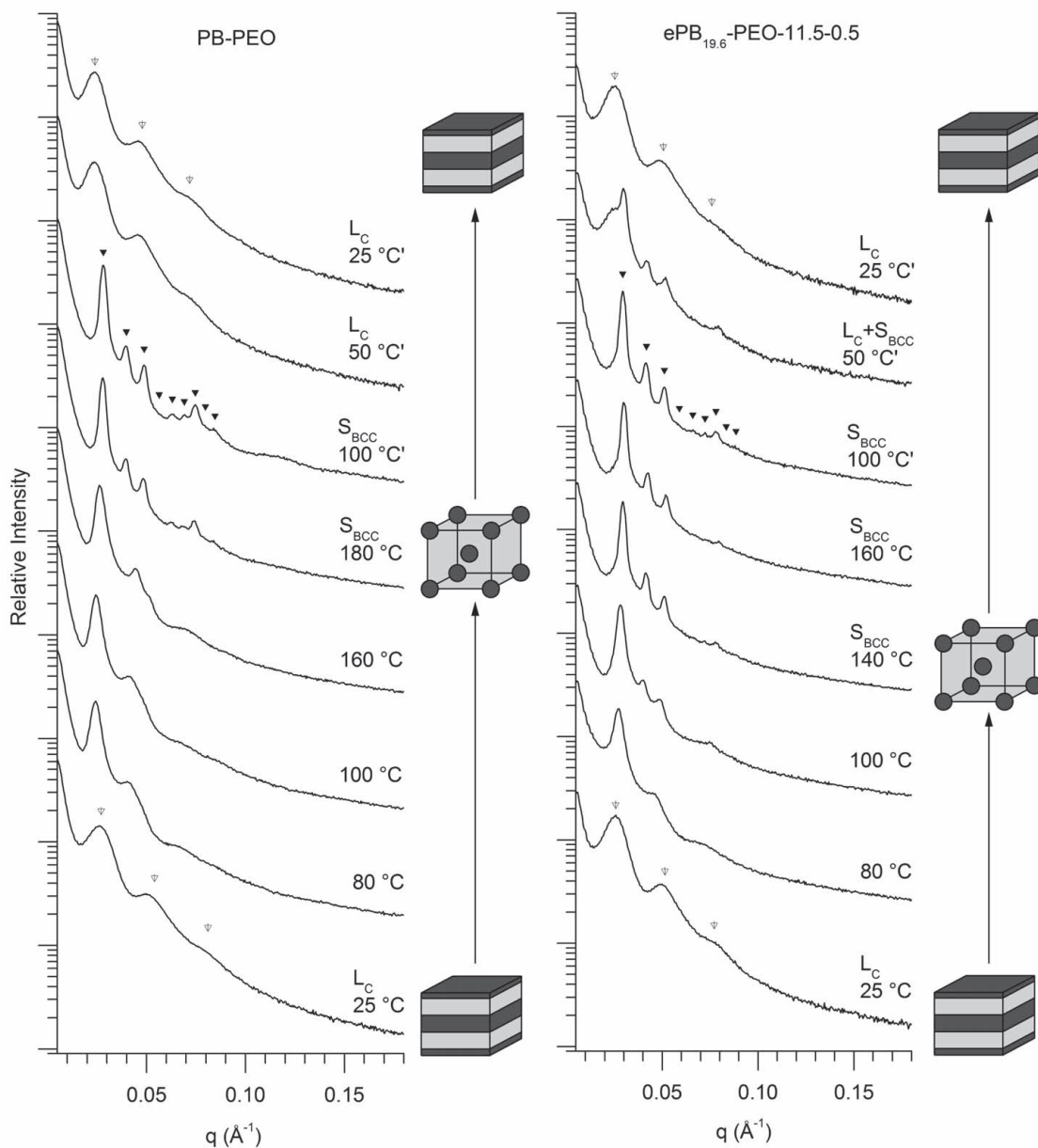


Figure 4-5. SAXS data of PB-PEO (left) and ePB_{19.6}-PEO-11.5-0.5 (right) along a complete heating and cooling (designated with primes) thermal cycle. Morphologies observed during heating include a distorted lamellae-like crystalline phase (L_C), an initial melt phase consisting of a transition between the original distorted lamellar-like morphology and a liquid-like packing of spherical domains, and finally a pure S_{BCC} phase. Upon cooling, a mixed ($L_C + S_{BCC}$) phase is present for ePB_{19.6}-PEO-11.5-0.5 before complete adoption of the L_C phase. Inverted triangles represent the location of the allowed reflections for the designated morphology, based on the position of the primary scattering wave vector $q^* = q_{100}$ (absent for S_{BCC}): (L_C) q/q^* at $\sqrt{1}, \sqrt{4}, \sqrt{9}$, etc.; (S_{BCC}) q/q^* at $\sqrt{2}, \sqrt{4}, \sqrt{6}, \sqrt{8}, \sqrt{10}, \sqrt{12}, \sqrt{14}, \sqrt{16}, \sqrt{18}$, etc.

(see rheology Figure 4–4A), the copolymer becomes highly ordered with multiple higher order reflections consistent for S_{BCC} , with no indication of any mixed phase morphology. During cooling, the highly ordered S_{BCC} structure is retained until the PEO begins to crystallize ($T_m \sim 65$ °C). With the inception of crystallization of PEO, a mixed phase structure is produced in $e\text{PB}_{19.6}\text{-PEO-11.5-0.5}$ likely consisting of mixed crystalline lamellae and a distorted form of the original sphere-based structure. After complete cooling at room temperature, only the L_C phase is observed. The mixed behavior consisting of $L_C + S_{\text{BCC}}$ upon cooling can be largely attributed to the rapid PEO crystallization induced distortion of the lattice. Similar behavior for PI–PEO systems have also been reported.^{30,40} A region of mixed morphological behavior upon cooling was not observed for the parent PB–PEO. However, after complete cooling of all copolymer samples in this study, no evidence of a residual BCC lattice is observed, only the distorted lamellar-like morphology is present. The more subtle transition evident in the rheology near 170 °C for PB–PEO and 110 °C for $e\text{PB}_{19.6}\text{-PEO-11.5-0.5}$ during heating appears to be related to a transition to a pure S_{BCC} phase. The persistence of the underdeveloped intermediate structure is likely an artifact of slow ordering kinetics during the transition to the energetically preferred S_{BCC} phase, and not the product of a true thermodynamic OOT phase transition. This is supported by the eventual development of highly ordered S_{BCC} phases at temperatures below this transition after annealing of $e\text{PB}_{19.6}\text{-PEO-11.5-0.5}$ at 80 °C (30 °C below the observed mixed lamellae to pure S_{BCC} transition) under vacuum for several hours (Figure 4–S3, Appendix II). Importantly, this delay in obtaining the pure S_{BCC} morphology is not unique to only the PB–PEO and $e\text{PB}_{19.6}\text{-PEO-11.5-0.5}$ sample, but is observed in all copolymer samples synthesized in this work, including PB–PEO–11.5, and $e\text{PB}_{19.6}\text{-PEO-11.5}$ with S_{BCC} transitions at 174 and 107 °C, respectively (SAXS shown in Figure 4–S1 and 4–S2, rheology shown in Figure 4–4A). Notably, such slowly developing S_{BCC} copolymer structures have been previously reported in which there exist sufficient delays during the evolution of the liquid-like packed state and the onset of a fully developed S_{BCC} morphology.^{46,47}

Interestingly, there are therefore two distinct ways to melt process the $e\text{PB}_{19.6}\text{-PEO-11.5-}$

0.5 copolymers to obtain a highly ordered S_{BCC} structure prior to curing; either (1) rapidly heat samples above the S_{BCC} transition at 110 °C (Figure 4–4A), or anneal the system for several hours at a temperature below the observed transition. Importantly, without the excellent thermal stability of the IPDPST photoacid, neither of the aforementioned melt-processing techniques would be possible. The use of photoactivated cationic cross-linking overcomes the thermal instabilities and constraints of many classic cross-linking strategies, and provides tremendous flexibility in thermal processing time prior to initiation of cure.³³

4.3.3 Trapping of the S_{BCC} Morphology in $ePB_{19.6}$ -PEO-11.5-0.5

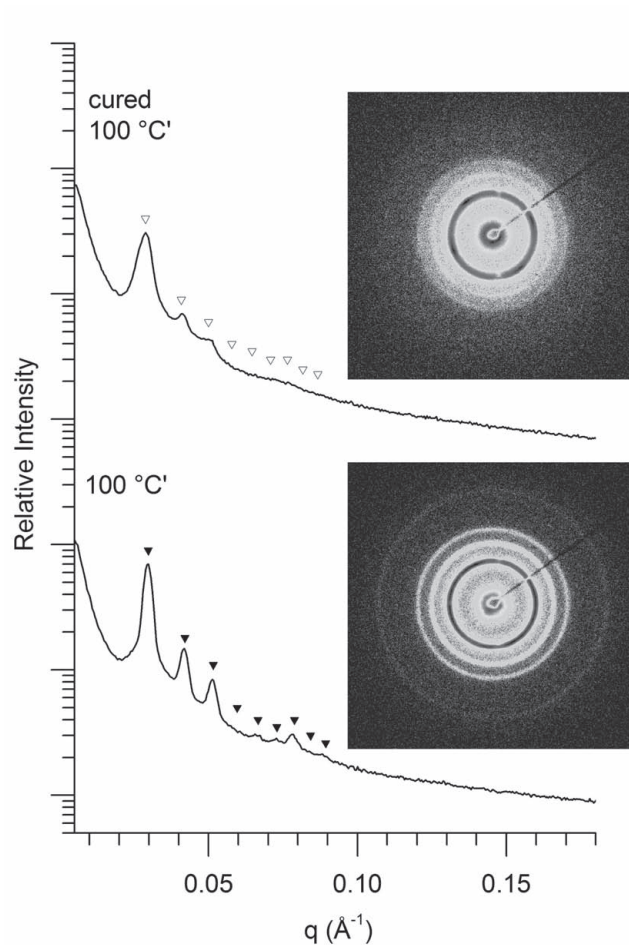


Figure 4–6. Comparison of SAXS data (collected at 100 °C from cooling) on pre- and post-cured $ePB_{19.6}$ -PEO-11.5-0.5. Following cure, the $ePB_{19.6}$ -PEO-11.5-0.5 solid retains the ordered spherical structure. Inverted triangles represent the location of the allowed reflections for S_{BCC} morphology. Inset pictures are the 2D scattering patterns.

The sufficient delay time in obtaining the pure S_{BCC} morphology has important implications on the melt processing of these materials. It is critical that the system exist as highly ordered S_{BCC} , and not as an undeveloped mixture of morphologies. Extended melt processing such as annealing for several hours is time consuming and has the undesirable consequence of inciting chain degradation if air-free precautions are not taken; it was therefore preferable to rapidly heat above the S_{BCC} transition and then cool the system to the curing temperature. This method afforded minimal processing time and the desired ordered S_{BCC} structure. To cure the S_{BCC} structure, ePB_{19.6}-PEO-11.5-0.5 samples were pressed as discs (8.18 mm x 0.33 mm) at 100 °C for 60 s, quenched, and then placed on Kapton film over a peltier heating element. The disc was then reheated to 140 °C, allowed to soak for 60 s, and then cooled to and held at 100 °C. Some flow deformation of the original disc occurs during this unconfined processing step, such that the disc diameter increases by about 10% (thickness also decreases accordingly). A quartz parallel plate (TA instruments) was aligned directly over the sample leaving a 0.5 mm gap between the sample and the plate surface. The samples were then exposed for 240 s with broad-spectrum UV light (mercury-xenon lamp, $\sim 100 \text{ mW cm}^{-2}$) using a light guide with a condenser lens aligned $\sim 1 \text{ cm}$ from a reflecting mirror within the quartz parallel plate. After cooling, the cured copolymer samples appeared light amber in color, rigid and insoluble in aqueous or organic solvents (vide infra). Characterization with SAXS confirmed the high fidelity translation of the S_{BCC} morphology to the cured solid (Figure 4–6), with multiple higher order reflections still present. Within the 110 and 200 diffraction rings, several higher intensity spots indicate the presence of large pseudo-single crystalline grains within the cured sample. Interestingly, the emergence of such spot patterns during cure has been commonplace, suggesting that cure induced coarsening of the grain structure may be occurring. However, such phenomena have not been explored in any level of detail.

Similar phase behavior is observed along the entire thermal cycle for both pre- and post-cure samples. For example, crystalline, post-cured samples also exhibit a similar distorted L_{C} -like morphology. This is consistent with an elastic distortion of the cured lattice induced by the PEO

crystallization event. After heating through the PEO melting transition, the ordered S_{BCC} morphology is again recovered, however, now without any extended annealing, as was required of the uncured samples. The post-cured samples exhibit a slightly larger (110) interplanar spacing of 21.8 nm, compared to 21.2 nm in pre-cured samples. Additionally, there is some broadening of the diffraction peaks that suggests a slight smearing of the lattice spacing distribution. This is likely the result of small degrees of temperature heterogeneity during curing, associated with thermal gradients produced from the peltier heating configuration, the irradiation profile as a function of sample depth, and the exothermic nature of the cationic cross-linking chemistry. However, the persistence of multiple higher order reflections confirms a highly ordered sample is maintained regardless. UV exposure times of 240–360 s (at $\sim 100 \text{ mW cm}^{-2}$) were found to provide mechanically rigid, insoluble solids, all with high translation fidelity (as verified with SAXS).

Attempts to quantify the percentage of the epoxide groups reacted through FT-IR and ^1H NMR experiments proved quantitatively inconclusive, due to significant interference from signals associated with the PEO blocks in the former (Figure 4–S4, Appendix II),^{48,49} and insolubility of the samples in the case of the latter. Confirmation of curing was conclusively established through a combination of swelling and rheological experiments. Cured samples retained their disc shape indefinitely when swollen in either water or chloroform, while uncured samples dissolved (or dispersed) within minutes (control experiment) under the same conditions. Because of the isolated nature of the cured core domains, rheological analysis of the melt-state samples, (sans solvent) pre- and post-cure, could also be performed. A comparison of dynamic temperature ramp behavior (Figure 4–7) demonstrates both an increased elastic modulus and the clear absence of a disorder transition following cure (thermal degradation is observed for cured samples around 270 °C). Although the majority matrix PEO contributes most of the melt-state rheological character in the sample, the anchoring ends of the tethering blocks become covalently fixed within the spherical domains and change the nature of the material compliance under small strain (1%) oscillatory shear. The inability to disorder is consistent with structural

permanence imposed by cured PB domains, which are no longer able to mix with PEO above the original pre-cure ODT around 200 °C. Notably, these results suggests the conversion of epoxide groups during cationic cross-linking at these cure times, while not currently quantifiable, is at least sufficient to permanently fix the ePB domains.

4.3.4 Swelling Behavior of Cured $ePB_{19,6}$ -PEO-11.5-0.5

After curing, a disc of $ePB_{19,6}$ -PEO-11.5-0.5 was placed in DI water. Swelling was obvious within several seconds, with equilibrium dimensions established within approximately 1 hr (determined by point at which there was consistent size and mass of the gel). The swelling was isotropic and preserved the original disc shape. The dry (cured) polymer disc had a volume of 17.3 mm³ which swelled to a final value of 182.2 mm³ upon reaching its equilibrium swollen dimensions. This volumetric swelling ratio of 10.5, together with the measured increase in hydrogel diameter (relative to the dry sample) of 2.19, are consistent with perfectly isotropic

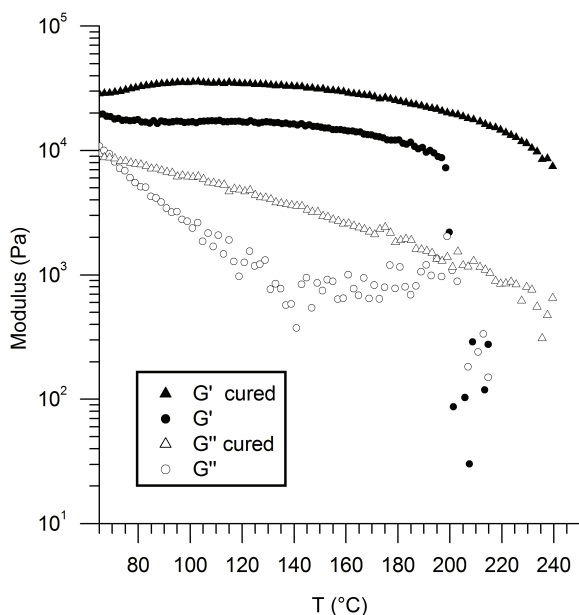


Figure 4-7. Dynamic temperature ramps of $ePB_{19,6}$ -PEO-11.5-0.5 pre- (circles) and post-cure (triangles) at 1 °C min⁻¹ (1 rad s⁻¹ and 1% strain). The cured sample exhibits a slightly higher modulus, with the absence of an order-to-disorder transition observed in the uncured sample.

swelling expected for the S_{BCC} lattice. Mechanical performance of the hydrogel was examined by probing the dynamic mechanical response of the gel at room temperature under oscillatory shear (Figure 4–8). The elastic (G') and loss (G'') moduli both exhibit near frequency independence over the range of 0.1–50 rad s^{-1} , with a five-fold difference in magnitude between the two moduli. This behavior is typical of elastic solids, and consistent with the behavior observed for our PS-based hydrogel systems previously reported.²⁷ As expected, the hydrogel modulus (Figure 4–8) is reduced relative to that found for the cured, but unswollen melt (Figure 4–7). Simple rubber elasticity theory predicts a modulus of the swollen hydrogel dependent on temperature (T), the polymer volume fraction (ϕ_2), and the number of effective strands (ν_e) per unit dry polymer volume (V_0), with the reduction in modulus due to solvent uptake entirely accounted for by the polymer volume fraction to the one-third power:

$$\text{Modulus} \propto T \phi_2^{1/3} \left(\frac{\nu_e}{V_0} \right) \quad \text{Equation 4-1}$$

However, the decrease in modulus measured is significantly greater (~90%) than that predicted (~45%) considering the solvent uptake alone, given a ϕ_2 value of 0.095. This result is actually consistent with our previous work in which found that the number of triblock copolymer molecules in the sample grossly underestimates the number of effective strands in the system. Effective strands involve any polymer segments contributing to the network, and simply counting triblock copolymer molecules fails to account for a large number of additional entanglements in the system. We have found these additional entanglements have a significant effect on the modulus of the swollen and unswollen networks. The source of these entanglements is largely two-fold; those produced when topologically constrained triblocks have adopted paths that force direct tether interaction upon swelling, and those produced through significant coronal layer overlap between the dangling (non-tethered) PEO chains coating the spherical domains. In our continued work on the PS-PEO system, we have found that these coronal layer entanglements can account for roughly 90% of the overall modulus, and are a critical component of the mechanical performance of tethered micelle networks. In the current system, the large decrease

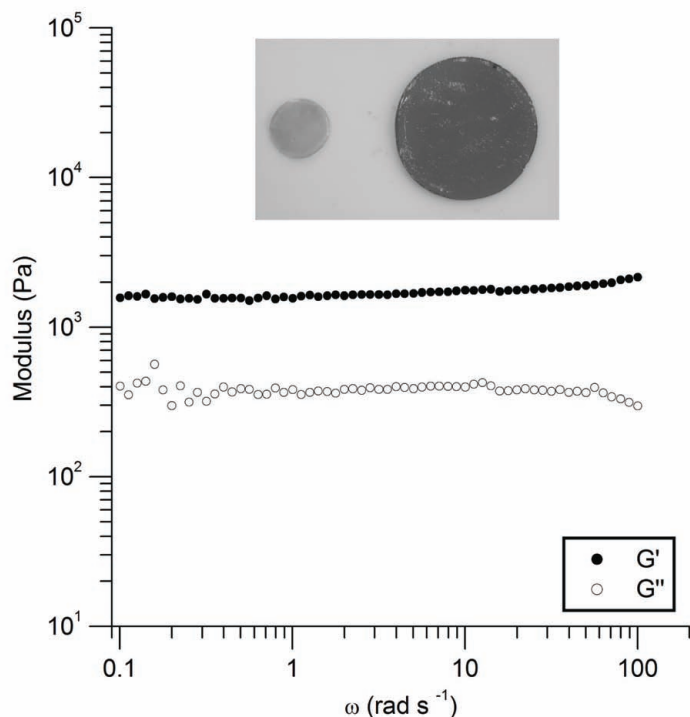


Figure 4–8. Dynamic frequency dependence of a swollen $ePB_{19.6}$ -PEO-11.5-0.5 hydrogel under oscillatory shear at room temperature. Inset photograph shows the relative size of pre-swollen and post swollen hydrogel. The hydrogel was dyed for photographic clarity.

in modulus upon swelling (relative to the unswollen melt) is thus likely the result of a concurrent decrease in the number of effective coronal layer entanglements upon introduction of solvent. At higher frequencies above 50 rad s^{-1} , there is a slight increase in the elastic modulus, and a slight decrease in the loss modulus. This increase in elastic character may be the result of topological entanglements (present between tethering midblocks) becoming more relevant at higher frequencies.

In an attempt to characterize the impact of swelling on the S_{BCC} lattice, the $ePB_{19.6}$ -PEO-11.5-0.5 hydrogel formed was swollen to equilibrium dimensions, sealed in an air-tight kapton cell, and analyzed via SAXS (Figure 4–9). In its swollen state, both transmittance and electron density contrast are severely reduced, and the signal to noise ratio is such that very long exposure times (12 hr) were required to produce the data plotted in Figure 4–9. Despite unfavorable scattering conditions, a primary scattering peak is quite discernible. Comparison

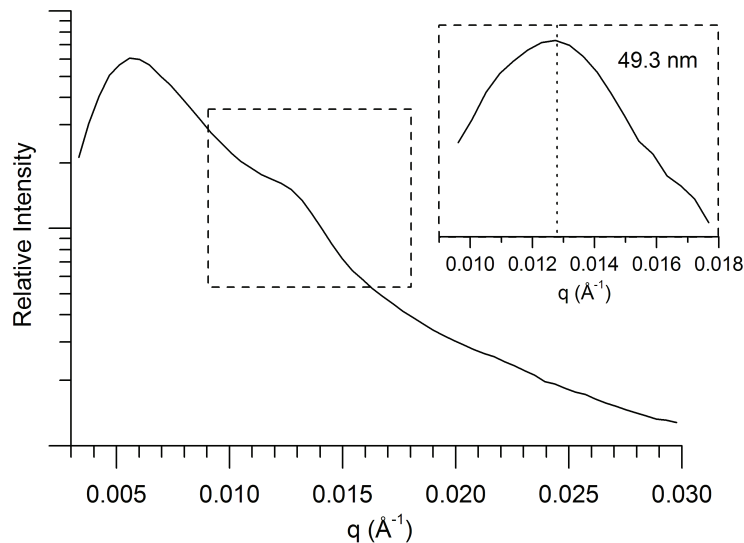


Figure 4–9. SAXS data for the $ePB_{19.6}$ -PEO-11.5-0.5 cured hydrogel, collected at room temperature over a 12 hr exposure. Inset contains the background subtracted primary peak, which has a peak maximum at 49.3 nm.

of the pre- and post-swollen lattice constants (21.8 nm and 49.3 nm, respectively) calculated from their respective primary scattering vectors, suggests a swelling ratio of 2.26, in excellent agreement with that predicted via direct measurement (2.19). The appearance of a primary scattering peak suggests, at the very minimum, that the hydrogel has short-range order in the equilibrium-swollen state, and more importantly, the inter-sphere distances are highly uniform over macroscopic distances within the sample. Whether the spherical domains within the hydrogel retain average positions that continue to lie on a BCC lattice cannot be discerned using such long exposure times and reduced lab source intensities; future investigations with synchrotron source SAXS and USAXS will be required.

4.3.5 Photopatterning of $ePB_{19.6}$ -PEO-11.5-0.5

An extremely interesting consequence of the use of photocuring chemistry to fix the hydrogel structure is the inherent capability to simultaneously photopattern the hydrogels three-dimensionally. To demonstrate the potential of ePB -PEO based block copolymers in photopatterning applications, an opaque star mask was applied on the surface of the quartz curing attachment.



Figure 4-10. Photopatterned $ePB_{19,6}$ -PEO-11.5-0.5 hydrogel. The original mask on the quartz curing attachment (left) has been transferred to the hydrogel after UV curing. Swelling in water dissolved the uncured, masked region, resulting in excellent translation of the star pattern. Notably, the size of the star increases with swelling. The hydrogel was dyed for photographic clarity.

A slightly larger disc (12.8 mm diameter x 0.4 mm thickness) of $ePB_{19,6}$ -PEO-11.5-0.5 was subjected to the same aforementioned thermal treatment (heat to 140 °C before cooling to 100 °C) and then exposed to broad spectrum UV light for 300 s. After cooling, the disc appeared amber with a white star in the middle. The polymer disc was allowed to swell in water, and the uncured star dissolved as the disc swelled (Figure 4-10). Notably, the swollen pattern is much larger than the star mask. However, the shape is preserved, with the only difference being an isotropic expansion of the star shape void (~2X its original size from star point to point). The ability to wash away masked patterns with aqueous or organic solvents not only provides convincing evidence of the curing efficacy, but serves as a promising launching point for more advanced photopatterning experiments with these materials. Current experiments establishing limits in patterning resolution and line width roughness are underway.

4.4 CONCLUSIONS

Pre-structuring hydrogels from the melt-state of self-assembled copolymers has now been extended to chemically cross-linked PB-PEO systems. Previously, this method was limited to physically cross-linked glassy polymers.²⁷⁻²⁹ In addition, thermally stable photocuring chemistry, with the use of a cationic photoinitiator, has now been shown to successfully cure BCC spheres

(this report), hexagonally packed cylinders³⁰, and bicontinuous gyroid³⁰ morphologies in BCP melt systems. The highly ordered sphere forming systems (S_{BCC}) cured in this report, comprised of partially epoxidized PB-PEO diblock and PB-PEO-PB triblock copolymers, provide a facile means of pre-structuring the hydrogel network morphology with precise, self-assembly based control. Cured discs swelled in water and chloroform, exhibited excellent mechanical properties in their swollen state, and preserved their macroscopic shape upon swelling. Lastly, the potential for simultaneous photopatterning during cure was demonstrated via the use of a simple mask, opening the possibility for more complex photopatterning applications.

4.5 EXPERIMENTAL

4.5.1 Materials and Methods

1,3 Butadiene (99+%, 100 ppm *p*-tert-butylcatechol inhibitor, Aldrich) was purified by static vacuum (15-30 mTorr) distillations from *n*-butyllithium (1.6 M in hexanes, Aldrich) at -20 °C. Ethylene oxide (99.5+%, compressed gas, Aldrich) was purified by successive distillations from di-*n*-butylmagnesium (1.0 M in heptane, Aldrich) at 3 °C. *sec*-butyllithium (1.3 M in cyclohexane/hexane, Fisher) was used as received. The concentration before use was determined to be 1.1 M using the double Gilman titration method⁵⁰ with 1,2-dibromoethane (99%, Aldrich). Potassium naphthalenide solution was prepared according to a previous report.³⁰ 3-chloroperoxybenzoic acid (MCPBA, 70-75%, Acros Organics) was dissolved in methylene chloride and dried over anhydrous sodium sulfate. (4-iodophenyl)diphenylsulfonium triflate (IPDPST) photoinitiator (Aldrich) and α,α -Dibromo-*p*-xylene (97%, Aldrich) were used as received. Tetrahydrofuran (THF) was degassed by sparging with argon (10 psi) for a period of 45 minutes and then purified over two molecular sieve columns of neutral alumina (Glass Contour, Inc.) Cyclohexane (CHX) was degassed with argon and purified through a column of neutral alumina followed by a column of Q5 copper (II) oxide catalyst (Glass Contour, Inc.). Other common chemicals and solvents were used as received unless otherwise stated. Ultra high purity argon (99.998% Airgas) was passed through a column of 5 Å molecular sieves with

drierite (Agilent) and an oxygen absorbing purifier column (Matheson Tri-gas). Glassware and polymerization reactors were flamed under vacuum and backfilled with argon (3 x).

4.5.2 Measurements

NMR spectra were recorded at room temperature on a Varian Inova 400 MHz spectrometer with a d1 pulse delay of 20 s to ensure complete relaxation of end-groups. Spectra were referenced to the residual protio solvent, CHCl_3 . Gel permeation chromatography (GPC) spectra were collected on a Viscotek GPC-Max chromatography system outfitted with three 7.5 x 340 mm Polypore™ (Polymer Laboratories) columns in series, a Viscotek differential refractive index (RI) detector, and an Alltech column oven (mobile phase THF, 40 °C, 1 mL min⁻¹). Rheological melt experiments were run on a TA Instruments Advanced Rheometric Expansion System (ARES) rheometer. Copolymer samples were pressed as solid discs (8 x 1 mm, samples for curing were 8.18 x 0.33 mm) at 100 °C with an applied pressure of 500 psi for 30 s. Discs were positioned between two parallel plates (8 mm diameter). The rheometer parallel plates were heated to 75 °C and the gap was reduced and adjusted to ensure even distribution of the sample. Typical gaps were 0.4–0.6 mm for uncured samples and ~0.3 mm for cured disks. Dynamic temperature ramp tests were performed while heating and cooling at 1 °C min⁻¹ at angular frequency of 1 rad s⁻¹ and a strain of 1 % (well within the linear viscoelastic regime, determined by dynamic strain sweep experiments for each copolymer). Rheological swollen hydrogel frequency sweep experiments were run at room temperature using a peltier lower tool apparatus and a 25 mm stainless steel upper parallel plate. A slight force was applied (5–10 g) to the hydrogel samples to prevent slip. Strain rates were adjusted depending on the linear viscoelastic regime (0.5–1%). Small Angle X-ray Scattering (SAXS) data were collected on a Rigaku S-Max 3000 High Brilliance three pinhole SAXS system outfitted with a MicroMax-007HFM rotating anode (CuK α), Confocal Max-Flux™ Optic, Gabriel multiwire area detector, and a Linkam thermal stage. Dry polymer samples were sandwiched between kapton windows (0.05 mm thick x 10 mm diameter). Exposure times for uncured samples were typically on the order

of 600–1200 s. Cured sample exposure times varied between 1800–3600 s. Equilibrium swollen hydrogels were sealed in a Kapton window cell. A shim washer was placed around the swollen hydrogel, and industrial Loctite® two-component epoxy glue was used to bond the kapton film together. After the epoxy glue was fully hardened, DOW Corning high vacuum grease was applied around the glue seal. Before collecting SAXS data, the Kapton window containing the hydrogel was checked for leaks under high vacuum. The exposure time for swollen hydrogel SAXS was 6–12 h.

4.5.3 ω -hydroxy-polybutadiene (PB)

Purified 1,3-butadiene monomer (45.3 g, 12 h) was added very slowly (*Caution: If butadiene monomer is added too quickly, the pressure will rise uncontrollably*) over a period of 3 h to a 2 L reactor flask containing 1 L of cyclohexane (40 °C) and sec-butyllithium (11.98 mL, 1.1 M) under a slight initial positive pressure of argon (1 psi). During the monomer addition, the pressure was allowed to rise to a maximum of 8 psi. Once the monomer polymerized and the pressure dropped below 3 psi, more butadiene monomer was added. Ethylene oxide (12.6 g, 20 h) was used as an end-capping agent. After purging the reactor of excess ethylene oxide, the terminal alkoxide was quenched with wet methanol (26 mL, 25:1 MeOH–H₂O). The homopolymer was washed (2X) with 250 mL deionized H₂O and precipitated from 3:1 MeOH–EtOH (8 L). The product was dissolved in benzene and freeze-dried in vacuo (25°C, 72 h). Recovered sticky clear viscous liquid, 42.0 g (93%). GPC (Polystyrene standards): $M_w/M_n = 1.05$. ¹H NMR (400 MHz, CDCl₃, δ): 5.3–5.7 (b, $-\text{CH}_2-\text{CH}=\text{CH}-\text{CH}_2-$ and $\text{CH}_2=\text{CH}-\text{C}(\text{R})\text{H}-$), 4.9–5.1 (b, $\text{CH}_2=\text{CH}-$), 3.6–3.7 (m, $-\text{CH}_2-\text{OH}$), 1.7–2.3 (b, $-\text{CH}_2-\text{CH}=\text{CH}-\text{CH}_2-$ and $\text{CH}_2=\text{CH}-\text{C}(\text{R})\text{H}-$), 1.1–1.7 (b, $\text{CH}_2=\text{CH}-\text{C}(\text{R})\text{H}-\text{CH}_2-$), 0.8–0.9 (m, $\text{CH}_3-\text{CH}_2-\text{C}(\text{R})\text{H}-\text{CH}_3$, initiator fragment). M_n (calcd. from ¹H NMR integrations) = 3300 g mol⁻¹. 1,2 content = 8.3 %.

4.5.4 ω -hydroxy-polybutadiene-*b*-poly(ethylene oxide) (PB-PEO)

PB (3.2 g) was dissolved in 250 mL THF and added via cannula to a 2 L reactor flask containing 800 mL THF at 40 °C. PB alkoxide chain ends were formed by titrating the solution with

potassium naphthalenide slowly until a light green color remained for at least 5 min. Ethylene oxide (26.4 g, 24 h) was added to the reactor under a slight positive pressure of argon (1 psi), the solution turned clear after several seconds. The reactor was quenched with wet methanol (20 mL, 3:1 MeOH-H₂O) and the solution changed color from charcoal blue to rose red immediately. The polymeric solution was reduced to ~1/2 its volume on a roto-evaporator. The block copolymer alcohol product precipitated from -20 °C pentane (4 L). Filtration and drying in vacuo (25°C, 24 h) gave the block copolymer as a light tan powder. Yield= 26.6 g (90 %). GPC (Polystyrene standards): $M_w/M_n = 1.03$ ¹H NMR (400 MHz, CDCl₃, δ): 5.2–5.6 (b, -CH₂-CH=CH-CH₂- and CH₂=CH-C(R)H-), 4.8–5.0 (b, CH₂=CH-), 3.3–3.9 (b, -CH₂-CH₂-O-), 1.6–2.3 (b, -CH₂-CH=CH-CH₂- and CH₂=CH-C(R)H-), 1.0–1.5 (b, CH₂=CH-C(R)H-CH₂-), 0.7–0.9 (m, CH₃-CH₂-C(R)H-CH₃, initiator fragment). $f_{PB} = 0.13$, $M_n = 29\,500\text{ g mol}^{-1}$ (calcd. from ¹H NMR integrations).

4.5.5 Polybutadiene-*b*-poly(ethylene oxide)-*b*-polybutadiene (PB-PEO-PB)

PB-PEO (4.3 g) was dissolved in 50 mL of THF and titrated to a light green color with potassium naphthalenide under argon. α,α-Dibromo-*p*-xylene was dissolved in THF (0.50 mL, 0.6 M, 1:0.5 eq PB-PEO: α,α-Dibromo-*p*-xylene), and was added at a rate of 0.1 mL h⁻¹ with a Chemyx Fusion 200 syringe pump to the titrated PB-PEO flask. The copolymer mixture precipitated from -20 °C pentane (1.5 L). Filtration and drying in vacuo (25°C, 48 h) gave the copolymer as a light yellow rubbery powder. Yield = 3.7 g (86 %). The copolymer mixture was 89.6 % triblock by mass (calcd. from GPC peak integrations).

4.5.6 Epoxidation of PB-PEO/PB-PEO-PB Blends (ePB_{19,6}-PEO-11.5)

PB-PEO-PB triblock mixture (0.5 g) and PB-PEO (1.96 g) were codissolved in 40 mL CH₂Cl₂. The copolymer mixture represents an 11.5 mol % triblock composition. Controlled partial epoxidation was carried out with MCPBA (0.231 g) described in a previous report by Scalfani and Bailey.³⁰ An additional purification step of precipitating from pentane (1 L) was added to the procedure. Filtration and drying in vacuo (25 °C, 48 h) gave the epoxidized copolymer as an

off-white powder. Yield = 2.15 g (87 %). GPC (Polystyrene standards): $M_w/M_n = 1.15$ (bimodal due to intentional blending with triblock). $^1\text{H NMR}$ (400 MHz, CDCl_3 , δ): 7.3 (s, $-\text{O}-\text{CH}_2-\text{C}_6\text{H}_4-\text{CH}_2-\text{O}-$, coupling agent) 5.2–5.6 (b, $-\text{CH}_2-\text{CH}=\text{CH}-\text{CH}_2-$ and $\text{CH}_2=\text{CH}-\text{C}(\text{R})\text{H}-$), 4.8–5.0 (b, $\text{CH}_2=\text{CH}-$), 4.5 (s, $-\text{O}-\text{CH}_2-\text{C}_6\text{H}_4-\text{CH}_2-\text{O}-$), 3.3–4.0 (b, $-\text{CH}_2-\text{CH}_2-\text{O}-$), 2.8–3.0 (b, $-\text{CH}_2-\text{CH}(\text{O})\text{CH}-\text{CH}_2-$, epoxidized 1,4 cis), 2.6–2.7 (b, $-\text{CH}_2-\text{CH}(\text{O})\text{CH}-\text{CH}_2-$, epoxidized 1,4 trans), 1.0–2.3 (b, $-\text{CH}_2-\text{CH}=\text{CH}-\text{CH}_2-$, $-\text{CH}_2-\text{CH}(\text{O})\text{CH}-\text{CH}_2-$, $\text{CH}_2=\text{CH}-\text{C}(\text{R})\text{H}-$, $\text{CH}_2=\text{CH}-\text{C}(\text{R})\text{H}-\text{CH}_2-$), 0.7–0.9 (m, $\text{CH}_3-\text{CH}_2-\text{C}(\text{R})\text{H}-\text{CH}_3$, initiator fragment). Epoxidized units: Total = 19.6%, 1,4 cis = 9.8% , 1,4 trans = 9.8%, 1,2 = 0 % (calcd. from $^1\text{H NMR}$ integrations).

4.5.7 Photocuring of $e\text{PB}_{19.6}-\text{PEO}-11.5-0.5$

$e\text{PB}_{19.6}-\text{PEO}-11.5$ samples were codissolved with 0.5 mol % (relative to initial PB repeat units) (4-iodophenyl)diphenylsulfonium triflate in a 3:1 benzene–chloroform mixture and freeze dried overnight. Samples were pressed as 8.18 mm X 0.33 mm discs at 100 °C for 60 s, then quenched in liquid nitrogen to minimize crystallization induced roughening of the surface. Discs were placed on a TA Instruments ARES rheometer outfitted with a peltier and a reflecting mirror on a quartz parallel plate (kapton film was used in-between the sample and peltier attachment to prevent sticking). The quartz attachment was aligned to be 0.5 mm from the surface of the sample. A Hamamatsu Lightning Cure LC8 UV spot cure system was utilized with a 200-Watt mercury-xenon lamp, synthetic silica light guide and short focal point condenser lens. The light guide was positioned approximately 1 cm from the upper quartz reflecting mirror. The lamp was allowed to stabilize for 15 min before curing. The intensity at the cure site was 95–103 mW cm^{-2} (measured in the range of 230–410 nm with a Con-Trol-Cure Silver Line UV-Radiometer). Prior to cure, the samples were heated to 140 °C on the peltier and then cooled to the curing temperature of 100 °C. Samples were exposed to UV light for 4–5 min. After curing, the discs became mechanically rigid, insoluble and light amber in color.

4.6 ACKNOWLEDGEMENTS

This work was supported by the National Science Foundation (Grant DMR-0645781) and the Colorado State University. The SAXS instrument at CSU is supported by the Central Instrument Facility of the Chemistry Department and the National Science Foundation MRI Program (Grant DMR-0821799).

4.7 SUPPORTING INFORMATION AVAILABLE

Temperature dependent SAXS of PB-PEO-11.5, and ePB_{19.6}-PEO-11.5 (Figures 4-S1 and 4-S2); Evolution of S_{BCC} morphology after low temperature 80 °C annealing (Figure 4-S3); FT-IR comparison of PB-PEO-11.5 and ePB_{19.6}-PEO-11.5 (Figure 4-S4) in Appendix II.

4.8 REFERENCES

1. Hoare, T. R.; Kohane, D. S. *Polymer* **2008**, *49* (8), 1993-2007.
2. Slaughter, B. V.; Khurshid, S. S.; Fisher, O. Z.; Khademhosseini, A.; Peppas, N. A. *Adv. Mater.* **2009**, *21*, 3307-3329.
3. Tokarev, I.; Minko, S. *Adv. Mater.* **2010**, *22*, 3446-3462.
4. Wang, C.; Varshney, R. R.; Wang, D.-A. *Advanced Drug Delivery Reviews* **2010**, *62* (7-8), 699-710.
5. Zohuriaan-Mehr, M.; Omidian, H.; Doroudiani, S.; Kabiri, K. *J. Mater. Sci.* **2010**, *45* (21), 5711-5735.
6. Peppas, N. A.; Hilt, J. Z.; Khademhosseini, A.; Langer, R. *Adv. Mater.* **2006**, *18* (11), 1345-1360.
7. Desai, P. N.; Yuan, Q.; Yang, H. *Biomacromolecules* **2010**, *11* (3), 666-673.
8. Galperin, A.; Long, T. J.; Ratner, B. D. *Biomacromolecules* **2010**, *11* (10), 2583-2592.
9. Hou, Y.; Schoener, C. A.; Regan, K. R.; Munoz-Pinto, D.; Hahn, M. S.; Grunlan, M. A. *Biomacromolecules* **2010**, *11* (3), 648-656.
10. Lee, K. Y.; Mooney, D. J. *Chem. Rev.* **2001**, *101* (7), 1869-1880.
11. Stile, R. A.; Burghardt, W. R.; Healy, K. E. *Macromolecules* **1999**, *32* (22), 7370-7379.
12. Xu, Y.; Sato, K.; Mawatari, K.; Konno, T.; Jang, K.; Ishihara, K.; Kitamori, T. *Adv. Mater.* **2010**, *22* (28), 3017-3021.
13. Kozlovskaya, V.; Sukhishvili, S. A. *Macromolecules* **2006**, *39* (18), 6191-6199.
14. Dai, H.; Chen, Q.; Qin, H.; Guan, Y.; Shen, D.; Hua, Y.; Tang, Y.; Xu, J. *Macromolecules* **2006**, *39* (19), 6584-6589.
15. Gong, C.; Shi, S.; Wang, X.; Wang, Y.; Fu, S.; Dong, P.; Chen, L.; Zhao, X.; Wei, Y.; Qian, Z. *The Journal of Physical Chemistry B* **2009**, *113* (30), 10183-10188.
16. Annaka, M.; Matsuura, T.; Kasai, M.; Nakahira, T.; Hara, Y.; Okano, T. *Biomacromolecules* **2003**, *4* (2), 395-403.
17. Susanto, H.; Ulbricht, M. *Langmuir* **2007**, *23* (14), 7818-7830.
18. Tokuyama, H.; Iwama, T. *Langmuir* **2007**, *23* (26), 13104-13108.
19. Calvert, P. *Adv. Mater.* **2009**, *21* (7), 743-756.
20. Bates, F. S. *Science* **1991**, *251* (4996), 898-905.
21. Bates, F. S.; Fredrickson, G. H. *Phys. Today* **1999**, *52*, 32-38.
22. He, C. L.; Kim, S. W.; Lee, D. S. *J. Controlled Release* **2008**, *127* (3), 189-207.
23. Minh, K. N.; Lee, D. S. *Macromol. Biosci.* **2010**, *10* (6), 563-579.
24. Vermonden, T.; Besseling, N. A. M.; van Steenbergen, M. J.; Hennink, W. E. *Langmuir* **2006**, *22* (24), 10180-10184.
25. Sanabria-DeLong, N.; Crosby, A. J.; Tew, G. N. *Biomacromolecules* **2008**, *9* (10), 2784-2791.
26. Censi, R.; Vermonden, T.; Deschout, H.; Braeckmans, K.; di Martino, P.; De Smedt, S. C.; van Nostrum, C. F.; Hennink, W. E. *Biomacromolecules* **2010**, *11* (8), 2143-2151.
27. Guo, C.; Bailey, T. S. *Soft Matter* **2010**, *6* (19), 4807-4818.
28. Nykaenen, A.; Nuopponen, M.; Laukkanen, A.; Hirvonen, S.-P.; Rytelae, M.; Turunen, O.; Tenhu, H.; Mezzenga, R.; Ikkala, O.; Ruokolainen, J. *Macromolecules* **2007**, *40* (16), 5827-5834.
29. Xu, C.; Fu, X.; Fryd, M.; Xu, S.; Wayland, B. B.; Winey, K. I.; Composto, R. J. *Nano Lett.* **2006**, *6* (2), 282-287.
30. Scalfani, V. F.; Bailey, T. S. *Chem. Mater.* **2010**, *22* (21), 5992-6000.

31. Crivello, J. V. *Ann. Rev. Mater. Sci.* **1983**, *13*, 173-190.
32. Crivello, J. V. *J. Polym. Sci., Part A: Polym. Chem.* **1999**, *37*, 4241-4254.
33. For a detailed overview comparing classic BCP cross-linking strategies to cationic photo-initiators, see ref. 30.
34. Hillmyer, M. A.; Bates, F. S. *Macromolecules* **1996**, *29* (22), 6994-7002.
35. Hsieh, H. L.; Quirk, R. P., *Anionic Polymerization, Principles and Practical Applications*. Marcel Dekkar, Inc.: New York, 1996.
36. Kossuth, M. B.; Morse, D. C.; Bates, F. S. *J. Rheol.* **1999**, *43* (1), 167-196.
37. Mai, S.-M.; Mingvanish, W.; Turner, S. C.; Chaibundit, C.; Fairclough, J. P. A.; Heatley, F.; Matsen, M. W.; Ryan, A. J.; Booth, C. *Macromolecules* **2000**, *33* (14), 5124-5130.
38. Matsen, M. W.; Thompson, R. B. *J. Chem. Phys.* **1999**, *111* (15), 7139-7146.
39. Fetters, L. J.; Lohse, D. J.; Richter, D.; Witten, T. A.; Zirkel, A. *Macromolecules* **1994**, *27* (17), 4639-4647.
40. Floudas, G.; Vazaiou, B.; Schipper, F.; Ulrich, R.; Wiesner, U.; Iatrou, H.; Hadjichristidis, N. *Macromolecules* **2001**, *34* (9), 2947-2957.
41. Müller, A.; Balsamo, V.; Arnal, M., Nucleation and Crystallization in Diblock and Triblock Copolymers. In *Block Copolymers II*, Abetz, V., Ed. Springer Berlin / Heidelberg: 2005; Vol. 190, pp 1-63.
42. Cavicchi, K. A.; Lodge, T. P. *Macromolecules* **2003**, *36* (19), 7158-7164.
43. Kinning, D. J.; Thomas, E. L. *Macromolecules* **1984**, *17* (9), 1712-1718.
44. Schwab, M.; Stuhn, B. *Phys. Rev. Lett.* **1996**, *76* (6), 924.
45. Wang, X.; Dormidontova, E. E.; Lodge, T. P. *Macromolecules* **2002**, *35* (26), 9687-9697.
46. Yamaguchi, D.; Hashimoto, T.; Vaidya, N. Y.; Han, C. D. *Macromolecules* **1999**, *32* (22), 7696-7699.
47. Lee, S.-H.; Char, K.; Kim, G. *Macromolecules* **2000**, *33* (19), 7072-7083.
48. De Risi, F. R.; D'Ilario, L.; Martinelli, A. *J. Polym. Sci., Part A: Polym. Chem.* **2004**, *42* (12), 3082-3090.
49. Dissanayake, M. A. K. L.; Frech, R. *Macromolecules* **1995**, *28* (15), 5312-5319.
50. Gilman, H.; Cartledge, F. K. *J. Organomet. Chem.* **1964**, *2* (6), 447-454.

CHAPTER 5

TUNABLE MECHANICAL PERFORMANCE OF BLOCK COPOLYMER HYDROGEL NETWORKS VIA UV PHOTOCOUPLING OF ANTHRACENE END-GROUPS

The contents of this dissertation chapter were written by Vincent F. Scalfani. Vincent F. Scalfani and Travis S. Bailey developed and designed the experiments. John R. Ekblad, Brett D. Hill (undergraduate students at Colorado State University), and Ralf Niemann (graduate student at Universität Duisburg-Essen, Germany) performed the photocoupling and SEC experiments. Vincent F. Scalfani performed all other experiments including synthesis, rheology and SAXS data. Lastly, Chen Guo provided the rheology data for the pre-blended PS-PEO hydrogels.

5.1 CONSPECTUS

Nanostructured hydrogel networks were developed through UV photocoupling of anthracene functional AB diblock copolymer melts. The networks are based on a pre-structuring technique prior to swelling where a sphere forming light-reactive block copolymer (BCP) is first melt-processed, and then exposed to UV light directly in the melt-phase. The UV light activates the photo-cycloaddition of integrated anthracene end-groups which results in the formation of ABA tethers between adjacent spheres. The tethered network of AB diblock and ABA photocoupled triblock is comprised of hydrophobic junction points (A domains) connected through hydrophilic (B) domains which are selectively swollen in aqueous media. Specifically, the hydrogel tethered networks in this report were fabricated from anthracene terminated poly(styrene)-*b*-poly(ethylene oxide) diblock (PS-PEO-An, $f_{\text{PS}} = 0.13$, $M_n = 70\,100\text{ g mol}^{-1}$). Disks of PS-PEO-An (0.29 mm thickness) were melt pressed and then photocoupled directly in the melt for 2–20 min with 365 nm filtered UV light. AB/ABA photocoupled blends contained triblock concentrations of 11.7 to 45 mol %. Photocoupled disks were then swollen in water and found to exhibit highly elastic properties, tunable mechanical properties (based on UV irradiation time), and complete preservation of pre-photocoupled shape. The photocoupled hydrogel networks were compared to homogeneous pre-blended AB/ABA composites and found to exhibit similar properties with slight differences arising from an asymmetric distribution of triblock in the photocoupled gels. The PS-PEO-An hydrogels prepared herein are proposed to be excellent future candidates for asymmetric hydrogels because of their simple fabrication and excellent mechanical properties. The potential reversibility of the anthracene coupling reaction and its impact on hydrogel behavior concludes this report.

5.2 INTRODUCTION

Hydrogel networks¹⁻³ have continued to be of current interest for their utility and compatibility in a variety of applications including tissue scaffolds,⁴⁻⁸ encapsulation matrices,^{9, 10} delivery agents,^{11, 12} and separation membranes.¹³⁻¹⁵ Numerous successful methods to produce hydrogel

networks have been reported, and are most often based on the random physical or chemical cross-linking of hydrophilic polymers in solution.¹ The incorporation of light-responsive functionality,¹⁶ such as anthracene that can undergo reversible $[4\pi + 4\pi]$ photo-cycloaddition¹⁷, into hydrophilic polymers has been reported by several groups¹⁸⁻²¹ as one successful method to produce randomly cross-linked hydrogel networks. In these systems there are several advantages over a purely physical or chemical cross-linked system, such as mild reaction conditions, adjustable cross-link density based on UV irradiation time, and reversibility of the network. However, these reported light sensitive hydrogel systems are still very similar to conventional hydrogel networks that can suffer from weakly-defined structures having a large distribution of mesh sizes arising from the random nature of the unstructured cross-linking process. Non-uniformity in structure and mesh size across the sample profile results in inconsistencies in mechanical properties, swelling and mass transport within the hydrogel.² Our group has been working with pre-structured hydrogels based on self-assembled block copolymers (BCPs) in the melt-state as one method to overcome these limitations of non-uniformity.^{22,23}

BCPs are ideal candidates for hydrogel formation due to their inherent ability to self-assemble on the nanometer length scale.^{24,25} Recently, our group has developed a new tethered hydrogel system based on self-assembled sphere forming blends of AB diblock and ABA triblock copolymers that are pre-structured through self-assembly in the melt-state.^{22,23} The pre-structured morphology contains a periodic lattice comprised of densely packed spherical aggregates of AB diblock copolymers tethered together with an adjustable amount of ABA triblock bridges. Integrity and preservation of both nano- and macro-scale structure is achieved through either physical²² or chemical²³ cross-linking of the hydrophobic spherical A domains prior to preferential swelling of the coronal and bridging B domain. Upon swelling, the tethered network adopts an equilibrium swelling dimension that is determined by a combination of osmotic swelling forces, entropic penalties associated with stretching of the B midblock and topological entanglements associated with the tethering midblock. We have found the developed pre-structured hydrogel systems exhibit highly elastic properties and long-term preservation

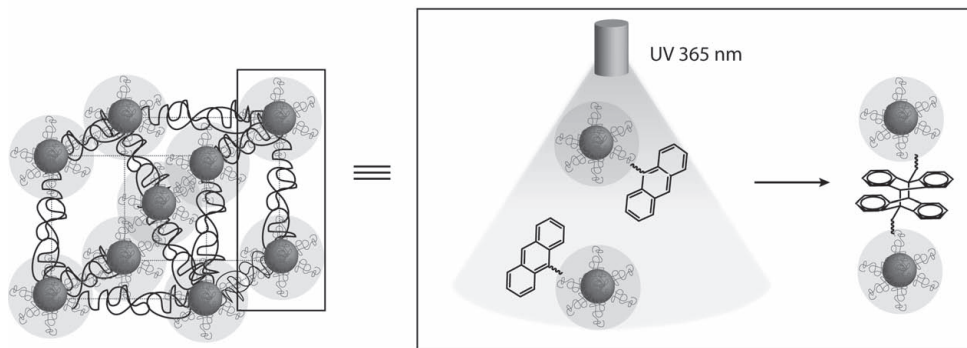


Figure 5-1. Melt pre-structuring of diblock anthracene functional hydrogels. The anthracene terminated diblock is first allowed to self-assemble in the melt, forming a spherical structure with anthracene functional groups around the corona of the spheres. During the melt-processing step the structure is exposed to 365 nm UV filtered light. The UV irradiation allows for in situ generation of photocoupled triblock tethers between spheres. The tethers serve to preserve the network structure through the hydrophobic junction points when swollen in water.

of shape (months). Further, the gels are highly tunable with adjustable mechanical properties (concentration of triblock)²² and pore sizes (length of triblock tether).²⁶ Interestingly, only a small percentage of triblock (~10 mol %) is necessary to produce gels that are easily handled and have excellent mechanical properties.^{22, 23} Notably, these pre-structured hydrogel systems with blend compositions containing a majority of diblock copolymer relative to triblock contain a high density of hydroxyl end-groups in the corona of each spherical aggregate; this provides a straightforward route to directly incorporate functionality within the interior of the hydrogel.

In this report, we further demonstrate the versatility of the pre-structured tethered network by incorporating light reactive anthracene end-groups within the hydrogel. The hydrogels reported herein are based on physically cross-linked spherical forming poly(styrene)-*b*-poly(ethylene oxide) PS-PEO diblock. The PS-PEO diblock was first end-functionalized with anthracene through the activation of terminal hydroxyl groups. Anthracene functional PS-PEO (PS-PEO-An) was then melt-processed allowing for the self-assembly of the targeted spherical morphology. The tethering PS-PEO-PS triblock is generated *in situ* with 365 nm UV

light in the melt-state, eliminating the necessity to pre-blend a fixed amount of triblock prior to swelling (Figure 5-1). After photocoupling in the melt-phase, gels swelled isotropically in water, were easily handled, and highly elastic.

5.3 RESULTS AND DISCUSSION

5.3.1 Synthesis and Physical Characterization

PS-PEO diblock²² ($f_{\text{PS}} = 0.13$, $M_n = 70\ 100\ \text{g mol}^{-1}$, PDI = 1.05) was end-functionalized with anthracene through a straightforward nucleophilic substitution reaction modified from a previous report by Coursan et al. where low MW hydroxyl functional polystyrene was end-tagged with anthracene.²⁷ In this report, hydroxyl functional PS-PEO is titrated with potassium naphthalenide in THF allowing the formation of active alkoxide chain ends which are then terminated with an excess of 9-(chloromethyl)anthracene. The functionality of end-tagging with anthracene was quantitative as determined by ¹H NMR, comparing the relative peak integrations of initiator fragment to the methylene protons adjacent to the added anthracene group (Figure 5-2). Relative integrations of the aromatic protons to initiator fragment were avoided as these are far less accurate due to the strong dissimilarity of the aromatic protons compared to the linear initiator protons. Notably, ¹H resonances from free 9-(chloromethyl)anthracene were absent in the purified product. The quantitative addition of end-groups was only achieved after adding the 9-(chloromethyl)anthracene as a dried powder; efforts to add the terminating agent as a solution in “dry” THF resulted in end-tagging efficiencies of 40–90%, which is consistent with a previous report.²⁷ The SEC trace of PS-PEO-An was nearly identical to the parent PS-PEO with no evidence of chain degradation or coupling (Figure 5-2, inset). Pre-blended samples (without anthracene end-tagging) containing a physical blend of PS-PEO and PS-PEO-PS were prepared analogous to a previous report utilizing the coupling agent, α,α' -Dibromo-*p*-xylene.²²

5.3.2 Melt-State Morphological Characterization

The targeted sphere morphology for the PS-PEO and PS-PEO-An pure diblock copolymers

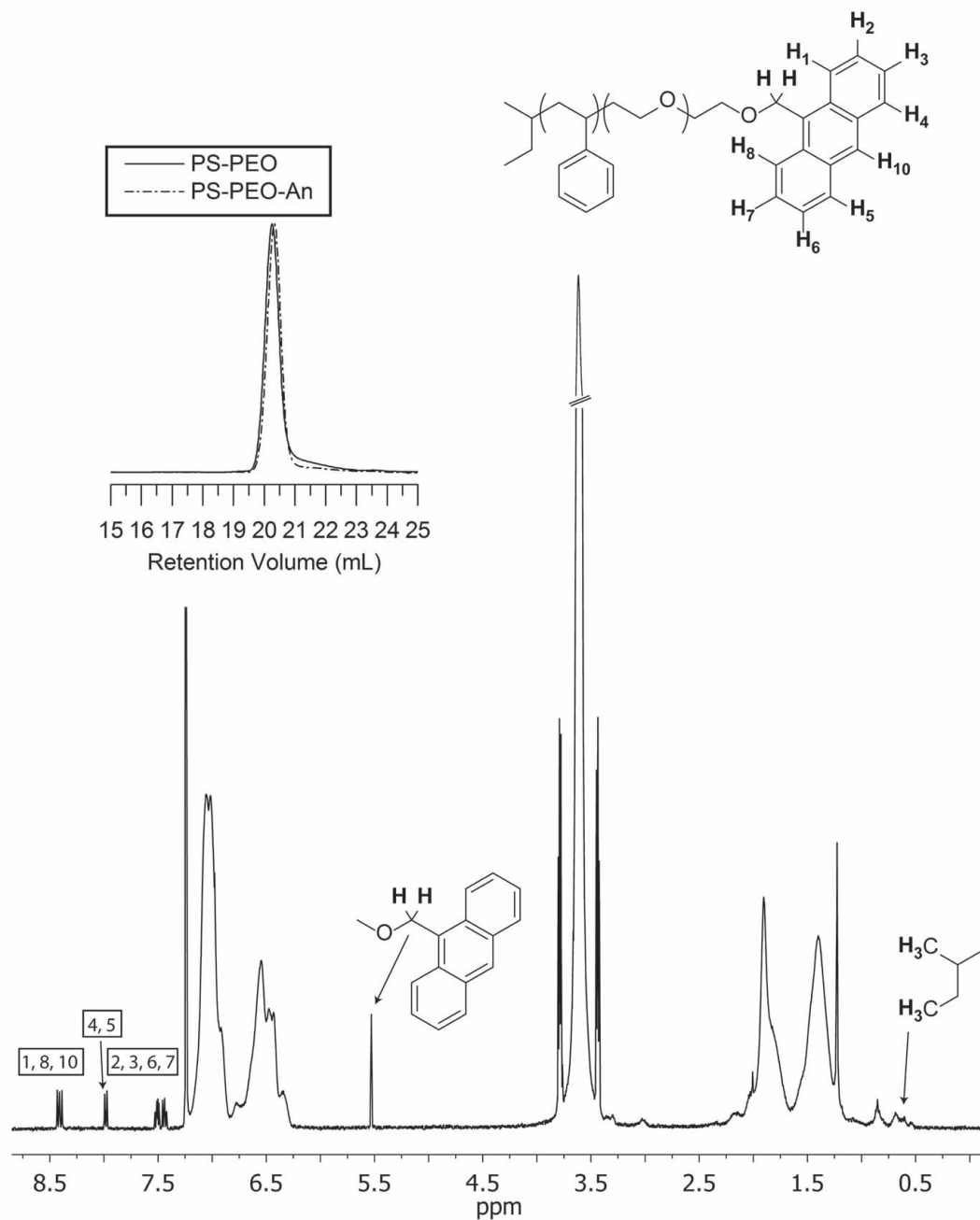


Figure 5-2. ^1H NMR end-group assignments of PS-PEO-An. SEC traces of PS-PEO and PS-PEO-An showing near identical molecular weight distributions (inset).

were confirmed through a combination of dynamic rheology and small-angle X-ray scattering (SAXS). Both samples have near identical melt-state phase behavior that is prototypical of a phase-separated sphere morphology with liquid-like packing (LLP).^{22, 28-31} Rheological temperature ramp experiments show a steady decrease in moduli upon heating with a larger loss modulus (G'') than the storage modulus (G'). This behavior is characteristic of viscoelastic materials with enhanced viscous liquid-like properties. The absence of a plateau response of the moduli and presence of a gradual transition to the disordered state with increased heating is consistent with spherical morphologies with LLP^{22, 28} (Figure 5-3). SAXS data at 100 °C is shown in Figure 5-3. Both PS-PEO and PS-PEO-An show a primary scattering reflection at 0.0226 \AA^{-1} and 0.0230 \AA^{-1} , respectively, this further confirms the phase separated state of the BCPs. Higher order reflections are absent or severely broadened which is also consistent with phase separated morphologies exhibiting liquid-like packing.²⁸⁻³¹

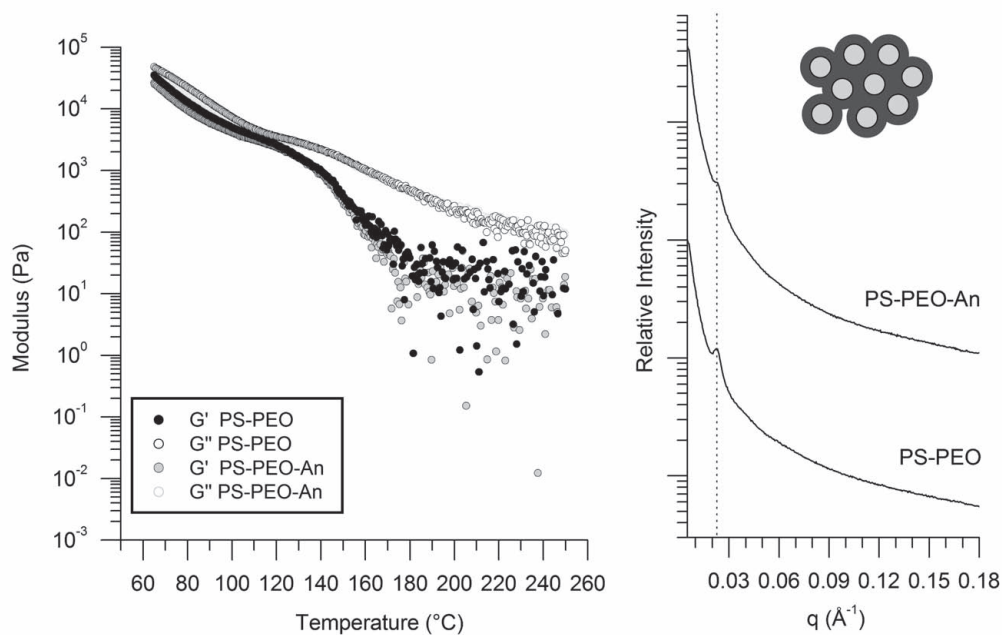


Figure 5-3. Rheological temperature ramps of PS-PEO and PS-PEO-An while heating at $1 \text{ }^\circ\text{C min}^{-1}$ with angular frequency of 1 rad s^{-1} and strain of 5 %. The steady decrease in moduli and absence of a plateau region is consistent with BCP melts containing a liquid-like packing of domains (left). Azimuthally integrated SAXS data at 100 °C for PS-PEO and PS-PEO-An. Higher order reflections are absent which also characteristic of BCPs having LLP (right).

5.3.3 UV Photocoupling of PS-PEO-An in the Melt-State

To photocouple PS-PEO-An pre-structured hydrogels, samples were pressed as round disks (8.14 x 0.29 mm) at 150 °C, cooled to room temperature and placed between hydrophobic surface treated quartz cover clips. The copolymer/quartz sandwich was then reheated on a hot plate to 150 °C and cooled to and held at 100 °C during the photocoupling. A quartz curing attachment with reflecting mirror was positioned ~1–2 mm from the surface of the sample before exposing to 365 nm filtered UV light (mercury-Xenon lamp with 365 nm band-pass filter, 30–38 mW cm⁻² at exposure site). Samples were exposed to 365 nm UV light for 2–20 min (discs were flipped over half way), cooled to room temperature and removed from the quartz slides. Figure 5–4 depicts SEC traces of several photocoupled samples containing various concentrations of triblock relative to the parent PS-PEO-An pure diblock. Notably, a small percentage of side-reactions resulting in high molecular weight copolymers are present in the photocoupled samples despite conducting the experiments under a purge of argon. A total of six samples were photocoupled at exposure times ranging from 2–20 min, resulting in the formation of triblock with

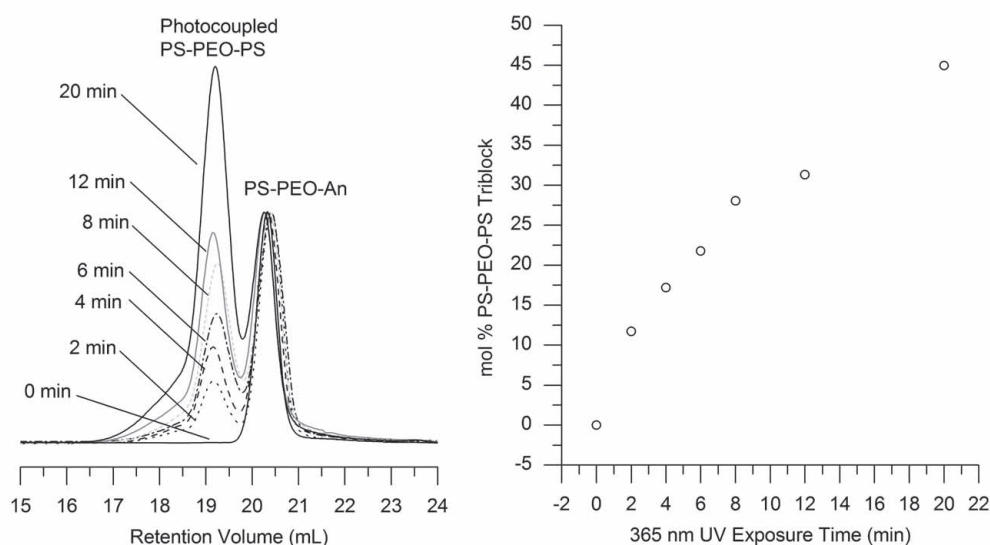


Figure 5–4. SEC traces of PS-PEO-An samples that have been photocoupled with 365 nm UV filtered light at 100 °C for 0–20 min. The concentration of photocoupled PS-PEO-PS triblock could be controlled with UV irradiation time.

average concentrations of 11.7–45.0 mol % (calcd. from SEC relative peak height to avoid error associated with high MW side-reaction products). The ability to precisely control the amount of triblock with UV light alone greatly simplifies the synthetic protocol, that is, the single parent PS–PEO–An BCP can be utilized for numerous pre-structured hydrogels. Direct comparison of photocoupling efficiency is difficult across even similar chemical systems (e.g. similar architecture, reaction media, and MW) due to variations in bulb intensity, lenses, and distance to sample, etc.; Therefore any comparisons to other reports are extremely difficult. With this, we only seek to mention that our system utilizing anthracene coupling in the neat melt phase with a BCP of about 70 kDa (very *low* concentration of end-groups) appears to be controlled and rapid, producing a wide range of coupling efficiencies within a reasonable amount of time of less than 30 minutes. Coupling reactions of polymer-bound functional groups in the melt have been reported previously,³²⁻³⁴ and can be very fast and efficient in miscible³³ or immiscible³² polymer systems between anhydride and amine groups, for example. Interestingly, to the author's knowledge there is only one prior report by Russell and coworkers with an anthracene functional BCP that is UV photocoupled in the melt.³⁵ Notably, we have had past success with UV cationic cross-linking of partially epoxidized poly(diene)-based BCPs in the melt phase^{23, 36} and speculate UV induced photocoupling in the melt-state will also prove to be applicable to wide range of self-assembled BCP structures that can incorporate light sensitive functionality.

5.3.4 Swelling Behavior of UV Photocoupled PS–PEO–An Hydrogels

Photocoupled disks were placed in DI water; the onset of swelling was immediate. Hydrogels reached equilibrium swelling in about 1–2 hours (determined by constant mass and size). PS–PEO–An hydrogels preserved the original 3D disk melt shape and swelled quite dramatically compared to the dry disk which is shown in Figure 5–5 (inset). Preservation of shape and isotropic swelling is characteristic of expansion from a pre-structured spherical morphology. Similarly to our previous report²² of pre-blended PS–PEO–PS/PS–PEO hydrogels, the amount of swelling decreased in the PS–PEO–An gels as the concentration of photocoupled triblock

increased. A reduction in swelling with an increase in triblock content is attributed to the additional triblock macromolecules forming a larger amount of bridging and topological entanglements between adjacent spheres within the gel network structure, effectively increasing the cross-link density.²² The amount of water absorbed (g H₂O per g dry polymer, Q) was tunable in the range of 19.2–5.7 g depending on the concentration of photocoupled triblock present within the sample (Figure 5–5).

While the general trend of decreased swelling with a higher concentration of triblock is observed in both pre-blended PS–PEO and PS–PEO–An gels, significant differences are apparent. The swelling ratio, Q, is about 20 % greater in the PS–PEO–An gels compared to the pre-blends, save for the sample with the highest amount of triblock studied (45 mol %) where the swelling is nearly identical. The differences in swelling behavior are likely related to a decrease in UV flux as a function of depth within the copolymer melt disk, that is; a UV photocoupled gel is produced that contains an asymmetric distribution of triblock throughout the depth profile. In order for the PS–PEO–An to photocouple with UV light, two chains have to come in direct contact where one of the anthracene chain-end molecules is in a very short-lived photoexcited state (nanoseconds).^{37, 38} The probability of photocoupling increases with UV flux, and therefore coupling within the melt-disk (0.3 mm thick) will be most efficient at the surface and least efficient in the middle (when flipped over during irradiation). It is worth noting here that end-group photocoupling is much less efficient compared to our previously reported^{23, 36} UV cationic photocuring of epoxidized ePB (PI)-PEO melt disks for two reasons: (1) end-group photocoupling has a much lower concentration of reactivity sites compared to random cross-linking across multiple sites on a polymer backbone, and (2) in UV initiated cationic photocuring, a polymerization is taking place in which once the photoactive acid is generated by the UV light, the propagation continues until the chain is terminated (no more reactive monomers, water, hydrogen abstraction, etc.). That is, there is no requirement of having a species in the excited state in order to react.

If a gradient of triblock is formed in the PS–PEO–An gels where a higher concentration

of triblock is present on the surface and a lower concentration in the center of the hydrogel, the center of the hydrogel will contain fewer junction points (bridging between spheres) and topological entanglements compared to the outer portion of the gel. This asymmetric nature of the hydrogel results in a greater amount of water absorbed within the “soft” interior of the hydrogel relative to the outer “hard” surface skin containing a higher density of effective bridges and entanglements. Importantly, the interior of the hydrogel is still very homogeneous since the overall structure is determined by the primary self-assembled spherical AB diblock. The added triblock only serves to form a secondary network of topological entanglements which

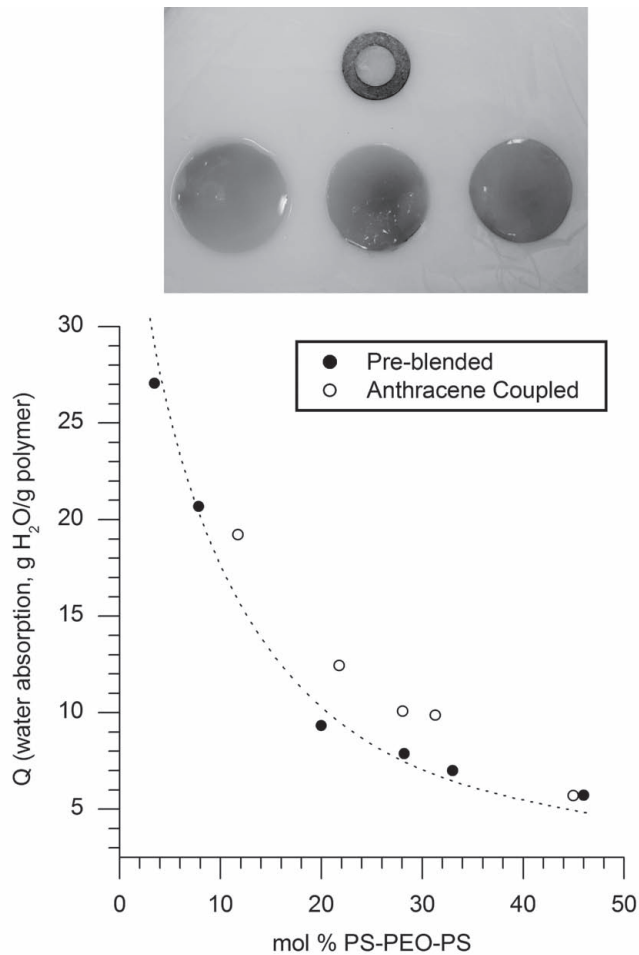


Figure 5-5. Swelling ratios of pre-blended PS-PEO and anthracene coupled PS-PEO hydrogels. In both systems, the ratio of swelling (Q) could be controlled with concentration of triblock. Examples of swollen PS-PEO-An hydrogels, the original disk is shown inside the washer (inset).

reduces the mesh size of the primary structure. A near perfect homogenous or symmetric hydrogel mesh represented by the pre-blended samples (regardless of thickness) should exhibit constant swelling throughout the entire depth of the sample. In support of this claim, as the amount of UV photocoupling time is increased to 20 minutes, a sample with ~45 mol% triblock is produced with swelling that is nearly identical to a pre-blended sample (Figure 5-5). This result is consistent with a decrease in asymmetry likely arising from the longer UV irradiation time and increased efficiency of anthracene coupling within the center of the disk. Longer UV exposure times suggest a secondary mesh throughout the gel that is fairly homogeneous.

The asymmetric nature of the PS-PEO-An gels appears to be subtle enough such that the gels preserve their original pre-structured form. Efforts to quantify the concentration of triblock with depth have been difficult due to the limited amount of material within a photocoupled disk (~15 mg); however, future studies that utilize larger disks and microtome techniques are being investigated to obtain a triblock concentration depth profile of the disks after photocoupling. In addition, microscopy imaging techniques may prove useful providing the hydrogel network does not completely collapse when dried. Interestingly, these results are rather intriguing, as asymmetric hydrogels are highly sought after materials. Asymmetric hydrogels combine the high selectivity of a surface layer (small mesh size) with the high throughput of an interior non-selective layer (large mesh size).³⁹⁻⁴² We believe our self-assembled PS-PEO-An system may be an excellent candidate for the future development of self-supporting asymmetric hydrogels.

5.3.5 Mechanical Performance of UV Photocoupled PS-PEO-An Hydrogels

The dynamic mechanical response of the PS-PEO-An gels under oscillatory shear at room temperature was studied and is shown in Figure 5-6. The data plotted is a summary of the storage modulus (G') taken at 1 rad s^{-1} from a dynamic frequency sweep experiment as a function of mol % triblock. As the amount of triblock concentration increases the modulus increases, consistent with a larger amount of tethers and topological entanglements. Increased entanglements and tethers serve to produce a greater physical cross-link density that inhibits

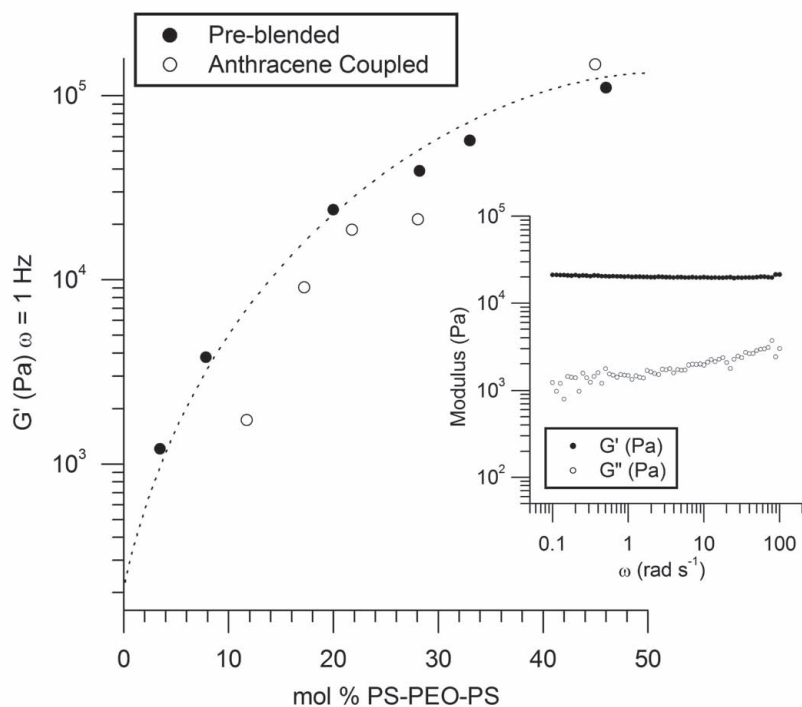


Figure 5-6. Storage modulus of pre-blended PS-PEO and anthracene coupled PS-PEO hydrogels taken from dynamic frequency sweeps at 1 rad s^{-1} . In both hydrogel systems, the modulus could be controlled with concentration of triblock. Dynamic frequency sweep of PS-PEO-An hydrogel that has been UV photocoupled for 8 min. The plateau response is prototypical of highly elastic solids (inset). Dotted line is a visual guide.

deformation of the hydrogel. In the range of photocoupled samples studied with 11.7 to 45 mol % triblock content, the modulus was highly tunable and varied from 10^3 – 10^5 Pa. The inset in Figure 5-6 is a representative plot of a full frequency sweep of a PS-PEO-An gel that has been photocoupled for 8 min forming on average of 28.1 mol% triblock. The frequency independent response of the moduli coupled with a decade difference between the storage (G') and loss (G'') modulus is prototypical of highly elastic solids and consistent with our previously reported hydrogels.^{22, 23} All photocoupled and pre-blended samples exhibited a near perfect plateau response of moduli with varying frequencies in the range of 0.1 – 200 rad s^{-1} . The majority of PS-PEO-An gels exhibit lower moduli values in the frequency sweep experiments, compared to the pre-blended PS-PEO hydrogels. Lower moduli values in the PS-PEO-An gels are attributed to the soft interiors of the asymmetric hydrogels. The asymmetric nature of the gels allows the

softer interior with fewer junctions and entanglements between spheres to more easily deform under load compared to the outer more densely triblock populated hard skin layer of the gel. In contrast, pre-blended samples should ideally contain a complete homogeneous distribution of triblock throughout the depth of the sample. A homogeneous hydrogel would not contain a softer more deformable core and therefore exhibits higher modulus values. Interestingly, in the sample with the highest amount of triblock, 45 mol %, the modulus is very similar to the pre-blended sample of comparable triblock content, suggesting the asymmetric nature is greatly reduced. This is consistent with a longer UV photocoupling time allowing for a greater concentration of triblock to be formed in interior of the disk, providing a much less drastic gradient (or lack thereof). Further, this is in very good agreement with that observed for the swelling, where the 45 mol % sample exhibited near identical swelling to the pre-blended sample, a result of the more homogeneous nature of the 20 min photocoupled hydrogel.

The mechanical behavior of the hydrogels was further characterized through the response of unconfined compression–decompression cycles. Figure 5–7 depicts the compressive stress at 40 % strain of PS–PEO–An and pre-blended PS–PEO hydrogels. The compressive stress increases linearly with added amount of triblock, and quite remarkably there appears to be little difference in the overall compressive stress between anthracene coupled and pre-blended samples at 40 % compression. A representative series of compression–decompression cycles (two complete cycles) of a PS–PEO–An gel photocoupled for 8 min is shown in the Figure 5–7 inset. Each photocoupled hydrogel was able to recover completely after the decompression cycle, albeit with some hysteresis arising from diffusion limitations of the trapped water distributed within the material.²² The second compression–decompression cycle is nearly identical to the first (typical for all samples) showing the excellent elastic recovery properties of the hydrogels and suggesting constant water absorption between cycles. There is an initial compression–decompression non-linearity region from about 1–15% strain in the majority of PS–PEO–An gels, such behavior is limited to 1–5 % in pre-blended samples (verified with compression–decompression cycles, not shown). The small window of non-linearity in pre-blended samples is attributed to the

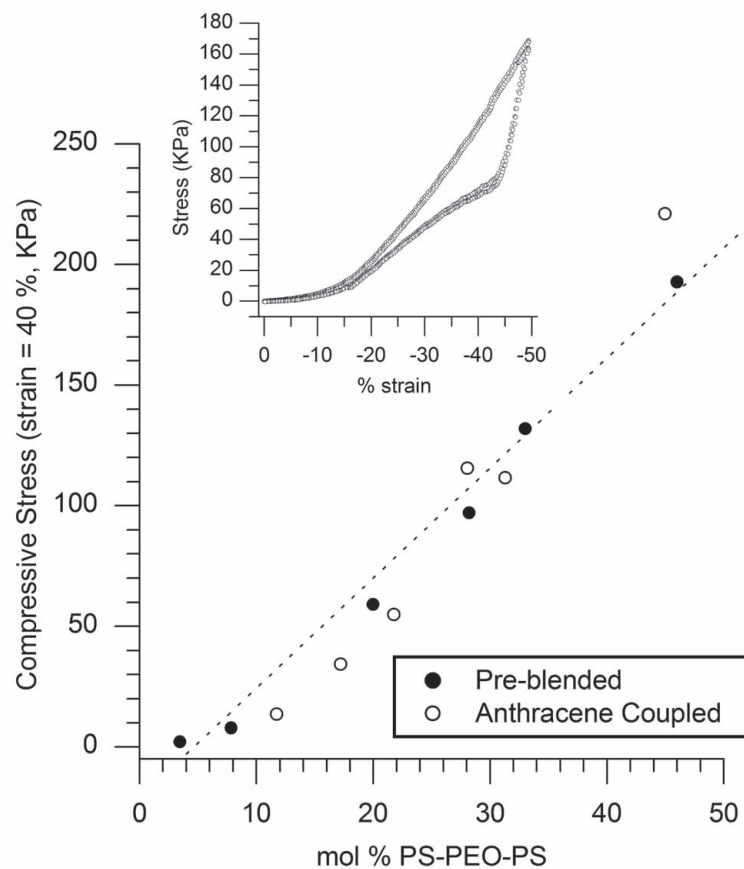


Figure 5-7. Compressive stress at 40 % strain compiled from unconfined compression-decompression cycles. Compressive stress vs. strain for two complete compression-decompression cycles of a PS-PEO-An hydrogel that has been UV photocoupled for 8 min

expulsion of excess water.²² The larger non-linear region observed in the photocoupled samples is likely a result of the asymmetric properties of the material, where the soft interior is more easily deformable at low strain % until the soft interior collapses at around 15% strain. Interestingly, in the 20 min photocoupled sample (45 mol %) the non-linearity region is reduced to just 5%, consistent with the asymmetry in the hydrogel becoming less drastic with increasing photocoupling time.

5.3.6 Preliminary Photoreversibility Experiment

Despite, past reported success of hydrogels incorporating anthracene functionality with reversibility;^{18,21} preliminary efforts to test for reversibility of the anthracene hydrogels reported herein

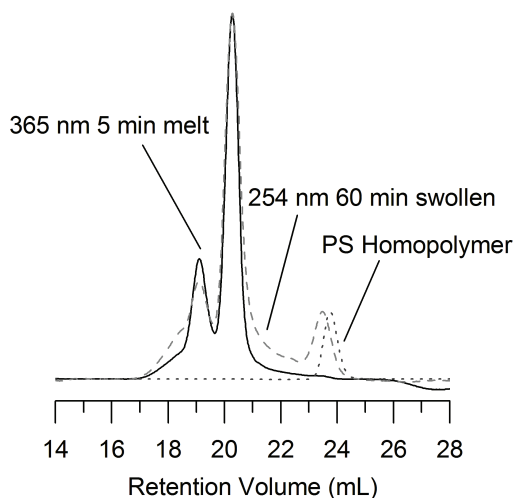


Figure 5–8. SEC traces of reversibility experiment. After 254 nm UV exposure, only about 5% of the triblock decoupled. In addition, there is evidence of a large amount of smaller MW degradation products.

were unsuccessful. Figure 5–8 shows the SEC chromatographs of a PS–PEO–An sample that was coupled in the melt with 365 nm UV light for 5 min and an attempted decoupling experiment with 254 nm UV light. A portion of the PS–PEO–An disk was swollen in water, allowed to equilibrate and blotted dry before exposing to 254 nm UV light for 60 min (intensity of 254 nm UV light is about 1/2 of the 365 nm intensity with the instrument setup). Only approximately 5% of the triblock copolymer was decoupled along with the appearance of higher and smaller MW degradation products (Figure 5–8). The lower MW degradation product appears to be cleaved polystyrene homopolymer since the MW and polydispersity are nearly identical; however a mechanism for this cleavage is not yet understood. Further efforts to achieve reversibility and characterization of the degradation products are currently being investigated. We also suspect that once the photocoupled triblock is formed, access to the anthracene dimer is severely limited due to increased entanglements and steric hindrance within the pre-structured hydrogel interior.

5.4 CONCLUSIONS

A series of pre-structured hydrogels built from self-assembled, light-responsive block copolymers were fabricated. Copolymer samples of anthracene end-functional PS-PEO (PS-PEO-An) are melt-processed as disks and then photocoupled directly in the melt phase. The photocoupling produces PS-PEO-PS triblock in situ which serves to tether the network through the hydrophobic junction points when swollen in water. Through adjustment of UV irradiation time, the synthesized hydrogels were found to be highly tunable in swelling and mechanical properties dependent on the concentration of photocoupled anthracene triblock. The photocoupled hydrogels exhibited properties that were similar to a series of pre-blended PS-PEO/PS-PEO-PS hydrogels, but differences in the behavior were suggestive of an asymmetric mesh size profile as a function of thickness. Future work on the applicability of these hydrogels towards asymmetric materials is actively being explored. Lastly, preliminary experiments suggest that at present there is limited potential for reversibility of this particular hydrogel system.

5.5 EXPERIMENTAL

5.5.1 Materials and Methods

Styrene (99%, 50 ppm *p*-tert-butylcatechol inhibitor, Aldrich) was purified by static vacuum (15-30 mTorr) distillations from di-*n*-butylmagnesium (1.0 M in heptane, Aldrich) at 40 °C. Ethylene oxide (99.5+%, compressed gas, Aldrich) was purified by successive distillations from di-*n*-butylmagnesium (1.0 M in heptane, Aldrich) at 3 °C. *sec*-butyllithium (1.3 M in cyclohexane/hexane, Fisher) was used as received. Potassium naphthalenide solution was prepared according to a previous report [refs]. 9-(Chloromethyl)anthracene (98%, Aldrich) and α,α' -Dibromo-*p*-xylene (97%, Aldrich) were dried under high vacuum for several hours prior to use. Tetrahydrofuran (THF) was degassed by sparging with argon (10 psi) for a period of 45 minutes and then purified over two molecular sieve columns of neutral alumina (Glass Contour, Inc.). Cyclohexane (CHX) was degassed with argon and purified through a column of neutral alumina followed by a column of Q5 copper (II) oxide catalyst (Glass Contour, Inc.).

Other common chemicals and solvents were used as received unless otherwise stated. Ultra high purity argon (99.998% Airgas) was passed through a column of 5 Å molecular sieves with drierite (Agilent) and oxygen absorbing purifier column (Matheson Tri-gas). Glassware and polymerization reactors were flamed under vacuum and backfilled with argon (3 X).

5.5.2 Measurements

NMR spectra were recorded at room temperature on a Varian Inova 400 MHz spectrometer with a d1 pulse delay of 20 s to ensure complete relaxation of end-groups. Spectra were referenced to the residual protio solvent, CHCl_3 . Gel permeation chromatography (GPC) spectra were collected on a Viscotek GPC-Max chromatography system outfitted with three 7.5 x 340 mm Polypore™ (Polymer Laboratories) columns in series, a Viscotek differential refractive index (RI) detector, and an Alltech column oven (mobile phase THF, 40 °C, 1 mL min⁻¹). Rheological melt experiments were run on a TA Instruments Advanced Rheometric Expansion System (ARES) rheometer. Copolymer samples for melt rheology were pressed as solid discs (8 x 1 mm, 150 °C, 500 psi for 60 s). Discs were positioned between two parallel plates (8 mm diameter). The rheometer parallel plates were heated to 75 °C and the gap was reduced and adjusted to ensure even distribution of the sample (typical gaps were 0.5–0.7 mm). Dynamic temperature ramp tests were performed while heating and cooling at 1 °C min⁻¹ at angular frequency of 1 rad s⁻¹ and a strain of 5 % (well within the linear viscoelastic regime, determined by dynamic strain sweep experiments for each copolymer). Rheological swollen hydrogel frequency sweep and compression experiments were run at room temperature using a water bath lower tool apparatus and an 8 mm stainless steel upper parallel plate. Before starting the rheological experiments, hydrogels were blotted dry with KimWipes and humidity covers were placed over the water bath to prevent evaporation. A constant force was applied (10 % compression) to all hydrogel samples to prevent slip. Strain rates were adjusted depending on the linear viscoelastic regime (typically 0.1–1%). Small Angle X-ray Scattering (SAXS) data were collected on a Rigaku S-Max 3000 High Brilliance three pinhole SAXS system outfitted with a MicroMax-007HFM

rotating anode (CuK α), Confocal Max-Flux™ Optic, Gabriel multiwire area detector, and a Linkam thermal stage. Dry polymer samples were sandwiched between kapton windows (0.05 mm thick X 10 mm diameter). Exposure times for samples were typically on the order of 3600 s.

5.5.3 Synthesis of PS-PEO and PS-PEO-PS

Hydroxyl terminal polystyrene-*b*-poly(ethylene oxide) (PS-PEO) was synthesized according to a previously reported procedure [refs] using two-step anionic polymerization of styrene and ethylene oxide monomer. The volume fraction of the PS block was determined to be 0.13 and the overall M_n 70 100 g mol⁻¹ calculated from relative ¹H NMR integrations. GPC (Polystyrene standards): $M_w/M_n = 1.05$. The synthesis of triblock PS-PEO-PS for the pre-blended samples was accomplished via coupling using α,α -Dibromo-*p*-xylene (1 equiv of PS-PEO: 0.5 equiv of α,α -Dibromo-*p*-xylene) according to previous reports.

5.5.4 Synthesis of PS-PEO-An

PS-PEO (1.16 g, 0.017 mmol) was dissolved in 100 mL dry THF. The solution was slowly titrated with potassium naphthalenide such that the solution remained light green for at least 20 min. A large excess of 9-(Chloromethyl)anthracene (0.113 g, 0.5 mmol, ~30x excess) was then immediately added to the PS-PEO alkoxide solution under a slight positive pressure of argon at room temperature. The solution was allowed to stir overnight under argon. The anthracene terminated block copolymer product was precipitated from 25 °C pentane (1 L) twice. Filtration and drying in vacuo (25 °C, 24 h) gave the block copolymer as an off-white powder. Yield = 0.96 g (83 %). GPC (Polystyrene standards): $M_w/M_n = 1.04$. ¹H NMR (400 MHz, CDCl₃, δ): 8.4–8.5 (m, anthracene H₁, H₈ and H₁₀), 7.9–8.0 (d, anthracene H₄ and H₅), 7.4–7.6 (m, anthracene H₂, H₃, H₆ and H₇), 6.2–7.2 (b, -CH₂-C(R)H-C₆H₅), 5.5 (s, -O-CH₂-anthracene), 3.4–3.8 (b, -CH₂-CH₂-O-), 1.1–2.3 (b, -CH₂-C(R)H-C₆H₅), 0.8–0.9 (b, CH₃-CH₂-C(R)H-CH₃), 0.5–0.7 (b, CH₃-CH₂-C(R)H-CH₃). See Figure 5–2 for clarification of anthracene proton assignments. They are consistent with a previous report.²⁷ Relative integrations of anthracene to initiator protons suggest a quantitative addition within ¹H NMR integration error (~5%).

5.5.5 UV Photocoupling PS-PEO-Anthracene in the Melt Phase

PS-PEO-An for the photocoupling experiments were pressed as solid discs (8.14 x 0.29 mm, 150 °C, 500 psi for 60 s) and stored in the dark before use. The copolymer disk was sandwiched between two quartz cover slips (0.25 mm thickness). The quartz cover slips were pre-treated in a solution with 10: 1 volumetric ratio of toluene: trimethylchlorosilane overnight prior to use to make the surface hydrophobic. Immediately before use, the quartz cover slips were rinsed with ethanol to remove any excess solution. The PS-PEO-An disk sandwiched between the quartz slides were placed on a hotplate and heated to 150 °C for 1 min and cooled to 100 °C (5 min cooling time) under a purge of argon. A TA Instruments ARES quartz parallel plate with reflecting mirror tool was positioned approximately 1–2 mm above the surface of the sample. A Hamamatsu Lightning Cure LC8 UV spot cure system was utilized with a 200-Watt mercury-Xenon lamp, Asahi Spectra Co high transmission band pass 365 nm filter, synthetic silica light guide and short focal point condenser lens. The light guide was positioned approximately 1 cm from the quartz reflecting mirror. The intensity at the surface of the sample was 30–38 mW cm⁻² (measured in the range of 200–600 nm with an Omnicure R2000 Radiometer). Samples were exposed to UV 365 nm filtered light for 2–20 min and flipped over halfway through the exposure time.

5.6 ACKNOWLEDGEMENTS

This work was supported by the National Science Foundation (Grant DMR-0645781) and the Colorado State University. The SAXS instrument at CSU is supported by the Central Instrument Facility of the Chemistry Department and the National Science Foundation MRI Program (Grant DMR- 0821799). V.F.S. thanks C.G. for her assistance with the hydrogel rheological measurements.

5.7 REFERENCES

1. Hoare, T. R.; Kohane, D. S. *Polymer* **2008**, *49* (8), 1993-2007.
2. Slaughter, B. V.; Khurshid, S. S.; Fisher, O. Z.; Khademhosseini, A.; Peppas, N. A. *Adv. Mater.* **2009**, *21*, 3307-3329.
3. Tokarev, I.; Minko, S. *Adv. Mater.* **2010**, *22*, 3446-3462.
4. Desai, P. N.; Yuan, Q.; Yang, H. *Biomacromolecules* **2010**, *11* (3), 666-673.
5. Galperin, A.; Long, T. J.; Ratner, B. D. *Biomacromolecules* **2010**, *11* (10), 2583-2592.
6. Hou, Y.; Schoener, C. A.; Regan, K. R.; Munoz-Pinto, D.; Hahn, M. S.; Grunlan, M. A. *Biomacromolecules* **2010**, *11* (3), 648-656.
7. Lee, K. Y.; Mooney, D. J. *Chem. Rev.* **2001**, *101* (7), 1869-1880.
8. Stile, R. A.; Burghardt, W. R.; Healy, K. E. *Macromolecules* **1999**, *32* (22), 7370-7379.
9. Kozlovskaya, V.; Sukhishvili, S. A. *Macromolecules* **2006**, *39* (18), 6191-6199.
10. Xu, Y.; Sato, K.; Mawatari, K.; Konno, T.; Jang, K.; Ishihara, K.; Kitamori, T. *Adv. Mater.* **2010**, *22*, 3017-3021.
11. Dai, H.; Chen, Q.; Qin, H.; Guan, Y.; Shen, D.; Hua, Y.; Tang, Y.; Xu, J. *Macromolecules* **2006**, *39* (19), 6584-6589.
12. Gong, C.; Shi, S.; Wang, X.; Wang, Y.; Fu, S.; Dong, P.; Chen, L.; Zhao, X.; Wei, Y.; Qian, Z. *J. Phys. Chem. B* **2009**, *113* (30), 10183-10188.
13. Annaka, M.; Matsuura, T.; Kasai, M.; Nakahira, T.; Hara, Y.; Okano, T. *Biomacromolecules* **2003**, *4* (2), 395-403.
14. Susanto, H.; Ulbricht, M. *Langmuir* **2007**, *23* (14), 7818-7830.
15. Tokuyama, H.; Iwama, T. *Langmuir* **2007**, *23* (26), 13104-13108.
16. Schumers, J. M.; Fustin, C. A.; Gohy, J. F. *Macromol. Rapid Commun.* **2010**, *31* (18), 1588-1607.
17. Becker, H. D. *Chem. Rev.* **1993**, *93* (1), 145-172.
18. Froimowicz, P.; Frey, H.; Landfester, K. *Macromol. Rapid Commun.* **2011**, *32* (5), 468-473.
19. Wells, L. A.; Brook, M. A.; Sheardown, H. *Macromolecular Bioscience* **2011**, *11* (7), 988-998.
20. Wells, L. A.; Furukawa, S.; Sheardown, H. *Biomacromolecules* **2011**, *12* (4), 923-932.
21. Zheng, Y.; Micic, M.; Mello, S. V.; Mabrouki, M.; Andreopoulos, F. M.; Konka, V.; Pham, S. M.; Leblanc, R. M. *Macromolecules* **2002**, *35* (13), 5228-5234.
22. Guo, C.; Bailey, T. S. *Soft Matter* **2010**, *6* (19), 4807-4818.
23. Scalfani, V. F.; Bailey, T. S. *Macromolecules* **2011**, *44* (16), 6557-6567.
24. Bates, F. S. *Science* **1991**, *251* (4996), 898-905.
25. Bates, F. S.; Fredrickson, G. H. *Phys. Today* **1999**, *52*, 32-38.
26. Guo, C. Development of Tethered-Micelle Hydrogel Networks through Melt State Self-Assembly of Sphere-forming AB Diblock and ABA Triblock Copolymer blends. Colorado State University, **2012**.
27. Coursan, M.; Desvergne, J. P.; Deffieux, A. *Macromolecular Chemistry and Physics* **1996**, *197* (5), 1599-1608.
28. Cavicchi, K. A.; Lodge, T. P. *Macromolecules* **2003**, *36* (19), 7158-7164.
29. Kinning, D. J.; Thomas, E. L. *Macromolecules* **1984**, *17* (9), 1712-1718.
30. Lee, S.-H.; Char, K.; Kim, G. *Macromolecules* **2000**, *33* (19), 7072-7083.
31. Wang, X.; Dormidontova, E. E.; Lodge, T. P. *Macromolecules* **2002**, *35* (26), 9687-9697.
32. Jeon, H. K.; Macosko, C. W.; Moon, B.; Hoyer, T. R.; Yin, Z. H. *Macromolecules* **2004**, *37* (7), 2563-2571.

33. Orr, C. A.; Cernohous, J. J.; Guegan, P.; Hirao, A.; Jeon, H. K.; Macosko, C. W. *Polymer* **2001**, *42* (19), 8171-8178.
34. Macosko, C. W.; Jeon, H. K.; Hoyer, T. R. *Prog. Polym. Sci.* **30** (8-9), 939-947.
35. Chen, W.; Wang, J.-Y.; Zhao, W.; Li, L.; Wei, X.; Balazs, A. C.; Matyjaszewski, K.; Russell, T. P. *J. Am. Chem. Soc.* **2011**, *133* (43), 17217-17224.
36. Scalfani, V. F.; Bailey, T. S. *Chem. Mater.* **2010**, *22* (21), 5992-6000.
37. Greene, F. D.; Misrock, S. L.; Wolfe, J. R. *J. Am. Chem. Soc.* **1955**, *77* (14), 3852-3855.
38. Goldbach, J. T.; Russell, T. P.; Penelle, J. *Macromolecules* **2002**, *35* (11), 4271-4276.
39. Ulbricht, M. *Polymer* **2006**, *47* (7), 2217-2262.
40. Dai, W. S.; Barbari, T. A. *J. Membr. Sci.* **1999**, *156* (1), 67-79.
41. Luo, Y.; Dalton, P. D.; Shoichet, M. S. *Chem. Mater.* **2001**, *13* (11), 4087-4093.
42. Tenhaeff, W. E.; Gleason, K. K. *Chem. Mater.* **2009**, *21* (18), 4323-4331.

CHAPTER 6

SUMMARY — PART I — ACCESS TO UV PHOTOCURED NANOSTRUCTURES VIA SELECTIVE MORPHOLOGICAL TRAPPING OF BLOCK COPOLYMER MELTS

The contents of this dissertation chapter were written by Vincent F. Scalfani.

6.1 MAJOR RESULTS

There are three major achievements in Part I of this dissertation including: 1) development of a thermally stable UV cationic photocuring system that can be used for selectively solidifying BCP self-assembled melt morphologies (Chapter 3). 2) Application of the developed photocuring chemistry to fabricate nanostructured BCP hydrogels (Chapter 4), 3) development of nanostructured hydrogels through UV photocoupling of light-responsive BCP melts (Chapter 5).

In Chapter 3, the thermally stable photocuring system was developed through the addition of a UV activated cationic photoinitiator (~1 mol %) to partially epoxidized poly(isoprene)-*b*-poly(ethylene oxide) BCPs. The synthesized PI-PEO BCP showed complex phase morphology with well-defined regions of a crystalline distorted lamellar-like phase, hexagonally packed cylinders, and bicontinuous gyroid phase. The composite blends exhibited near-identical complex morphological melt behavior compared to the neat PI-PEO. Partial epoxidation of PI-PEO acts only to shift morphological thermodynamic transitions quantitatively to lower temperatures, while completely preserving the overall qualitative morphological behavior. Interestingly, the thermodynamic transition temperatures can be tuned by controlling the percent epoxidation of the poly(isoprene) backbone. Addition of the photoacid (~ 1 mol %) also preserves the overall qualitative morphology; however addition of the photoacid shifts the thermodynamic transitions to slightly higher temperatures (much less drastic compared to epoxidation). Exposure of the photoacid/ePI-PEO blends to UV irradiation at a selected melt-processing temperature allowed for permanent trapping of both the cylinder and gyroid morphologies from a single BCP composite sample. Cured samples of both the cylindrical and gyroid morphologies exhibited high fidelity translation of the selected melt morphology to the solid analogue.

In Chapter 4, the photocuring chemistry was successfully extended to cross-link sphere forming block copolymers. Nanostructured hydrogels were fabricated with the developed photocuring chemistry through translation of the pre-structured sphere melt morphology to the solidified analogue. The hydrogel networks are based on a tethered network system of hydro-

phobic spherical junction points (A domains) connected through hydrophilic (B) domains, that are selectively swollen in compatible media. Blends of partially epoxidized poly(butadiene)-*b*-poly(ethylene oxide) and poly(butadiene)-*b*-poly(ethylene oxide)-poly(butadiene) triblock (ePB-PEO/ ePB-PEO-ePB) with added photoacid were first melt-processed, allowing the composite BCP system to self-assemble into highly ordered spheres on a BCC lattice, and then exposed to UV irradiation directly in the melt-phase, permanently solidifying the structure. High fidelity translation of the spherical melt morphology to the solidified state was observed and proved to be an effective means for the fabrication of nanostructured hydrogel networks. Cured disks of ePB-PEO/ ePB-PEO-ePB swelled isotropically in water (or organic solvents) and were highly elastic. A simple photopatterning experiment showed that uncured (masked) material could be easily dissolved (or dispersed) away when swollen in water.

In Chapter 5, a similar tethered sphere nanostructured hydrogel network as discussed above was fabricated through UV photocoupling of anthracene functional AB diblock copolymer melts. Sphere forming anthracene terminated poly(styrene)-*b*-poly(ethylene oxide) was photocoupled directly in the melt with 365 nm filtered UV irradiation. This unique approach allowed the necessary triblock tethers to be formed *in situ* at varying concentrations. Notably, in contrast to the PB-PEO based hydrogels where the polybutadiene domains are chemically cross-linked, the polystyrene domains in the anthracene terminal PS-PEO hydrogels are physically cross-linked through vitrification. Swollen photocoupled disks preserved their original shape, were highly elastic and had tunable mechanical properties and tunable swelling based on UV irradiation time. Comparison of the anthracene terminal PS-PEO photocoupled gels to pre-blended PS-PEO/PS-PEO-PS gels suggest that the photocoupled networks have some asymmetric properties arising from a gradient distribution of photocoupled triblock.

6.2 BROAD IMPACTS TO THE SCIENTIFIC COMMUNITY

- Epoxidation and/or addition of cationic photoacids does not disrupt self-assembled morphologies in polydiene-based BCP systems. Both provide a means to tune thermodynamic transitions.
- The use of thermally stable UV cationic photoacids is one successful approach to cross-linking and preserving self-assembled BCP melt morphologies.
- Pre-structuring hydrogels via self-assembled block copolymer tethered spherical networks is an effective means to easily produce highly elastic hydrogels with excellent mechanical properties.
- Composite blends of photoacid/BCPs may be used for photopatterning
- Hydrogels fabricated from self-assembled light-responsive BCPs in the melt-phase may be useful for future development of well-defined asymmetric materials.

PART II — MORPHOLOGICAL PHASE BEHAVIOR OF POLY(RTIL)
CONTAINING BLOCK COPOLYMER MELTS

CHAPTER 7

SYNTHESIS AND ORDERED PHASE SEPARATION OF IMIDAZOLIUM- BASED AKYL-IONIC DIBLOCK COPOLYMERS MADE VIA ROMP

The contents of this dissertation chapter have been adapted from a manuscript published in *ACS Macromolecules*: Wiesenauer, E. F.; Edwards, J. P.; Scalfani, V. F.; Bailey, T. S.; Gin, D. L. *Macromolecules* **2011**, *44*, 5075-5078. The synthesis and physical characterization (NMR, DSC, etc.) of the charged imidazolium block copolymers were developed and performed by Erin F. Wiesenauer, Julian P. Edwards and Douglas L. Gin (University of Colorado Boulder). The nanoscale melt-state characterization of the block copolymers through rheology and SAXS were developed and performed by Vincent F. Scalfani and Travis S. Bailey. The manuscript and adapted dissertation chapter was prepared jointly through a collaborative effort of all authors.

7.1 CONSPECTUS

A new type of imidazolium-based, alkyl-ionic block copolymer (BCP) has been synthesized that undergoes ordered phase separation in the melt-state (25 °C) and exhibits surfactant behavior in several non-aqueous solvents. This new BCP platform is synthesized via the sequential, living ring-opening metathesis polymerization of a hydrophobic, non-charged alkyl-norbornene monomer and a cationic imidazolium-norbornene ionic liquid (IL) monomer. This living polymerization behavior, which was experimentally confirmed for both monomers, provides convenient block molecular weight and length control. Small-angle X-ray scattering analysis on samples containing block ratios of 1: 0.90; 1: 0.66; and 1: 0.42 (alkyl:imidazolium repeat units) (i.e., 25-*b*-23; 30-*b*-20; and 35-*b*-15 alkyl:imidazolium BCP lengths) revealed that all three diblock copolymer compositions exhibited diffraction patterns indicative of ordered microphase-separation in the solvent-free melt state, with all three forming highly periodic lamellar phases. Extensive control experiments indicated that the ordered phase-separation of these new alkyl-imidazolium copolymers is due to block architecture, and that these copolymers behave very differently from a physical blend of the analogous homopolymers in solution and the melt state. To our knowledge, this system is one of the first documented examples of a poly(IL)-containing BCP that forms phase-separated, ordered nanostructures in the melt state.

7.2 INTRODUCTION

Polymerized ionic liquids (poly(IL)s) are a new class of polyelectrolytes that are valuable for a number of engineering applications.¹ These cationic polymers are typically made via the covalent polymerization of imidazolium-based organic salt monomers that are liquids at ≤ 100 °C.¹ Imidazolium-based poly(IL)s are particularly useful as functional materials because of their unique combination of physical properties, such as high intrinsic CO₂ gas solubility and ion conductivity.¹ Consequently, these poly(IL)s have been applied as new membrane materials for separating CO₂ from other light gases,² as solid-state ion conductors,³ as specialty dispersants/surfactants,⁴ and as platforms for electrochemical devices,⁵ to name just a few. Unfortunately,

imidazolium-based poly(IL)s have only been synthesized in a limited number of polymer architectures so far. The majority of examples have been linear sidechain homopolymers (including sidechain liquid-crystalline (LC) derivatives).¹ Only a handful of examples of other homopolymer architectures (e.g., main-chain polymers;⁶ amorphous⁷ and ordered (LC)⁸ cross-linked networks) and copolymer architectures (e.g., random⁹ and blocky¹⁰) have been reported. Since differences in polymer architecture and composition often lead to different physical properties and morphologies, this represents an opportunity to explore and synthesize new imidazolium poly(IL)s with potentially enhanced performance in the aforementioned applications.

Phase-separated block copolymers (BCPs) represent an interesting polymer architecture for exploration of new imidazolium-based poly(IL) materials, especially for gas and ionic transport applications. Prior work with conventional, non-ionic, phase-separated diblock copolymers have shown that orientation of the ordered phases can affect light-gas transport.¹¹ If constructed with ionic blocks, copolymers with anisotropic ion-conducting domains may be produced, similar to the LC-sidechain poly(IL) electrolytes described in the literature.¹ An added benefit of BCPs is that their chemical composition can be altered to obtain different mechanical properties and morphologies and incorporate the ability to selectively transport a secondary solute, without affecting the basic properties of the individual domains. In contrast, composition changes in alternating and random copolymers often result in dilution or significant modification of the overall polymer properties. Prior work documenting the solution¹²⁻¹⁵ and melt-state¹⁶⁻¹⁸ assembly of BCPs containing an ionic component have primarily focused on more traditional polyelectrolyte systems, such as those containing acrylic acid,¹²⁻¹⁵ sulfonated styrene,¹⁶⁻¹⁸ or protonated lysine residues.^{13,14} However, the demonstrated formation of phase-separated ordered nanostructures in a solvent-free melt-state by poly(IL)-containing BCPs is largely unprecedented. This is particularly true for the very few (< 5) examples of imidazolium-containing BCPs reported in the literature so far.¹⁰

Herein, we present a new type of imidazolium-based, alkyl-ionic diblock copolymer (**1**) synthesized using living ring-opening metathesis polymerization (ROMP) that forms ordered

nanostructures via phase-separation in the solvent-free melt state at 25 °C (Figure 7–1). Control of the relative composition and molecular weights of the hydrophobic alkyl and imidazolium blocks in these BCPs afforded initial compositions of **1** [i.e., samples **1a–c** with block ratios of 1: 0.90 to 1: 0.42 (alkyl: imidazolium repeat units); total polymer length: 50 repeat units) all of which exhibit phase separation and form highly periodic lamellar phases. Furthermore, in solution, these alkyl-imidazolium diblock copolymers all show surfactant behavior in several non-aqueous solvents. Control experiments with physical blends of the two homopolymers do not show this ordered phase-separation in the melt-state nor surfactant behavior in solution.

7.3 RESULTS AND DISCUSSION

7.3.1 Synthesis

Imidazolium BCPs **1a–c** were synthesized via sequential living ROMP of hydrophobic alkyl monomer **2** and cationic imidazolium IL monomer **3** using Grubbs' 1st-generation olefin

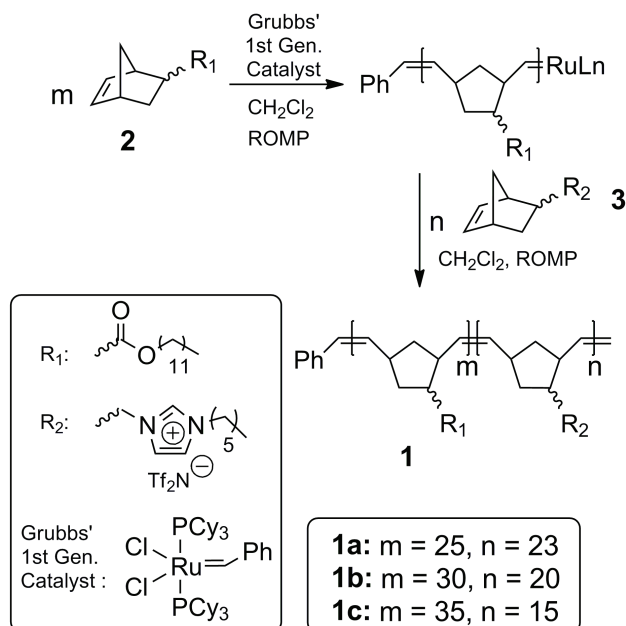


Figure 7–1. The synthesis and structures of alkyl-imidazolium diblock copolymers **1a–c** made via ROMP that show ordered phase-separation in the melt-state. The values of m and n depicted in **1a–c** are derived from the observed NMR block length ratios of the BCPs and the monomer-to-catalyst ratios as used in the living ROMP of **2** and **3**.

metathesis catalyst in CH_2Cl_2 solution as shown in Figure 7-1 (see Appendix II for details).¹⁹ Monomers **2** and **3** were both synthesized from commercially available starting materials in relatively high yields (Appendix II). ROMP was the desired polymerization technique for synthesizing phase-separated alkyl-imidazolium BCPs due to its living and linear character, precise molecular weight control, low polydispersity (PDI), and tolerance of a diverse range of functional groups, including imidazolium units.²⁰ Norbornene derivatives are ideal monomers for ROMP because of their facile synthesis and modularity for functional group attachment, as well as their relatively high ring strain ($27.2 \text{ kcal mol}^{-1}$, the relief of which drives the ROMP reaction).²¹ In our block copolymerizations, **2** was first polymerized to form an initial hydrophobic block, followed by living addition of **3** to form the subsequent ionic block. This order of copolymerization was used because the living polymerization of monomer **2** proceeds faster than the ionic monomer **3** (ca. 3–4 times faster at room temp). By varying the molar ratios of **2** and **3** in the sequential ROMP reactions, alkyl-imidazolium BCPs with different alkyl vs. imidazolium block length ratios were successfully formed.

The ability to polymerize monomers **2** and **3** sequentially to afford BCPs **1a–c** with distinct block composition ratios and lengths was confirmed by ^1H NMR analysis on the polymers and experimental confirmation of living ROMP behavior for the two monomers. The alkyl: imidazolium repeat unit molar ratios for each BCP prepared were directly determined by integrating and comparing distinct ^1H NMR signals indicative of each block. The block lengths (Figure 7-1) were then calculated from the NMR-based repeat unit ratios and the copolymerization monomer-to-catalyst ratios, after confirming living ROMP homopolymerization character for each monomer (see Appendix II for details).²² The M_n values for BCPs **1a–c** were then approximated by multiplying the calculated block lengths by the repeat unit molecular weights. The approximate M_n values for **1a**, **1b**, and **1c** are 20 100, 20 000, and 18 800 g mol^{-1} , respectively (Appendix II). The absolute M_n values for the BCPs **1a–c** could not be determined directly using ^1H NMR endgroup analysis as in the case of the individual homopolymers because the imidazolium proton signals are shifted slightly in the BCPs and overlap with the five phenyl

end-group protons. Unfortunately, conventional methods used to typically determine the molecular weight, molecular weight distribution, and block architecture of copolymers (e.g., GPC, matrix-assisted laser desorption ionization time-of-flight mass spectrometry, and dynamic light scattering) were attempted on **1a–c**, but all yielded inconclusive results. These difficulties were largely associated with the challenges inherent in the characterization of such highly charged macromolecules.¹ Since the block architecture of **1a–c** could not be determined using conventional polymer molecular weight characterization methods, a combination of alternative methods was used to verify a block architecture and to differentiate their behavior from that of a simple physical blend of homopolymers of **2** and **3**. These alternative methods included surfactant behavior and solubility analysis, diffusion-ordered spectroscopy (DOSY), differential scanning calorimetry (DSC), rheological measurements, and small-angle X-ray scattering (SAXS) studies.

7.3.2 Solution-State Phase Behavior

With respect to surfactant and solubility behavior, it was found that copolymers **1a–c** all show surfactant behavior (i.e., extensive foaming when agitated) when mixed in hexanes, THF, CHCl₃, EtOAc, MeOH, and CH₃CN, as would be expected from amphiphilic BCPs. Control experiments with physical blends of poly(**2**) and poly(**3**) of the same length as in the copolymers do not show this behavior. Copolymers **1a–c** also show very different solubility behavior compared to physical blends of the two homopolymers, poly(**2**) and poly(**3**). For example, when mixed with hexanes (10 mg mL⁻¹) **1a** forms opaque heterogeneous suspensions, whereas the physical blend yields a brown solid within a clear solution on top (i.e., poly(**2**) is soluble in hexanes while poly(**3**) is insoluble) (Figure 7–2). Similar results were observed when comparing samples **1a–c** to their physical blends in ethyl acetate and acetonitrile, where poly(**3**) is soluble and poly(**2**) is insoluble.

In NMR DOSY studies, it was found that copolymer **1a** in CD₂Cl₂ (10 mg mL⁻¹) only showed one room-temperature diffusion coefficient (3.68 x 10⁻¹⁰ m² s⁻¹) whereas a physical blend of the

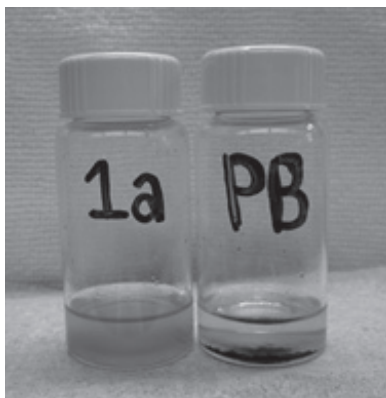


Figure 7–2. Different solubilities of copolymer **1a** and a physical blend (PB) of poly(**2**) + poly(**3**) in hexanes at room temperature.

two homopolymers of comparable length exhibited two distinct diffusion coefficients ($8.8 \times 10^{-10} \text{ m}^2 \text{ s}^{-1}$ and $10.6 \times 10^{-10} \text{ m}^2 \text{ s}^{-1}$). **1a** consists of only one macromolecular species and is different than the physical blend of two distinct macromolecular species. Collectively, the results of these comparative studies are consistent with a covalently-linked BCP architecture for **1a–c**, instead of a physical blend of the two homopolymers.

7.3.3 Melt-State Phase Behavior

Further verification of the block architecture of copolymers **1a–c** and their collective ability to form phase-separated structures was established via a combination of DSC, dynamic rheology, and SAXS data collection. DSC studies on samples of **1a–c** revealed the presence of two broad but distinct thermal transitions near -28 and 7 °C, consistent with crystallization of the *n*-dodecyl sidechains and the vitrification of the imidazolium blocks, respectively (Appendix II). The thermal transitions at ca. 7 °C for BCPs **1b** and **1c** exhibit decreased intensity since they are associated with smaller imidazolium block regions. These DSC results do not directly verify connectivity between the polymer blocks but do establish their phase-separated state in the melt. Slight shifts in the transition temperatures of the BCPs of several degrees relative to those of the individual homopolymers are also consistent with restricted domain sizes and finite interfacial widths typical of ordered BCP morphologies.

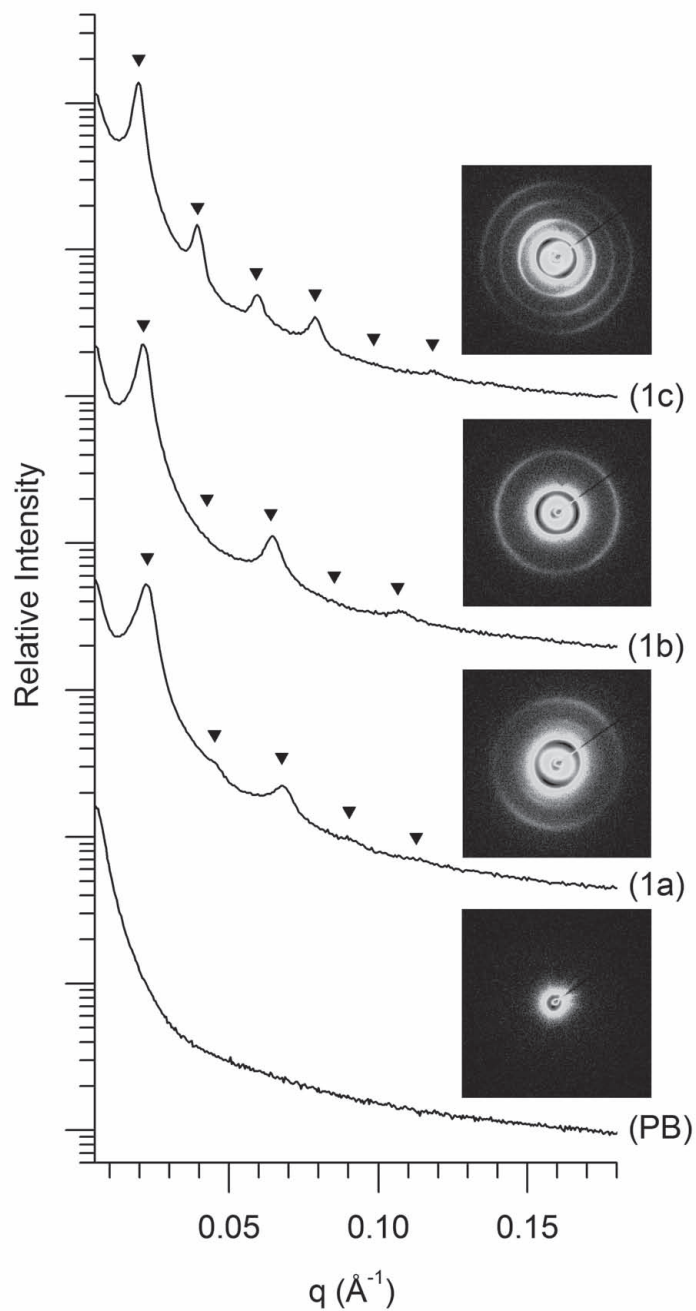


Figure 7-3. Representative SAXS data for imidazolium BCPs containing block ratios of 1: 0.90 (**1a**), 1:0.66 (**1b**), and 1:0.42 (**1c**), with the corresponding 2D detector images (inset). Inverted triangles represent the location of the allowed reflections for the lamellar morphology, calculated based on the position of the primary scattering wave vector q_{100} : $(L) q/q^*$ at $\sqrt{1}$, $\sqrt{4}$, $\sqrt{9}$, $\sqrt{16}$, $\sqrt{25}$, $\sqrt{36}$, etc. The physical blend (PB) of poly(2) and poly(3) shows no observable diffraction peaks, in contrast to the BCPs.

The combination of solubility, NMR DOSY, DSC, and rheology studies confirmed the connected block structure and phase-separated state of **1a–c**. SAXS analysis was used to establish the length scale (and thus block connectivity) and domain geometry of the ordered melts of these samples. SAXS analysis on each of the compositionally unique BCPs verified phase separation on the nanoscale and thus block connectivity with absolute certainty. Representative 25 °C SAXS data are shown in Figure 7–3 for each of the alkyl–imidazolium BCPs synthesized, together with data collected for the physical blend (PB) of the two homopolymers for comparison. At each of the block ratios synthesized, prominent principal diffraction peaks plus multiple higher order reflections are consistent with melt-state lamellar (L) phase morphologies.²³ Notably, the domain spacings ($d = 2\pi/q$) for the three BCP species are very similar (**1a**: 28.6 nm, **1b**: 29.4 nm, **1c**: 32.1 nm), although increasing slightly as the composition shifts towards greater fractions of the non-ionic block (poly(2)). Interestingly, the principal domain spacings ($d = 2\pi/q$) in the range of 30 nm are quite large compared to many traditional BCP systems, considering both the targeted degree of polymerization (~50) and approximate average molecular weights in the 20 000 g mol⁻¹ range. For comparison, a PS–PVP lamellar block copolymer of similar molecular weight would be expected to have a domain spacing around only 20 nm.²⁴ However, the manner in which mass is distributed along these two BCP chains is quite different, with the PS–PVP chain described above having a contour length about 60% longer than **1a–c**. Thus, mass (and volume) is concentrated more densely along the length of **1a–c** (repeat unit molecular weights of monomer **2** and **3** of 307 and 540 g mol⁻¹, respectively), resulting in stiffer, “fatter” chains that favor larger domain spacings. Notably, the mass fraction of the imidazolium block in BCPs **1a–c** ranges from 0.43 (**1c**) to 0.54 (**1b**) to 0.62 (**1a**) which, while difficult to accurately correlate to volume fractions without known homopolymer densities, appears highly consistent with the expected location of the L phase window exhibited by other classic BCP systems.²³ The variations in higher-order diffraction peak intensities for the three samples is also consistent with changes in composition, as the relative thicknesses of the alkyl and ionic domains making up the lamellar period directly affect the superposition product of the form (particle) and structure

(lattice) factor scattering contributions. For example, the notable absence of the reflections at $q/q^* = \sqrt{4}$ and $\sqrt{16}$ in sample **1b** suggests the 1: 0.66 repeat unit ratio is approaching a nearly symmetric volume fraction of 0.5, in which the minima in the form factor scattering cancels out the diffraction intensity associated with the lamellar periodicity for even-order diffraction maxima.²⁵ Dynamic rheological measurements on BCPs **1a–c** also revealed behavior prototypical of traditional lamellar BCP melts, exhibiting elastic and loss moduli of similar magnitudes, with a tendency to decrease together monotonically with increasing temperature (Appendix II).²³ None of the systems revealed any order-to-order transitions below 150 °C. Importantly, a physical blend of the two homopolymers (poly(**2**) + poly(**3**)) does not exhibit any observable scattering or diffraction, confirming the necessity of the covalent bond between the blocks for microphase separation.

7.4 CONCLUSIONS

In summary, a new type of imidazolium-based, alkyl-ionic BCP has been synthesized that undergoes ordered phase separation in the melt state and exhibits surfactant behavior in non-aqueous solvent. This new BCP platform is based on the sequential ROMP of alkyl- and imidazolium IL-norbornene monomers, which provides convenient block ratio and length control. Extensive control experiments indicated that the ordered phase separation of these new alkyl-imidazolium copolymers is due to a block architecture, and that these copolymers behave very differently from a physical blend of the analogous homopolymers in solution and the melt state. To our knowledge, this system is one of the first examples of a poly(IL)-containing BCP that forms phase-separated, ordered nanostructures in the melt state. We are in the process of exploring a wider range of block length ratios for this BCP system in order to map out its full phase behavior. We are also currently extending this project to new monomer systems and ROMP catalysts, testing the performance of these nanostructured imidazolium BCPs as gas separation membranes, and exploring the synthesis of imidazolium triblock copolymers.

7.5 ACKNOWLEDGEMENTS

Primary financial support for the work performed at CU Boulder was provided by the Defense Threat Reduction Agency (grant: HDTRA1-08-1-0028) and the Advanced Research Projects Agency–Energy (grant: DE-AR0000098). E.E.F. thanks M. Moran, Dr. R. K. Shoemaker, and B. Norris for their extensive help with the DSC, DOSY NMR, and attempted GPC work. J.P.E. thanks the Undergraduate Research Opportunities Program at CU Boulder for support of his work in this effort. Primary financial support for the work performed at CSU was provided by the National Science Foundation (grant: DMR-0645781). SAXS studies were performed at CSU using a regional instrument supported by National Science Foundation MRI Program (grant: DMR-0821799).

7.6 SUPPORTING INFORMATION AVAILABLE

Details for the synthesis and chemical characterization of monomers **2** and **3**, BCPs **1a–c**, and homopolymers poly(**2**) and poly(**3**); procedure for estimating M_n values of **1a–c** via block composition analysis and confirmation of living polymerization with predictable M_n control; comparative DSC and NMR DOSY data on **1a–c** and the control polymers; procedures and parameters for performing the rheology and SAXS studies. This information is contained within Appendix II.

7.7 REFERENCES

1. For a comprehensive review of poly(IL)s and their applications, see: (a) Green, O.; Grubjesic, S.; Lee, S.; Firestone, M. A. *J. Macromol. Sci. C: Polym. Rev.* **2009**, *43*, 339. (b) Green, M.; Long, R. *J. Macromol. Sci., Part C: Polym. Rev.* **2009**, *49*, 291. (c) Lu, J.; Yan, F.; Texter, J. *Prog. Polym. Sci.* **2009**, *34*, 431. (d) Anderson, E.; Long, T. *Polymer* **2010**, *51*, 2447. (e) Jaeger, W.; Bohrisch, J.; Laschewsky, A. *Prog. Polym. Sci.* **2010**, *35*, 511.
2. For leading examples of poly(IL)s as membrane materials for CO₂ separations, see: (a) Ding, S.; Tang, H.; Radosz, M.; Shen, Y. *J. Polym. Sci. A: Polym. Chem.* **2004**, *42*, 5794. (b) Bara, J. E.; Lessmann, S.; Gabriel, C. J.; Hatakeyama, E. S.; Noble, R. D.; Gin, D. L. *Ind. Eng. Chem. Res.* **2007**, *46*, 5397.
3. For leading examples of poly(IL)s as ion conductors, see: (a) Ohno, H.; Ito, K. *Chem. Lett.*, **1998**, *27*, 751. (b) Ohno, H.; Yoshizawa, M.; Ogihara, W. *Electrochim. Acta*, **2004**, *50*, 255. (c) Vygodskii, Y.; Shaplov, A.; Lozinskaya, E.; Lyssenko, K.; Golovanov, D.; Malyshkina, I.; Gavrilova, N.; Buchmeiser, M. *Macromol. Chem. Phys.* **2008**, *209*, 40.
4. For leading examples of poly(IL)s as dispersants and surfactants, see: (a) Marcilla, R.; Curri, M. L.; Cozzoli, P. D.; Mart'inez, M. T.; Loinaz, I.; Grande, H.; Pomposo, J. A.; Mecerreyes, D. *Small* **2006**, *2*, 507. (b) Fukushima, T.; Kosaka, A.; Yamamoto, Y.; Aimiya, T.; Notazawa, S.; Takigawa, T.; Inabe, T.; Aida, T. *Small* **2006**, *2*, 554.
5. For leading examples of poly(IL)s used in electrochemical devices, see: (a) Ho, H. A.; Leclerc, M. *J. Am. Chem. Soc.*, **2003**, *125*, 4412. (b) Ricks-Laskoski, H. L.; Snow, A. W. *J. Am. Chem. Soc.* **2006**, *128*, 12402.
6. (a) Suzuki, K.; Yamaguchi, M.; Hotta, S.; Tanabe, N.; Yanagida, S. *J. Photochem. Photobiol. A: Chem.* **2004**, *164*, 81. (b) Li, F.; Cheng, F.; Shi, J.; Cai, F.; Liang, M.; Chen, J. *J. Power Sources* **2007**, *165*, 911. (c) Liang, Z. Y.; Lu, C. X.; Luo, J.; Dong, L. B. *J. Fluorine Chem.* **2007**, *128*, 608.
7. (a) Muldoon, M. J.; Gordon, C. M. *J. Polym. Sci. A: Polym. Chem.* **2004**, *42*, 3865. (b) Nakajima, H.; Ohno, H. *Polymer* **2005**, *46*, 11499. (c) Marcilla, R.; Sanchez-Paniagua, M.; Lopez-Ruiz, B.; Lopez-Cabarcos, E.; Ochoteco, E.; Grande, H.; Mecerreyes, D. *J. Polym. Sci. Part A: Polym. Chem.* **2006**, *44*, 3958. (d) Bara, J. E.; Hatakeyama, E. S.; Gabriel, C. J.; Lessmann, S.; Gin, D. L.; Noble, R. D. *J. Membr. Sci.* **2008**, *316*, 186.
8. Yoshio, M.; Kagata, T.; Hoshino, K.; Mukai, T.; Ohno, H.; Kato, T. *J. Am. Chem. Soc.* **2006**, *128*, 5570.
9. (a) Zhang, G.; Liu, X.; Li, B.; Bai, Y. *J. Appl. Polym. Sci.*, **2009**, *112*, 3337. (b) Tan, R.; Yin, D.; Yu, N.; Zhao, H.; Yin, D. *J. Catal.*, **2009**, *263*, 284.
10. (a) Stancik, C. M.; Lavoie, A. R.; Schutz, J.; Achurra, P. A.; Lindner, P.; Gast, A. P.; Waymouth, R. M. *Langmuir* **2004**, *20*, 596. (b) Vijayakrishna, K.; Jewrajka, S. K.; Ruiz, A.; Marcilla, R.; Pomposo, J. A.; Mecerreyes, D.; Taton, D.; Gnanou, Y. *Macromolecules* **2008**, *41*, 6299. (c) Mori, H.; Yahagi, M.; Endo, T. *Macromolecules* **2009**, *42*, 8082. (d) Vijayakrishna, K.; Mecerreyes, D.; Gnanou, Y.; Taton, D. *Macromolecules*, **2009**, *42*, 5167. (e) Gu, Y.; Lodge, T. *Macromolecules* **2011**, *44*, 1732.
11. Drzal, P. L.; Halasa, A. F.; Kofinas, P. *Polymer* **2000**, *41*, 4671.
12. Annaka, M.; Morishita, K.; Okabe, S. *J. Phys. Chem. B* **2007**, *111*, 11700.
13. Gebhardt, K. E.; Ahn, S.; Venkatchalam, G.; Savin, D. A. *Langmuir* **2007**, *23*, 2851.
14. Naik, S. S.; Savin, D. A. *Macromolecules* **2009**, *42*, 7114.
15. Zhang, L.; Shen, H.; Eisenburg, A. *Macromolecules* **1997**, *30*, 1001.
16. Lu, X.; Weiss, R. A. *Macromolecules* **1993**, *26*, 3615.

17. Park, M. J.; Balsara, N. P. *Macromolecules* **2008**, *41*, 3678.
18. Saito, T.; Mather, B. D.; Costanzo, P. J.; Beyer, F. L.; Long, T. E. *Macromolecules* **2008**, *41*, 3503.
19. Commercially available Grubbs' 1st- and 2nd-generation olefin metathesis catalysts were tested for ROMP of **2** and **3**. Grubbs' 1st- generation catalyst was found to be the best catalyst of the two for this system. Other ROMP catalysts such as Grubbs' 3rd- generation catalyst were not tested for this initial proof-of-concept study because they are not commercially available, but they will be tested in follow-up studies.
20. (a) Bielawski, C. W.; Grubbs, R. H. *Prog. Polym. Sci.* **2007**, *32*, 1. (b) Arstad, E.; Barrett, A.; Tedeschi, L. *Tetrahedron Lett.*, **2003**, *44*, 2703. (c) Vygodskii, Y.; Shaplov, A.; Lozinskaya, E.; Filippov, O.; Shubina, E.; Bandari, R.; Buchmeiser, M. *Macromolecules* **2006**, *39*, 7821. (d) Zheng, L.; Chen, F.; Xie, M.; Han, H.; Dai, Q.; Zhang, Y.; Song, C. *React. Funct. Polym.* **2007**, *67*, 19.
21. Walker, R.; Conrad, R. M.; Grubbs, R. H. *Macromolecules* **2009**, *42*, 599.
22. In addition, samples taken of poly(**2**) prior to the addition of **3** during the sequential ROMP polymerizations confirmed that the molecular weight distribution of poly(**2**) was symmetric and monomodal, with PDI values consistently in the 1.15-1.17 range for all samples.
23. Hamley, I. W. *The Physics of Block Copolymers*; Oxford University Press: Oxford, 1999; p. 432.
24. Matsushita Y.; Mori, K.; Saguchi, R.; Nakao, Y.; Noda, I.; Nagasawa, M. *Macromolecules*, **1990**, *23*, 4313.
25. (a) Hasegawa, H.; Hashimoto, T.; Kawai, H.; Lodge, T. P.; Amis, E. J.; Glinka, C. J.; Han, C. C. *Macromolecules* **1986**, *18*, 67. (b) Hashimoto, T.; Nagatoshi, K.; Todo, A.; Hasegawa, H.; Kawai, H. *Macromolecules* **1974**, *7*, 364.

CHAPTER 8

MORPHOLOGICAL PHASE BEHAVIOR OF POLY(RTIL) CONTAINING DIBLOCK COPOLYMER MELTS

The contents of this dissertation chapter have been adapted from a manuscript that has been submitted for publication in **2012**: Scalfani, V. F.; Wiesnauer, E. F.; Ekblad, J. R.; Edwards, J. P.; Gin, D. L.; Bailey, T. S. Morphological Phase Behavior of Poly(RTIL) Containing Diblock Copolymer Melts. *Macromolecules*, **2012**, submitted. The synthesis and physical characterization (NMR, TGA, etc.) of the charged imidazolium block copolymers were developed and performed by Erin F. Wiesnauer, Julian P. Edwards and Douglas L. Gin (University of Colorado Boulder). The nanoscale melt-state characterization of the block copolymers through rheology and SAXS were developed and performed by Vincent F. Scalfani, John R. Ekblad and Travis S. Bailey. The manuscript and adapted dissertation chapter was written by Vincent F. Scalfani with collaborative editing of all authors.

8.1 CONSPECTUS

The development of nanostructured polymeric systems containing directionally continuous poly(ionic liquid) (poly(IL)) domains has considerable implications towards a range of transport-dependent, energy-based technology applications. The controlled, synthetic integration of poly(IL)s into block copolymer architectures provides a promising means to this end, based on their inherent ability to self-assemble into a range of defined, periodic morphologies. In this work, we report the melt-state phase behavior of an imidazolium-containing alkyl-ionic block copolymer (BCP) system, derived from the sequential ring-opening metathesis polymerization (ROMP) of imidazolium- and alkyl-substituted norbornene monomer derivatives. A series of 16 BCP samples were synthesized, varying both the relative volume fraction of the poly(norbornene dodecyl ester) block ($f_{\text{DOD}} = 0.42\text{--}0.96$) and the overall molecular weights of the block copolymers (M_n values from 5000–20100 g mol⁻¹). Through a combination of small-angle X-ray scattering and dynamic rheology, we were able to delineate clear compositional phase boundaries for each of the classic block copolymer phases, including lamellae (Lam), hexagonally packed cylinders (Hex), and spheres on a body-centered cubic lattice (S_{BCC}). Additionally, a liquid-like packing (LLP) of spheres was found for samples located in the extreme asymmetric region of the phase diagram, and a persistent coexistence of Lam and Hex domains was found in lieu of the bicontinuous gyroid phase for samples located at the intersection of Hex and Lam regions. Thermal disordering was opposed even in very low molecular weight samples, detected only when the composition was highly asymmetric ($f_{\text{DOD}} = 0.96$). Annealing experiments on samples exhibiting Lam and Hex coexistence revealed the presence of extremely slow transition kinetics, ultimately selective for one or the other, but not the more complex gyroid phase. In fact, no evidence of the bicontinuous network was detected over a two-month annealing period. The ramifications of these results, for transport dependent applications targeting the use of highly segregated poly(IL)-containing block copolymer systems, is carefully considered.

8.2 INTRODUCTION

Polymerized ionic liquids (poly(IL)s) are a relatively new class of charged polymers (typically cationic) that combine the unique thermal, chemical, and transport properties of ionic liquids (ILs) with the physical and mechanical properties of polymeric materials. The result are macromolecules implicitly suited for a range of valuable engineering applications, most notably those involving selective transport phenomena in energy and energy industry related technologies.¹⁻⁵ The predominance of the recent synthetic efforts to produce poly(IL)s have focused on repeat units containing charged imidazolium groups^{4, 6-21}, some of which have already shown considerable promise as membrane materials for CO₂/light gas separations^{22, 23}, solid-state ion conductors²⁴⁻²⁶, and electrochemical devices.^{27, 28} Such target applications are predicated on exploiting the inherent CO₂ gas solubility, ion conductivity, and tunable amphiphilicity associated with the charged imidazolium species. However, true performance optimization in these applications requires an ability to tune not only the charge or gas molecule transport behavior, but the mechanical properties as well. In such singular, homopolymer based materials this becomes largely impractical, given the opposing dependence of mechanical response and transport on local chain mobility. That is, the integration of high crosslink densities, entanglements, or crystalline domains to provide the robust mechanical performance needed for long term usage is inherently deleterious to the material's ability to simultaneously achieve high ion and gas molecule transport rates.

One very promising solution to this dilemma can be achieved through direct integration of poly(IL)s into block copolymer (BCP) architectures with other, nonionic, polymer species. Such an arrangement can provide access to single molecule systems capable of phase separating into a range of morphologies, in which the ionic and nonionic polymer segments occupy separate domains spatially organized on the five to fifty nanometer length scale. Through the phase separation, the bulk mechanical property and transport characteristics of each polymer block can be largely retained, although the intra and inter-grain domain continuity associated with the morphology ultimately determines the macroscopic behavior of the sample. With the

exception of the network phases such as gyroid^{29,30}, most identified block copolymer morphologies have geometries that constrain intra-grain continuity, in at least one block, to two or fewer dimensions.³¹ However, arbitrary inter-grain orientation randomizes this intra-grain orientational preference and can effectively restore three-dimensional continuity.³² Of course, net transport rates are reduced by the added tortuosity imposed on the transport process, as well as defects and dead ends generated at grain boundary interfaces. The effects on ion conductivity have been studied in detail by Balsara and coworkers in lithium^{33, 34} and imidazolium³⁴ doped poly(styrene)-*b*-poly(ethylene oxide) BCPs, and more recently by Mahanthappa and coworkers in BCPs containing pendant charged imidazolium groups.²¹ Processing methods in BCPs that produce increased orientational order and larger grain sizes can theoretically improve performance, and have been the subject of significant study.³⁵⁻⁴¹ Such methods have been recently applied to the orientation of ordered phases in conventional, non-ionic, phase-separated diblock copolymers and shown to affect transport for both light gas⁴² and ethanol⁴³ separations. It is worth mentioning that much of the processing effort associated with producing preferred domain orientations can be potentially eliminated using one of the continuous network phases, such as the bicontinuous gyroid phase found in AB diblock copolymer melts.²⁹ The continuity in both domains, combined with an inherent propensity to form very large grain sizes during annealing, create a potential advantage for transport applications, making it a worthy target. Unfortunately, the gyroid phase has often been found to be experimentally confined to weakly segregated systems, making its use challenging in systems for which the Flory interaction parameter between blocks is high, or the molecular weight is large.

Over the last several years, we have been particularly interested in the application of imidazolium-based poly(IL)s as selective components in CO₂/light gas separation membranes. In this regard, we have been focused on developing BCP systems containing imidazolium-based poly(IL)s that can ultimately produce the combined mechanical properties and gas molecule transport performance necessary for efficient high volume separations. To this end, our group recently reported the direct synthesis of an imidazolium-based alkyl-ionic diblock copolymer

employing sequential ring-opening metathesis polymerization (ROMP) polymerization of alkyl ester and charged imidazolium norbornene monomer derivatives.⁴⁴ This synthetic route stands as one of the first examples of poly(IL)-based BCP synthesis that does not require post-polymerization modification to introduce the IL component.^{16-18, 20, 21}

Given the importance of morphology on the transport process, a detailed characterization of the thermal and compositional BCP phase behavior for these highly charged molecules is the subject of this report. In general, the presence of the charged-uncharged architecture, and its influence on the classically observed phase behavior exhibited by uncharged systems, has received only limited attention. This is particularly true for poly(IL) containing BCPs. Prior work documenting solution⁴⁵⁻⁴⁸ and melt-state⁴⁹⁻⁵¹ phase-separation of ionic-containing BCPs have primarily focused on different polyelectrolyte systems, such as those containing acrylic acid⁴⁵⁻⁴⁹, sulfonated styrene⁴⁹⁻⁵¹, or protonated lysine residues.^{46, 47} Documented phase separation in imidazolium-based poly(IL) BCPs in the solvent-free melt state is largely unprecedented, being limited to recent work by Mahanthappa and coworkers²¹ and our preliminary report focused on the BCP synthesis.⁴⁴ In any event, the ability to access each of the different phases classically observed in BCP systems has not yet been established for these unusual systems. Of particular interest is the impact of the charged-uncharged architecture on the ability of the block copolymer to form the idealized (for transport applications) gyroid network. We believe this is the first detailed investigation into the phase behavior of imidazolium-based poly(IL) containing BCPs.

In this report, we present the melt-state phase behavior of a series of 16 imidazolium-based poly(IL) block copolymers spanning the composition range of 42–96 vol % poly(norbornene dodecyl ester), characterized through a combination of small-angle X-ray scattering (SAXS) and dynamic rheology. Of the 16 BCPs studied, 14 were found to have a high degree of long-range order, even those having relatively low molecular weights. A detailed morphological analysis of each sample is presented in this report, and the impact of the charged-uncharged architecture on the degree of segregation and the resulting phase behavior is discussed. The implications for

the apparent absence of the gyroid phase from this and other charged-uncharged BCP systems are also considered.

8.3 RESULTS AND DISCUSSION

Synthesis of Alkyl-Imidazolium Diblock Copolymers. A total of 16 block copolymer samples (**1A-P**) were synthesized via the sequential ROMP using Grubbs' first-generation catalyst of two norbornene monomer derivatives (Figure 8-1); one substituted with a hydrophobic dodecyl ester (**2**) and the other with a cationically charged imidazolium based ionic liquid (**3**). The synthesis and characterization details can be found in our recent communication.⁴⁴ The majority of BCP samples synthesized (13 out of 16) were targeted to contain 50 total repeat units while varying the relative volume fraction of the poly(norbornene dodecyl ester) block from 0.42–0.96. As discussed in our previous communication, M_n values were targeted through monomer/catalyst ratios, and verified through end-group analysis on a sample of poly(norbornene dodecyl ester) homopolymer taken from the reactor just prior to the addition of the second (**3**) monomer. The final BCP M_n values were then inferred using this homopolymer M_n values and the ^1H NMR spectra for BCP. Direct analysis of M_n of the BCP through ^1H NMR was not possible due to peak overlap in the with the initiator fragment protons in the final ^1H NMR spectra. Final

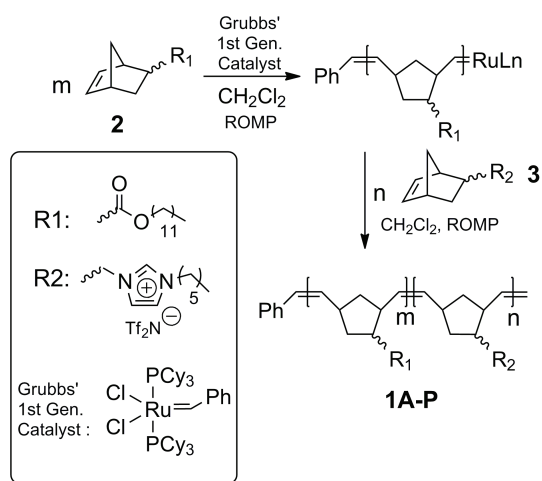


Figure 8-1. Sequential ROMP of monomer **2** and **3** to yield imidazolium-based alkyl ionic BCPs **1A-P**.

BCP molecular weights (M_n) varied from 5000–20 100 g mol⁻¹ (Table 8–1). SEC analysis of the BCPs could not be performed due to the inherent complications of charged species interacting with the columns. Poly(norbornene dodecyl ester) homopolymer samples extracted prior to addition of the imidazolium block were found to have typical PDI values of 1.15–1.2.⁴⁴

Table 8–1. Summary of synthesized imidazolium-based alkyl-ionic BCPs and their corresponding phase behavior.

Sample Name	$m : n^a$	$M_{n(\text{DOD})}^b$	$M_{n(\text{IMD})}^c$	wt % _{(DOD)}^d}	f_{DOD}^e	Morphological Behavior
1A	48.5 : 1.4	14 900	800	0.95	0.96	LLP → Dis
1B	47.0 : 3.8	14 400	2000	0.88	0.89	LLP
1C	45.0 : 5.6	13 800	3000	0.82	0.84	LLP → S _{BCC}
1D	43.5 : 6.9	13 400	3700	0.78	0.81	LLP → Hex
1E	42.0 : 9.5	12 900	5100	0.71 ₆	0.74 ₇	LLP → Hex
1F	40.0 : 9.1	12 300	4900	0.71 ₅	0.74 ₆	LLP → Hex
1G	38.5 : 11.3	11 800	6100	0.66	0.69	Lam + Hex
1H	37.5 : 12.8	11 500	6900	0.63	0.66	Lam + Hex
1I	36.5 : 13.9	11 200	7500	0.60	0.64	Lam + Hex
1J	35.6 : 14.4	10 900	7800	0.58	0.62	Lam
1K	30.0 : 12.8	9200	6900	0.57	0.61	Lam
1L	32.0 : 18.0	9800	9700	0.50	0.54	Lam
1M	7.5 : 5.0	2300	2650	0.46 ₅	0.50 ₄	Lam
1N	30.0 : 20.0	9200	10 800	0.46 ₀	0.50 ₀	Lam
1O	15.0 : 10.3	4600	5600	0.45	0.49	Lam
1P	25.0 : 23.0	7700	12 400	0.38	0.42	Lam

^a $m : n$ ratio determined from relative ¹H NMR peak integrations in combination with poly(norbornene dodecyl ester) (DOD) M_n values.⁴⁴ ^b M_n of DOD were calculated from monomer-to-catalyst loading ratios (with complete monomer consumption as per a living polymerization) and verified by ¹H NMR. ^c M_n of poly(norbornene imidazolium) (IMD) inferred from ¹H NMR of DOD homopolymer and final BCP. ^dweight fraction of DOD calculated as $M_{n(\text{DOD})}/[M_{n(\text{DOD})} + M_{n(\text{IMD})}]$. ^eVolume fraction of DOD calculated with $f_{\text{DOD}} = kM_{n(\text{DOD})}/[kM_{n(\text{DOD})} + M_{n(\text{IMD})}]$, with $k = \rho_{(\text{IMD})}/\rho_{(\text{DOD})} = 1.17_3$, determined using SAXS of sample 1N, as described in the main text. LLP = liquid-like packing, Dis = disordered, S_{BCC} = spheres on a body-centered cubic lattice, Hex = hexagonally packed cylinders, Lam = lamellae.

8.3.1 Overview of Melt-State Phase Behavior.

A combination of dynamic rheology and small-angle X-ray scattering (SAXS) was utilized to study the self-assembled melt-state phase behavior of the 16 DOD-IMD BCP samples spanning 42–96 vol % poly(norbornene dodecyl ester) (DOD). The systematic characterization of the BCP phase behavior was carried out by first measuring the elastic (G') and loss modulus (G'') response as a function of temperature with dynamic rheology (in the linear viscoelastic regime) under a complete thermal heating (up to 200 °C) and cooling (back to R.T.) cycle. The cooling cycle was then immediately followed by a second heating ramp. In an effort to probe each sample for additional thermal transitions and in particular a transition to the isotropic disordered state, the second heating ramp in the cycle was extended past 200 °C. However, all samples exhibited a rapid and irreversible increase in modulus in the range of 210–240 °C, which appears to be associated, not with a phase transition, but thermally induced crosslinking of the samples. TGA analysis confirmed degradation (loss of mass) onset temperatures around 350 °C, suggesting the observed spike in modulus is likely a cross-linking, not an early degradation event (supporting information, Appendix II). Preliminary experiments with adding 0.02 wt % butylated hydroxytoluene (BHT) to prevent cross-linking appeared to substantially alter the rheological response, presumably through the interaction with the charged imidazolium block. Since such a change in rheological response is indicative of a potential morphological change, it was decided to restrict study of the morphological behavior to temperatures less than 200 °C, to avoid the potential interference associated with additives. Samples prepared for SAXS analysis were restricted to a single, complete heating and cooling cycle up to a maximum of 200 °C, based on the rheologically established instability above this temperature. We note, however, that for the most asymmetric samples **1A** and **1B**, the rheological experiments were limited to ~140 °C. These limits were imposed due to disordering in the former, and reaching the low torque resolution limits of the rheometer in the latter. In both cases the increased liquid-like nature of and degree of disorder in these samples (**1A** and **1B**) at such moderate temperatures made use of the full cycle unnecessary.

A phase diagram plotted as a function of temperature and volume fraction of the DOD block has been assembled in Figure 8–2 from the rheological and SAXS data collected. For clarity, only data from the 13 BCPs having approximately 50 combined repeat units are included in this diagram. Generally, direct morphological assignments were possible by comparing multiple diffracted reflections obtained from SAXS to those calculated for symmetries of documented diblock copolymer morphologies. Importantly, the SAXS data presented in this report contain data markers located at specific positions in q . These data markers are not pointing to features in the data, but more appropriately to the calculated positions of the allowed reflections for the particular assigned morphology. The vertical dotted line boundaries in Figure 8–2 are visual guides chosen arbitrarily to separate the observed morphologies, not experimental divisions. In general, different shaped symbols have been used to designate the specific morphology located at each point in the diagram. Weakly ordered morphologies, such as LLP spheres, have

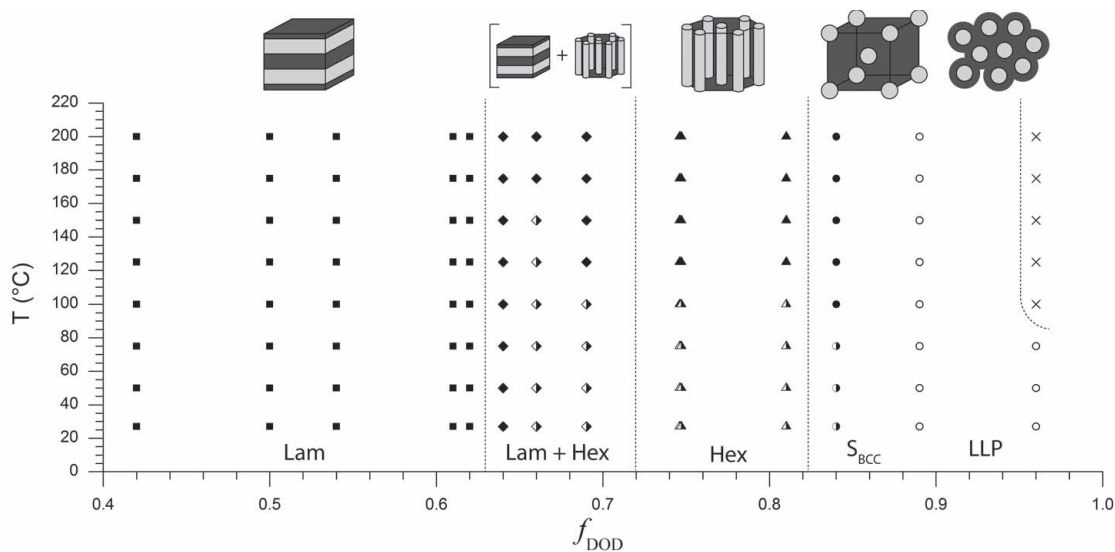


Figure 8–2. Phase diagram of morphologies observed in the imidazolium-based alkyl-ionic copolymer melt system including lamellae (Lam), hexagonally packed cylinders (Hex), coexisting Lam and Hex, spheres on a body-centered cubic lattice (S_{BCC}), and a liquid-like packing (LLP) of spheres. Solid symbols represent regions of well-defined ordered structures, observed by multiple resolved SAXS diffraction reflections, semi-filled and open circles represent regions of poorly-ordered structures, evident by broad peaks in SAXS, and cross symbols depict the disordered region.

been designated using open symbols. Highly ordered morphologies assigned from multiple higher reflections in the SAXS data have been designated using solid symbols. While only one sample in the very asymmetric region ($f_{\text{DOD}} = 0.96$) clearly disordered in an experimentally accessible temperature range, disordered sample locations are designated with a simple cross. In many of the BCP samples, there was a sufficient delay upon heating before obtaining highly ordered structures, defined here as scattering patterns with multiple well-resolved reflections. Upon further cooling or reheating, the high level of order established during initial heating was retained, with no reversion to the initial weakly ordered state. This behavior was also reflected in the rheological response of the materials, in which subtle transitions in moduli detected during the initial heating ramp were consistent with the evolution of a highly ordered state. In these cases, subsequent cooling and heating ramps were nearly identical, absent of the “ordering” transitions observed on first heating, and with little hysteresis over the range of temperatures studied (27–200 °C). However, because of the apparent importance of the thermal processing history on the degree of order in these samples, we have chosen to indicate the region of slow ordering kinetics on the phase diagram, directly. The temperature ranges over which weakly ordered samples were initially observed (as assigned from broad reflections observed in the SAXS patterns) are represented by semi-filled symbols. The transition from semi-filled to solid symbols at a particular volume fraction is indicative of the location at which the high degree of order finally develops in each particular sample. Again, the high degree of order developed above this transition point is retained upon subsequent cooling of the sample. The dependence of the sample order on the thermal history is thus signified by the semi-filled symbols.

Across the 16 samples studied, three of the four classically observed equilibrium diblock morphologies were identified including lamellae (Lam), hexagonally packed cylinders (Hex), and spheres on a body-centered cubic lattice (S_{BCC}). The bicontinuous gyroid phase was not detected; instead, a metastable coexistence of lamellae and hexagonally packed cylinders was found to occupy volume fractions within the traditional gyroid boundaries. In addition, we observed at least one sample (**1B**) in which a LLP of spheres was persistent, and failed to develop

into an ordered BCC lattice over the temperature range studied. Thermodynamic order-to-order transitions between phases (OOT) were not observed directly in rheological time scales for any of the BCPs studied, although in at least one sample showing phase coexistence, very slow (months) transition kinetics favoring one phase over the other (Hex over Lam in **1G**) appeared to be present.

In the following sections, we present and discuss a subset of the characterization data collected for samples **1A–P** in order to generate the phase diagram in Figure 8–2. For the interested reader we have included complete rheological temperature ramp data along with the complete SAXS analysis (heating and cooling up to 200 °C with data collected every 25 °C) for *all* BCPs studied in this report within the Supporting Information. It is also worth noting that direct imaging of these samples using AFM and TEM were unsuccessful due to the inherent stickiness of the BCP samples. In general, direct imaging is advantageous for characterization of morphology when assignment through SAXS is ambiguous, which fortunately is not the case with regard to these samples. As such, the absence of characterization by direct imaging, while unfortunate, does not affect our conclusions about the phase behavior of this BCP system.

8.3.2 Lamellae

Samples exhibiting lamellar morphologies include BCPs **1J–P** which represents a composition range of 42–62 vol % DOD. Dynamic rheological temperature ramp data collected for samples **1J–P** are presented in Figure 8–3. Each of these samples shows elastic and loss response behavior prototypical of lamellar BCP phases, with G' and G'' values that remain similar in magnitude and parallel, with a steady decrease in both moduli upon heating.^{44,52} In the melt, each displayed numerous higher ordered SAXS diffraction reflections at q/q^* ratios of $\sqrt{1}$, $\sqrt{4}$, $\sqrt{9}$, $\sqrt{16}$, $\sqrt{25}$, $\sqrt{36}$, etc. (where q^* is the position of the primary scattering wave vector, Lam = q_{100}), consistent with the allowed reflection conditions for layered periodic symmetry (Figure 8–3). Domain spacings (d_{100}) for samples, **1P**, **1N**, **1L**, and **1J**, each with approximately 50 total norbornene repeat units (M_n values of centered around 20 000 g mol⁻¹), were all nearly identical with a mean

value of 26.5 ± 2.6 nm (at 125 °C). The shorter lamellae forming samples, including **1K** ($M_n = 16\,100$ g mol⁻¹), **1O** ($M_n = 10\,200$ g mol⁻¹), and **1M** ($M_n = 5000$ g mol⁻¹) had interplanar domain spacings of 22.5, 16.6, and 13.1 nm at 125 °C, respectively. Notably, the domain spacings were found to be considerably larger (~30%) than that expected for lamellae formed in typical BCPs such as PS–PVP of comparable molecular weights.^{44, 53} The increase is likely attributable to chain stiffness associated with the inherent bulkiness of the imidazolium and dodecyl ester substituents compressed along the polynorbornene backbone, in combination with the strong chemical dissimilarity (large χ parameter) between the two blocks. Both attributions would favor a strong degree of segregation and associated larger domain spacings.⁵⁴ The variations in the relative intensities of the observed SAXS reflections are consistent with changes in chemical composition, as the relative ratio of domain thicknesses comprising the lamellar period directly affects the net product of the form and structure factor contributions to the scattered signal. The suppression of the even-order reflections at q/q^* ratios of $\sqrt{4}$, $\sqrt{16}$, and $\sqrt{36}$ in samples **1O**, **1N**, and **1M** suggest an almost perfectly symmetric volume fraction of 0.5, where the near-zero minima in the particle form factor coincide with the even-order diffraction positions produced by the lamellar structure, such that reflections at these positions are effectively extinguished in the final scattering product.^{44, 55, 56}

Generally speaking, the relative block volume fraction of a BCP is estimated using known homopolymer densities at an arbitrarily selected temperature, usually constrained by the availability of tabulated data⁵⁷ for the polymers comprising the BCP. The use of a fixed temperature density data is typically justified recognizing that, although the densities themselves can be temperature dependent, the *ratio* of densities, which sets the volume fraction, is much less sensitive to changes in temperature. Unfortunately, due to the lack of available data tabulating the imidazolium and norbornene dodecyl ester functional polymers densities, we were unable to estimate the volume fraction of the DOD–IMD BCPs via this method. However, the noted absence of even-order diffraction reflections in several of the lamellae forming BCP samples provided a unique opportunity to independently establish the relative ratio of densities for the

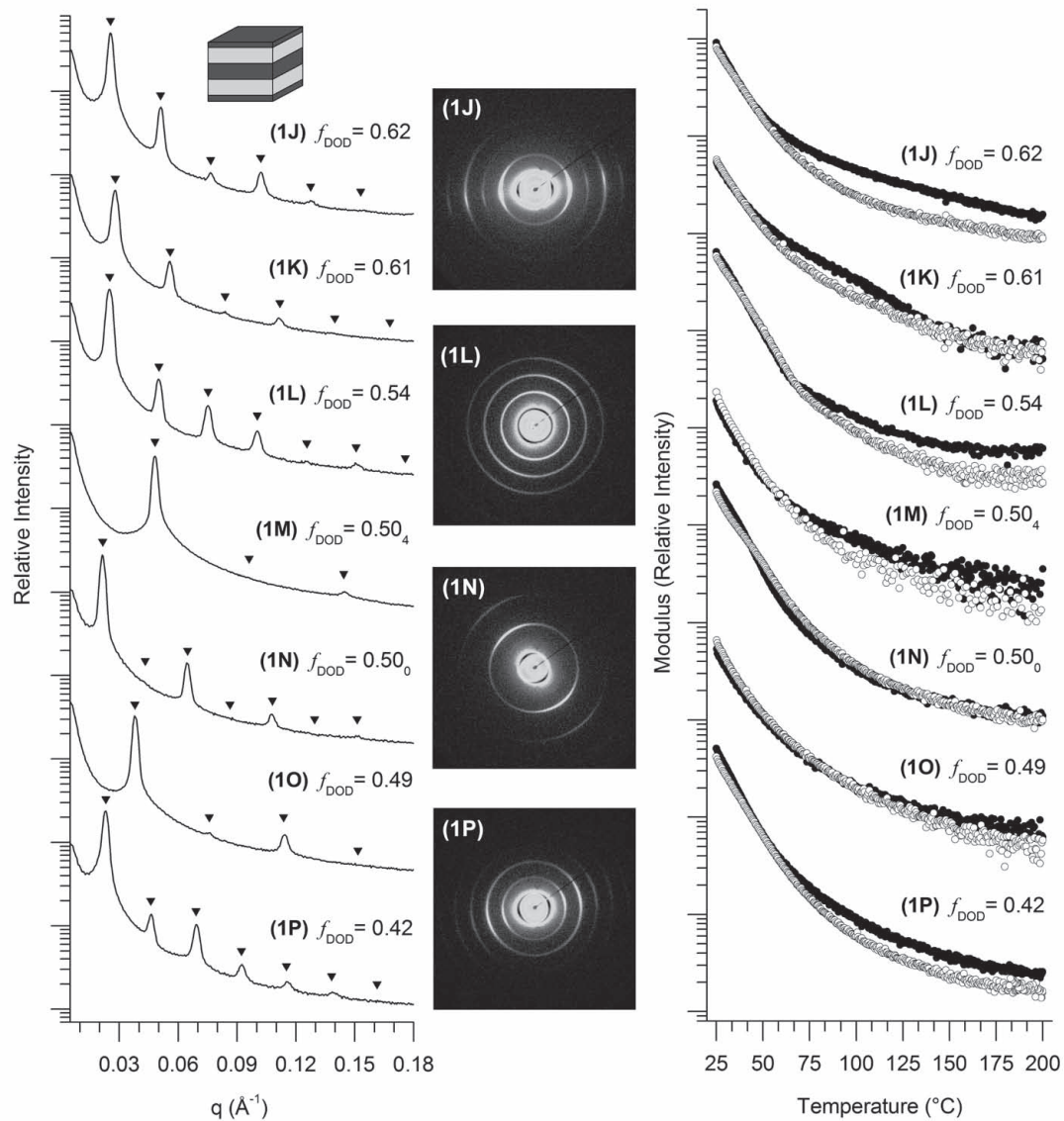


Figure 8-3. (left) SAXS data at 125 °C (first heating cycle) for Lam forming BCPs **1J–P**. Inverted solid triangles represent the locations of allowed reflections for the Lam morphology, based on the position of the primary scattering wave vector $q^* = q_{100}$: q/q^* at $\sqrt{1}$, $\sqrt{4}$, $\sqrt{9}$, $\sqrt{16}$, $\sqrt{25}$, $\sqrt{36}$, etc. The near complete suppression of even order reflections in samples **1O**, **1N** and **1M** suggest an almost perfect symmetric volume fraction of 0.5.^{55, 56} (center) Samples of 2D scattering patterns. (right) Dynamic temperature ramps (first heating cycle) of BCPs **1J–P** at 1 °C min⁻¹, 1 rad s⁻¹ and with strain values of 2.5–8 % (within the linear viscoelastic regime). Solid and open circles represent G' and G'' , respectively.

two blocks. From this ratio, then, the relative block volume fractions in each of the remaining DOD–IMD BCPs could be assigned. BCP **1N** was selected for its near complete suppression of the even order (q/q^* ratios = $\sqrt{4}$, $\sqrt{16}$, and $\sqrt{36}$) reflections over a large temperature range and the relative volume fraction set to be exactly 0.500. A relative ratio of the block densities was then estimated ($k = \rho_{(\text{IMD})}/\rho_{(\text{DOD})} = 1.17_3$) using this assigned volume fraction in combination with the ^1H NMR calculated molecular weights for the individual blocks. This ratio of densities (k) was then used to determine the relative volume fractions of BCPs **1A–P**. We note that the region of composition space where the even-order reflections are absent in the lamellar forming BCP samples appears to be fairly narrow, based on the reemergence of the even-order reflections in samples **1L** ($f_{\text{DOD}} = 0.54$) and, in particular, **1O** ($f_{\text{DOD}} = 0.49$). Based on this level of sensitivity, the calculated volume fractions are believed to be at least as accurate, if not more accurate, than estimations based on tabulated homopolymer densities at arbitrary temperatures. Reassuringly, the assigned morphologies for all remaining samples fall within ranges of relative volume fractions reported for other experimental BCP systems.^{58, 59}

In an attempt to measure the Flory interaction parameter, χ , for these DOD–IMD BCPs, we synthesized three BCPs with nearly symmetric volume fractions of $f_{\text{DOD}} = 0.5$ but of varied overall molecular weights. These included BCPs **1N**, **1O**, and **1M** with M_n values of 20 000, 10 200, and 5000 g mol^{-1} , respectively (Figure 8–3). We initially targeted two methods generally used to experimentally determine $\chi(T)$ in BCP systems.^{60, 61} The first is to measure the order-to-disorder transition (ODT) temperatures in a series of BCPs, typically using dynamic rheology to quantify the transition temperature.^{62–65} The value of $\chi(T)$ can then be extracted by the use of a theoretically predicted $(\chi N)_{\text{ODT}}$ value at $f_A = f_B = 0.5$, defined by the mean field theory (MF theory) developed by Leibler⁶⁶ or the adjusted fluctuation theory developed by Brazovskii⁶⁷, Fredrickson and Helfand⁶⁸ (BLFH theory). The second method for extracting $\chi(T)$ for BCPs involves collecting SAXS or SANS data for a single molecular weight sample at various temperatures above the T_{ODT} , that is, the correlation hole scattering⁶⁹ of the mixed isotropic disordered melt.^{60, 61, 70} The value of $\chi(T)$ is then extracted from the disordered state structure factor predicted

by MF⁶⁶ or BLFH theory.^{60, 67, 68} Both approaches require BCPs that can become disordered at experimentally accessible temperatures. And while a symmetric BCP is not a necessity in either method, it offers the most accurate calculation as the error associated with composition is minimized by the plateau behavior of the phase diagram at the ODT boundary. Unfortunately, all three BCPs remained ordered up to the experimentally determined limit of 200 °C, which was confirmed through the persistence of intense diffraction over the complete temperature range. The inability to disorder the samples prevented the determination of $\chi(T)$ with either of the aforementioned methods. Notably, the smallest BCP, **1M**, with an average M_n of 5000 g/mol has just 12 total repeat units, suggesting the Flory interaction parameter, χ , is extremely large, forcing even low molecular weight materials into the strongly-segregated regime. An estimation of χ for strongly segregated BCPs systems is possible through a comparison of domain spacings measured via SAXS and those predicted using strong segregation theory by Semenov^{71, 72} which depend on a range of BCP parameters characterizing the balance between interfacial energy (χ) and entropic chain stretching penalties. Unfortunately, the expressions for predicting domain spacing^{71, 72} require statistical segment lengths of each of the blocks in order to calculate χ . To our knowledge, accurate chain dimensions of substituted polynorbornene polymers are absent from the literature, and therefore preclude the estimation of χ via this approach, as well. At the very least, the inability to disorder these materials at such low degrees of polymerization confirms the system is very strongly segregated. As discussed below, this has significant consequences with respect to the ability of the system to adopt balance of curvatures required by more complex morphologies, such as the gyroid network.

8.3.3 Hexagonally Packed Cylinders

This region of phase space is defined by samples **1D**, **1E** and **1F** with a range of composition of 74–81 vol % DOD. SAXS data revealed diffraction reflections consistent with hexagonally packed cylinders at q/q^* ratios of $\sqrt{1}$, $\sqrt{3}$, $\sqrt{4}$, $\sqrt{7}$, $\sqrt{9}$, $\sqrt{12}$, $\sqrt{13}$, etc. (where q^* is the position of the primary scattering wave vector, Hex = q_{100}), consistent with the allowed reflections

conditions for hexagonal symmetry (Figure 8–4). As was discussed for the lamellae forming samples, relative differences in the reflection intensities are a result of changes in the distribution of volume as the relative block composition is changed. The shifting distribution of volume affects the superposition of the form and structure factor scattering contributions, affecting the composite intensity produced from the scattering experiment. Most notably, the near complete suppression of the $\sqrt{4}$ reflection in sample **1F** ($f_{\text{DOD}} = 0.74_6$) is consistent with its predicted extinction at a volume fraction of 0.726^{73,74}, based on coincidence of the cylinder particle form factor minima and the position of the (200) reflections. One can clearly see the trend towards

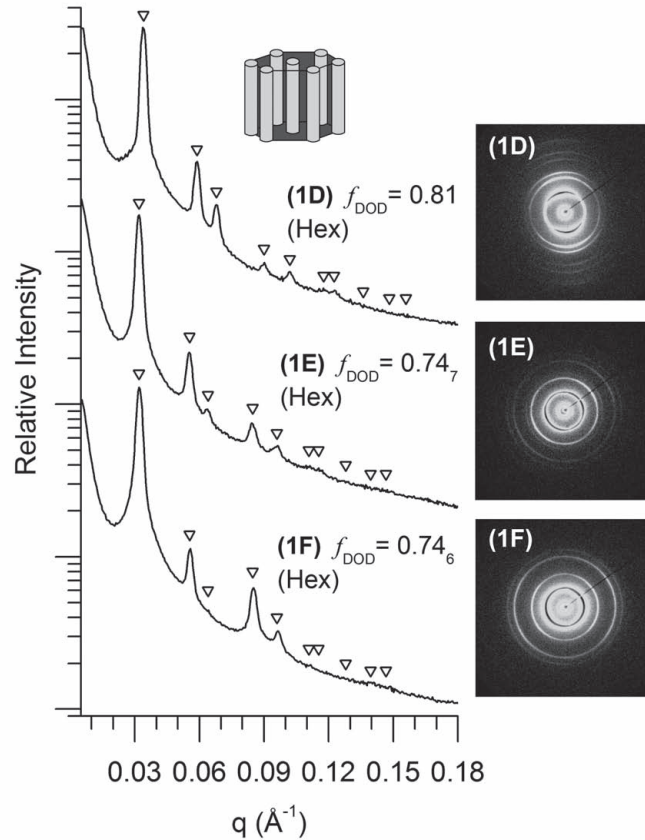


Figure 8–4. SAXS data at 150 °C (upon cooling) for Hex forming BCPs **1D–F**. Inverted open triangles represent the locations of allowed reflections for the Hex morphology, based on the position of the primary scattering wave vector $q^* = q_{100}$; q/q^* at $\sqrt{1}$, $\sqrt{3}$, $\sqrt{4}$, $\sqrt{7}$, $\sqrt{9}$, $\sqrt{12}$, $\sqrt{13}$ etc. Relative intensity differences are consistent with variations in composition, most notably the near complete suppression of the $\sqrt{4}$ reflection in sample **1F**, which is suggestive of approaching a volume fraction of 0.726.^{73,74} Inset pictures are the 2D scattering patterns.

extinction by following the relative intensity changes across the three samples **1D–F** in Figure 8–4. The intercylinder distance ($2d_{100}/\sqrt{3}$) for BCPs **1D–F** is fairly consistent between these three samples based on the consistent overall polynorbornene degree of polymerization of ~ 50 units, having an average spacing of $22.3 \text{ nm} \pm 1.0$ (at $125 \text{ }^\circ\text{C}$). Molecular weights in these samples do shift to smaller values (average M_n of $17\,400 \text{ g mol}^{-1}$) relative to the lamellar samples of similar degree of polymerization just discussed, due to the reduction in the relative number of heavier IMD repeat units found in the BCP.

In contrast to the lamellar forming BCPs, where highly ordered structures are present without any extended thermal processing (see complete thermal SAXS cycles in the supporting information), the hexagonally packed cylinder forming BCPs require an initial heating step to achieve a level of order that produces highly resolved diffraction patterns. As shown in Figure 8–5 for BCP **1D**, there is a sufficient delay in obtaining highly ordered hexagonally packed cylinders during the first heating cycle. The gradual ordering process evident by an evolution of the diffraction pattern from one with broad, poorly defined reflections at room temperature, to one with multiple, easily resolved reflections at $125 \text{ }^\circ\text{C}$ and above. The rheological behavior is also consistent with the observed delay in the ordering process, evident by a decade relaxation in shear moduli starting at $90 \text{ }^\circ\text{C}$ and ending at $130 \text{ }^\circ\text{C}$ in the dynamic temperature ramp experiment (Figure 8–5). These characteristically broad reflections have been observed previously in cylindrical systems^{75, 76}, and have been attributed to scattering off a non-lattice structure comprised of individual cylinders with an underdeveloped, weakly ordered, liquid-like packing (LLP). This behavior is also prevalent in spherical forming BCPs where liquid-like packing often predominates prior to adopting a fully developed S_{BCC} lattice.^{77–79} The initial weakly-ordered structure is presumably an artifact of slow ordering kinetics, and not a true equilibrium phase in the thermodynamic sense. In support of this claim, once the highly ordered structure is established through thermal annealing, the order is preserved during subsequent cooling and heating cycles with no further evidence of any rheological transitions or decay in diffraction intensity which would accompany any return to the weakly-ordered state (Figure 8–5).

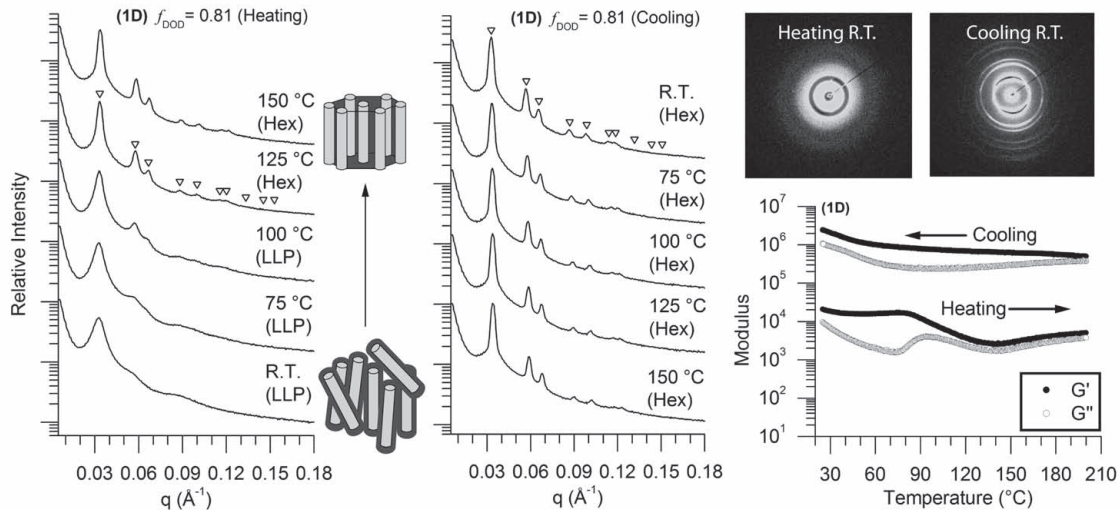


Figure 8-5. SAXS data of sample **1D** along a complete heating (left) and cooling (center) thermal cycle. Morphologies observed during heating include a distorted poorly-ordered LLP of cylindrical domains before obtaining the well-ordered Hex morphology. Upon cooling, the highly ordered Hex phase is preserved. Inverted open triangles represent the locations of allowed reflections for the Hex morphology, based on the position of the primary scattering wave vector $q^* = q_{100}$; q/q^* at $\sqrt{1}$, $\sqrt{3}$, $\sqrt{4}$, $\sqrt{7}$, $\sqrt{9}$, $\sqrt{12}$, $\sqrt{13}$ etc. Dynamic temperature ramp heating and cooling cycle of **1D** (right) at $1\text{ }^\circ\text{C min}^{-1}$, 1 rad s^{-1} and 8 % strain (within the linear viscoelastic regime). The cooling cycle has been shifted vertically two orders of magnitude for clarity. The rheological behavior mimics that of the SAXS, where a subtle transition is observed upon obtaining the well-ordered Hex morphology during heating, while any transitions are notably absent upon cooling. Insets are 2D scattering patterns depicting the initial weakly ordered morphology and final highly ordered morphology after the melt-processing.

8.3.4 Coexistence of Lamellae and Hexagonally Packed Cylinders

Samples **1G-I**, with a range in composition spanning 60–66 vol % DOD, were found to exhibit a persistent coexistence of both lamellae and hexagonally packed cylinders. The SAXS patterns for samples defining this region of phase space (Figure 8-6) contain two sets of reflections at $q/q^{*,lam}$ ratios of $\sqrt{1}$, $\sqrt{4}$, $\sqrt{9}$, $\sqrt{16}$, $\sqrt{25}$, $\sqrt{36}$, etc. and $q/q^{*,hex}$ ratios of $\sqrt{1}$, $\sqrt{3}$, $\sqrt{4}$, $\sqrt{7}$, $\sqrt{9}$, $\sqrt{12}$, $\sqrt{13}$, etc., where $q^{*,lam}$ and $q^{*,hex}$ are slightly shifted in position relative to one another. Importantly, the reflection positions were not consistent with the metastable hexagonally perforated lamellae phase in either the ABAB ($P6_3/mmc$) or ABCABC ($R\bar{3}m$) stacking pattern.⁸⁰⁻⁸³ Notably, the allowed reflections for either of these HPL morphologies are not simple superpositions of

those expected for the Lam and Hex morphologies taken independently, and so a clear distinction between simple coexistence and either of the HPL phases can be conclusively made for strongly diffracting materials. Each of the SAXS patterns for samples **1G–I** have presented in Figure 6 with separate labeling of expected reflection positions for both the Lam and Hex phases. For convenience, the SAXS patterns for single-phase Lam and Hex samples located just outside the coexistence region (**1J** and **1F**, respectively) have also been included in Figure 8–6. A comparison of the relative intensities of the lamellae specific reflections, with those specific to the hexagonal phase, reveals a clear composition dependence across the three samples. More specifically, the relative intensity of a set increase as it approaches the phase boundary with its pure state. We interpret these differences in intensity between the two sets of reflections as a direct indicator of the relative amounts of each phase present. For example, BCP **1I** is the closest to the pure Lam boundary, and has a diffraction pattern in which the lamellar reflections, particularly those at $q/q^{*,lam}$ ratios of $\sqrt{1}$, $\sqrt{4}$, $\sqrt{16}$ dominate the scattering, while the hexagonal reflections are far less pronounced, with only $q/q^{*,hex}$ ratios of $\sqrt{1}$ and $\sqrt{7}$ observed. In contrast, sample **1G**, which is nearest to the Hex phase boundary, has a scattering profile that most closely resembles the Hex phase, with well-resolved reflections at $q/q^{*,hex}$ ratios of $\sqrt{1}$, $\sqrt{3}$, $\sqrt{7}$, and $\sqrt{9}$. Some lamellae character is also present with superimposed reflections at $q/q^{*,lam}$ ratios of $\sqrt{1}$, $\sqrt{4}$, and $\sqrt{16}$, these reflections are far less pronounced compared with the same reflections in samples **1I** and **1H**. In addition, samples **1G** and **1H** exhibited the same delay in ordering kinetics found to exist in the hexagonal phase BCPs **1D–F**, where an initial heating cycle was required to induce high levels of diffraction. This is consistent with the conclusion that samples **1G** and **1H** have a higher content of hexagonally packed cylindrical domains, and share the slower ordering kinetics associated with that phase. On the other hand, Sample **1I**, which is closer to the lamellar boundary, exhibited high levels of lamellar diffraction without any thermal treatment necessary, similar to the pure lamellar BCPs (**1J–P**) discussed earlier. This result is consistent with conclusion sample **1I** is enriched in lamellae and contains far fewer hexagonally packed cylinder domains.

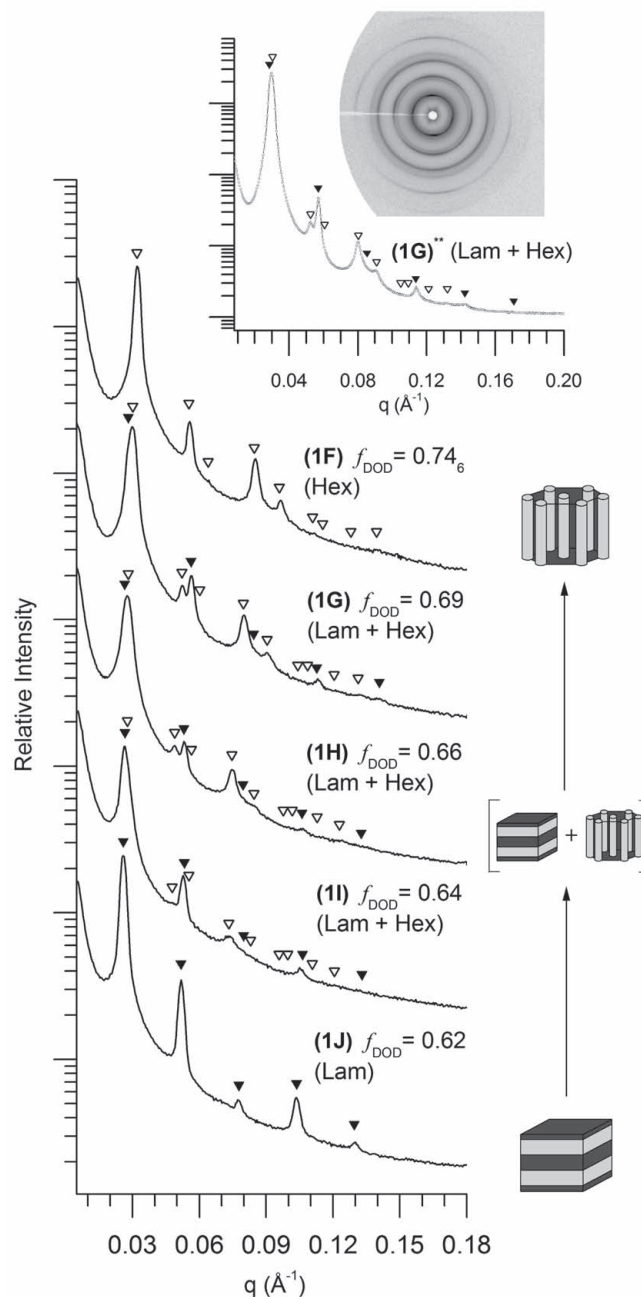


Figure 8-6. SAXS data at 150 °C (upon cooling) for coexisting Lam + Hex forming BCPs **II-G**, plotted with the samples **IJ** and **IF**, that exhibit a fully developed pure Lam and Hex phase, respectively for comparison. Inverted open triangles represent the locations of allowed reflections for the Hex morphology, based on the position of the primary scattering wave vector $q^* = q_{100} : q/q^{*,hex}$ at $\sqrt{1}, \sqrt{3}, \sqrt{4}, \sqrt{7}, \sqrt{9}, \sqrt{12}, \sqrt{13}$ etc, and Inverted solid triangles represent the locations of allowed reflections for the Lam morphology, $q^* = q_{100} : q/q^{*,lam}$ at $\sqrt{1}, \sqrt{4}, \sqrt{9}, \sqrt{16}, \sqrt{25}, \sqrt{36}$, etc. Relative diffraction intensity difference are consistent with variations in composition (relative amounts of coexisting Lam + Hex domains), most notably the scattering profile of **II** most closely resembles that of **IJ** (pure Lam), while **IG** most closely resembles sample **IF** (pure Hex). Inset figure is the high-resolution synchrotron integrated and 2D SAXS data of sample **IG**, donated with asterisks, showing the primary peak could not be resolved.

As shown in the overlaid data markers of Figure 8–6, the assignment of phase coexistence requires $q^{*,lam}$ and $q^{*,hex}$ positions that are in very close proximity to one another, but do not, in fact, coincide. Qualitatively, a comparison of the primary peak widths for samples **1G–I** with the primary peak widths for the adjacent single-phase Hex and Lam samples **1F** and **1J** shows a broadening in the former that suggests the overlap of two primary peaks is plausible. In an effort to resolve these two primary peaks definitively, we collected high resolution synchrotron data for sample **1G**. The scattering data is presented in inset of Figure 8–6. Unfortunately, the proposed Hex and Lam principal reflections could not be resolved, with the synchrotron source providing little improvement over the laboratory grade Rigaku S-Max 3000 used for the initial data collection. Despite our inability to resolve these two peaks, the quality of the peak assignments across the SAXS data from all three samples, combined with the results of additional rheology and annealing experiments (presented below), gives us great confidence in the conclusion of phase coexistence in these samples.

The rheological temperature ramp profiles of samples **1G–I** are presented in Figure 8–7, bracketed again by the corresponding pure Hex and Lam data from adjacent samples **1F** and **1J**. Similar to that found in the SAXS, these samples present rheology profiles that appear intermediate to that typical of the two pure phases, with a consistent shift in character as one traverses across the coexistence region. For example, sample **1I** more closely resembles the rheology profile of the adjacent pure lamellar phase sample, **1J**, having similar magnitudes of G' and G'' with a steady relaxation in both moduli with heating. Likewise, sample **1G** more closely resembles the rheology profile of the adjacent pure hexagonal phase sample, **1F**, where there is only a slight decrease in G' and slight recovery of G'' with heating. While the determination of actual phase coexistence by rheology is not particularly warranted, the data is at least consistent with the more convincing SAXS data for these samples. Notably, however, in contrast to the rheology of Hex samples **1D–F** where subtle rheological transitions could be observed for the delay in ordering kinetics, no such transitions were observed for samples in the coexistence region. This, despite the kinetic delay in ordering clearly demonstrated in the SAXS data for two

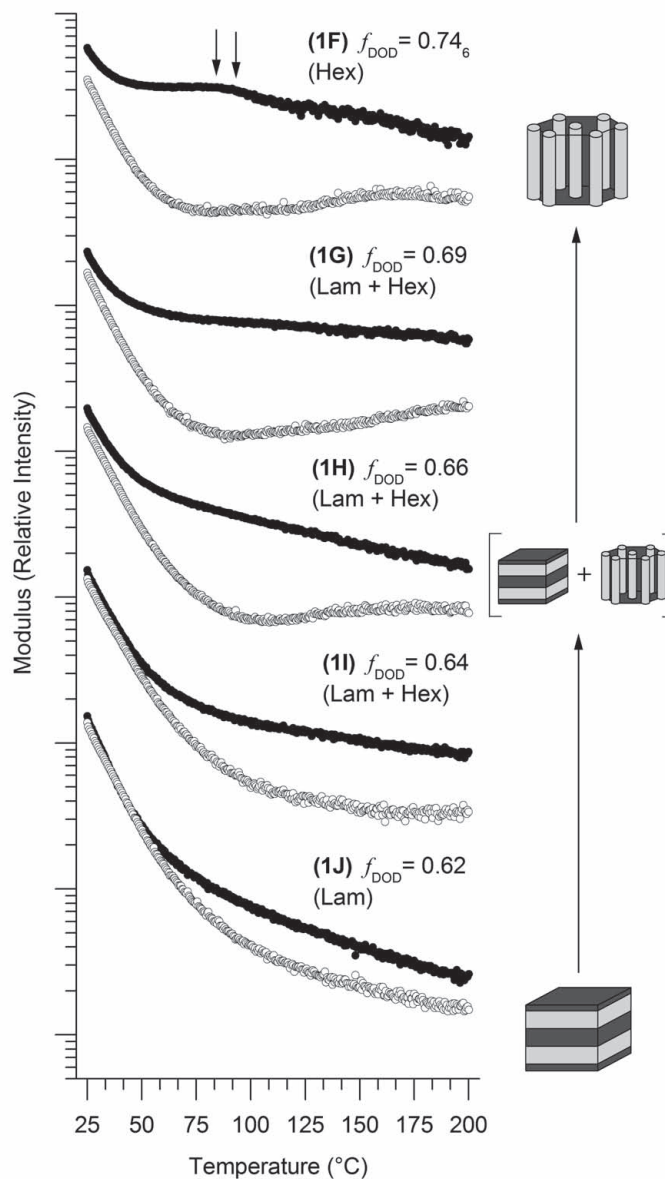


Figure 8-7. Dynamic temperature ramps (first heating cycle) at $1\text{ }^{\circ}\text{C min}^{-1}$, 1 rad s^{-1} and with strain values of 6–8 % (within the linear viscoelastic regime), for coexisting Lam + Hex forming BCPs **II–G**, plotted with the samples **IJ** and **IF** that exhibit a fully developed pure Lam and Hex phase, respectively for comparison. Solid circles represent G' and open circles represent G'' . Differences in rheological response is consistent with variations in composition (relative amounts of coexisting Lam + Hex domains), most notably the temp ramp profile of **II** most closely resembles that of **IJ** (pure Lam), while **IG** most closely resembles the profile of sample **IF** (pure Hex).

of the samples (**1H** and **1G**). We note that while the temperature ramp profiles used by rheology (continuous) and SAXS (stepped) were fundamentally different, both ramp rates produced an average heating rate of approximately 1 °C/min.

Theoretically, the composition region located between lamellae and hexagonally packed cylinders should be occupied, at equilibrium, by the bicontinuous gyroid phase.^{29,30,84,85} However, in many experimental systems, the gyroid network is often displaced by alternate morphologies, such as the near free energy equivalent, but metastable HPL phase^{84, 86, 87}, or a coexistence of Lam and Hex phases like that observed here.^{21, 50, 73, 76, 88-93} Typically, such metastable phases or phase coexistence are generated as a byproduct of post-synthesis, non-equilibrium solvent removal,^{73,76,89} and have been shown in several cases to eventually adopt the equilibrium gyroid morphology with extended annealing.^{88,92} However, recent theoretical efforts⁹⁴ have shown that high levels of polydispersity can give rise to thermodynamically favored phase coexistence. Such polydispersity-driven phase coexistence has now been suspected in a number of recently studied experimental systems.⁹⁵⁻⁹⁸ Given the limited knowledge of the overall polydispersity in our samples, both solvent-induced (non-equilibrium) and polydispersity-driven (equilibrium) coexistence stand as possible explanations for the coexistence region.

In an attempt to shed light on the true nature and stability of the observed phase coexistence, sample **1G** was annealed (under vacuum) at 150 °C for a total of two months. As shown in Figure 8, the relative intensities of Hex and Lam reflection sets change quite dramatically. In the initial scattering collected after only 5 minutes annealing, the primary scattering peak is fairly broad with strong reflections at $q/q^{*,lam}$ ratios of $\sqrt{1}$, $\sqrt{4}$, and $\sqrt{16}$, and $q/q^{*,hex}$ ratios of $\sqrt{1}$, $\sqrt{3}$, $\sqrt{7}$, and $\sqrt{9}$, indicating the presence of both phases in relatively significant quantities. After 10 days of annealing, the primary scattering peak has begun to sharpen, with hexagonal phase reflections increasing in magnitude and becoming more easily resolved. In contrast, the lamellae scattering intensity has begun to decrease, revealing the sample composition shift towards the hexagonal phase. Most notably, the lamellae diffraction peak at $q/q^{*,lam} = \sqrt{4}$ changes from being more intense than the hexagonal diffraction peak at $q/q^{*,hex} = \sqrt{3}$, to being nearly equal. At two

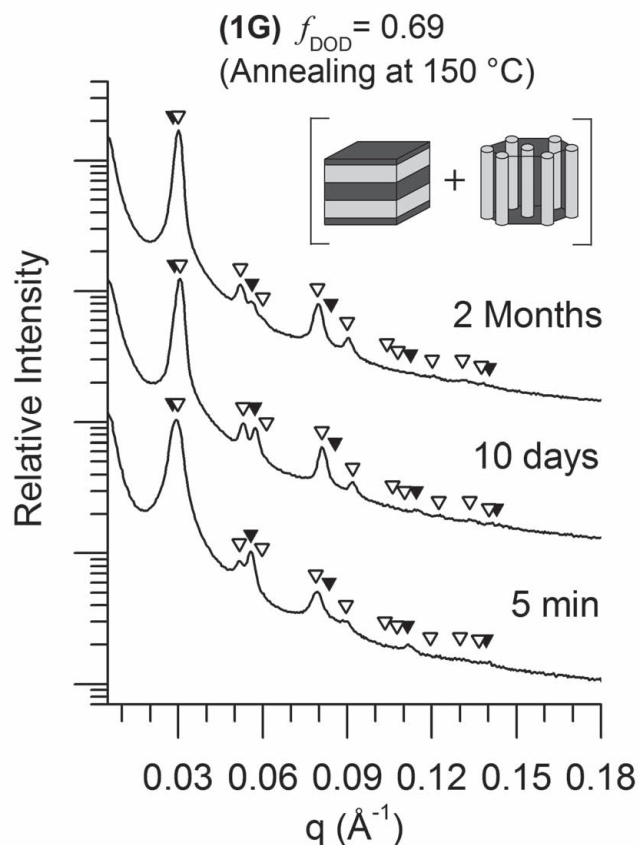


Figure 8–8. SAXS data of sample **1G** annealing at 150 °C for a total of 2 months, depicting the very slow ordering kinetics that suppresses the Lam phase and transitions towards a pure Hex phase which is evident by the increased intensity of Hex reflections coupled with the substantial decrease in Lam reflection intensity with time. Inverted open triangles represent the locations of allowed reflections for the Hex morphology, based on the position of the primary scattering wave vector $q^* = q_{100}$: $q/q^{*,\text{hex}}$ at $\sqrt{1}$, $\sqrt{3}$, $\sqrt{4}$, $\sqrt{7}$, $\sqrt{9}$, $\sqrt{12}$, $\sqrt{13}$ etc, and Inverted solid triangles represent the locations of allowed reflections for the Lam morphology, $q^* = q_{100}$: $q/q^{*,\text{lam}}$ at $\sqrt{1}$, $\sqrt{4}$, $\sqrt{9}$, $\sqrt{16}$, $\sqrt{25}$, $\sqrt{36}$, etc.

months the Lam character has decreased further, with the lamellae diffraction peak at $q/q^{*,\text{lam}} = \sqrt{4}$ now much less intense compared to the hexagonal diffraction peak at $q/q^{*,\text{hex}} = \sqrt{3}$, and the lamellae diffraction peak at $q/q^{*,\text{lam}} = \sqrt{16}$ now completely absent. In addition, the primary peak continues to sharpen, and the hexagonal diffraction peak at $q/q^{*,\text{hex}} = \sqrt{4}$ has become more pronounced. The sharpening of the primary peak throughout the annealing process is assumed to be a consequence of the decreasing contribution by $q^{*,\text{lam}}$. From this data, it is clear that the sample is evolving towards a higher concentration of the hexagonal phase. However, the two month experiment does not provide sufficient evidence to determine whether a new (equi-

librium), Hex-rich distribution of Hex and Lam is simply being established, or the sample is evolving exclusively towards the Hex phase as its equilibrium morphology. It appears, at least, that the initial concentration of Lam and Hex phases is likely influenced by rapid removal of CH_2Cl_2 during the synthetic workup, and the sample thermodynamically prefers larger concentrations of the hexagonal phase. Clearly, however, the phase coexistence is quite persistent in these DOD-IMD BCPs, and cannot be easily displaced even if it is a non-equilibrium state.

Importantly, no evidence of any evolution towards the gyroid phase was found in sample **1G** after the two month annealing experiment. Persistent Hex and Lam phase coexistence in the gyroid region has been reported for a number of experimental diblock copolymer systems.^{21, 88, 92} The majority of incidences are associated with BCPs that, due to high degrees of polymerization, or high values of χ , are inherently strongly segregated in the phase-separated state. Not coincidentally, the gyroid phase boundaries were originally suspected to converge upon reaching the intermediate segregation regime^{84, 99}, which appeared to be supported by experimental results. However it has been more recently shown by Cochran et. al¹⁰⁰ that the gyroid phase window actually extends deep into the intermediate to strong segregation regime, albeit over a very narrow composition window. These new results seem to bolster an earlier report by Lodge and coworkers,⁷² in which they had conclusively identified the existence of the gyroid phase in strongly segregated polybutadiene-poly(hexafluoropropylene oxide) BCPs. However, that report appears to be the exception, not the rule, for most highly segregated systems studied thus far. Of particular relevance in that list are the very recent studies by Mahanthappa²¹ on BCPs containing charged imidazolium based IL derivatives of polystyrene, where they found persistent Hex and Lam coexistence at the apparent expense of the gyroid morphology. Somewhat related, Lodge and coworkers⁹¹ also just reported Hex and Lam coexistence in solutions of uncharged BCPs dissolved in charged ionic liquid solvents. The persistence of Hex and Lam coexistence in samples **1G-I**, considered with the coexistence behavior documented in these other ionic BCP systems^{21, 91} suggests that strong degree of segregation imposed by the charged-uncharged architecture severely hinders gyroid formation. The significant penalties for

mixing, and therefore chain rearrangement, effectively create a large activation energy for the transformation of the Hex/Lam mixture to the gyroid phase.¹⁰¹ This is, of course, compounded by the (predicted) narrowness of the gyroid phase window in the strong segregation regime.¹⁰⁰ Access to the gyroid morphology may require highly controlled synthetic methodologies able to pinpoint compositions precisely, as well as extensive combinations of solvent, thermal and mechanical annealing treatments to facilitate its formation from non-equilibrium starting positions. Applications targeting cocontinuous networks such as the gyroid phase in imidazolium poly(IL) containing diblock copolymers may ultimately prove impractical.

8.3.5 Spherical

This region of the phase diagram is defined by the most asymmetric samples **1A–C** with a composition range of 84–96 vol % DOD. Samples **1A** and **1B** both exhibited scattering characterized by broad, subtle oscillations typical of form factor scattering from individual spheres. The absence of clear diffraction peaks other than the primary reflection (Figure 8–9) is consistent with a poorly ordered liquid-like packing (LLP) commonly observed at such asymmetric BCP compositions. The absence of an organized lattice is typically attributed to sphere polydispersity associated with limited chain diffusion and mobility.^{102–107} Rheological temperature ramp tests of samples **1A** and **1B** show viscoelastic properties indicative of enhanced liquid-like behavior, characterized by a loss modulus (G'') exceeding the storage modulus (G') throughout the temperature ramp profile. There is no evidence of a sharp decrease in moduli characteristic of a traditional order-to-disorder (ODT) transition; in contrast, both samples **1A** and **1B** show a steady decrease in moduli with heating. The noise in the rheology profiles of samples **1A** and **1B** at higher temperatures is an artifact of torque resolution limits associated with the rheology instrumentation using the 8 mm, parallel plate configuration. Use of larger diameter plates to improve the signal-to-noise ratio was constrained by limited material availability. As an alternative, the presence of an ODT in samples **1A** and **1B** was probed by looking for a clear transition to correlation hole scattering^{52, 69} using temperature dependent SAXS. This transition, marked

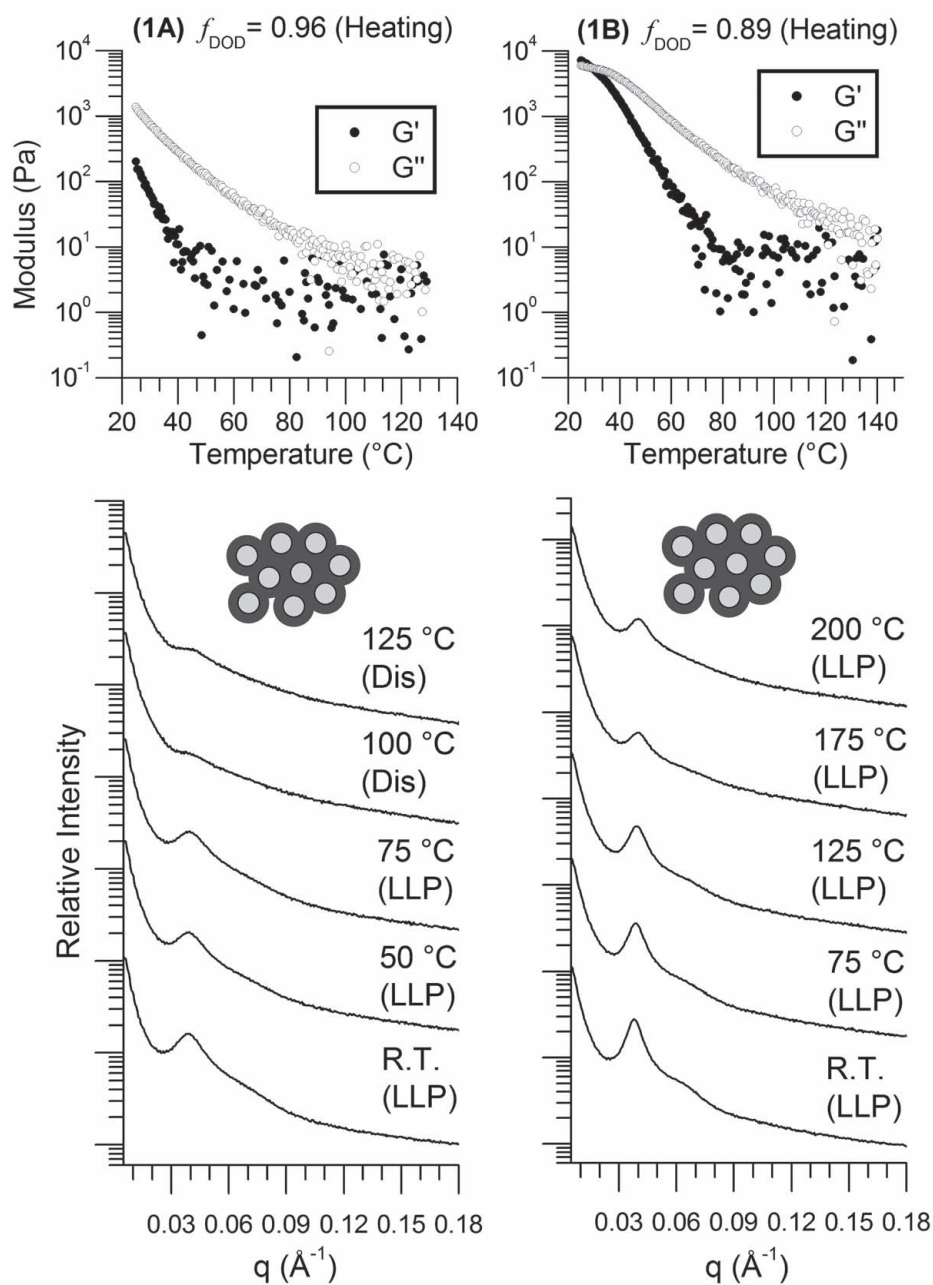


Figure 8-9. Dynamic temperature ramp (first heating cycle) for samples **1A** (left) and **1B** (right) at $1\text{ }^{\circ}\text{C min}^{-1}$, 1 rad s^{-1} with 30 and 8 % strain, respectively (within the linear viscoelastic regime). The rheological behavior of both samples is characteristic of enhanced liquid-like properties where G'' is greater than G' . No clear ODT is observed via rheology in either sample. SAXS data of sample **1A** (left) and **1B** (right) along a complete heating thermal cycle are both indicative of a LLP of spheres, evident by broadness of scattering and absence of higher order diffraction reflections. Sample **1A** appears to clearly disorder upon heating marked by the drastic decrease in intensity and enhanced broadness of the scattering. In contrast, sample **1B** retains a fairly intense primary scattering peak throughout the entire heating cycle.

by increased broadness in the primary peak location, and a sharp decrease in intensity as the BCP becomes a homogenous isotropic liquid, can be difficult to identify in the absence of a strongly diffracting ordered phase. For sample **1A**, there appears to be a significant change in the SAXS profile upon heating past 75 °C, where the intensity of the scattering is severely reduced and the second oscillation in the particle form factor becomes indistinguishable from the broad primary peak. Evidence of disordering was even more ambiguous in sample **1B**, where around 175 °C there is a twofold decrease in scattering intensity, but the primary scattering reflection seems to maintain some degree of sharpness. We suspect that sample **1B** may be exhibiting a persistence of disordered spherical micelles¹⁰⁵ across a large temperature range due in part to the very strong segregation of the DOD and IMD blocks. Due to the ambiguity of order in both samples **1A** and **1B**, coupled with the extreme asymmetry in composition, no efforts were made to extract $\chi(T)$ from the scattering data for these samples (as previously discussed).

Highly ordered spheres on a body-centered cubic lattice (S_{BCC}) were observed in sample **1C** with a volume fraction of 0.84 DOD. SAXS data are plotted in Figure 8–10 for sample **1C** and show diffraction peaks consistent with the symmetry of the S_{BCC} lattice with q/q^* ratios of $\sqrt{2}$, $\sqrt{4}$, $\sqrt{6}$, $\sqrt{8}$, $\sqrt{10}$, $\sqrt{12}$, $\sqrt{14}$, etc. Here, $q^* = q_{100}$ which is absent due to the reflection conditions associated with the BCC symmetry. The q_{110} interplanar spacing at 125 °C is 16.4 nm. Similar to the Hex forming BCPs, sample **1C** required an initial heating step to achieve a level of order that produces highly resolved S_{BCC} diffraction patterns. As shown in the SAXS data of Figure 10, there is a sufficient delay in obtaining highly ordered BCC spheres in the first heating cycle. The gradual ordering process, evident by an evolution of the diffraction pattern from one with broad, form factor oscillations at room temperature, to one with multiple, easily resolved diffraction peaks at 100 °C and above. The rheological behavior is also consistent with the observed delay in the ordering process, evident by clear transition at 100 °C in the dynamic temperature ramp experiment (also Figure 8–10). As mentioned previously, this type of behavior in which liquid-like packing of spheres often exists prior to development of the fully organized S_{BCC} lattice is fairly common in other BCP systems.⁷⁷⁻⁷⁹ As with the Hex forming samples, the highly ordered

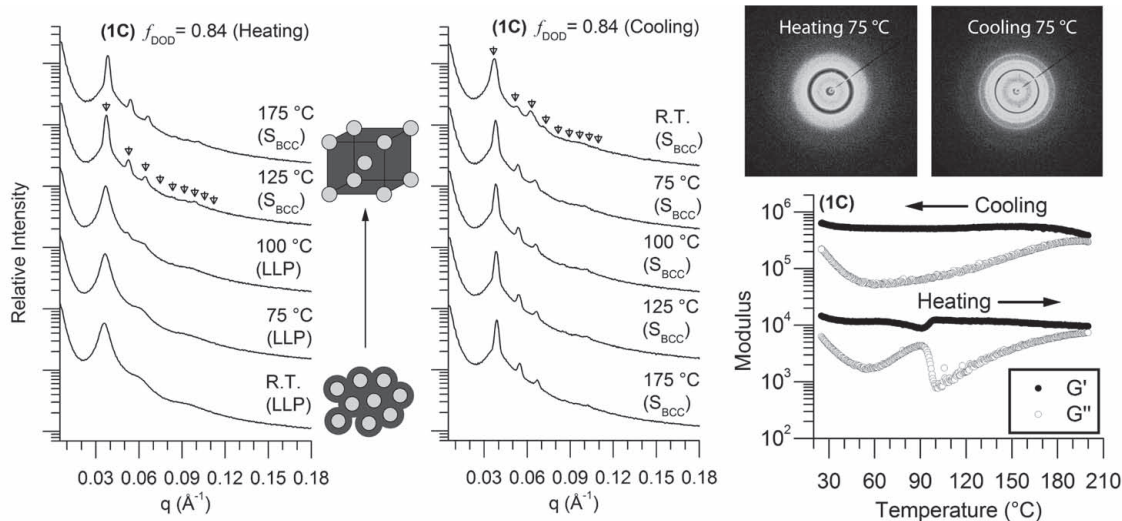


Figure 8–10. SAXS data of sample **1C** along a complete heating (left) and cooling (center) thermal cycle. Morphologies observed during heating include a distorted poorly-ordered LLP of spherical domains before obtaining the well-ordered S_{BCC} morphology. Upon cooling, the highly ordered S_{BCC} phase is preserved. Inverted triangles with a strikethrough represent the locations of allowed reflections for the S_{BCC} morphology, based on the position of the primary scattering wave vector $q^* = q_{100}$ (absent for S_{BCC}): q/q^* at $\sqrt{2}$, $\sqrt{4}$, $\sqrt{6}$, $\sqrt{8}$, $\sqrt{10}$, $\sqrt{12}$, $\sqrt{14}$ etc. Dynamic temperature ramp heating and cooling cycle of **1C** (right) at $1\text{ }^\circ\text{C min}^{-1}$, 1 rad s^{-1} and 8 % strain (within the linear viscoelastic regime). The cooling cycle has been shifted vertically two orders of magnitude for clarity. The rheological behavior mimics that of the SAXS, where a subtle transition is observed upon obtaining the well-ordered S_{BCC} morphology during heating, while any transitions are notably absent upon cooling. Insets are 2D scattering patterns depicting the initial weakly ordered morphology and final highly ordered morphology after the melt-processing.

structure established during the initial heating remains preserved during subsequent cooling and heating cycles, with no further evidence of any rheological transitions or decay in diffraction intensity signaling a return to the weakly-ordered state (Figure 8–10).

8.4 CONCLUSIONS

A total of 16 DOD–IMD BCPs spanning compositions of 42–96 vol % DOD were extensively characterized using SAXS and rheology to develop a clear picture of the morphological phase behavior in these novel poly(IL)-based BCP systems. The unique charged-uncharged BCP architecture produced each of the classic equilibrium morphologies (including lamellae (Lam), hexagonally packed cylinders (Hex), and spheres on a body-centered cubic lattice (S_{BCC}) with

the exception of the bicontinuous gyroid phase. In general, the level of order achieved by the samples was exceptional, routinely producing diffraction patterns with numerous higher order reflections. Hex and S_{BCC} forming DOD-IMD BCPs were found to require an initial heating step to induce highly periodic lattice formation, but showed no signs of structure degradation during subsequent cooling and heating cycles. Lam samples showed no kinetic delay in ordering. Importantly, all samples (outside of the two most asymmetric) showed excellent preservation of structural order at room temperature, which is extremely important for the future preparation of functional materials built from these poly(IL)-based BCPs. Additional morphologies identified include a coexistence of Hex and Lam phases in three samples occupying the traditional gyroid region, and a poorly-defined liquid-like packing of spheres in the two most asymmetric samples. Annealing experiments on one of the three samples exhibiting Hex and Lam phase coexistence revealed extremely slow transition kinetics favoring increased Hex phase concentrations. Complete elimination of the coexisting Lam phase was not possible over a two-month annealing period. Likewise, no evidence of gyroid formation was detected in the coexistence region, or any other sample investigated. Ultimately, the strong degree of segregation inherent to the charged-uncharged architecture may limit the ability of the system to form the idealized gyroid network often sought for transport related applications. Additional experiments involving advanced solvent, thermal, and mechanical annealing combinations may be necessary to achieve its formation. The inherent segregation strength also resulted in difficulties accessing order-to-disorder transitions, and therefore complicated the measurement of a Flory interaction parameter, χ for the system. Failure to disorder even the lowest molecular weight symmetric sample with degree of polymerization of approximately 12 confirmed that accessible phase behavior for these BCPs is likely constrained to that of the strongly-segregated regime. Application of these DOD-IMD BCPs as membranes in CO_2 /light gas separations is currently underway.

8.5 EXPERIMENTAL

8.5.1 Materials and Methods

1-Bromohexane, 1-dodecanol, 5-norbornene-2-carboxylic acid, ethyl vinyl ether, and oxalyl dichloride (Sigma-Aldrich), dicyclopentadiene, 1-vinylimidazole (TCI America), were used as received without further purification. Lithium bis(trifluoromethylsulfonyl)amide (LiTf_2N) was purchased as Fluorad™ Lithium Trifluoromethane Sulfonimide from the 3M company. All solvents were purchased from Sigma-Aldrich or Mallinckrodt, Inc., and purified/dehydrated via N_2 -pressurized activated alumina columns, and subsequently de-gassed. Additionally, the CH_2Cl_2 used as the solvent in ring-opening metathesis polymerization (ROMP) reactions was purified by re-filtering over activated alumina prior to de-gassing. H_2O used for synthesis was purified and de-ionized, with resistivity greater than $12 \text{ M}\Omega \text{ cm}^{-1}$. All chemical syntheses were carried out in a dry argon atmosphere using standard Schlenk line techniques, unless otherwise noted. Silica gel purification was performed using 230–400 mesh, normal-phase silica gel purchased from Sorbent Technologies.

8.5.2 General Synthetic Procedures for the synthesis of imidazolium-based poly(alkyl)-Ionic BCPs

Bicyclo[2.2.1]hept-5-ene-2-carboxylic acid dodecyl ester (endo:exo 80:20) (Monomer 2) and 3-Bicyclo[2.2.1]hept-5-en-2-ylmethyl-1-hexyl-3H-imidazolium bis(trifluoromethylsulfonyl)amide (endo:exo 80:20) (Monomer 3), were prepared as previously described in the literature and found to have consistent spectroscopic and purity analysis.⁴⁴ In a procedure adapted from Wiesenauer et al.⁴⁴, a flame-dried Schlenk flask with a Teflon spinbar was charged with the desired amount of Grubbs 1st-generation catalyst CH_2Cl_2 solution under a positive pressure of argon. Monomer 2 was then added to the catalyst solution from a dry degassed CH_2Cl_2 stock solution via syringe under argon atmosphere. Upon complete consumption of monomer 2 (as verified by ^1H NMR analysis) to form the first copolymer block, the second monomer 3 was added from a dry, degassed stock CH_2Cl_2 solution via syringe. After complete consumption of monomer 3 (as verified by ^1H NMR analysis), the ROMP diblock copolymerization mixture

was quenched with an excess of ethyl vinyl ether. The resulting diblock copolymer was then isolated by removal of the solvent in vacuo (48 h, 25 °C). ¹H NMR analysis of BCPs **1A–P** also confirmed the absence of any residual monomer. The alkyl:imidazolium block fractions were determined by relative integrations of the ¹H NMR signals of each block. The number of repeat units of the dodecyl and imidazolium blocks were calculated based on the predetermined catalyst-to-monomer loading ratios assuming complete conversion of monomers 2 and 3, evident by the absence of monomer in ¹H NMR and living character determined in our previous report.⁴⁴ Lastly, the M_n values are estimated by multiplying the block lengths by the corresponding monomer repeat unit molecular weight values.⁴⁴

8.5.3 Representative Synthesis of Diblock Copolymer **1P**

Under an argon atmosphere, Grubbs' 1st-generation catalyst (16.4 mg, 0.0199 mmol) was dissolved in dry, degassed CH₂Cl₂ (0.75 mL). Monomer 2 (7.65 g, 24.9 mmol) was diluted to a total volume of 25 mL with CH₂Cl₂. From this monomer solution, 0.49 mL (0.49 mmol) was added to the catalyst solution, and the reaction mixture was stirred at room temperature until the polymerization of 2 was complete (~3 h). Monomer 3 (13.5 g, 25.1 mmol) was diluted to a total volume of 25 mL with CH₂Cl₂. Monomer 3 (0.49 mL, 0.49 mmol) was then added to the living ROMP polymerization mixture containing polymerized 2, and the reaction stirred at room temperature for 12 h. The ROMP copolymerization mixture was then quenched by addition of excess ethyl vinyl ether (1 mL). The resulting diblock copolymer **1P** was isolated by removal of excess solvent and other volatile compounds in vacuo (48 h, 25 °C). Yield = 0.435 g, 99%. ¹H NMR (300 MHz, CDCl₃) δ: 8.50–8.75 (br s, imidazolium C2), 7.27–7.47 (br s, imidazolium C4 and C5), 5.27–5.52 (b, –C(H)=C(H)–), 3.75–4.45 (b, –COO–CH₂–, –C(H)₂–N–CH–N–C(H)₂–(CH₂)₄CH₃), 2.35–3.15 (br m, –imidazolium–(CH₂)₅–CH₃), 1.50–2.25 (b, –COO–(CH₂)₁₁–CH₃), 0.95–1.45 (br m, –COO–CH₂–(CH₂)₁₀–CH₃), 0.72–0.90 (br m, –imidazolium–CH₂–(CH₂)₄–CH₃). Block repeat unit molar ratio = 1:0.90 (alkyl:imidazolium); block length composition = 25–b–23; estimated M_n = 20 100 g mol⁻¹.

8.5.4 Physical Measurements

^1H and ^{13}C NMR spectra were obtained using a Bruker 300 Ultrashield™ (300 MHz for ^1H) spectrometer. Chemical shifts are reported in ppm relative to residual protio solvent, CHCl_3 . Thermogravimetric analysis (TGA) was performed using a Mettler Toledo TGA/DCS 1 series thermal gravimetric analyzer. For TGA, samples were tested from 30–500 °C at a temperature ramp rate of 20 °C min^{-1} in an aluminum pan under N_2 atmosphere.

8.5.5 Dynamic Mechanical Spectroscopy

Rheological experiments were run using a TA Instruments Advanced Rheometric Expansion System (ARES) Rheometer outfitted with a nitrogen purged oven. Samples were roughly formed as discs by hand and then positioned between two parallel plates (8 mm diameter). The gap was reduced and adjusted to ensure even distribution of the sample. Typical gaps were 0.3–0.5 mm. Dynamic temperature ramp tests were performed under nitrogen while heating and cooling at 1 °C min^{-1} at an angular frequency of 1 rad s^{-1} and a constant strain (generally 6–8 % for the majority of BCP samples studied herein) depending on the linear viscoelastic regime of each copolymer that provides high enough torque values (> 0.01 g·cm) for acceptable signal-to-noise ratios. Larger parallel plates (> 8 mm) could be used to increase torque (and subsequently increase signal-to-noise), however such measurements were avoided due to the significant amount of material required.

8.5.6 Small Angle X-ray Scattering (SAXS)

Small-angle X-ray scattering (SAXS) data were collected using a Rigaku S-Max 3000 High Brilliance three-pinhole SAXS system outfitted with a MicroMax-007HFM rotating anode ($\text{CuK}\alpha$, $\lambda = 1.54$ Å), sample-to-detector distance of 2.19 m, Confocal Max-Flux Optics, Gabriel multiwire area detector (1024 X 1024 pixel resolution), and a Linkam thermal stage. Copolymer samples were sandwiched between Kapton windows (0.05 mm thick X 10 mm diameter). All samples were annealed under vacuum for at least 5 min before data collection unless otherwise stated.

Data was collected under vacuum (~100 mtorr) with exposure times for samples typically on the order of 1200–1800 s. SAXS data were azimuthally integrated from the 2D detector patterns and plotted as logarithmic intensity vs. the scattering wave vector, q , defined as $q = (4\pi/\lambda) \sin(2\theta_B/2)$, where $2\theta_B$ is the angle between the incident and scattered waves.

8.5.7 Synchrotron SAXS Characterization

Synchrotron small-angle X-ray scattering measurements were performed at the 5-ID-D beamline of the DuPont-Northwestern-DOW Collaborative Access Team (DND-CAT) at the Advanced Photon Source (Argonne, IL). Experiments employed a beam energy of 17 keV ($\lambda = 0.7293 \text{ \AA}$) and a sample-to-detector distance of 2.979 m. Two-dimensional SAXS patterns were recorded on a MAR-CCD detector (133 mm diameter active circular area) with 2048 x 2048 pixel resolution. Samples were heated to the desired temperature in a Linkam DSC and allowed to equilibrate for 5 or 10 minutes prior to data collection with exposure times of 0.1–0.2 s.

8.6 ACKNOWLEDGMENTS

T.S.B., V.F.S, and J.R.E. thank the National Science Foundation (grant DMR-0645781) and the Colorado State University (CSU) for supporting the portion of this work performed at CSU. D.L.G., E.F.W., and J.P.E. thank the Advanced Research Projects Agency – Energy (grant DE-AR0000098) and the Defense Threat Reduction Agency (grant HDTRA1-08-1-0028) for support of the portion of this work performed at CU Boulder. The SAXS instrument at CSU is supported by the Central Instrument Facility of the Chemistry Department and the National Science Foundation MRI Program (grant DMR-0821799). We also gratefully thank Adam K. Schmitt and Prof. Mahesh K. Mahanthappa of the University of Wisconsin-Madison for collection of the synchrotron SAXS data on sample 1G.

8.7 SUPPORTING INFORMATION AVAILABLE

Full temperature dependent SAXS and rheology plots of BCPs **1A–P**. TGA analysis of representative sample **1E** located in Appendix II.

8.8 REFERENCES

1. Green, O.; Grubjesic, S.; Lee, S. W.; Firestone, M. A. *Polym. Rev.* **2009**, *49*, 339-360.
2. Green, M. D.; Long, T. E. *Polym. Rev.* **2009**, *49*, 291-314.
3. Lu, J. M.; Yan, F.; Texter, J. *Prog. Polym. Sci.* **2009**, *34*, 431-448.
4. Anderson, E. B.; Long, T. E. *Polymer* **2010**, *51*, 2447-2454.
5. Jaeger, W.; Bohrisch, J.; Laschewsky, A. *Prog. Polym. Sci.* **2010**, *35*, 511-577.
6. Suzuki, K.; Yamaguchi, M.; Hotta, S.; Tanabe, N.; Yanagida, S. *J. Photochem. Photobiol. A-Chem.* **2004**, *164*, 81-85.
7. Li, F. J.; Cheng, F. Y.; Shi, J. F.; Cai, F. S.; Liang, M.; Chen, J. J. *Power Sources* **2007**, *165*, 911-915.
8. Liang, Z. Y.; Lu, C. X.; Luo, J.; Bin Dong, L. *J. Fluorine Chem.* **2007**, *128*, 608-611.
9. Muldoon, M. J.; Gordon, C. M. *J. Polym. Sci. Pol. Chem.* **2004**, *42*, 3865-3869.
10. Nakajima, H.; Ohno, H. *Polymer* **2005**, *46*, 11499-11504.
11. Marcilla, R.; Sanchez-Paniagua, M.; Lopez-Ruiz, B.; Lopez-Cabarcos, E.; Ochoteco, E.; Grande, H.; Mecerreyes, D. *J. Polym. Sci. Pol. Chem.* **2006**, *44*, 3958-3965.
12. Bara, J. E.; Hatakeyama, E. S.; Gabriel, C. J.; Zeng, X. H.; Lessmann, S.; Gin, D. L.; Noble, R. D. *Journal of Membrane Science* **2008**, *316*, 186-191.
13. Yoshio, M.; Kagata, T.; Hoshino, K.; Mukai, T.; Ohno, H.; Kato, T. *J. Am. Chem. Soc.* **2006**, *128*, 5570-5577.
14. Zhang, G. B.; Liu, X. H.; Li, B. X.; Bai, Y. G. *J. Appl. Polym. Sci.* **2009**, *112*, 3337-3340.
15. Tan, R.; Yin, D. H.; Yu, N. Y.; Zhao, H. H.; Yin, D. L. *J. Catal.* **2009**, *263*, 284-291.
16. Stancik, C. M.; Lavoie, A. R.; Schütz, J.; Achurra, P. A.; Lindner, P.; Gast, A. P.; Waymouth, R. M. *Langmuir* **2003**, *20*, 596-605.
17. Vijayakrishna, K.; Jewrajka, S. K.; Ruiz, A.; Marcilla, R.; Pomposo, J. A.; Mecerreyes, D.; Taton, D.; Gnanou, Y. *Macromolecules* **2008**, *41*, 6299-6308.
18. Mori, H.; Yahagi, M.; Endo, T. *Macromolecules* **2009**, *42*, 8082-8092.
19. Vijayakrishna, K.; Mecerreyes, D.; Gnanou, Y.; Taton, D. *Macromolecules* **2009**, *42*, 5167-5174.
20. Gu, Y.; Lodge, T. P. *Macromolecules* **2011**, *44*, 1732-1736.
21. Weber, R. L.; Ye, Y. S.; Schmitt, A. L.; Banik, S. M.; Elabd, Y. A.; Mahanthappa, M. K. *Macromolecules* **2011**, *44*, 5727-5735.
22. Ding, S. J.; Tang, H. D.; Radosz, M.; Shen, Y. Q. *J. Polym. Sci. Pol. Chem.* **2004**, *42*, 5794-5801.
23. Bara, J. E.; Lessmann, S.; Gabriel, C. J.; Hatakeyama, E. S.; Noble, R. D.; Gin, D. L. *Ind Eng Chem Res* **2007**, *46*, 5397-5404.
24. Ohno, H.; Ito, K. *Chem. Lett.* **1998**, *8*, 751-752.
25. Ohno, H.; Yoshizawa, M.; Ogihara, W. *Electrochim. Acta* **2004**, *50*, 255-261.
26. Vygodskii, Y. S.; Shaplov, A. S.; Lozinskaya, E. I.; Lyssenko, K. A.; Golovanov, D. G.; Malyshkina, I. A.; Gavrilova, N. D.; Buchmeiser, M. R. *Macromol. Chem. Phys.* **2008**, *209*, 40-51.
27. Ho, H. A.; Leclerc, M. *J. Am. Chem. Soc.* **2003**, *125*, 4412-4413.
28. Ricks-Laskoski, H. L.; Snow, A. W. *J. Am. Chem. Soc.* **2006**, *128*, 12402-12403.
29. Hajduk, D. A.; Harper, P. E.; Gruner, S. M.; Honeker, C. C.; Kim, G.; Thomas, E. L.; Fetters, L. J. *Macromolecules* **1994**, *27*, 4063-4075.
30. Bates, F. S.; Fredrickson, G. H. *Phys. Today* **1999**, *52*, 32-38.

31. The presence of intra-grain defects can produce three dimensional continuity across the grain.
32. Sphere based morphologies are an exception. The isolated nature of the spherical domains precludes it from contributing directly to ion or gas molecule transport unless the surrounding matrix is also conductive.
33. Wanakule, N. S.; Panday, A.; Mullin, S. A.; Gann, E.; Hexemer, A.; Balsara, N. P. *Macromolecules* **2009**, *42*, 5642-5651.
34. Wanakule, N. S.; Virgili, J. M.; Teran, A. A.; Wang, Z.-G.; Balsara, N. P. *Macromolecules* **2010**, *43*, 8282-8289.
35. Almdal, K.; Koppi, K. A.; Bates, F. S. *Macromolecules* **1993**, *26*, 4058-4060.
36. Bodycomb, J.; Funaki, Y.; Kimishima, K.; Hashimoto, T. *Macromolecules* **1999**, *32*, 2075-2077.
37. Koo, C. M.; Wu, L.; Lim, L. S.; Mahanthappa, M. K.; Hillmyer, M. A.; Bates, F. S. *Macromolecules* **2005**, *38*, 6090-6098.
38. Park, S.; Kim, B.; Xu, J.; Hofmann, T.; Ocko, B. M.; Russell, T. P. *Macromolecules* **2009**, *42*, 1278-1284.
39. Park, S.; Wang, J.-Y.; Kim, B.; Xu, J.; Russell, T. P. *ACS Nano* **2008**, *2*, 766-772.
40. Segalman, R. A.; Hexemer, A.; Kramer, E. J. *Macromolecules* **2003**, *36*, 6831-6839.
41. Xu, T.; Goldbach, J. T.; Russell, T. P. *Macromolecules* **2003**, *36*, 7296-7300.
42. Drzal, P. L.; Halasa, A. F.; Kofinas, P. *Polymer* **2000**, *41*, 4671-4677.
43. Jha, A. K.; Chen, L.; Offeman, R. D.; Balsara, N. P. *Journal of Membrane Science* **2011**, *373*, 112-120.
44. Wiesenauer, E. F.; Edwards, J. P.; Scalfani, V. F.; Bailey, T. S.; Gin, D. L. *Macromolecules* **2011**, *44*, 5075-5078.
45. Annaka, M.; Morishita, K.; Okabe, S. *J. Phys. Chem. B* **2007**, *111*, 11700-11707.
46. Gebhardt, K. E.; Ahn, S.; Venkatachalam, G.; Savin, D. A. *Langmuir* **2007**, *23*, 2851-2856.
47. Naik, S. S.; Savin, D. A. *Macromolecules* **2009**, *42*, 7114-7121.
48. Zhang, L.; Shen, H.; Eisenberg, A. *Macromolecules* **1997**, *30*, 1001-1011.
49. Lu, X.; Weiss, R. A. *Macromolecules* **1993**, *26*, 3615-3622.
50. Park, M. J.; Balsara, N. P. *Macromolecules* **2008**, *41*, 3678-3687.
51. Saito, T.; Mather, B. D.; Costanzo, P. J.; Beyer, F. L.; Long, T. E. *Macromolecules* **2008**, *41*, 3503-3512.
52. Hadjichristidis, N., *Block copolymers synthetic strategies, physical properties, and applications*. Wiley-Interscience: Hoboken, N.J., **2003**.
53. Matsushita, Y.; Mori, K.; Saguchi, R.; Nakao, Y.; Noda, I.; Nagasawa, M. *Macromolecules* **1990**, *23*, 4313-4316.
54. Semenov, A. N.; Nyrkova, I. A.; Khokhlov, A. R. *Macromolecules* **1995**, *28*, 7491-7500.
55. Hasegawa, H.; Hashimoto, T.; Kawai, H.; Lodge, T. P.; Amis, E. J.; Glinka, C. J.; Han, C. C. *Macromolecules* **1985**, *18*, 67-78.
56. Hashimoto, T.; Nagatoshi, K.; Todo, A.; Hasegawa, H.; Kawai, H. *Macromolecules* **1974**, *7*, 364-373.
57. Fetters, L. J.; Lohse, D. J.; Richter, D.; Witten, T. A.; Zirkel, A. *Macromolecules* **1994**, *27*, 4639-4647.
58. Floudas, G.; Vazaiou, B.; Schipper, F.; Ulrich, R.; Wiesner, U.; Iatrou, H.; Hadjichristidis, N. *Macromolecules* **2001**, *34*, 2947-2957.
59. Khandpur, A. K.; Foerster, S.; Bates, F. S.; Hamley, I. W.; Ryan, A. J.; Bras, W.; Almdal, K.; Mortensen, K. *Macromolecules* **1995**, *28*, 8796-8806.

60. Maurer, W. W.; Bates, F. S.; Lodge, T. P.; Almdal, K.; Mortensen, K.; Fredrickson, G. H. *J. Chem. Phys.* **1998**, *108*, 2989-3000.
61. Floudas, G.; Ulrich, R.; Wiesner, U. *J. Chem. Phys.* **1999**, *110*, 652-663.
62. Bates, F. S.; Schulz, M. F.; Rosedale, J. H.; Almdal, K. *Macromolecules* **1992**, *25*, 5547-5550.
63. Rosedale, J. H.; Bates, F. S.; Almdal, K.; Mortensen, K.; Wignall, G. D. *Macromolecules* **1995**, *28*, 1429-1443.
64. Almdal, K.; Hillmyer, M. A.; Bates, F. S. *Macromolecules* **2002**, *35*, 7685-7691.
65. Floudas, G.; Vlassopoulos, D.; Pitsikalis, M.; Hadjichristidis, N.; Stamm, M. *J. Chem. Phys.* **1996**, *104*, 2083-2088.
66. Leibler, L. *Macromolecules* **1980**, *13*, 1602-1617.
67. Brazovskii, S. A. *Sov. Phys. JETP* **1975**, *41*, 85.
68. Fredrickson, G. H.; Helfand, E. *J. Chem. Phys.* **1987**, *87*, 697-705.
69. Bates, F. S. *Macromolecules* **1985**, *18*, 525-528.
70. Russell, T. P.; Hjelm, R. P.; Seeger, P. A. *Macromolecules* **1990**, *23*, 890-893.
71. Semenov, A. N. *Macromolecules* **1992**, *25*, 4967-4977.
72. Zhu, S.; Edmonds, W. F.; Hillmyer, M. A.; Lodge, T. P. *J. Polym. Sci., Part B: Polym. Phys.* **2005**, *43*, 3685-3694.
73. Hajduk, D. A.; Gruner, S. M.; Rangarajan, P.; Register, R. A.; Fetters, L. J.; Honeker, C.; Albalak, R. J.; Thomas, E. L. *Macromolecules* **1994**, *27*, 490-501.
74. Hashimoto, T.; Kawamura, T.; Harada, M.; Tanaka, H. *Macromolecules* **1994**, *27*, 3063-3072.
75. Richards, R. W.; Thomason, J. L. *Macromolecules* **1983**, *16*, 982-992.
76. Sakurai, S.; Momii, T.; Taie, K.; Shibayama, M.; Nomura, S.; Hashimoto, T. *Macromolecules* **1993**, *26*, 485-491.
77. Yamaguchi, D.; Hashimoto, T.; Vaidya, N. Y.; Han, C. D. *Macromolecules* **1999**, *32*, 7696-7699.
78. Lee, S.-H.; Char, K.; Kim, G. *Macromolecules* **2000**, *33*, 7072-7083.
79. Scalfani, V. F.; Bailey, T. S. *Macromolecules* **2011**, *44*, 6557-6567.
80. Ahn, J.-H.; Zin, W.-C. *Macromolecules* **2000**, *33*, 641-644.
81. Foerster, S.; Khandpur, A. K.; Zhao, J.; Bates, F. S.; Hamley, I. W.; Ryan, A. J.; Bras, W. *Macromolecules* **1994**, *27*, 6922-6935.
82. Loo, Y.-L.; Register, R. A.; Adamson, D. H.; Ryan, A. J. *Macromolecules* **2005**, *38*, 4947-4949.
83. Zhu, L.; Huang, P.; Chen, W. Y.; Weng, X.; Cheng, S. Z. D.; Ge, Q.; Quirk, R. P.; Senador, T.; Shaw, M. T.; Thomas, E. L.; Lotz, B.; Hsiao, B. S.; Yeh, F.; Liu, L. *Macromolecules* **2003**, *36*, 3180-3188.
84. Matsen, M. W.; Bates, F. S. *Macromolecules* **1996**, *29*, 1091-1098.
85. Bates, F. S. *Science* **1991**, *251*, 898-905.
86. Hajduk, D. A.; Takenouchi, H.; Hillmyer, M. A.; Bates, F. S.; Vigild, M. E.; Almdal, K. *Macromolecules* **1997**, *30*, 3788-3795.
87. Matsen, M. W. *J. Phys.-Condes. Matter* **2002**, *14*, R21-R47.
88. Zhou, N. Polymeric Bicontinuous Microemulsions. University of Minnesota, **2007**.
89. Jeong, U.; Lee, H. H.; Yang, H.; Kim, J. K.; Okamoto, S.; Aida, S.; Sakurai, S. *Macromolecules* **2003**, *36*, 1685-1693.
90. Kim, S. Y.; Yoon, E.; Joo, T.; Park, M. J. *Macromolecules* **2011**, *44*, 5289-5298.
91. Simone, P. M.; Lodge, T. P. *ACS Applied Materials & Interfaces* **2009**, *1*, 2812-2820.
92. Mai, S.-M.; Fairclough, J. P. A.; Terrill, N. J.; Turner, S. C.; Hamley, I. W.; Matsen, M. W.;

- Ryan, A. J.; Booth, C. *Macromolecules* **1998**, *31*, 8110-8116.
93. Pitet, L. M.; Hillmyer, M. A. *Macromolecules* **2009**, *42*, 3674-3680.
94. Matsen, M. W. *Phys. Rev. Lett.* **2007**, *99*, (14).
95. Bendejacq, D.; Ponsinet, V.; Joanicot, M.; Loo, Y. L.; Register, R. A. *Macromolecules* **2002**, *35*, 6645-6649.
96. Matsushita, Y.; Noro, A.; Iinuma, M.; Suzuki, J.; Ohtani, H.; Takano, A. *Macromolecules* **2003**, *36*, 8074-8077.
97. Noro, A.; Iinuma, M.; Suzuki, J.; Takano, A.; Matsushita, Y. *Macromolecules* **2004**, *37*, 3804-3808.
98. Lynd, N. A.; Meuler, A. J.; Hillmyer, M. A. *Prog. Polym. Sci.* **2008**, *33*, 875-893.
99. Matsen, M. W.; Bates, F. S. *J. Chem. Phys.* **1997**, *106*, 2436-2448.
100. Cochran, E. W.; Garcia-Cervera, C. J.; Fredrickson, G. H. *Macromolecules* **2006**, *39*, 2449-2451.
101. Hajduk, D. A.; Ho, R. M.; Hillmyer, M. A.; Bates, F. S.; Almdal, K. *J. Phys. Chem. B* **1998**, *102*, 1356-1363.
102. Cavicchi, K. A.; Lodge, T. P. *Macromolecules* **2003**, *36*, 7158-7164.
103. Kinning, D. J.; Thomas, E. L. *Macromolecules* **1984**, *17*, 1712-1718.
104. Schwab, M.; St; uuml; hn, B. *Phys. Rev. Lett.* **1996**, *76*, 924.
105. Wang, X.; Dormidontova, E. E.; Lodge, T. P. *Macromolecules* **2002**, *35*, 9687-9697.
106. Balsara, N. P.; Garetz, B. A.; Chang, M. Y.; Dai, H. J.; Newstein, M. C.; Goveas, J. L.; Krishnamoorti, R.; Rai, S. *Macromolecules* **1998**, *31*, 5309-5315.
107. Cavicchi, K. A.; Lodge, T. P. *J. Polym. Sci. Pt. B-Polym. Phys.* **2003**, *41*, 715-724.

CHAPTER 9

SUMMARY — PART II — MORPHOLOGICAL PHASE BEHAVIOR OF POLY(RTIL) CONTAINING BLOCK COPOLYMER MELTS

The contents of this dissertation chapter were written by Vincent F. Scalfani.

9.1 MAJOR RESULTS

There are two major achievements in Part II of this dissertation: 1) Successful controlled synthesis of a new imidazolium-based alkyl-ionic BCP via the sequential ROMP of dodecyl ester- and imidazolium-based RTIL monomers (Chapter 7), and 2) A systematic analysis of the melt-state morphological behavior of over 16 poly(RTIL)-based BCPs with varying volume fractions for the development of a phase diagram (Chapters 7 and 8).

In Chapter 7, a new imidazolium-based alkyl-ionic BCP (poly(RTIL)-based BCP) was synthesized by directly polymerizing a dodecyl ester- and charged imidazolium IL-norbornene monomer via sequential ROMP. Typically, poly(RTIL)-based BCPs are first synthesized with neutral monomers and then post-functionalized. Straightforward methods to physically characterize the newly developed poly(RTIL)-based BCPs could not be utilized such as GPC, MALDI-TOF, and dynamic light scattering due to complications arising from the highly charged macromolecule. However, alternative techniques including NMR DOSY, DSC, rheology and SAXS proved to be successful techniques in the confirmation of the synthesized block architecture.

In Chapter 8, a total of 16 poly(RTIL)-based BCPs varying only by relative composition were synthesized analogous to the synthetic method developed in Chapter 7 through the sequential ROMP of a neutral dodecyl ester norbornene monomer followed by a charged imidazolium functional norbornene monomer. A phase diagram was developed through a systematic characterization of the morphological behavior with a combination of SAXS and dynamic rheology. The studied poly(RTIL)-based BCPs were found to self-assemble into many of the classic BCP morphologies including lamellae, hexagonally packed cylinders, and spheres on a BCC lattice. The self-assembled structures exhibited a high degree of long-range order that is preserved after an initial melt-processing step. Importantly, the bicontinuous gyroid region was absent due to the great dissimilarity of the charged and neutral blocks, effectively limiting the accessible phase space to the strong segregation limit (SSL). A coexistence of hexagonally packed cylindrical and lamellar domains are present in place of the gyroid morphology. Lastly, the accessible phase space within the SSL precludes straightforward measurement of the interaction parameter, χ .

9.2 BROAD IMPACTS TO THE SCIENTIFIC COMMUNITY

- A new method of sequential ROMP was reported for directly synthesizing charged BCPs.
- One of the first examples of a poly(RTIL)-based BCP that forms phase-separated ordered nanostructures in the melt phase was reported.
- Addition of full melt-state phase behavior of a poly(RTIL)-based BCP system to the library of well-developed BCP phase diagrams.
- Absence of gyroid phase suggests it will be difficult to access bicontinuous phases in other charged macromolecules.
- Limited access to disordered phase in highly charged BCP systems was found.

APPENDIX I

NETWORK FORMATION IN AN ORTHOGONALLY SELF-ASSEMBLING SYSTEM

The contents of this dissertation Appendix have been adapted from a manuscript published in *ACS Macro Letters*: Mes, T.; Koenigs, M. M. E.; Scalfani, V. F.; Bailey, T.S.; Meijer, E.W.; Palmans, A. R. A. *ACS Macro Lett.* **2011**, *1*, 105. The synthesis of the difunctional poly(butadiene) homopolymer and rheological melt characterization of the supramolecular polymers were developed and performed by Vincent F. Scalfani and Travis S. Bailey. Functionalization of the difunctional polymer with supramolecular motifs and the characterization experiments of both the solution- and solid-state properties were designed and performed by Tristan Mes, Marcel M.E. Koenigs, E.W. Meijer, and Anja R.A. Palmans (Eindhoven University of Technology, The Netherlands). The manuscript and adapted dissertation chapter was prepared jointly through a collaborative effort of all authors.

AI.1 CONSPECTUS

Many supramolecular motifs self-assemble into nanorods, forming the basis of the mechanical properties of supramolecular polymers. When integrated as end-caps in a bifunctional telechelic polymer, the motifs can phase segregate into the same or into another nanorod. In the latter case, a functional cross-link is formed by the bridging chain that strengthens the polymer network. This study introduces a supramolecular polymeric system that consists of two different nanorod forming supramolecular motifs. When end-capped to monofunctional polymers, these supramolecular motifs self-assemble in an orthogonal fashion in two separate types of noncross-linked nanorods, resulting in a viscous liquid lacking macroscopic properties. The addition of 15 mol % of an α,ω -telechelic polymer containing both supramolecular motifs, each on one end, transforms this viscous sticky liquid to a solid material with elastomeric properties due to network formation between the two types of nanorods.

AI.2 INTRODUCTION

To widen the scope of supramolecular materials, the orthogonal self-assembly of different types of highly specific, noninterfering interactions is currently attracting considerable interest.¹ Such materials can be tuned by various external stimuli through addressing each type of interaction separately. The combination of orthogonal binding motifs allowed the formation of supramolecular block copolymers², dendrimers³, nanostructured materials⁴, self-assembled fibrillar networks with encapsulated micelles⁵ and others.⁶ Combinations of i.a. hydrogen bonds and metal–ligand complexation,^{2a,c,f,3} metal–ligand complexation and ionic interactions⁷, hydrogen bonds and ionic interactions,^{4a,8} and different complementary hydrogen bonding motifs⁹ have been explored for this purpose. Despite all of these fascinating examples, the potential of orthogonal binding units to improve bulk material properties has not been fully exploited to date.¹⁰ Herein, we report on the ability of benzene-1,3,5-tricarboxamide (BTA) and 2-ureido-4[1H]-pyrimidinone (UPy) functionalized materials to self-assemble in an orthogonal fashion in the solid state by so-called self-sorting. BTAs self-assemble into helical, columnar

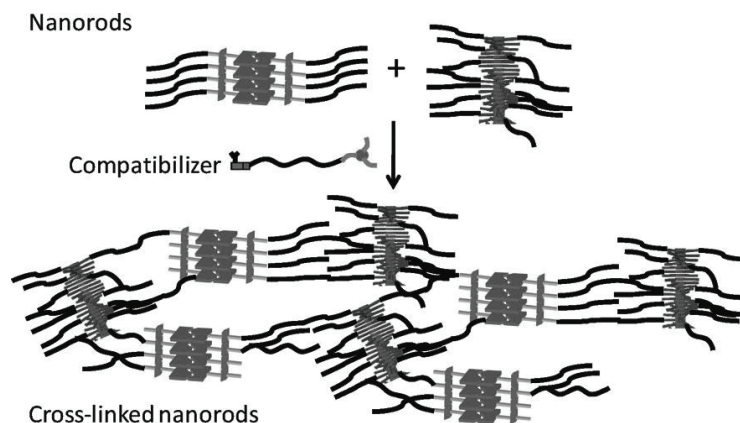


Figure A1–1. Addition of a supramolecular compatibilizer generates network formation and improves material properties in a supramolecular polymer blend.

aggregates,¹¹ while the UPy motif dimerizes via strong, quadruple hydrogen bonds.¹² Telechelic polymers end-capped with two UPy units or with two BTA motifs show thermoplastic elastomeric properties.^{13,14} In cases of telechelic polymers end-capped with the BTAs, the bulk material properties arise from the presence of phase-segregated nanorods consisting of helical, columnar BTA aggregates. In the UPy end-capped telechelic polymers, where a urethane group connects the UPy to the polymer, UPys form dimers aggregating via lateral hydrogen bonds of the urethane into stacks. These stacks then bundle via weak hydrogen bonds into nanofibrils.¹³ Supramolecular motifs attached to bifunctional telechelics with the ability to phase segregate into a nanorod can do this in the same (homo) or another (hetero) nanorod or nanofiber. In the latter case, a hetero (functional) cross-link is formed leading to network formation, while the first gives rise to nonfunctional loops. These heterofunctional cross-links contribute significantly to the network strength and thus to the elastomeric properties. However, the ratio of homo over hetero connections as well as the number of cross-links that is required has not been rigorously determined for thermoplastic elastomers studied so far.¹⁵ Hence, the threshold concentration of bifunctional crosslinker required to produce an infinite network of reasonable mechanical properties is currently not established, although the value could in theory be quite small for systems with extended nanorod length scales.

We now present a supramolecular polymeric system that consists of a mixture of low

AI.3.2 Solution-State Phase Behavior

In previous work, we successfully applied temperature dependent circular dichroism (CD) and ultraviolet (UV) spectroscopy to study BTA self-assembly. The 3-fold, helical arrangement of the intermolecular hydrogen bonds between consecutive BTAs in combination with a preferred helical sense upon introducing a stereogenic methyl group in the alkyl side chain are characterized by a λ_{\max} of 192 nm in UV spectroscopy and a Cotton effect at 223 nm with $|\Delta\epsilon| = 43 \text{ L/mol cm}$.¹¹ The dimerization of the UPy group is reliably probed by UV spectroscopy because the 4[1H] pyrimidinone tautomer (dimerized UPy) has a λ_{\max} of 260 nm, while the 6[1H]pyrimidinone tautomer (monomeric UPy) has a λ_{\max} of 285 nm.¹⁷ CD measurements on BTA-pEB **2** ($c = 5 \times 10^{-4} \text{ M}$) in the presence and absence of UPy-pEB **3** ($c = 5 \times 10^{-4} \text{ M}$) in methylcyclohexane (MCH, being a model of the pEB) shows that the Cotton effect of **2** mixed with **3** was equal in size as for pure compound **2** (Figure AI-2A), indicating that the UPy group is not capable of interfering with BTA aggregation in dilute solution. Also, BTA-pEB-UPy **1** (Scheme AI-1) shows a Cotton effect similar in shape as found for **2** ($c = 5 \times 10^{-4} \text{ M}$ in MCH; Figure AI-2B). Proof for the dimerization of the UPy at these conditions is found by analyzing the UV spectra: the shoulder around 275 nm at 80 °C indicates the loss of quadruple hydrogen bonding between the UPy groups. This suggests that the UPys are dimerized at 20 °C. Although the molar ellipticity of **1** is lower than that of **2** due to a reduction of the association constant K upon increasing the molecular weight of the side chain (see Figure AI-S1 for an additional explanation, Appendix II), these results show that the self-sorting is operative for **1**.

AI.3.2 Solid-State Phase Behavior

In order to study the supramolecular materials in their neat state, we prepared films of **1** and **2** with thicknesses of 340 and 260 nm, respectively, by spin-coating a CHCl_3 solution on quartz plates. The CD effect of the films was independent of the orientation of the quartz slide with respect to the beam and no linear dichroism effects were present. The Cotton effects were of nearly identical size (CD-effect = -10 mdeg , Figure AI-2C). Temperature-dependent CD

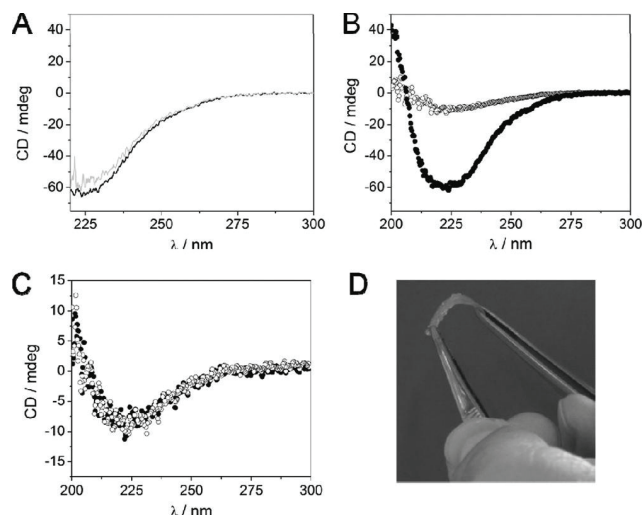


Figure A1-2. (A) CD spectra of **2** in MCH in the absence (gray line, $c = 5 \times 10^{-4}$ M) and presence of **3** (black line, $c = 5 \times 10^{-4}$ mol L $^{-1}$) at 20 °C. (B) CD spectra of **1** (open circles) and **2** (closed circles) at 20 °C, $c = 5 \times 10^{-4}$ M in MCH. (C) Solid state CD spectra of films of **1** (thickness = 340 nm, open circles) and **2** (thickness = 260 nm, closed circles) on quartz plates. (D) Physical appearance of **1/2/3** in 15/42.5/42.5 molar ratio.

spectra of these films (25–200 °C at a rate of 5 K min $^{-1}$ probed at $\lambda_{\text{max}} = 223$ nm) show a decrease of the CD effect upon heating; the CD effects of **1** and **2** disappear above 160 and 200 °C, respectively (Figure AI-S2). This transition reflects the loss of the hydrogen bonded helical arrangement stabilizing the BTA nanorods in the polymer matrix.^{14a}

While CD measurements provide detailed information on the aggregation behavior and ability of nanorod formation of BTAs in the presence or absence of UPys, details of the self-assembly processes involving the UPy group cannot be inferred from these measurements. Previous research showed that pEB end-capped with two UPy-urethane units (bis UPy-urethane-pEB) resulted in a material with a melting point of 62 °C and a corresponding ΔH of 1.98 J/g (Figure AI-S3).^{13a} As a result, we investigated the thermal behavior of compounds **1–3** in the solid state by combining differential scanning calorimetry (DSC) with polarized optical spectroscopy (POM) and variable-temperature infrared spectroscopy (VT-IR) to assign the origin of the thermal transitions. The data are summarized in Table AI-1.

The DSC trace of BTA-pEB **2** shows a T_g at -60 °C and an additional, small transition around 192 °C ($\Delta H_2 = 4.09$ J/g). Between room temperature and around 190 °C a mobile, birefringent

texture, typical for a nematic phase, is present. The transition at 192 °C coincides with the loss of the CD effect and is connected to the loss of intermolecular hydrogen bonding between BTAs, as revealed by VT-IR. The DSC trace of UPy-pEB **3** shows a T_g at around -67 °C and a small transition around 39 °C ($\Delta H_1 = 2.93$ J/g) originating from the melting of the UPy nanofibrils. Between room temperature and around 45 °C, a birefringent texture was observed. BTA-pEB-UPy **1** shows a T_g at -60 °C, resulting from the pEB part and a small transition around 140 °C ($\Delta H_2 = 0.7$ J/g). VT-IR showed that the transition at 140 °C corresponds to the loss of intermolecular hydrogen bonding between BTAs (Figure AI-S4).

Interestingly, polymer **1** does not show a thermal transition in DSC related to the melting of UPy nanofibrils. However, VT-IR shows a shift at $\nu = 1700$ cm^{-1} to 1695 cm^{-1} around 50 °C, which can be assigned to the isocytosine part of the UPy and is presumably connected to the loss of lateral UPy-urethane hydrogen bonding. The mobile, birefringent texture observed from 50 °C up to around 135 °C was typical for a nematic phase and the sample became isotropic at 135 °C. The combined results of solid state CD, IR and DSC of polymers **1–3** indicate that BTAs form nanorods consisting of helical columnar BTA aggregates in the presence and absence of UPys. The aggregation of UPy stacks into nanofibrils as seen for **3** seems to be less efficient in BTA-pEB-UPy **1**. The latter is most likely caused by the use of the isopropyl substituent on the 6-position of the isocytosine in polymer **1**.^{13b}

Table AI-1. Summary of NMR, GPC, and DSC data of copounds 1–3.

compound	ratio BTA/ UPy	yield (%)	M_n^a (kg/mol)	M_n^b (kg/mol)	M_w^b (kg/ mol)	PDI ^b	T_g^c (°C)	T_{m1}^c (°C)	ΔH_1^c (J/g)	T_{m2}^c (°C)	ΔH_2^c (J/g)
1	50/50	60	6.2	12.7	13.0	1.03	-60	—	—	140	0.7
2	100/0	95	4.0	7.6	7.8	1.03	-67	—	—	192	4.09
3	0/100	95	3.9	7.9	8.1	1.03	-60	39	2.93	—	—
2/3	50/50	—	—	—	—	—	-60	38	0.18	153	1.02
1/2/3	50/50	—	—	—	—	—	-62	37	0.29	147	1.01

^a Determined by 1H NMR. ^b Determined by GPC. ^c Determined from the second heating run of DSC at a rate of 40K min⁻¹.

The potential of supramolecular network formation by orthogonal binding motifs to improve bulk material properties was evaluated by mixing UPy-pEB-BTA **1** with a mixture

pEBBTA **2** and UPy-pEB **3** in a 15/42.5/42.5 molar ratio. DSC measurements revealed two phase transitions for the ternary blend of **1/2/3** at 38 °C ($\Delta H_1 = 0.286$ J/g) and at 147 °C ($\Delta H_2 = 1.012$ J/g) while those of the binary blend of **2/3** (50/50 mol %) were found at 38 °C ($\Delta H_1 = 0.18$ J/g) and at 152 °C ($\Delta H_2 = 1.016$ J/g; Table AI-1). The similar thermal behavior of **2** and **3** in the presence or absence of **1** show that compatibilizer **1** does not negatively affect the formation of BTA nanorods and UPy nanofibrils at a molecular scale. On the macroscopic scale, on the other hand, the addition of the compatibilizer **1** results in a dramatic change in the macroscopic properties of the blend. Visual inspection of the ternary blend reveals its elastomeric properties, which contrast strongly to the sticky, oily appearance of the binary blend of **2/3** (Figure AI-2D).

Evidence for a phase segregated structure of BTA-pEB-UPy **1** was obtained using atomic force microscopy (AFM; tapping mode in air at room temperature). Images clearly show a fibrillar structure (Figure AI-3A) reminiscent to that previously observed for bis-BTA-pEB and bis-UPy-urethane-pEB.^{14b,13b} The diameter of the fibrillar structures found for **1** was estimated around 7 nm and their length was about 100 nm. Unfortunately, the stickiness of polymers **2** and **3** hampered additional structural analysis of both the **2/3** binary blend and the **1/2/3** ternary blend, despite the dramatically improved macroscopic properties of the latter (Figure AI-2D).

AI.3.3 Mechanical Performance

To quantify the improved elasticity exhibited by the **1/2/3** blend, rheological measurements comparing the mechanical response of the **2/3** binary blend and the **1/2/3** ternary blend under oscillatory shear were performed. To test our hypothesis that the added mechanical advantage provided by the addition of **1** is predicated on its ability to provide orthogonal connectivity between the BTA nanorods and UPy nanofibrils as portrayed in Figure AI-1, we focused our attention on the temperature dependence of the rheological responses. Figure AI-3B shows the temperature ramp response quantifying both the elastic (G') and viscous (G'') moduli of the **2/3** and **1/2/3** blends as a function of temperature. Notably, the ternary blend of **1/2/3** has an

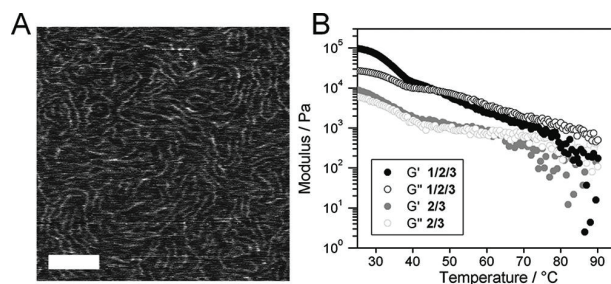


Figure AI-3. (A) AFM of **1** (scale bar = 100 nm). (B) Temperature dependence of the storage (G') and loss (G'') moduli in blends of **2/3** and **1/2/3** (heating at 1 K min^{-1} , frequency = 1 rad s^{-1} , and strain = 1%).

order of magnitude higher moduli when compared to the **2/3** blend at room temperature, consistent with the improved mechanical properties observed qualitatively in the compatibilized bulk material. This dramatic change in tactile response at room temperature is also captured through the relative magnitudes of the elastic and viscous moduli, with the **1/2/3** blend exhibiting an elastic response four times the magnitude of the viscous response. In contrast, the **2/3** blend exhibits a significantly smaller ratio of elastic to viscous contributions to the overall modulus, in addition to its reduced magnitude, when compared with the **1/2/3** blend. Heating both of the blend samples produces a visible transition in rheological response in the vicinity of $40 \text{ }^\circ\text{C}$, although this transition is more pronounced in the **1/2/3** blend in which the transition is characterized by a significant loss in elasticity. Notably this transition is consistent with that observed in DSC at $38 \text{ }^\circ\text{C}$, in which the loss of lateral hydrogen bonds between the UPy-urethane groups triggers the consequential melting of the UPy nanofibrils. Interestingly, while the melting of the UPy nanofibrils definitely reduces the elastic component of the **1/2/3** blend, the overall modulus remains significantly higher than that measured for the compatibilizer free **2/3** blend at a similar temperature. The origin of the increased modulus (even after nanofibril melting) is presumably related to the presence of dimerized UPys and suggests that the hetero-functional compatibilizer still contributes to the overall mechanical response. Dimerization of UPys leads to species that possess two BTA end-groups that still have the ability to cross-link

BTA nanorods. Continued heating reduces the modulus further, with an eventual crossover of the moduli in both blends such that the viscous character and both materials become more and more liquid-like at moderately high temperatures.

The frequency dependence of the rheological response on either side of the UPy nanofibrils melting transition also quantifies the elastic nature of the compatibilized **1/2/3** blend. At room temperature (Figure AI–S5, 25 °C), the **1/2/3** blend exhibits a near plateau elastic modulus, with the classically “U” shaped viscous response spanning the 10–1 to 10² Hz frequency range.¹⁸ Notably, this behavior is absent above the UPy melting transition (Figure AI–S5, 60 °C) where the system is no longer actively cross-linked. The response of the **2/3** blend at both temperatures is also included for comparison. Given the apparent thermoreversible nature of UPy nanofibril melting and formation, these low molecular weight supramolecular polymer blends would be highly amenable to classic melt processing techniques.

AI.4 CONCLUSIONS

In conclusion, we have introduced a supramolecular polymer blend that consists of two different supramolecular motifs that form separate phase segregated nanorods in an orthogonal fashion. The addition of only a small amount (15 mol %) of a supramolecular compatibilizer (α , ω -functionalized telechelic containing both supramolecular motifs) leads to a polymer exhibiting elastomeric properties. We have shown that a significant enhancement of material properties is obtained by cross-linking a relatively small part of the nanorods in a supramolecular fashion. Our future work is focused on quantitative measurements of the material properties of these supramolecular polymer blends

AI.5 SUPPORTING INFORMATION AVAILABLE

Experimental details, characterization of **1–3** using VT-IR, DSC, rheology measurements, and additional UV and CD spectra.

AI. 6 ACKNOWLEDGEMENTS

A.R.A.P. and T.M. would like to thank Wilco Appel and Mellany Ramaekers for help with the AFM measurements and SupraPolix BV for providing various UPy synthons. This research was supported by The Netherlands Organization for Scientific Research (NWO). V.F.S. and T.S.B. thank National Science Foundation (Grant DMR-0645781) and Colorado State University for financial support.

AI. 7 REFERENCES

1. (a) Pollino, J. M.; Weck, M *Chem. Soc. Rev.* **2005**, *34*, 193-207; (b) Yang, S. K.; Ambade, A. V.; Weck, M., *Chem. Soc. Rev.* **2011**, *40* (1), 129-137.
2. (a) Ambade, A. V.; Yang, S. K.; Weck, M., *Angew. Chem. Int. Ed.* **2009**, *48*, 2894-2898; (b) Yang, S. K.; Ambade, A. V.; Weck, M., *J. Am. Chem. Soc.* **2010**, *132*, 1637-1645; (c) Hofmeier, H.; Hoogenboom, R.; Wouters, M. E. L.; Schubert, U. S., *J. Am. Chem. Soc.* **2005**, *127*, 2913-2921; (d) Li, S. L.; Xiao, T. X.; Wu, Y. F.; Jiang, J. L.; Wang, L. Y., *Chem. Commun.* **2011**, *47*, 6903-6905; (e) Wang, F.; Han, C. Y.; He, C. L.; Zhou, Q. Z.; Zhang, J. Q.; Wang, C.; Li, N.; Huang, F. H., *J. Am. Chem. Soc.* **2008**, *130*, 11254-11255; (f) Mansfeld, U.; Hager, M. D.; Hoogenboom, R.; Ott, C.; Winter, A.; Schubert, U. S., *Chem. Commun.* **2009**, 3386-3388; (g) Groger, G.; Stepanenko, V.; Wurthner, F.; Schmuck, C., *Chem. Commun.* **2009**, 698-700; (h) Mather, B. D.; Baker, M. B.; Beyer, F. L.; Berg, M. A. G.; Green, M. D.; Long, T. E. *Macromolecules* **2007**, *40*, 6834-6845.
3. Grimm, F.; Hartnagel, K.; Wessendorf, F.; Hirsch, A., *Chem. Commun.* **2009**, 1331-1333
4. (a) Fitie, C. F. C.; Tomatsu, I.; Byelov, D.; de Jeu, W. H.; Sijbesma, R. P. *Chem. Mater.* **2008**, *20*, 2394-2404; (b) van Herikhuyzen, J.; Syamakumari, A.; Schenning, A.; Meijer, E. W., *J. Am. Chem. Soc.* **2004**, *126*, 10021-10027.
5. (a) Heeres, A.; van der Pol, C.; Stuart, M. C. A.; Friggeri, A.; Feringa, B. L.; van Esch, J. *J. Am. Chem. Soc.* **2003**, *125*, 14252-14253; (b) Brizard, A.; Stuart, M.; van Bommel, K.; Friggeri, A.; de Jong, M.; van Esch, J. *Angew. Chem. Int. Ed.* **2008**, *47*, 2063-2066.
6. (a) Yu, L.; Wang, Z.; Wu, J.; Tu, S.; Ding, K. *Angew. Chem. Int. Ed.* **2010**, *49*, 3627-3630; (b) Altintas, O.; Tunca, U.; Barner-Kowollik, C. *Polym. Chem.* **2011**, *2*, 1146-1155
7. (a) Ikeda, M.; Tanaka, Y.; Hasegawa, T.; Furusho, Y.; Yashima, E. *J. Am. Chem. Soc.* **2006**, *128*, 6806-6807; (b) Valkama, S.; Lehtonen, O.; Lappalainen, K.; Kosonen, H.; Castro, P.; Repo, T.; Torkkeli, M.; Serimaa, R.; ten Brinke, G.; Leskela, M.; Ikkala, O. *Macromol. Rapid Commun.* **2003**, *24* 556-560; (c) Groger, G.; Meyer-Zaika, W.; Bottcher, C.; Grohn, F.; Ruthard, C.; Schmuck, C. *J. Am. Chem. Soc.* **2011**, *133*, 8961-8971.
8. Nair, K. P.; Weck, M. *Macromolecules* **2007**, *40*, 211-219.
9. Burd, C.; Weck, M. *Macromolecules* **2005**, *38*, 7225-7230.
10. Nair, K. P.; Breedveld, V.; Weck, M. *Soft Matter* **2011**, *7*, 553-559;
11. (a) Smulders, M. M. J.; Schenning, A. P. H. J.; Meijer, E. W. *J. Am. Chem. Soc.* **2008**, *130*, 606-611; (b) Stals, P. J. M.; Smulders, M. M. J.; Martin-Rapun, R.; Palmans, A. R. A.; Meijer, E. W., *Chem. Eur. J.* **2009**, *15*, 2071-2080.
12. Sijbesma, R. P.; Beijer, F. H.; Brunsveld, L.; Folmer, B. J.; Hirschberg, J. H.; Lange, R. F.; Lowe, J. K.; Meijer, E. W. *Science* **1997**, *278*, 1601-1604;
13. (a) Kautz, H.; van Beek, D. J. M.; Sijbesma, R. P.; Meijer, E. W., *Macromolecules* **2006**, *39*, 4265-4267; (b) Appel, W. P. J.; Portale, G.; Wisse, E.; Dankers, P. Y. W.; Meijer, E. W. *Macromolecules* **2011**, *44*, 6776-6784.
14. (a) Mes, T.; Smulders, M. M. J.; Palmans, A. R. A.; Meijer, E. W., *Macromolecules* **2010**, *43*, 1981-1991; (b) Roosma, J.; Mes, T.; Leclere, P.; Palmans, A. R. A.; Meijer, E. W. *J. Am. Chem. Soc.* **2008**, *130*, 1120-1121.
15. (a) Watanabe H., *Macromolecules* **1995**, *28*, 5006-5011; (b) Brinkmann-Rengel, S.; Abetz, V.; Stadler, R.; Thomas, E. L., *KGK, Kautsch. Gummi Kunstst.* **1999**, *52*, 806-813.
16. (a) Frick, E.M.; Hillmyer, M.A., *Macromol. Rapid Commun.* **2000**, *21*, 1317; (b) Quirk, R.P.; Jang, S.H.; Yang, H.; Lee, Y. *Macromol. Symp.* **1998**, *132*, 281; (c) Quirk, R.P.; Ma, J.-J. *J. Polym. Sci., Part A: Polym. Chem.* **1988**, *26*, 2031.

17. de Greef, T. F. A.; Nieuwenhuizen, M.; Stals P. J. M.; Palmans, A. R. A.; Sijbesma, R. P.; Meijer, E. W., *Chem. Commun.* **2008**, 4306-4308.
18. Kossuth, M. B.; Morse, D. C.; Bates, F. S. *J. Rheol.* **1998**, *43*, 167-196.

APPENDIX II

SUPPLEMENTARY INFORMATION

The contents of this dissertation Appendix have been adapted from the supporting information contained in the following publications:

Chapter 3 — Scalfani, V. F.; Bailey, T. S. Thermally Stable Photocuring Chemistry for Selective Morphological Trapping in Block Copolymer Melt Systems. *Chem. Mater.* **2010**, *22*, 5992-6000.

Chapter 4 — Scalfani, V. F.; Bailey, T. S. Access to Nanostructured Hydrogel Networks Through Photocured Body-Centered Cubic Block Copolymer Melts. *Macromolecules* **2011**, *44*, 6557-6567.

Chapter 7 — Wiesenauer, E. F.; Edwards, J. P.; Scalfani, V. F.; Bailey, T. S.; Gin, D. L. Synthesis and Ordered Phase Separation of Imidazolium-Based Alkyl-Ionic Diblock Copolymers Made via ROMP. *Macromolecules* **2011**, *44*, 5075-5078.

Chapter 8 — Scalfani, V. F.; Wiesenauer, E. F.; Ekblad, J. R.; Edwards, J. P.; Gin, D. L.; Bailey, T. S. Morphological Phase Behavior of Poly(RTIL) Containing Diblock Copolymer Melts. *Macromolecules* (**2012**, submitted).

Appendix I — Mes, T.; Koenigs, M. M. E.; Scalfani, V. F.; Bailey, T.S.; Meijer, E.W.; Palmans, A. R. A. Network Formation in an Orthogonally Self-Assembling System *ACS Macro Lett.* **2011**, *1*, 105.

Note: Heading and subheading labels (i.e. AII.1, AII.1.1, etc.) were intentionally omitted in Appendix II to avoid confusion. In addition, all figures and equations are labeled such that they are related to the designated chapter for clarity (e.g. Figure 3–S1, Figure 3–S2, etc).

CHAPTER 3 — SUPPLEMENTARY INFORMATION — THERMALLY STABLE
PHOTOCURING CHEMISTRY FOR SELECTIVE MORPHOLOGICAL TRAPPING IN
BLOCK COPOLYMER MELT SYSTEMS

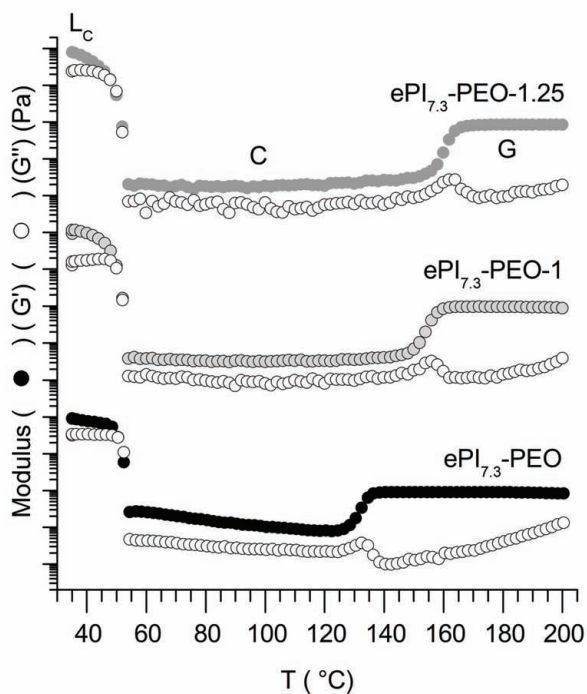


Figure 3-S1. Dynamic temperature ramps for $eP_{17.3}$ -PEO samples with differing IPDPST content (0 mol%, 1.0 mol%, 1.25 mol%, relative to PI repeat units). All samples progress through the same series of morphologies: crystalline lamellar (L_C), hexagonally packed cylinders (C), and gyroid (G). Samples were not disordered as the IPDPST becomes thermal unstable at about 200 °C. Increasing IPDPST content leaves the qualitative phase behavior intact, but shifts the transitions to the gyroid phase to higher temperatures. The initial transition from L_C to C is correlated to the melting of PEO crystallites and is unaffected by IPDPST content.

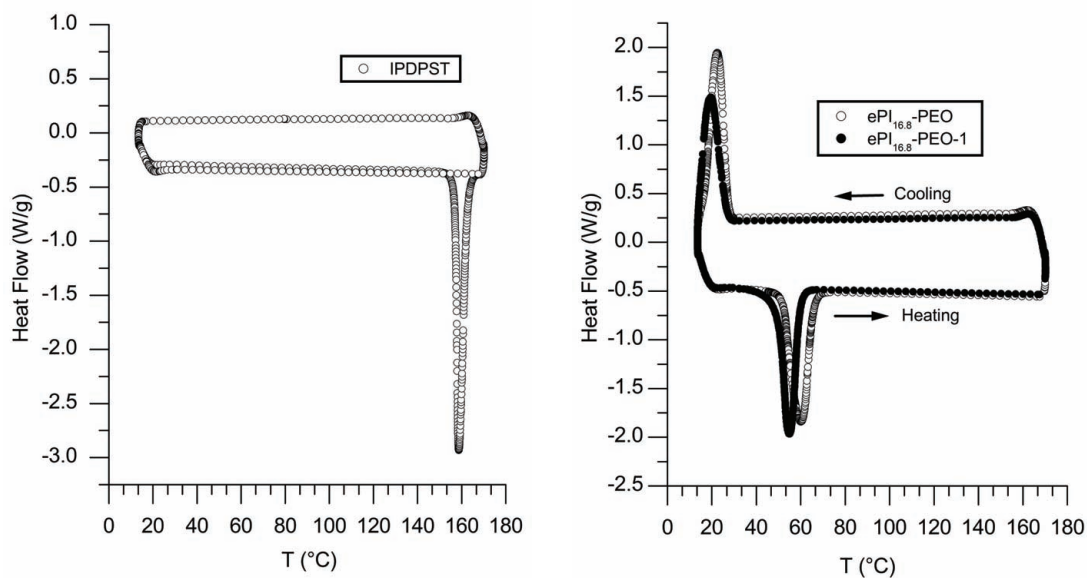


Figure 3-S2. Differential scanning calorimetry (DSC) of the neat IPDPST (left), ePI_{16.8}-PEO, and ePI_{16.8}-PEO-1 (right). Neat IPDPST exhibits a melting transition at 158 °C which is no longer present when blended with the ePI_{16.8}-PEO. Notably, the PEO melting transition in ePI_{16.8}-PEO is still present in the blend with IPDPST. Small shifts in the position of the melting transition cannot rule out the presence of the IPDPST in the PEO domains, but the rapid curing kinetics suggest its location is sufficient to activate curing in the ePI domains.

CHAPTER 4 — SUPPLEMENTARY INFORMATION — ACCESS TO
 NANOSTRUCTURED HYDROGEL NETWORKS THROUGH PHOTOCURED BODY-
 CENTERED CUBIC BLOCK COPOLYMER MELTS

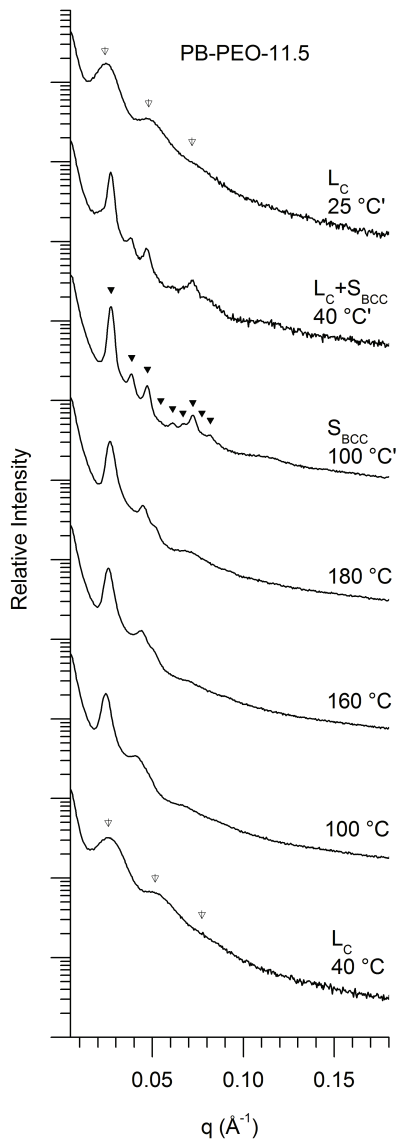


Figure 4-S1. SAXS data for PB-PEO-11.5 along a complete heating and cooling (designated with primes) thermal cycle. Morphologies observed during heating include a distorted lamellae-like crystalline phase (L_C), an initial melt phase consisting of a transition between the original distorted lamellar-like morphology and a liquid-like packing of spherical domains, and finally a pure S_{BCC} phase. Upon cooling, a mixed ($L_C + S_{BCC}$) phase is present before complete adoption of the L_C phase. Inverted triangles represent the location of the allowed reflections for the designated morphology, based on the position of the primary scattering wave vector $q^* = q_{100}$ (absent for S_{BCC}): (L_C) q/q^* at $\sqrt{1}, \sqrt{4}, \sqrt{9}$, etc.; (S_{BCC}) q/q^* at $\sqrt{2}, \sqrt{4}, \sqrt{6}, \sqrt{8}, \sqrt{10}, \sqrt{12}, \sqrt{14}, \sqrt{16}, \sqrt{18}$, etc.

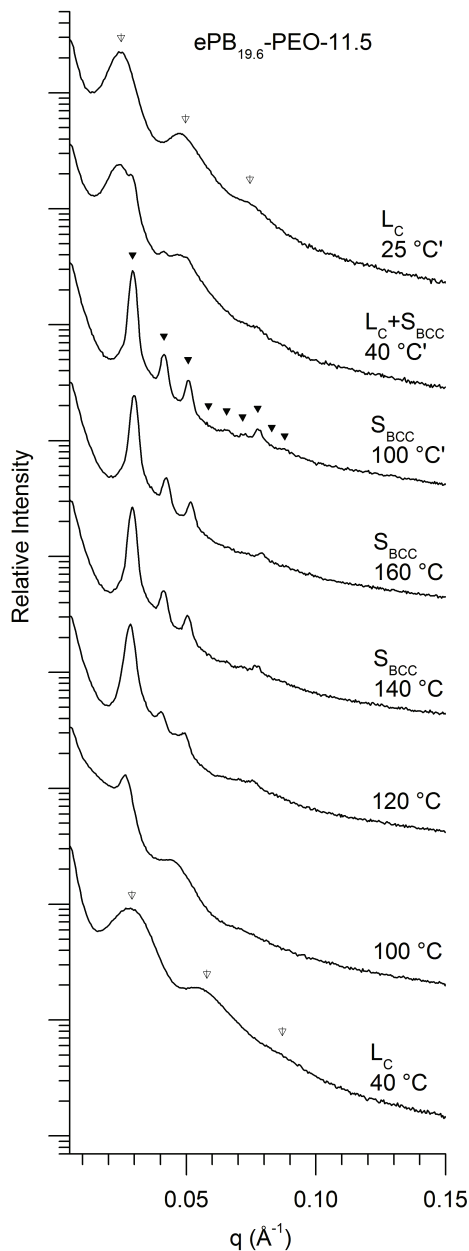


Figure 4-S2. SAXS data for ePB_{19.6}-PEO-11.5 along a complete heating and cooling (designated with primes) thermal cycle. Morphologies observed during heating include a distorted lamellae-like crystalline phase (L_C), an initial melt phase consisting of a transition between the original distorted lamellar-like morphology and a liquid-like packing of spherical domains, and finally a pure S_{BCC} phase. Upon cooling, a mixed ($L_C + S_{BCC}$) phase is present before complete adoption of the L_C phase. Inverted triangles represent the location of the allowed reflections for the designated morphology, based on the position of the primary scattering wave vector $q^* = q_{100}$ (absent for S_{BCC}): (L_C) q/q^* at $\sqrt{1}$, $\sqrt{4}$, $\sqrt{9}$, etc.; (S_{BCC}) q/q^* at $\sqrt{2}$, $\sqrt{4}$, $\sqrt{6}$, $\sqrt{8}$, $\sqrt{10}$, $\sqrt{12}$, $\sqrt{14}$, $\sqrt{16}$, $\sqrt{18}$, etc.

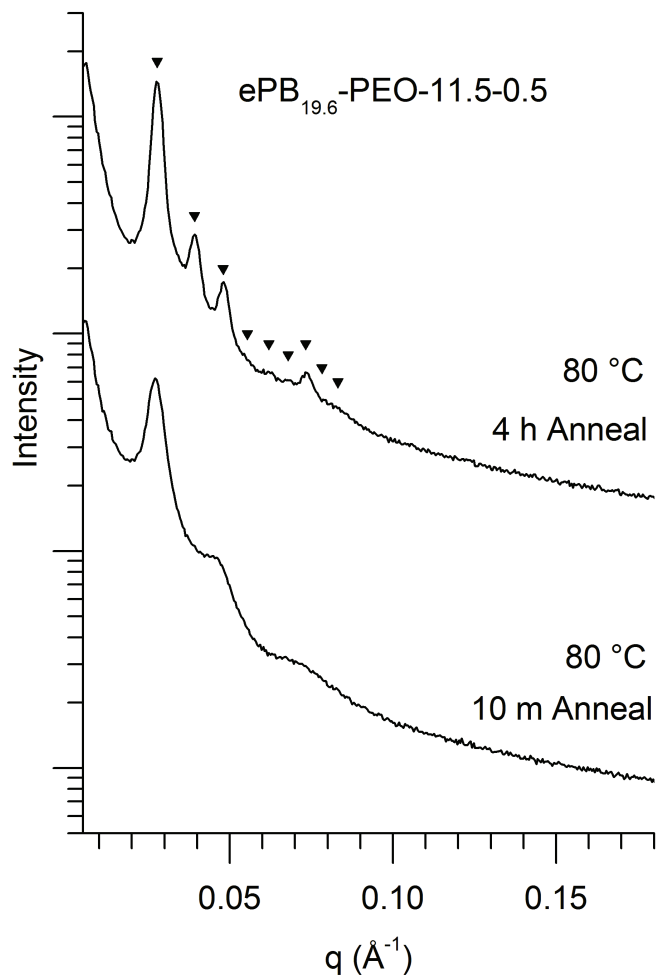


Figure 4-S3. Annealing experiment with $ePB_{19.6}-PEO-11.5-0.5$ at 80 °C results in highly ordered spheres after several hours. Alternatively, one can choose to heat above the phase transition as observed in the rheology around 110 °C (see main text) to obtain highly ordered spheres.

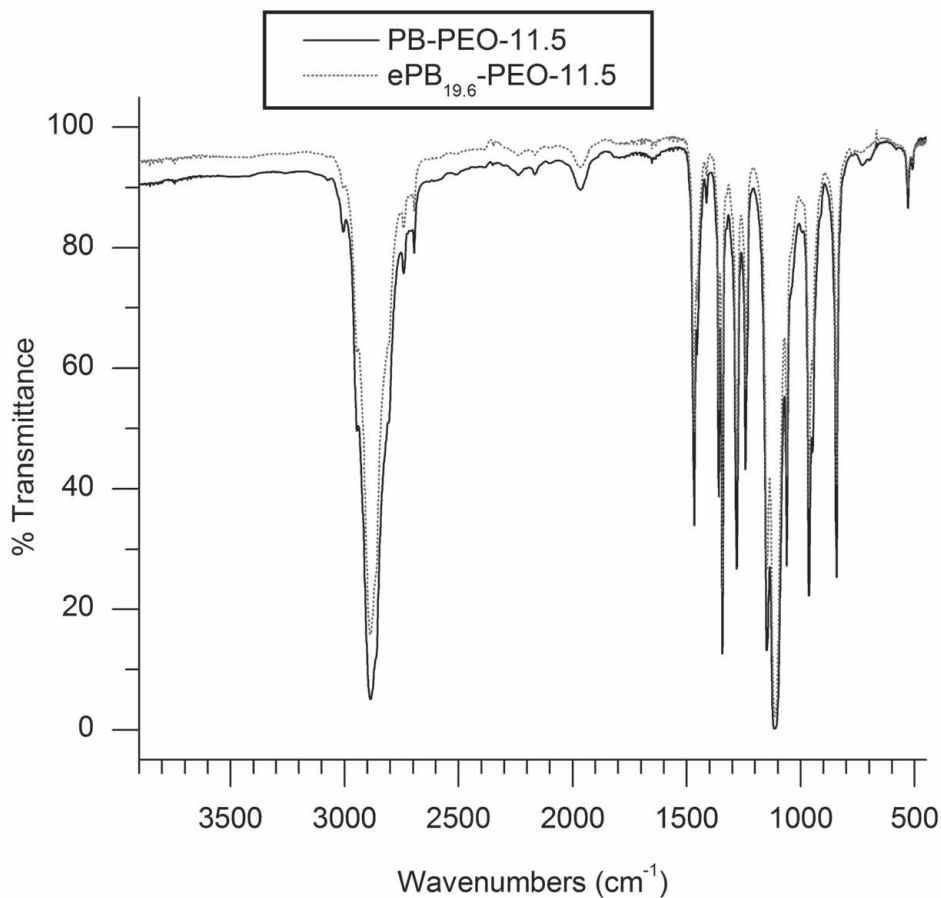


Figure 4-S4. FT-IR Data comparing ePB_{19.6}-PEO-11.5 and PB-PEO-11.5. The epoxide groups display IR signals in the same regions as PEO, as documented in the following references (ePB: De Risi, F. R.; D'ilario L.; Martinelli, A. *J. Polym. Sci.:Part A Polym. Chem.* **2004**, *42*, 3082-3090; PEO: Dissanayake, M. A. K. L.; Frech, R. *Macromolecules* **1995**, *28*, (15), 5312-5319.), and as shown in the above overlay. The large quantity of PEO in the system overwhelms the contributions to the FT-IR signals from both the new PEO (cross-links) and residual unreacted epoxide groups, prohibiting accurate analysis of the progression of the cross-linking reaction in these systems.

CHAPTER 7 — SUPPLEMENTARY INFORMATION — SYNTHESIS AND ORDERED
PHASE SEPARATION OF IMIDAZOLIUM-BASED ALKYL-IONIC DIBLOCK
COPOLYMERS MADE VIA ROMP

Materials and General Procedures

1-Bromohexane, 1-dodecanol, 5-norbornene-2-carboxylic acid, ethyl vinyl ether, and oxalyl dichloride were purchased from the Sigma Aldrich Co., and used as received. Dicyclopentadiene and 1-vinylimidazole were purchased from TCI America, and used as received. Lithium bis(trifluoromethylsulfonyl)amide (LiTf₂N) was purchased as Fluorad™ Lithium Trifluoromethane Sulfonimide from the 3M Company. All solvents were purchased from Sigma Aldrich or Mallinckrodt, Inc., and purified/dehydrated via N₂-pressurized activated alumina columns, and de-gassed. Additionally, the CH₂Cl₂ used as the solvent in ring-opening metathesis polymerization (ROMP) reactions was purified by re-filtering over activated alumina prior to de-gassing. The H₂O used for synthesis was purified and deionized, with resistivity greater than 12 MΩ cm⁻¹. All chemical syntheses were carried out in a dry argon atmosphere using standard Schlenk line techniques, unless otherwise noted. Silica gel purification was performed using 230–400 mesh, normal-phase silica gel purchased from Sorbent Technologies.

Instrumentation

¹H and ¹³C NMR spectra were obtained using a Bruker 300 Ultrashield™ (300 MHz for ¹H) spectrometer. Chemical shifts are reported in ppm relative to residual non-deuterated solvent. Fourier-transform infrared spectroscopy (FT-IR) measurements were performed using a Matteson Satellite series spectrometer (neat, thin film samples on Ge crystals). HRMS (ES) analysis was performed by the Central Analytical Facility in the Dept. of Chemistry and Biochemistry at the University of Colorado, Boulder. Differential scanning calorimetry (DSC) measurements were performed using a Mettler Toledo DSC823^e and a Julabo FT100 Intracooler. Gel permeation chromatography (GPC) spectra were collected using a Viscotek GPC-Max chromatography system outfitted with three 7.5 x 340 mm Polypore™ (Polymer Laboratories) columns in series, a Viscotek differential refractive index (RI) detector, and an

Alltech column oven (mobile phase THF, 40 °C, 1 mL min⁻¹). Molecular weight data obtained on this GPC system were referenced to polystyrene molecular weight standards. NMR diffusion ordered spectroscopy (DOSY) experiments were performed using a Varian Inova-400 NMR spectrometer. Small-angle X-ray scattering (SAXS) data was collected using a Rigaku S-Max 3000 High Brilliance three-pinhole SAXS system outfitted with a MicroMax-007HFM rotating anode (CuK α), Confocal Max-Flux Optic, Gabriel multi-wire area detector, and a Linkam thermal stage. Polymer samples were sandwiched between Kapton discs. Exposure times for samples were typically on the order of 600–1200 s. Rheological experiments were run using a TA Instruments Advanced Rheometric Expansion System (ARES) rheometer. Samples were roughly formed as discs and then positioned between two parallel plates (8 mm diameter). The gap was reduced and adjusted to ensure even distribution of the sample. Gaps were ~0.5 mm. Dynamic temperature ramp tests were performed while heating and cooling at 1 °C min⁻¹ at an angular frequency of 1 rad s⁻¹ and a strain of 1% (linear viscoelastic regime).

Bicyclo[2.2.1]hept-5-ene-2-carboxylic acid dodecyl ester (endo:exo 80:20) (2)

5-Norbornene-2-carboxylic acid (5.01 g, 0.0366 mol, predominantly endo) and DMF (2 mL) were stirred in CH₂Cl₂ (100 mL). Oxalyl dichloride (6.9 g, 0.055 mol) was added dropwise to the mixture at 0 °C, and the reaction mixture was stirred at room temperature for 18 h. The reaction mixture was then concentrated in vacuo (35 °C, 100 mtorr) before the addition of THF (70 mL), triethylamine (5 mL) and 1-dodecanol (6.6803 g, 0.035850 mol) at room temperature. After stirring for 24 h, the reaction mixture was then dried with anhydrous MgSO₄, filtered, and concentrated in vacuo (20 °C, 100 mtorr). The crude product was purified by silica gel column chromatography using a 75/25 hexanes/ethyl acetate (v/v) solution as the eluent. The final product was concentrated from the eluate in vacuo as a yellow oil (8.645 g, 78%). ¹H NMR (300 MHz, CDCl₃): δ 6.36–5.76 (m, 2H), 4.26–3.81 (m, 2H), 3.40–2.12 (m, 3H), 2.10–1.77 (m, 1H), 1.77–0.70 (m, 26H). ¹³C NMR (75 MHz, CDCl₃): δ 176.3, 174.8, 138.0, 137.7, 135.8, 132.4, 64.6, 64.3, 49.6, 46.6, 46.4, 45.7, 43.4, 43.2, 42.5, 41.6, 31.9, 30.3, 29.6, 29.6, 29.5, 29.3, 29.2, 29.1,

28.7, 25.9, 22.7, 14.1. IR (neat): 3064.1, 2952.9, 2929.6, 2854.4, 1735.6, 1467.6, 1384.5, 1334.9, 1272.2, 1184.8 cm^{-1} . HRMS (ES) calcd. for $\text{C}_{20}\text{H}_{34}\text{O}_2\text{Na}$ (M Na^+): 329.2451; observed: 329.2440.

1-Bicyclo[2.2.1]hept-5-en-2-ylmethyl-1H-imidazole (endo:exo 80:20) (4)

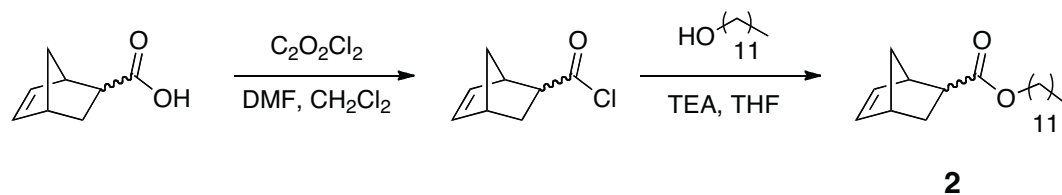
1-Allylimidazole (12.4 g, 0.115 mol) and dicyclopentadiene (3.79 g, 0.0287 mol) were stirred neat at 172 °C for 24 h. Excess 1-vinylimidazole was removed from the reaction mixture via vacuum distillation (100 mtorr, 40 °C). The remaining distillant was loaded onto a silica gel separation column, rinsed with hexanes (400 mL), and eluted with 10:4:0.8 (v/v/v) mixture of acetone/ CH_2Cl_2 /MeOH. After removal of the solvent in vacuo, pure **4** was isolated as a brown oil (8.47 g, 85%). ^1H NMR (300 MHz, CDCl_3): δ 7.45 (d, $J = 15.5$, 1H), 7.17–6.97 (m, 1H), 6.92 (dt, $J = 5.4$, 1.2, 1H), 6.35–5.93 (m, 2H), 3.78 (dddd, $J = 33.8$, 22.9, 13.8, 8.1, 2H), 2.99–2.20 (m, 3H), 1.89 (ddd, $J = 11.8$, 9.2, 3.8, 1H), 1.59–1.07 (m, 2H), 0.63 (ddd, $J = 11.8$, 4.4, 2.6, 1H). ^{13}C NMR (75 MHz, CDCl_3): δ 138.5, 137.2, 137.1, 137.0, 136.0, 131.6, 129.4, 129.3, 118.9, 118.8, 52.2, 50.9, 49.5, 44.8, 44.1, 44.1, 42.4, 41.8, 40.4, 40.6, 31.0, 30.1. IR (neat): 3131.6, 3105.4, 3057.4, 2960.0, 2940.4, 2868.5, 1648.2, 1568.8, 1505.4, 1448.4, 1394.1 cm^{-1} HRMS (ES) calcd. for $\text{C}_{11}\text{H}_{14}\text{N}_2\text{Na}$ (M Na^+): 197.1049; observed: 197.1053.

3-Bicyclo[2.2.1]hept-5-en-2-ylmethyl-1-hexyl-3H-imidazolium-bis(trifluoromethylsulfon-yl)amide (endo:exo 80:20) (3)

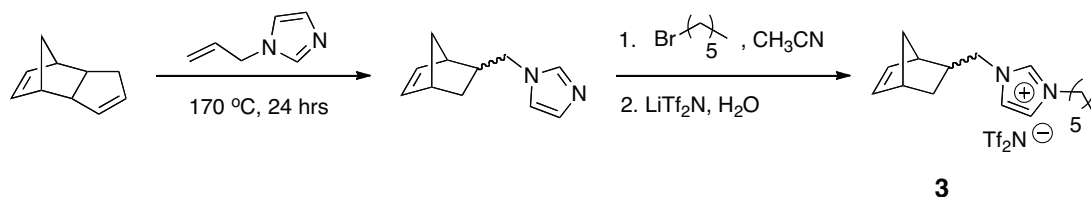
Compound **4** (2.00 g, 0.0115 mol) and 1-bromohexane (3.79 g, 0.0230 mol) were stirred in acetonitrile at reflux for 18 h. Upon cooling, the reaction mixture was concentrated to form a yellow viscous oil and washed with Et_2O (3 x 100 mL). The resulting oil was then dissolved in H_2O (100 mL), LiTf_2N (3.63 g, 0.0127 mol) was added, and the mixture stirred at room temperature for 12 h. A yellow oil was then extracted from this aqueous mixture with CH_2Cl_2 (3 x 50 mL). The CH_2Cl_2 layer was then washed with H_2O (3 x 150 mL), dried with anhydrous MgSO_4 , filtered, and concentrated to give monomer **3** as a yellow oil (yield: 5.33 g, 83%). ^1H NMR (300 MHz, CDCl_3): δ 8.83 (d, $J = 23.9$, 1H), 7.36 (ddd, $J = 7.2$, 4.0, 1.9, 2H), 6.47–5.87 (m, 2H), 4.46–3.73 (m, 4H), 3.07–2.42 (m, 3H), 2.09–1.72 (m, 3H), 1.61–0.52 (m, 11H). ^{13}C NMR (75

MHz, CDCl₃): δ 139.3, 137.5, 135.6, 135.4, 135.2, 130.8, 126.1, 122.4, 122.4, 122.3, 122.2, 121.8, 117.6, 113.3, 54.8, 54.0, 50.1, 49.5, 44.9, 44.1, 42.4, 41.8, 39.8, 30.9, 30.6, 30.1, 29.8, 25.7, 22.3, 13.8. IR (neat): 3147.47, 3114.20, 3089.90, 2960.89, 2937.45, 2872.85, 1563.32, 1456.09, 1348.19, 1331.51, 1225.74, 1183.60, 1135.87, 1054.68 cm⁻¹. HRMS (ES) calcd. for C₁₉H₂₇F₆N₃O₄S₂ (M⁺ Tf₂N⁻): 798.3516; observed: 798.3498.

General Procedure for ROMP of Monomers 2 and 3 to Form Diblock Copolymers



Scheme 7-S1. Synthesis scheme for hydrophobic alkyl-functionalized norbonene monomer **2**.

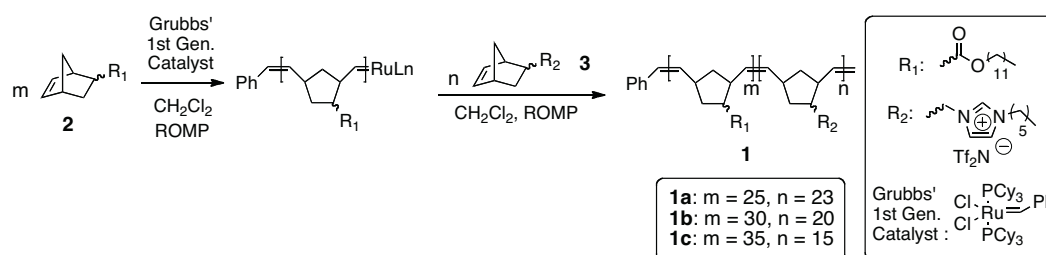


Scheme 7-S2. Synthesis scheme for imidazolium-functionalized norbonene monomer **3**.

A flame-dried Schlenk flask was charged with the desired amount of Grubbs 1st-generation catalyst and a stirbar under argon. The appropriate amount of CH₂Cl₂ was then added to the Schlenk flask to form a catalyst solution with the desired concentration. The appropriate amount of the first monomer (**2**) was then added to the catalyst solution from a dry, degassed stock solution (CH₂Cl₂ solvent) via syringe under argon atmosphere. Upon consumption of all of the monomer (as verified by ¹H NMR analysis) to form the first copolymer block, the second monomer (**3**) was added from a dry, degassed stock solution (CH₂Cl₂ solvent) via syringe. Upon complete consumption of monomer **3** (as verified by ¹H NMR analysis), the ROMP diblock

copolymerization mixture was quenched with excess of ethyl vinyl ether. The resulting diblock copolymer was then isolated by removal of the solvent in vacuo. NMR analysis of polymers **1a–c** confirmed the absence of any residual monomers.

Procedure for Sequential ROMP of Monomers 2 and 3 to Form Diblock Copolymer 1a



Scheme 7–S3. ROMP polymerization of diblock copolymers **1a**, **1b**, and **1c**.

Under argon atmosphere, Grubbs' 1st-generation catalyst (16.4 mg, 0.0199 mmol) was dissolved in dry, degassed CH_2Cl_2 (0.75 mL). Monomer **2** (7.65 g, 24.9 mmol) was diluted to a total volume of 25 mL with dry, gas-free CH_2Cl_2 . From this monomer solution, 0.49 mL (0.49 mmol) was added to the catalyst solution, and the reaction mixture stirred at room temperature until the polymerization of **2** was complete (3 h). Monomer **3** (13.5 g, 25.1 mmol) was diluted to a total volume of 25 mL with dry, gas-free CH_2Cl_2 . From this monomer solution, monomer **3** (0.49 mL, 0.49 mmol) was then added to the living ROMP polymerization mixture containing polymerized **2**, and the reaction stirred at room temperature for 12 h. The ROMP copolymerization mixture was then quenched by addition of excess ethyl vinyl ether (1 mL). The resulting diblock copolymer **1a** was isolated by removal of the solvent and other volatile compounds in vacuo at ambient temperature for 24 h (0.435 g, 99%). ^1H NMR (300 MHz, CDCl_3) δ 8.50–8.75 (br s, imidazolium C2), 7.47–7.27 (br s, imidazolium C4 and C5), 5.27–5.52 (b, $-\text{C}(\text{H})=\text{C}(\text{H})-$), 3.75–4.45 (b, $-\text{COO}-\text{CH}_2-$, $-\text{C}(\text{H})_2-\text{N}-\text{CH}-\text{N}-\text{C}(\text{H})_2-(\text{CH}_2)_4\text{CH}_3$), 2.35–3.15 (br m, $-\text{imidazolium}-(\text{CH}_2)_5-\text{CH}_3$), 1.50–2.25 (b, $-\text{COO}-(\text{CH}_2)_{11}-\text{CH}_3$), 0.95–1.45 (br m, $-\text{COO}-\text{CH}_2-$

$(\text{CH}_2)_{10}-\text{CH}_3$), 0.72–0.90 (br m, –imidazolium– CH_2 – $(\text{CH}_2)_4$ – CH_3). ^{13}C NMR (75 MHz, CDCl_3) δ 121.9, 117.7, 76.6, 31.9, 30.8, 29.5, 28.7, 26.1, 25.6, 22.7, 22.2, 14.1, 13.7. Block repeat unit molar ratio = 1:0.90 (alkyl: imidazolium); block length composition = 25–*b*–23; estimated M_n = 20,100 g mol^{-1} (calculated based on ^1H NMR repeat unit integrals, monomer-to-catalyst ratio for a living polymerization, and repeat unit molecular weights. See following sections for details on how the copolymer block composition, block lengths, and M_n were determined).

Procedure for Sequential ROMP of Monomers 2 and 3 to Form Diblock Copolymer 1b

Under argon atmosphere, Grubbs' 1st-generation catalyst (22.3 mg, 0.0271 mmol) was dissolved in dry, gas-free CH_2Cl_2 (2.0 mL). Monomer 2 (3.07 g, 10.0 mmol) was diluted to a total volume of 10 mL with dry, gas-free CH_2Cl_2 . From this monomer solution, monomer 2 (0.81 mL, 0.81 mmol) was added to the catalyst solution, and the reaction was mixture stirred at room temperature until the polymerization of 2 was complete as determined by ^1H NMR analysis (5 h). Monomer 3 (5.38 g, 9.98 mmol) was then diluted to a total volume of 10 mL with dry, gas-free CH_2Cl_2 . From this monomer solution, monomer 3 (0.54 mL, 0.54 mmol) was then added to the living ROMP reaction mixture containing polymerized 2, and the reaction mixture stirred at room temperature for 12 h. The ROMP copolymerization reaction was then quenched by adding ethyl vinyl ether (1 mL). The resulting diblock copolymer 1b was isolated by removal of the solvent and other volatile compounds in vacuo at ambient temperature for 24 h (0.561 g, 99%). ^1H NMR (300 MHz, CDCl_3) δ 8.50–8.75 (br s, imidazolium C2), 7.47–7.27 (br s, imidazolium C4 and C5), 5.27–5.52 (b, –C(H)=C(H)–), 3.75–4.45 (b, –COO– CH_2 –, –C(H) $_2$ –N–CH–N–C(H) $_2$ – $(\text{CH}_2)_4$ – CH_3), 2.35–3.15 (br m, –imidazolium– $(\text{CH}_2)_5$ – CH_3), 1.50–2.25 (b, –COO– $(\text{CH}_2)_{11}$ – CH_3), 0.95–1.45 (br m, –COO– CH_2 – $(\text{CH}_2)_{10}$ – CH_3), 0.72–0.90 (br m, –imidazolium– CH_2 – $(\text{CH}_2)_4$ – CH_3). ^{13}C NMR (75 MHz, CDCl_3) δ 121.9, 117.7, 76.6, 31.9, 30.8, 29.5, 28.7, 26.1, 25.6, 22.7, 22.2, 14.1, 13.7. Block repeat unit molar ratio = 1:0.66 (alkyl: imidazolium); block length composition = 30–*b*–20; estimated M_n = 20,000 g mol^{-1} (calculated based on ^1H NMR repeat unit integrals, monomer-to-catalyst ratio for a living polymerization,

and repeat unit molecular weights. See following sections for details on how the copolymer block composition, block lengths, and M_n were determined).

Procedure for Sequential ROMP of Monomers 2 and 3 to Form Diblock Copolymer 1c

Under argon atmosphere, Grubbs' 1st-generation catalyst (18.6 mg, 0.0226 mmol) was dissolved in dry, degassed CH_2Cl_2 (2.0 mL). Monomer **2** (3.07 g, 10.0 mmol) was diluted to a total volume of 10 mL with dry, gas-free CH_2Cl_2 . From this monomer solution, monomer **2** (0.79 mL, 0.79 mmol) was added to the catalyst solution, and the reaction mixture was stirred at room temperature until the polymerization of **2** was complete as determined by ^1H NMR analysis (5 h). Monomer **3** (5.38 g, 9.98 mmol) was then diluted to a total volume of 10 mL with dry, gas-free CH_2Cl_2 . From this monomer solution, monomer **3** (0.34 mL, 0.34 mmol) was added to the living ROMP polymerization mixture containing polymerized **2**, and the reaction stirred at room temperature until the polymerization of **3** was complete by ^1H NMR analysis (12 h). The ROMP copolymerization reaction was then quenched by addition of ethyl vinyl ether (1 mL). The resulting diblock copolymer **1c** was isolated by removal of the solvent and other volatile compounds in vacuo at ambient temperature for 24 h (0.431 g, 98%). ^1H NMR (300 MHz, CDCl_3) δ 8.50–8.75 (br s, imidazolium C2), 7.47–7.27 (br s, imidazolium C4 and C5), 5.27–5.52 (b, $-\text{C}(\text{H})=\text{C}(\text{H})-$), 3.75–4.45 (b, $-\text{COO}-\text{CH}_2-$, $-\text{C}(\text{H})_2-\text{N}-\text{CH}-\text{N}-\text{C}(\text{H})_2-(\text{CH}_2)_4\text{CH}_3$), 2.35–3.15 (br m, $-\text{imidazolium}-(\text{CH}_2)_5-\text{CH}_3$), 1.50–2.25 (b, $-\text{COO}-(\text{CH}_2)_{11}-\text{CH}_3$), 0.95–1.45 (br m, $-\text{COO}-\text{CH}_2-(\text{CH}_2)_{10}-\text{CH}_3$), 0.72–0.90 (br m, $-\text{imidazolium}-\text{CH}_2-(\text{CH}_2)_4-\text{CH}_3$). ^{13}C NMR (75 MHz, CDCl_3) δ 121.9, 117.7, 76.6, 31.9, 30.8, 29.5, 28.7, 26.1, 25.6, 22.7, 22.2, 14.1, 13.7. Block repeat unit length molar ratio = 1: 0.42; block length composition = 35–b–15; estimated M_n = 18,800 g mol^{-1} (calculated based ^1H NMR repeat unit integrals, monomer-to-catalyst ratio for a living polymerization, and repeat unit molecular weight. See following sections for details on how the copolymer block composition, block lengths, and M_n were determined). **Note on the use of solvents for NMR analysis of the BCPs:** Even though the BCPs show foaming behavior in CDCl_3 when agitated, we were able to use CDCl_3 as NMR solvent because we used lower BCP

loading levels, minimized the amount of solution agitation, and allowed the CDCl_3 solutions to settle and reach a non-foaming steady state before NMR analysis.

Determination of BCP Composition and Molecular Weights

Conventional methods used to experimentally and directly determine the molecular weights values of **1a–c** (e.g., GPC, NMR end-group analysis, matrix-assisted laser desorption ionization time-of-flight mass spectrometry, and dynamic light scattering) were attempted, but all yielded inconclusive results. These difficulties were largely associated with the very different physical properties of these highly charged macromolecules (e.g., solubility) compared to typical non-charged polymers.^{1d} Consequently, the block composition ratios, overall lengths, and estimated M_n values of BCPs **1a–c** were determined via a combination of ^1H NMR-based repeat unit/block length composition analysis and confirmation of living polymerization behavior with predictable molecular weight control for both monomers, as described below:

Block composition ratios (Alkyl: imidazolium) were determined to compare the block length of the hydrophobic (alkyl) block to the block length of the imidazolium (ionic) block via ^1H NMR analysis. The signals for the unstrained backbone protons for both blocks overlap to create a broad peak between 5.00–5.75 ppm (signal C in Figures 7–S1–S3). The signals for the protons adjacent to the ester linker of the hydrophobic block (made by ROMP of monomer **2**) and the protons adjacent to the imidazolium ring of the ionic block (made by ROMP of monomer **3**) appear as a broad peak between 3.75–4.50 ppm (signal D in Figures 7–S1–S3). There are 2 unstrained backbone protons per repeat unit for the hydrophobic block (m) and 2 unstrained backbone protons per repeat unit for the ionic block (n) (see Equation 7–S1). There are 2 methylene protons adjacent to the ester linker per repeat unit for the hydrophobic block (m) and 4 methylene protons adjacent to the imidazolium ring per repeat unit for the ionic block (n) (see Equation 7–S2).

$$2m + 2n = C_{^1\text{H NMR Integration}} \quad \text{Equation 7–S1}$$

$$2m + 4n = D_{1H\text{ NMR Integration}}$$

Equation 7-S2

Using the two equations to solve for the two unknowns, m and n , the alkyl: imidazolium block composition ratios (m , n) can be quantified for each BCP sample **1a**, **1b**, and **1c**, as shown below:

Block Composition Ratio for BCP **1a** (Figure 7-S1):

$$2m + 2n = 4.07$$

$$2m + 4n = 6.00$$

$$m = 1.0, n = 0.90$$

Block Composition Ratio for BCP **1b** (Figure 7-S2):

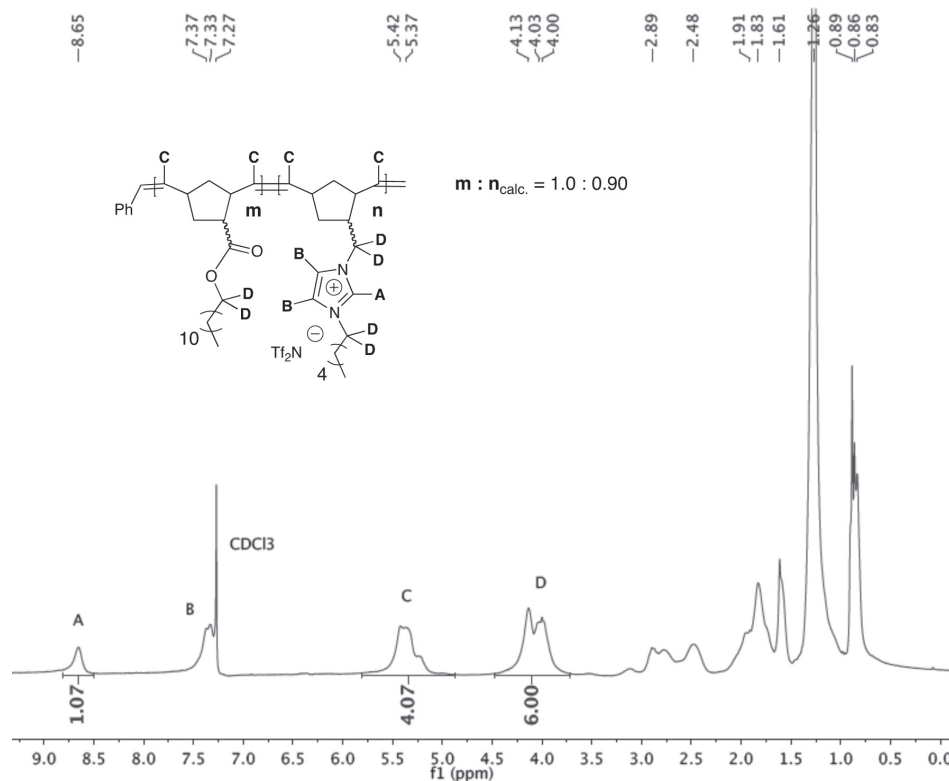


Figure 7-S1. An example ^1H NMR spectrum of BCP **1a**, and the ^1H NMR peak assignments used for calculating the alkyl: imidazolium block composition (i.e., repeat unit) ratio in **1a**.

$$2m + 2n = 4.29$$

$$2m + 4n = 6.00$$

$$m = 1.0, n = 0.66$$

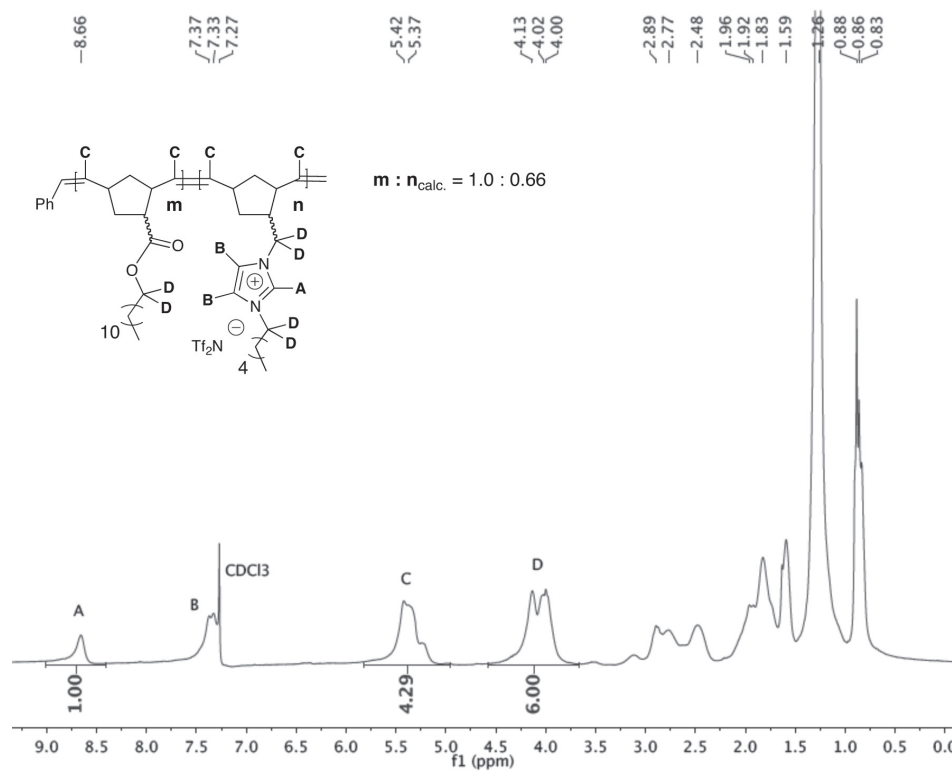


Figure 7-S2. An example ¹H NMR spectrum of BCP **1b**, and the ¹H NMR peak assignments used for calculating the alkyl:imidazolium block composition (i.e., repeat unit) ratio in **1b**.

Block Composition Ratio for BCP **1c** (Figure 7–S3):

$$2m + 2n = 4.63$$

$$2m + 4n = 6.00$$

$$m = 1.0, n = 0.42$$

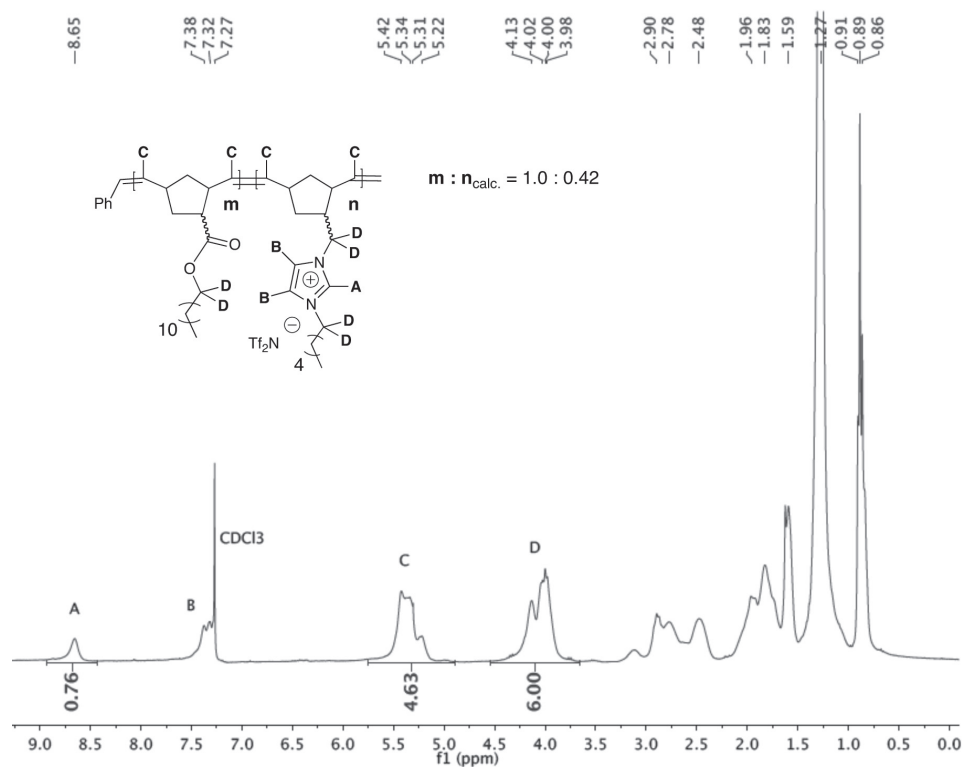
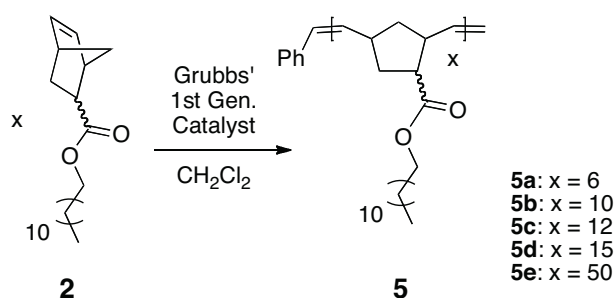


Figure 7–S3. An example ^1H NMR spectrum of BCP **1c**, and the ^1H NMR peak assignments used for calculating the alkyl:imidazolium block composition (i.e., repeat unit) ratio in **1c**.

Verification of living character with molecular weight control.

Systematic ROMP homopolymerizations of hydrophobic monomer **2** and imidazolium monomer **3** were used to help verify the linear molecular weight control and low PDI nature of these polymerization systems, in order to prepare the compositions and lengths of BCPs **1a–c**.

ROMP experiments with monomer **2** showed that increasing the monomer-to-catalyst ratio increases the (absolute) molecular weight of poly(**2**) samples in a linear fashion by ^1H NMR end-group analysis, indicative of a living polymerization with predictable molecular weight control. As can be seen in Figure S4, five samples of poly(**2**) (**5a–e**) were synthesized by polymerizing **2** with varying mole ratios of Grubbs' 1st-generation catalyst (Scheme 7–S4). The absolute number-average molecular weight (M_n) values of these model homopolymers were directly determined with ^1H NMR spectroscopy by integrating the distinct unstrained alkene backbone protons in the repeat units and comparing to those of the five phenyl endgroup protons from the catalyst initiation step. A linear relationship was observed between monomer-to-catalyst molar ratio used in the ROMP reactions and the absolute M_n values of the poly(**2**) samples formed (Figure 7–S4).



Scheme 7–S4. Hydrophobic poly(**2**) oligomers used for absolute M_n determination via ^1H NMR endgroup analysis in order to confirm living polymerization behavior.

In order to help verify the living character of the monomer **2** ROMP system with Grubbs' 1st generation catalyst, GPC analysis to obtain PDI information (THF solvent, polystyrene standards) of poly(**2**) prior to the addition of monomer **3** during sequential polymerizations yielded low PDI values (1.15–1.17) (Table 7–S1). This is also consistent with living polymerization behavior.

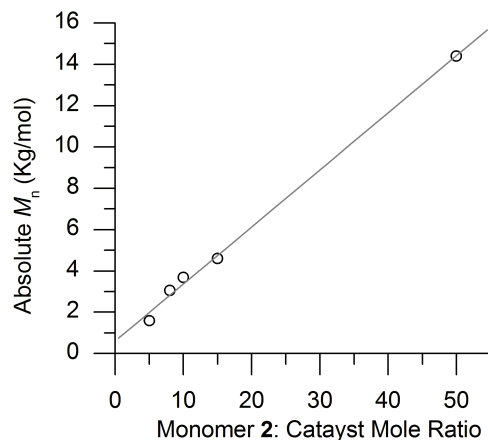


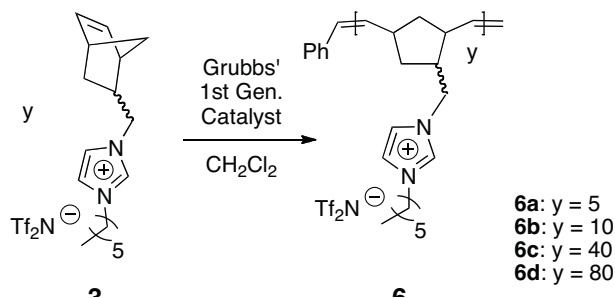
Figure 7-S4. Linear relationship between monomer-to-catalyst molar ratio used and absolute M_n from ^1H NMR endgroup analysis for various poly(**2**) oligomers. Note: this NMR-based polymer molecular weight data does not provide PDI information.

Table 7-S1. Relative M_n and M_w GPC Data (vs. Polystyrene Standards) and PDI Values for confirming the living ROMP of monomer **2**.

Poly(2) ROMP Experiment	Mon 2 : Cat Ratio	Relative M_n vs. PS stds ^a (g/mol)	Relative M_w vs. PS stds ^a (g/mol)	PDI
1 (precursor to 1a)	25: 1	14 500	16 800	1.16
2 (precursor to 1b)	30: 1	15 800	18 400	1.17
3 (precursor to 1c)	35: 1	21 000	24 000	1.15

^aThe raw M_n and M_w values obtained by GPC vs. PS stds are different than the expected absolute M_n and M_w values based on repeat unit molecular weights because Poly(**2**) is different than PS in solution.

Analogous experiments to verify the living ROMP character of monomer **3** with the Grubbs' 1st-generation catalyst were also performed. Unfortunately, the ionic poly(**3**) samples (like the BCPs) had sufficiently different solubility properties from conventional non-charged polymers^{1d} such that GPC analysis was inconclusive and did not yield any definitive PDI results. However, similar ^1H NMR end-group molecular weight analysis of model oligomers of poly(**3**) formed using varying monomer-to-catalyst ratios (**6a-d**) showed linearly increasing M_n values, again consistent with a living polymerization process (see Scheme 7-S5 and Figure 7-S5). This trend, coupled with the fact that a large number of norbornene-based monomers (including those with ionic substituents) are known to exhibit living ROMP behavior with Grubbs-type olefin metathesis catalysts,¹ suggests that the ROMP of **3** is living as well.



Scheme 7-S5. Imidazolium poly(3) oligomers used for absolute M_n determination via ^1H NMR endgroup analysis in order to confirm living polymerization behavior.

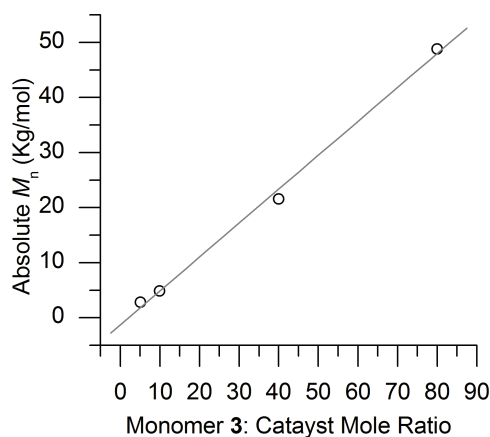


Figure 7-S5. Linear relationship between monomer-to-catalyst molar ratio used and absolute M_n from ^1H NMR endgroup analysis for various and poly(3) oligomers.

It is important to note that while the end-group protons (used to determine absolute M_n) for poly(3) homopolymers were distinct and separate from the imidazolium crown protons on ^1H NMR, end-group analysis could not be performed on the BCPs. This is because the formation of each BCP alters the chemical shift of the imidazolium crown protons such that they shift to overlap the end-group protons.

Calculating Block Length Composition

Based on the observed living characteristics for the ROMP of monomers **2** and **3** by the Grubbs 1st-generation catalyst, the block length compositions for the BCPs **1a-c** were calculated using the monomer-to-catalyst loading ratios (with complete monomer consumption as per a living po-

lymerization), and the observed block composition (i.e., repeat unit) ratios for each BCP via ^1H NMR analysis (see Equation 7–S3). The blocky polymer architecture and connectivity of **1a–c** are discussed and substantiated by the data presented in the main manuscript.

$$[(\text{Mon} : \text{Cat loading ratio})(m_{\text{block ratio}})] - b - [(\text{Mon} : \text{Cat loading ratio})(n_{\text{block ratio}})] \quad \text{Equation 7-3}$$

Block Length Composition for BCP **1a**:

$$[(25)(1.0)] - b - [(25)(0.90)] = 25 - b - 23$$

Block Length Composition for BCP **1b**:

$$[(30)(1.0)] - b - [(30)(0.66)] = 30 - b - 20$$

Block Length Composition for BCP **1c**:

$$[(35)(1.0)] - b - [(35)(0.42)] = 35 - b - 15$$

Calculating BCP Molecular Weight

As mentioned previously, conventional methods used to directly determine the molecular weights of BCPs **1a–c** (e.g., GPC, endgroup analysis, matrix-assisted laser desorption ionization time-of-flight mass spectrometry, and dynamic light scattering) were attempted, but all yielded inconclusive results. Consequently, the M_n value for each BCP **1a–c** was estimated by multiplying the calculated lengths of each block (as described in the preceding sections) with the molecular weight value of the appropriate repeat unit:

$$\text{BCP 1a:} \quad 25(307 \text{ g / mol}) + 23(540 \text{ g / mol}) \cong 20,100 \text{ g / mol}$$

$$\text{BCP 1b:} \quad 30(307 \text{ g / mol}) + 20(540 \text{ g / mol}) \cong 20,000 \text{ g / mol}$$

$$\text{BCP 1c:} \quad 35(307 \text{ g / mol}) + 15(540 \text{ g / mol}) \cong 18,800 \text{ g / mol}$$

Differential Scanning Calorimetry (DSC)

DSC studies on BCP **1a** revealed the presence of two distinct but broad thermal transitions

near $-28\text{ }^{\circ}\text{C}$ and $7\text{ }^{\circ}\text{C}$, consistent with crystallization of the *n*-dodecyl side chains on the poly(**2**) segments and the vitrification of the imidazolium blocks, respectively (Figure 7–S6). In comparison, DSC analysis of the two independent homopolymers showed that poly(**2**) has a thermal transition near $-35\text{ }^{\circ}\text{C}$, and that poly(**3**) has a broad thermal transition at ca. $-4\text{ }^{\circ}\text{C}$ (Figure 7–S6). BCPs **1b** and **1c** also show thermal transitions similar to BCP **1a**, with strong transitions at ca. $-28\text{ }^{\circ}\text{C}$ and weaker transitions at ca. $7\text{ }^{\circ}\text{C}$.

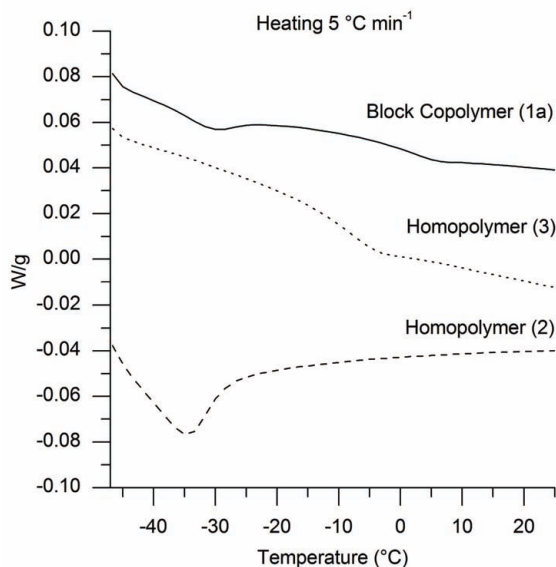


Figure 7–S6. DSC profiles of BCP **1a** and the respective homopolymers of **2** and **3**, performed at heating and cooling rates of $5\text{ }^{\circ}\text{C min}^{-1}$.

NMR DOSY Studies

NMR DOSY experiments were performed using a Varian Inova-400 NMR spectrometer at 400.157 MHz for ^1H observation in CD_2Cl_2 at 10 mg/mL. Gradients were calibrated to pure H_2O at $25.0\text{ }^{\circ}\text{C}$ such that $D_{(\text{H}_2\text{O})} = 29.9 \times 10^{-10}\text{ m}^2\text{ s}^{-1}$. Specific parameters were chosen as optimum to achieve nearly complete decay, and NMR diffusion data were processed using local covariance order DOSY (LOCODOSY).²

BCP 1a. The total gradient time (δ) used was 2.5 ms, the diffusion delay (Δ) was 90 ms, and 90° pulse-width (pw90) was 14.75 ms.

Physical Blend of (poly(2) + poly(3)). The total gradient time (δ) used was 2.0 ms, the diffusion delay (Δ) was 40 ms, and 90° pulse-width (pw90) was 13.8 ms.

Rheology

Measured dynamic elastic and loss moduli measured for BCPs **1a–c** were consistent with ordered block copolymer melts, with the general behavior typical of that observed for lamellar structured systems. Figure 7–S7 depicts the temperature dependence of those moduli for sample **1c**, as an example. Increased noise at higher temperatures is associated with instrument torque limitations prevalent when using the small sample (8mm diameter) parallel plate tool configuration.

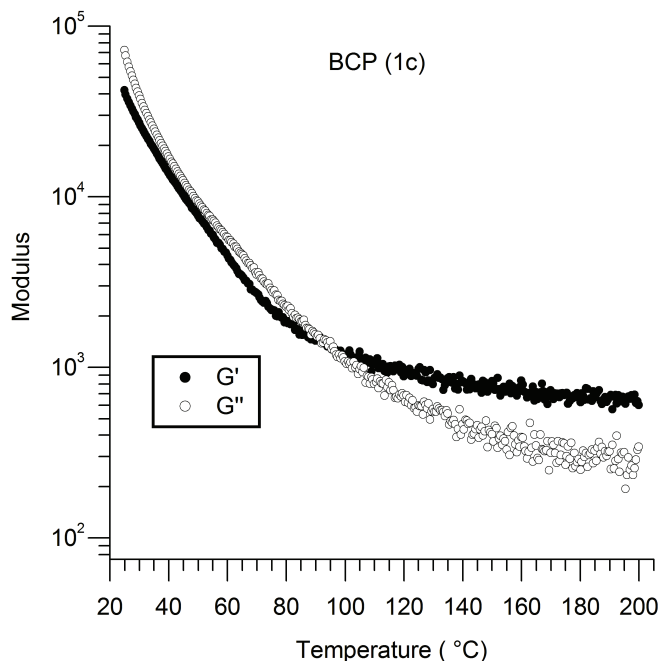


Figure 7–S7. Dynamic temperature ramp experiment data for 1c performed while heating at 1 °C min⁻¹ at an angular frequency of 1 rad s⁻¹ and a strain of 1%.

Preparation and Purification of Higher Length Homologues of BCPs 1a–c.

It is possible to prepare longer homologues of BCP platform **1** (e.g., 150–250 total repeat units) using the above procedures; however, with longer overall chain lengths, residual monomer has been observed in the resulting BCPs (2.5–9 mol%), thereby compromising sample purity. This residual monomer is very difficult to completely remove due to solubility complications and the ionic nature of the BCPs and monomer **3**.

References for Chapter 7 Supplementary Information

1. (a) Bielawski, C.; Grubbs, R. *Prog. Polym. Sci.*, **2007**, *32*, 1. (b) Lynn, D.; Mohr, B.; Grubbs, R.; Henling, L.; Day, M. *J. Am. Chem. Soc.*, **2000**, *122*, 6601. (c) Vygodskii, Y.; Shaplov, A.; Lozinskaya, E.; Filippov, O.; Shubina, E.; Bandari, R.; Buchmeiser, M. *Macromolecules*, **2006**, *39*, 7821. (d) Zheng, L.; Chen, F.; Xie, M.; Han, H.; Dai, Q.; Zhang, Y.; Song, C. *React. Funct. Polym.*, **2007**, *67*, 19.
2. Colbourne, A.; Morris, G.; Nilsson, M. *J. Am. Chem. Soc.*, **2011**, *133*, 7640.

CHAPTER 8 — SUPPLEMENTARY INFORMATION — MORPHOLOGICAL PHASE BEHAVIOR OF POLY(RTIL) CONTAINING DIBLOCK COPOLYMER MELTS

Table 8–S1. Summary of Poly(RTIL)-Based Diblock Copolymer Samples.

Lab Notebook Sample Name	Published Name	$m : n$	$M_n(\text{DOD})$	$M_n(\text{IMD})$	wt % _(DOD)	f_{DOD}	Morphological Behavior
III-064	1A	48.5 : 1.4	14 900	800	0.95	0.96	LLP → Dis
III-065	1B	47.0 : 3.8	14 400	2000	0.88	0.89	LLP
III-066	1C	45.0 : 5.6	13 800	3000	0.82	0.84	LLP → S _{BCC}
III-067	1D	43.5 : 6.9	13 400	3700	0.78	0.81	LLP → Hex
III-068	1E	42.0 : 9.5	12 900	5100	0.71 ₆	0.74 ₇	LLP → Hex
III-069	1F	40.0 : 9.1	12 300	4900	0.71 ₅	0.74 ₆	LLP → Hex
III-070	1G	38.5 : 11.3	11 800	6100	0.66	0.69	Lam + Hex
III-091	1H	37.5 : 12.8	11 500	6900	0.63	0.66	Lam + Hex
III-074	1I	36.5 : 13.9	11 200	7500	0.60	0.64	Lam + Hex
III-092	1J	35.6 : 14.4	10 900	7800	0.58	0.62	Lam
III-076	1K	30.0 : 12.8	9200	6900	0.57	0.61	Lam
III-072	1L	32.0 : 18.0	9800	9700	0.50	0.54	Lam
III-093	1M	7.5 : 5.0	2300	2650	0.46 ₅	0.50 ₄	Lam
III-037	1N	30.0 : 20.0	9200	10 800	0.46 ₀	0.50 ₀	Lam
III-075	1O	15.0 : 10.3	4600	5600	0.45	0.49	Lam
III-107	1P	25.0 : 23.0	7700	12 400	0.38	0.42	Lam

Thermogravimetric Analysis (TGA)

TGA was performed on BCPs **1A–P** in order to determine decomposition temperatures for each BCP. Decomposition onset temperatures were similar and ranged in value from 341.8 °C to 353.7 °C, with an average decomposition onset temperature of 347.8 °C.

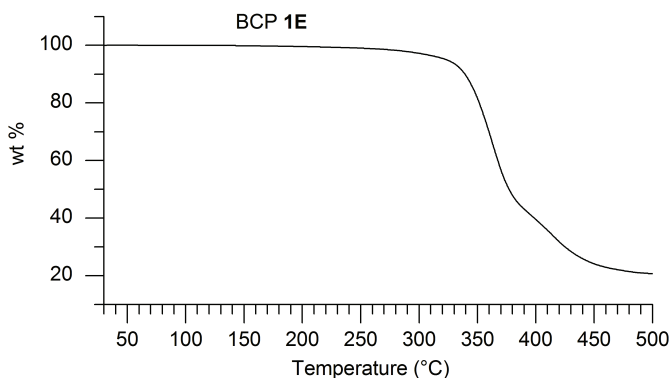


Figure 8–S1. Example TGA analysis profile of BCP 1E under N₂ (temperature ramp rate: 20 °C min⁻¹).

The following pages include:

- 1) Temperature dependent SAXS data (heating and cooling) for BCPs **1A–1D**. Inverted open triangles represent the locations of allowed reflections for the Hex morphology, based on the position of the primary scattering wave vector $q^* = q_{100}$; q/q^* at $\sqrt{1}$, $\sqrt{3}$, $\sqrt{4}$, $\sqrt{7}$, $\sqrt{9}$, $\sqrt{12}$, $\sqrt{13}$ etc, inverted solid triangles represent the locations of allowed reflections for the Lam morphology, $q^* = q_{100}$; q/q^* at $\sqrt{1}$, $\sqrt{4}$, $\sqrt{9}$, $\sqrt{16}$, $\sqrt{25}$, $\sqrt{36}$, and inverted triangles with a center vertical line represent the locations of allowed reflections for the S_{BCC} morphology, based on the position of the primary scattering wave vector $q^* = q_{100}$ (absent for S_{BCC}); q/q^* at $\sqrt{2}$, $\sqrt{4}$, $\sqrt{6}$, $\sqrt{8}$, $\sqrt{10}$, $\sqrt{12}$, $\sqrt{14}$ etc.
- 2) Dynamic temperature ramps for BCPs **1A–1D** at 1 °C min⁻¹, 1 rad s⁻¹ and a chosen strain rate within the linear viscoelastic regime (denoted in figure captions).

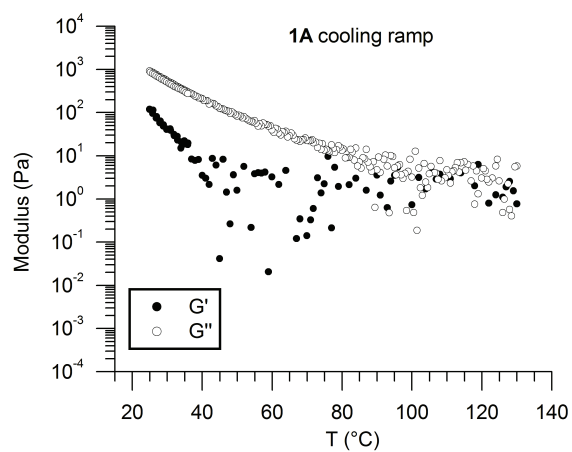
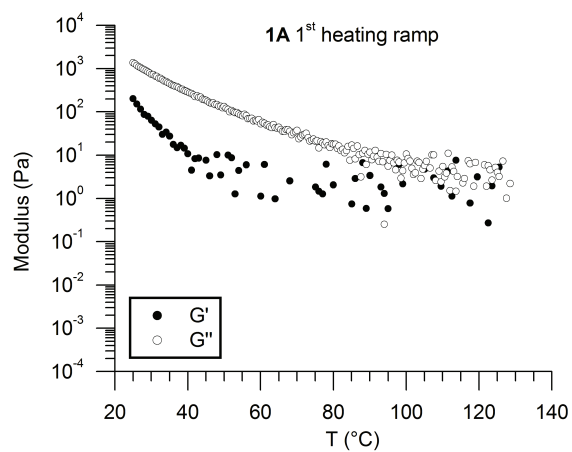


Figure 8-S2. Temperature ramps of BCP 1A, $f_{\text{DOD}} = 0.96$ at $1 \text{ }^\circ\text{C min}^{-1}$, 1 rad s^{-1} and 30 % strain.

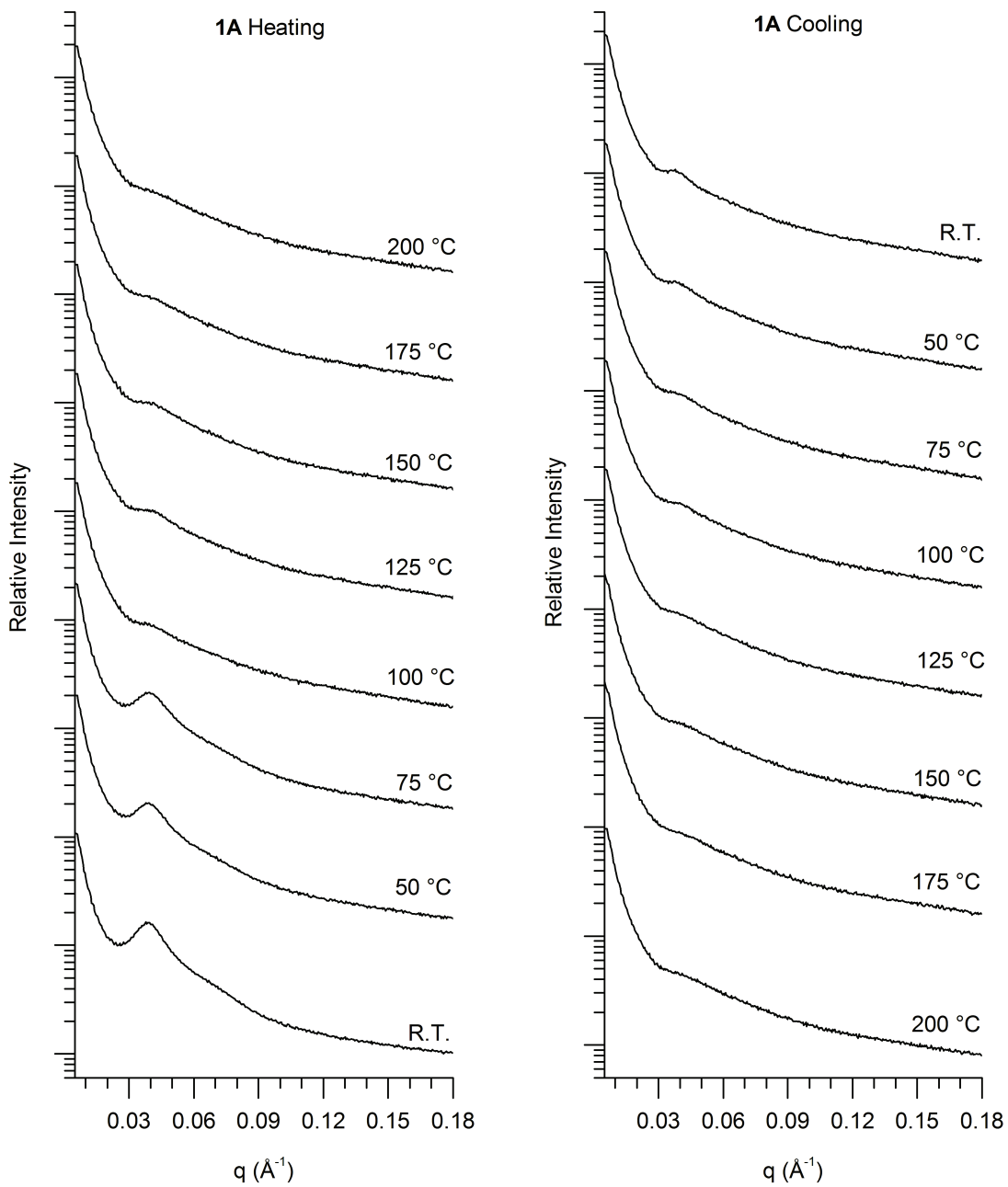
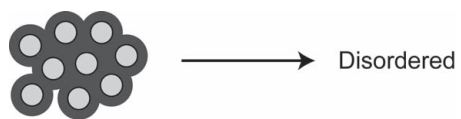


Figure 8-S3. Temperature dependent SAXS data for BCP 1A, $f_{\text{DOD}} = 0.96$.

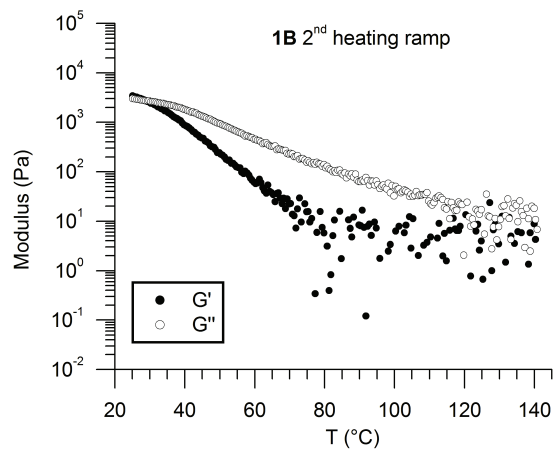
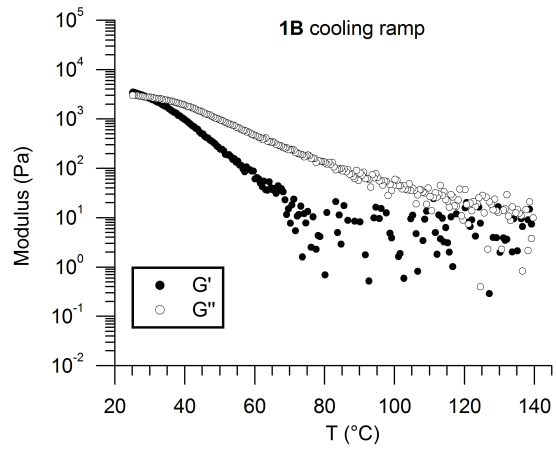
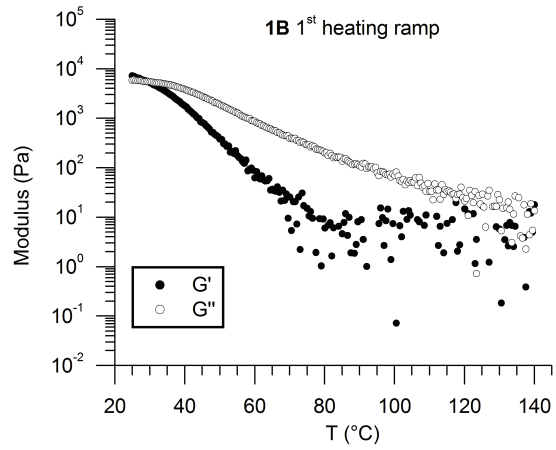


Figure 8-S4. Temperature ramps of BCP 1B, $f_{DOD} = 0.89$ at $1\text{ }^\circ\text{C min}^{-1}$, 1 rad s^{-1} and 8 % strain.

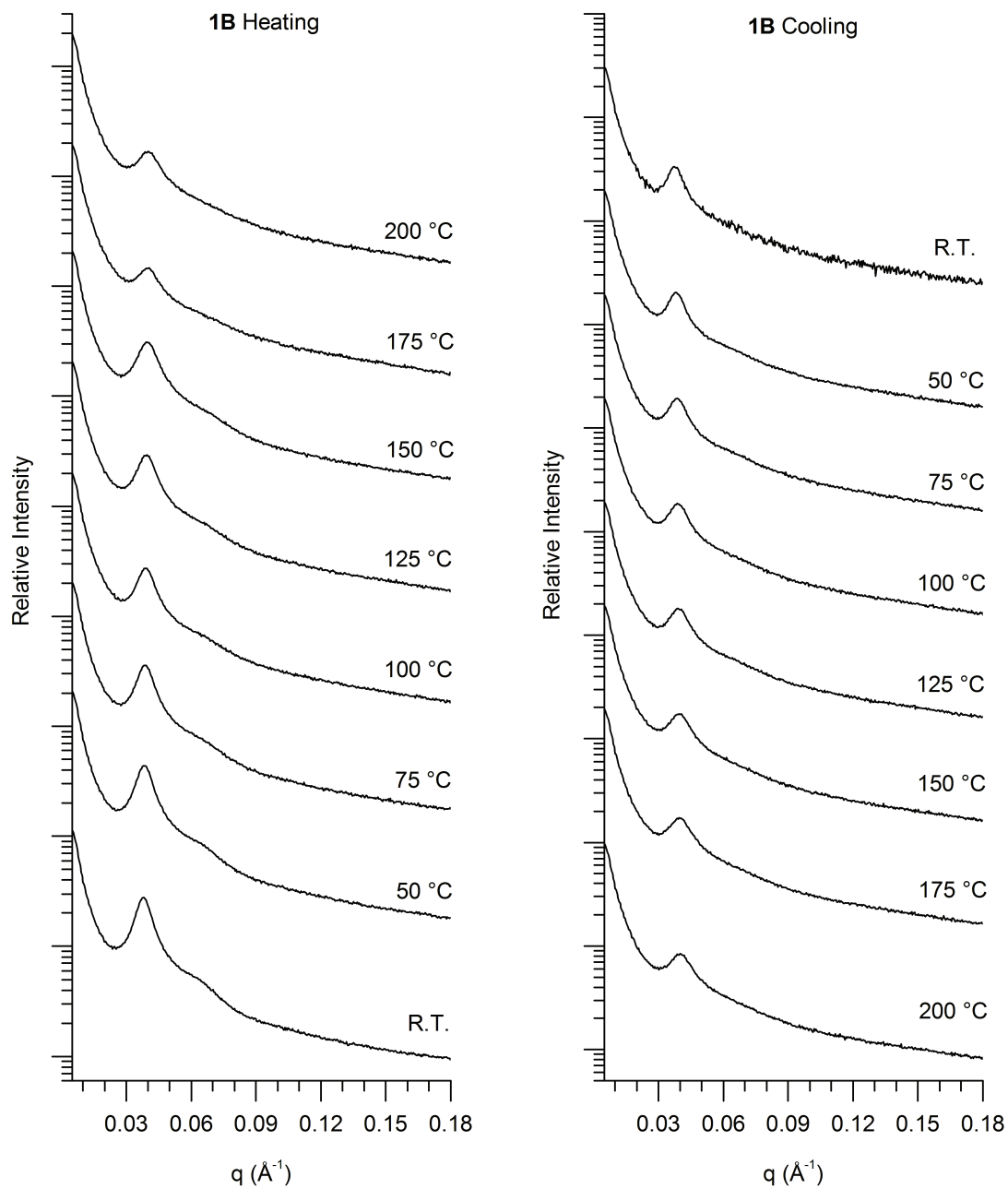


Figure 8-S5. Temperature dependent SAXS data for BCP 1B, $f_{\text{DOD}} = 0.89$.

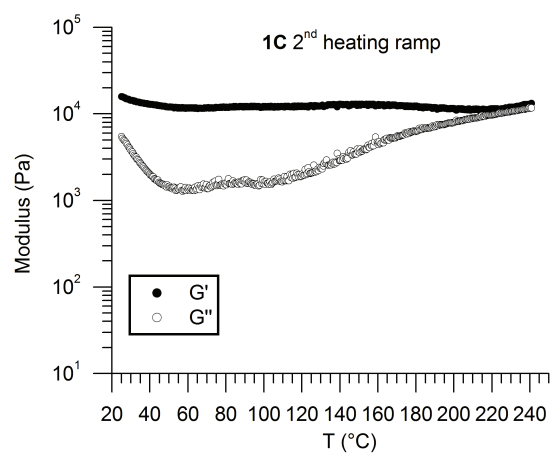
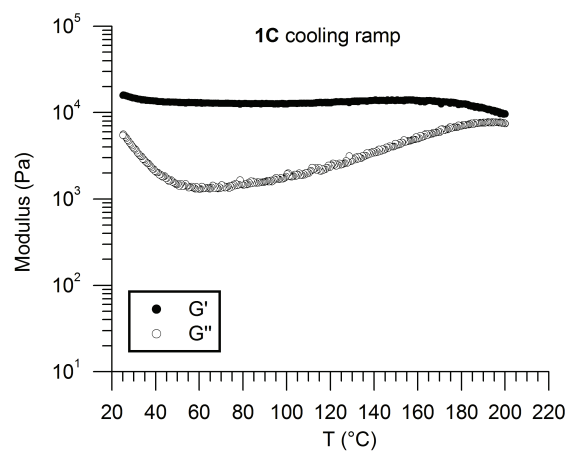
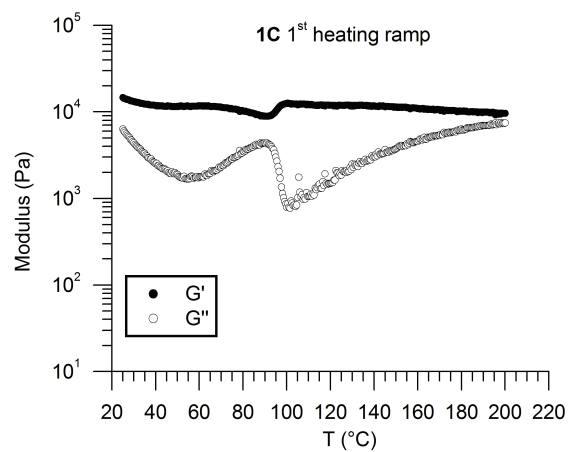


Figure 8-S6. Temperature ramps of BCP 1C, $f_{\text{DOD}} = 0.84$ at $1 \text{ }^\circ\text{C min}^{-1}$, 1 rad s^{-1} and 8 % strain.

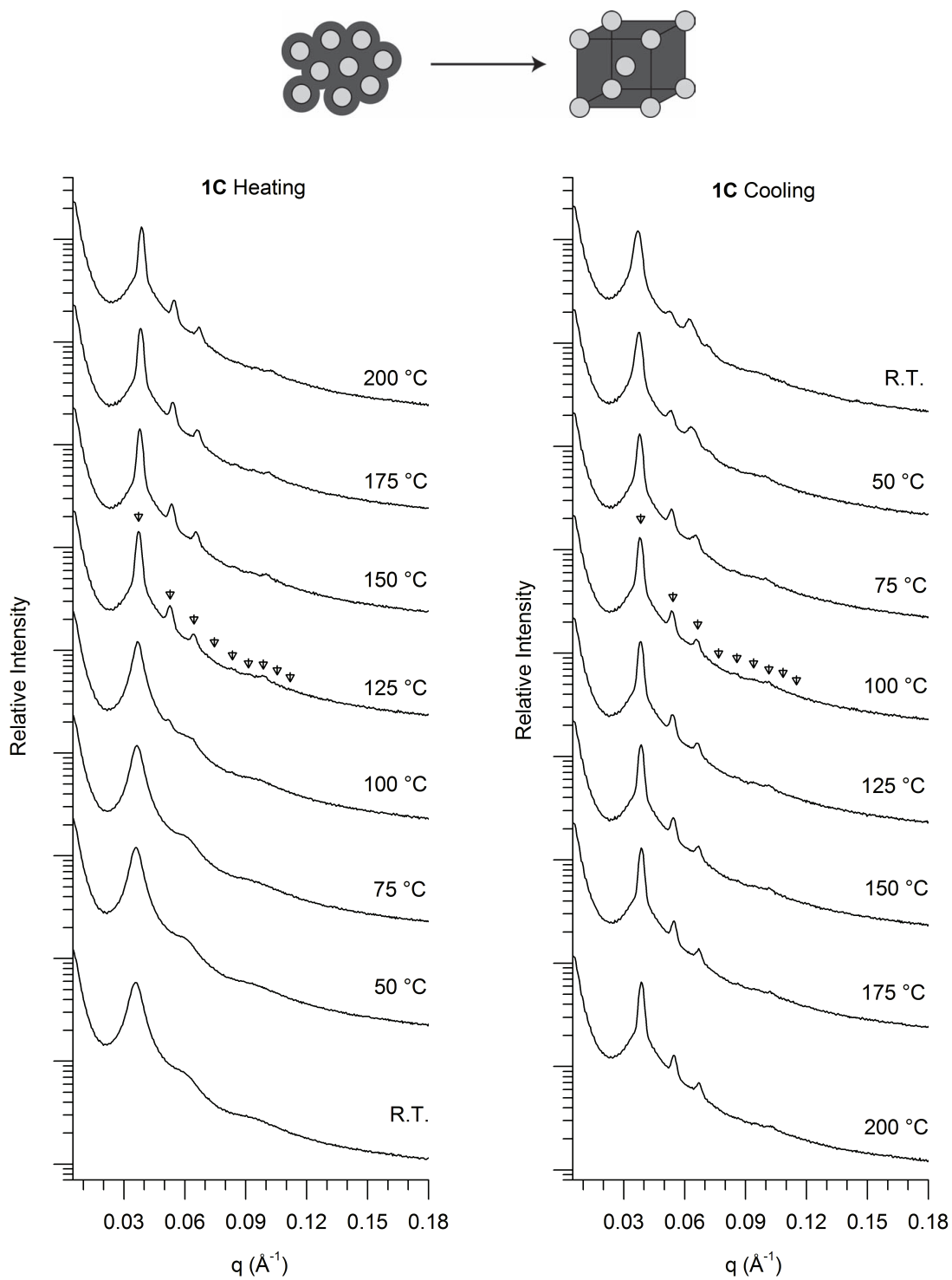


Figure 8–S7. Temperature dependent SAXS data for BCP 1C, $f_{\text{DOD}} = 0.84$.

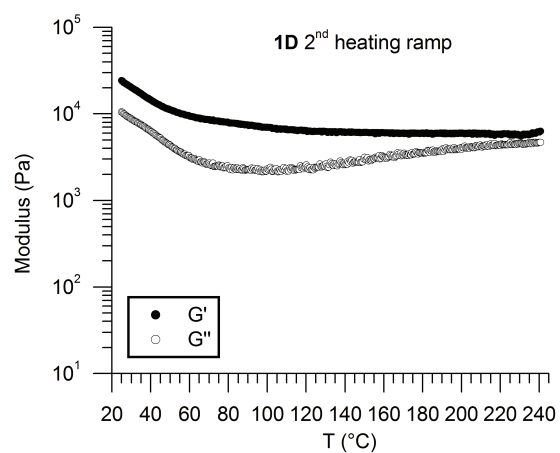
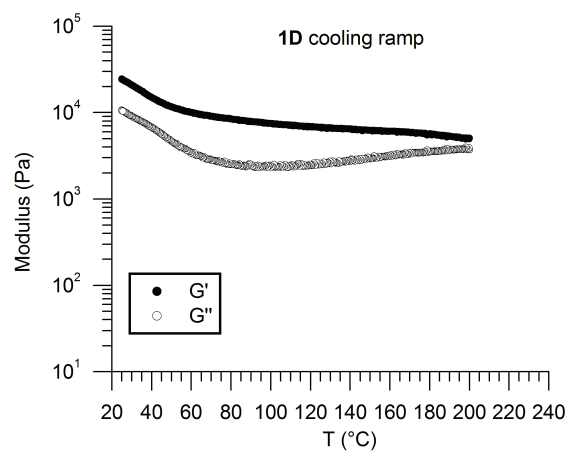
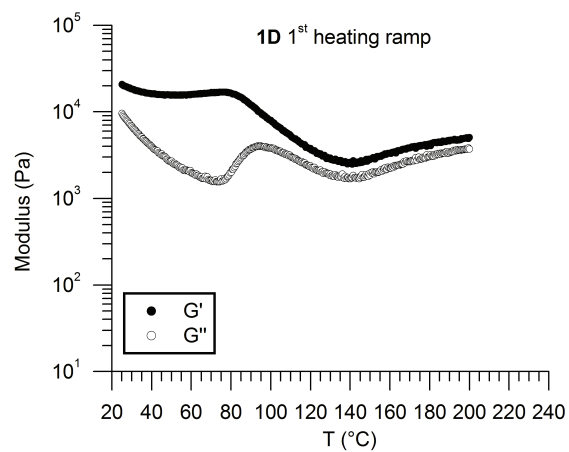


Figure 8-S8. Temperature ramps of BCP 1D, $f_{\text{DOD}} = 0.81$ at $1 \text{ }^\circ\text{C min}^{-1}$, 1 rad s^{-1} and 8 % strain.

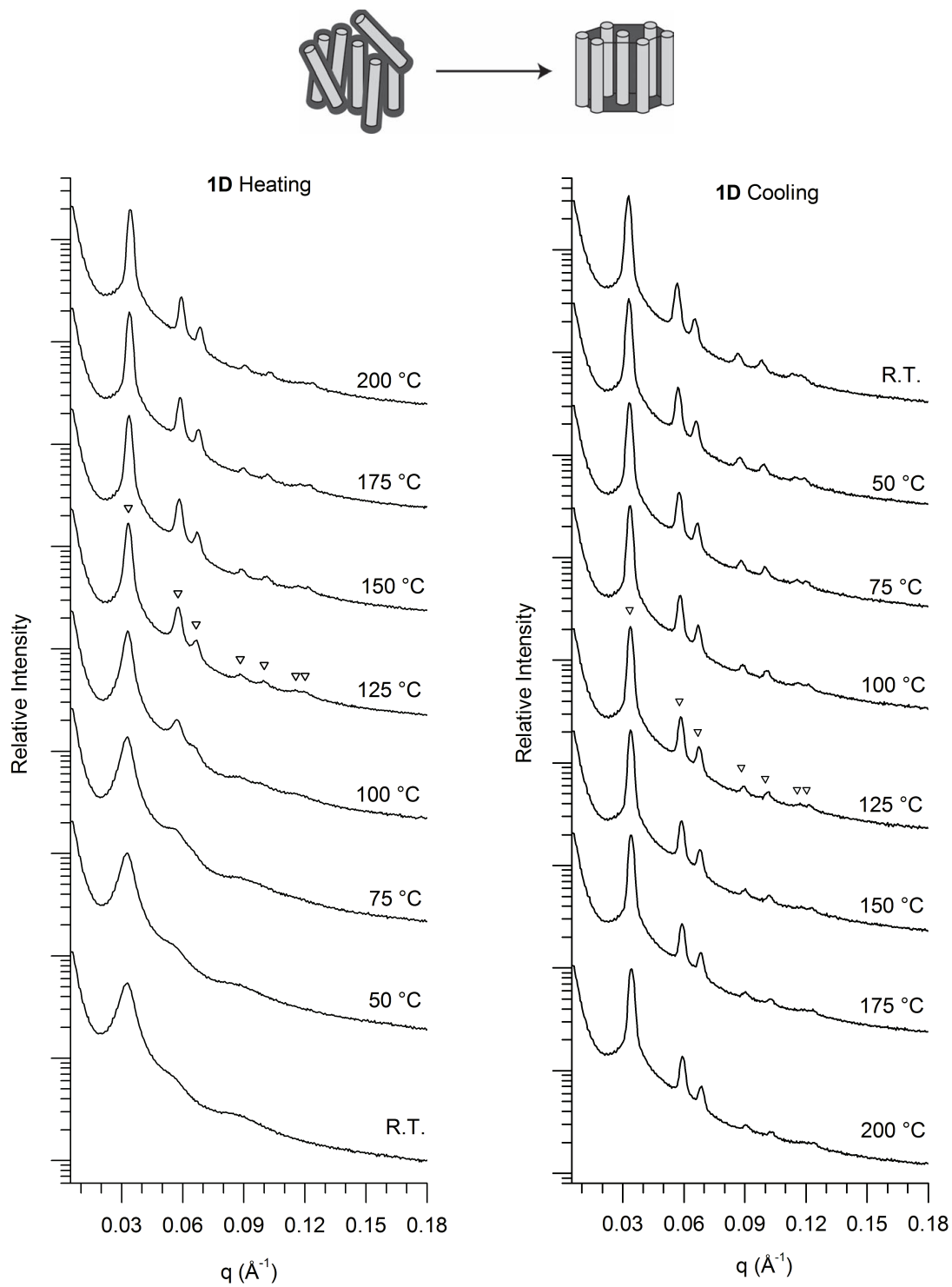


Figure 8–S9. Temperature dependent SAXS data for BCP 1D, $f_{\text{DOD}} = 0.81$.

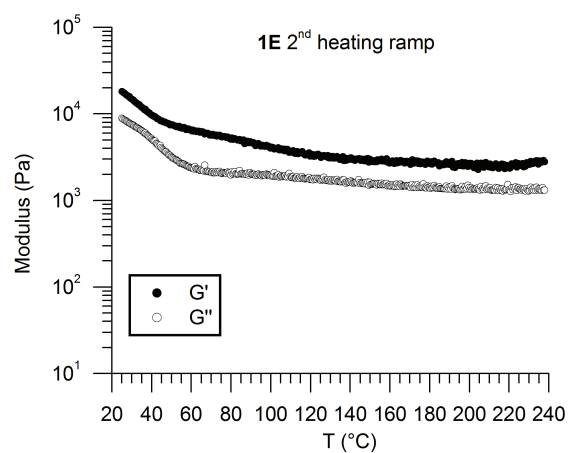
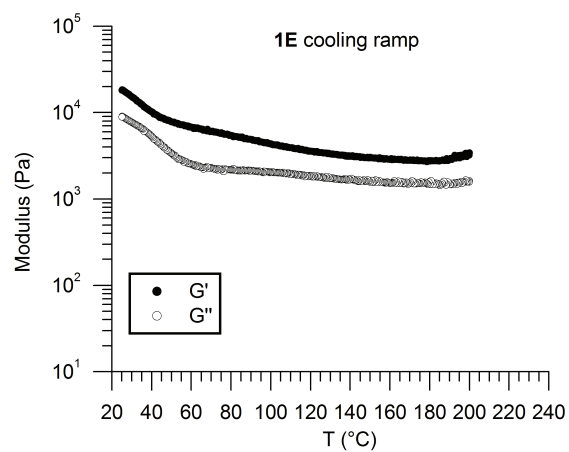
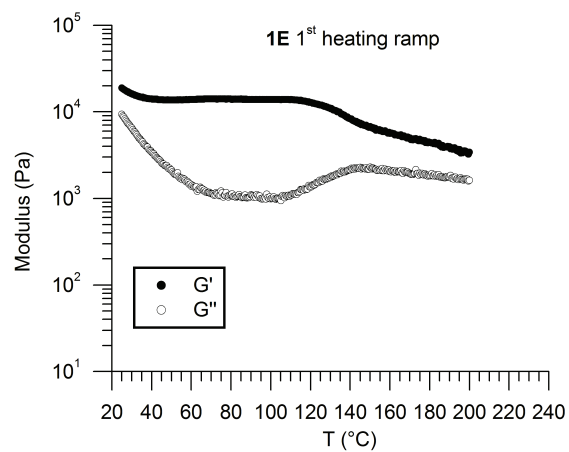


Figure 8-S10. Temperature ramps of BCP 1E, $f_{DOD} = 0.74$, at $1\text{ }^\circ\text{C min}^{-1}$, 1 rad s^{-1} and 7 % strain.

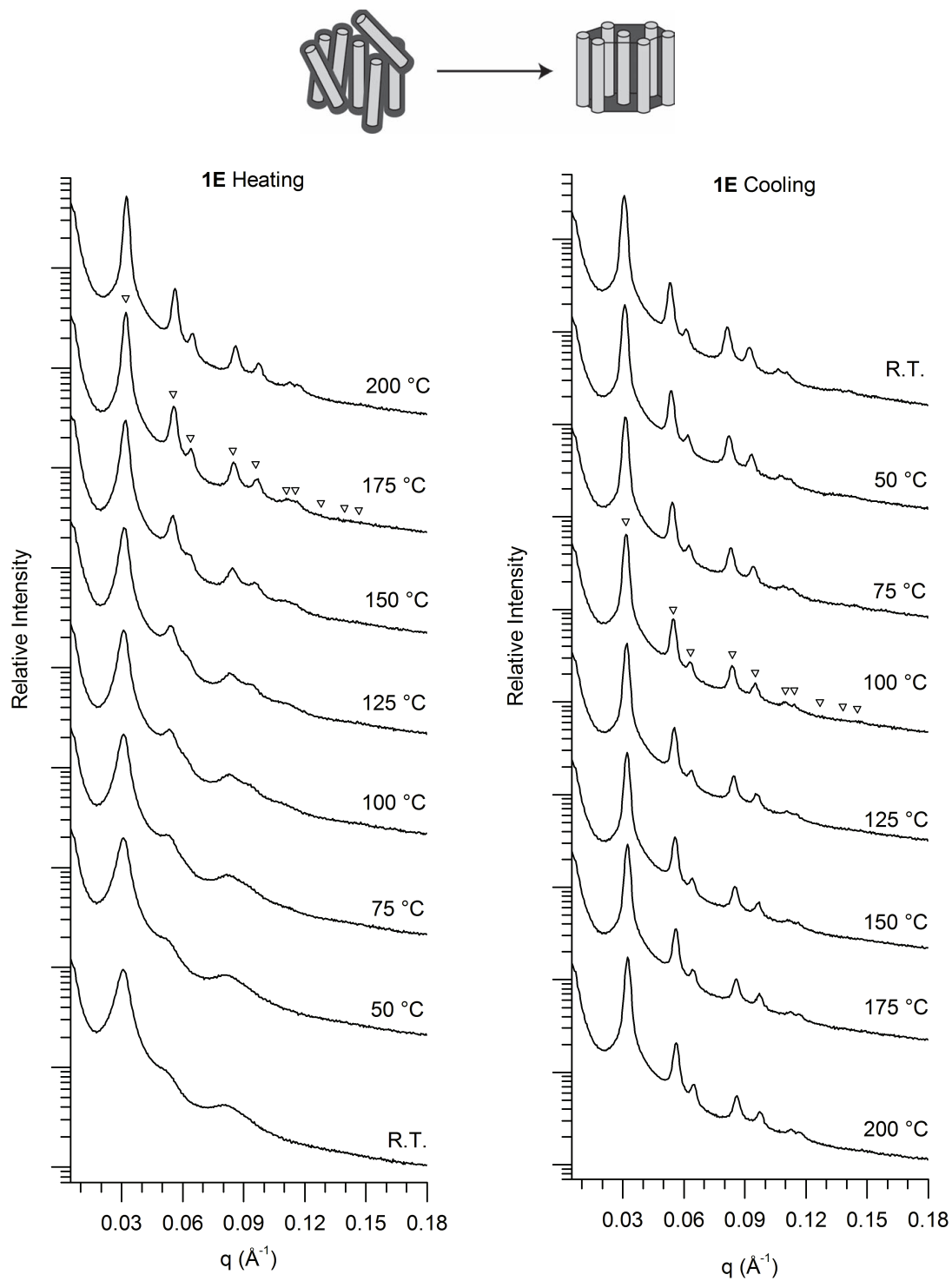


Figure 8-S11. Temperature dependent SAXS data for BCP 1E, $f_{\text{DOD}} = 0.74_7$.

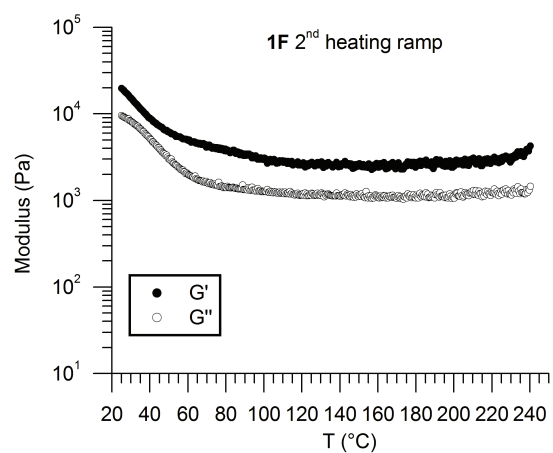
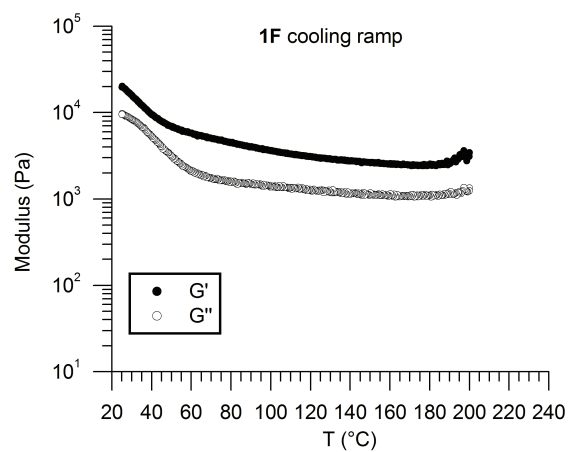
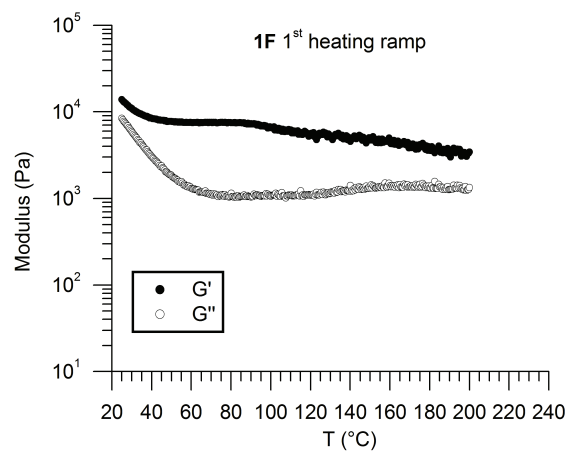


Figure 8-S12. Temperature ramps of BCP 1F, $f_{\text{DOD}} = 0.74_6$ at $1\text{ }^\circ\text{C min}^{-1}$, 1 rad s^{-1} and 7 % strain.

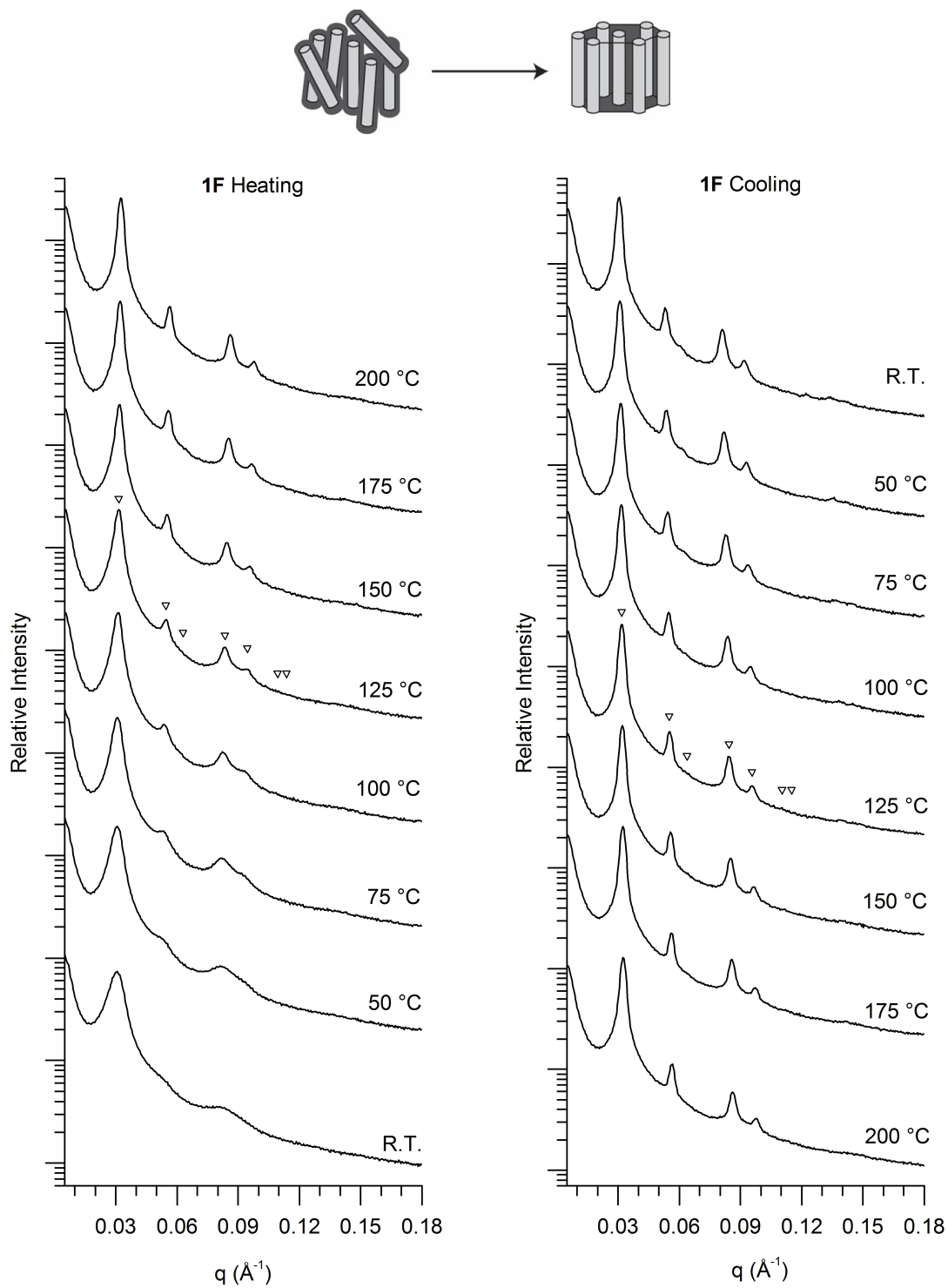


Figure 8-S13. Temperature dependent SAXS data for BCP 1F, $f_{\text{DOD}} = 0.74_6$.

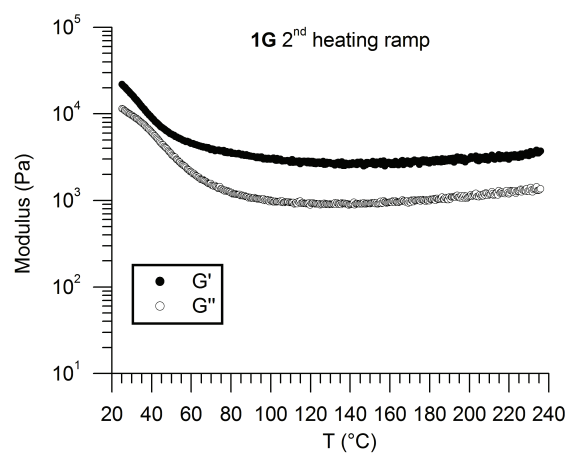
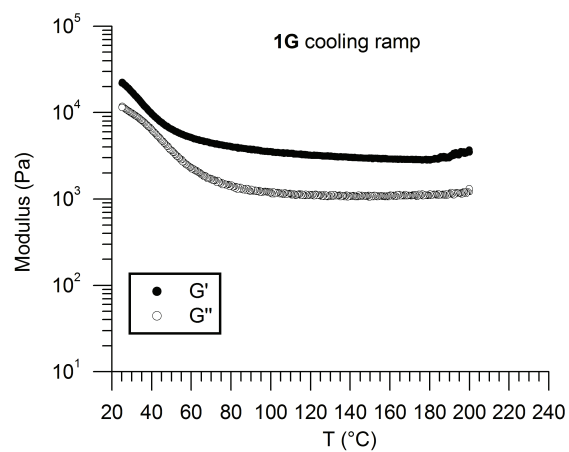
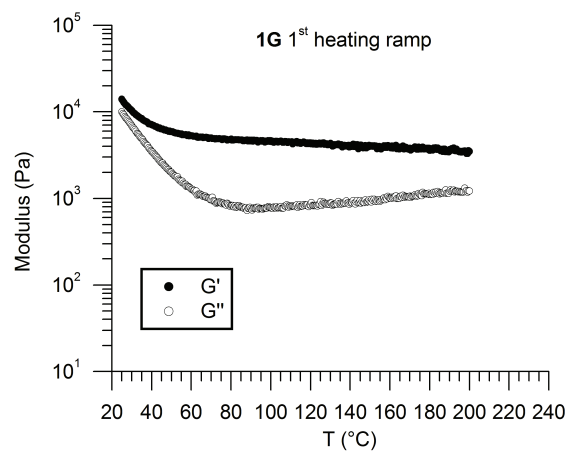


Figure 8-S14. Temperature ramps of BCP 1G, $f_{DOD} = 0.69$ at $1\text{ }^{\circ}\text{C min}^{-1}$, 1 rad s^{-1} and 7 % strain.

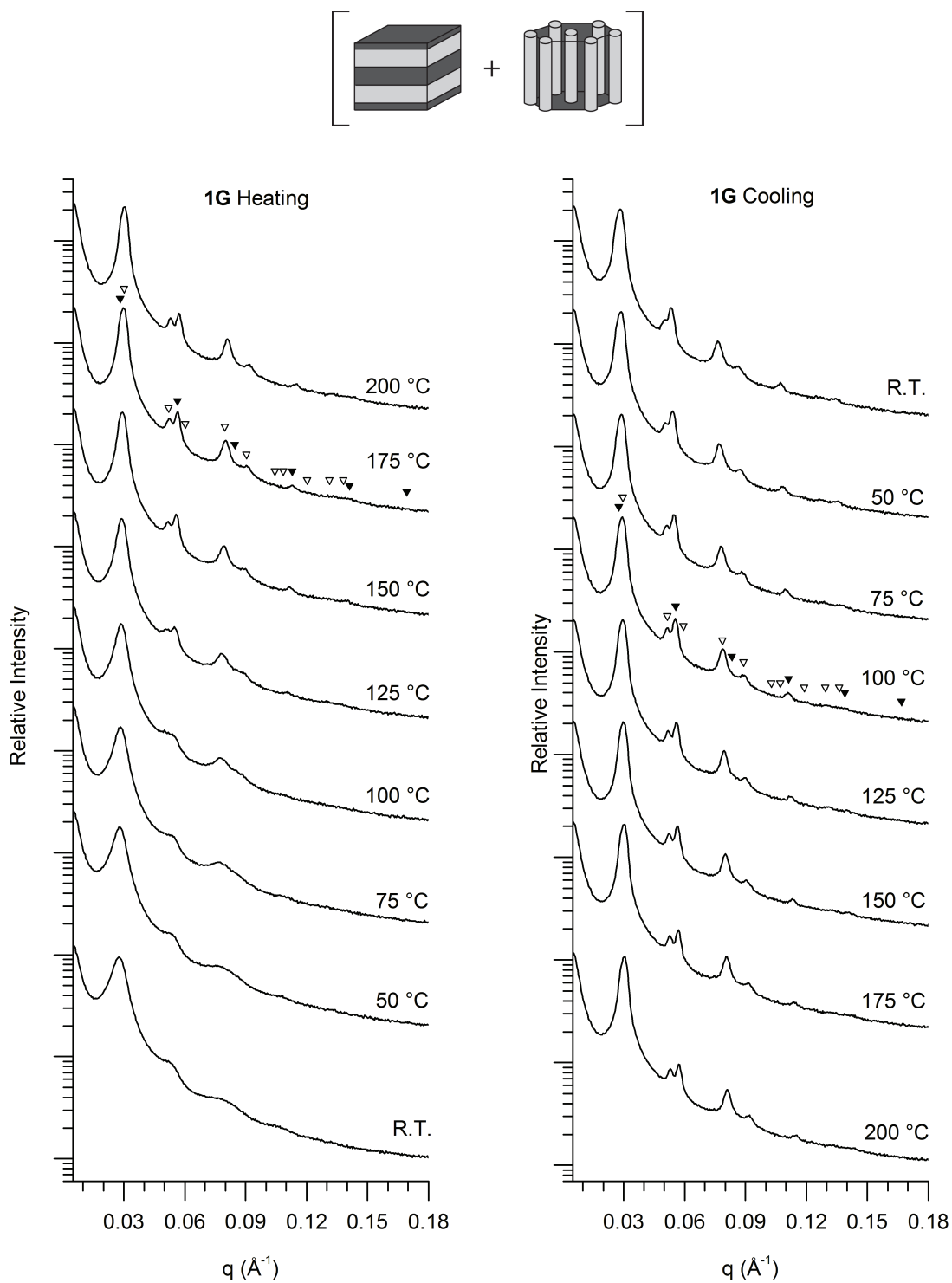


Figure 8-S15. Temperature dependent SAXS data for BCP 1G, $f_{\text{DOD}} = 0.69$.

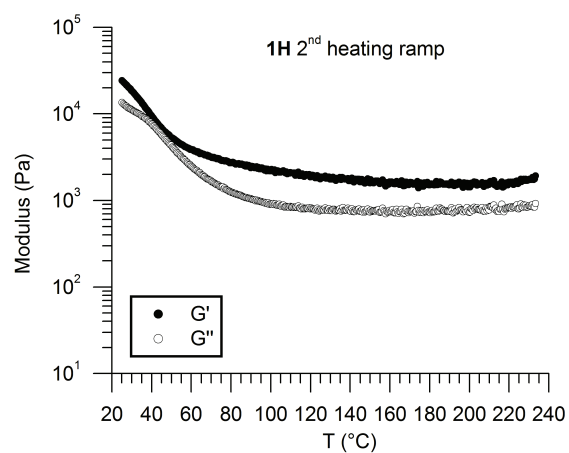
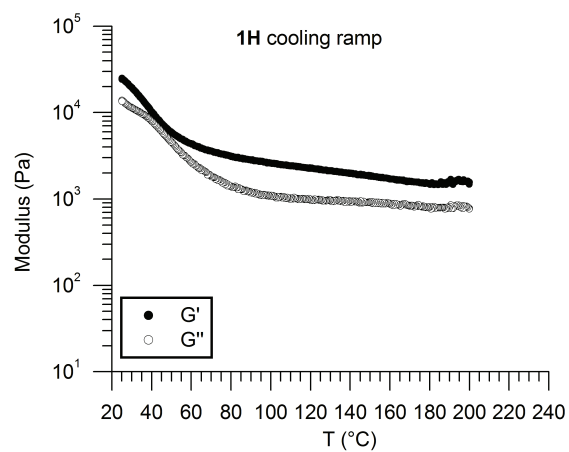
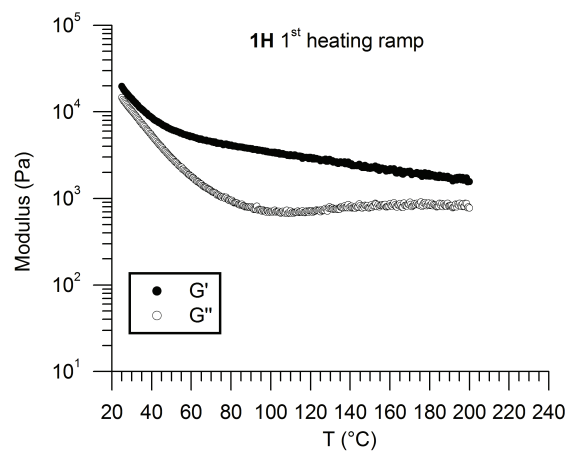


Figure 8-S16. Temperature ramps of BCP 1H, $f_{\text{DOD}} = 0.66$ at $1 \text{ }^\circ\text{C min}^{-1}$, 1 rad s^{-1} and 8 % strain.

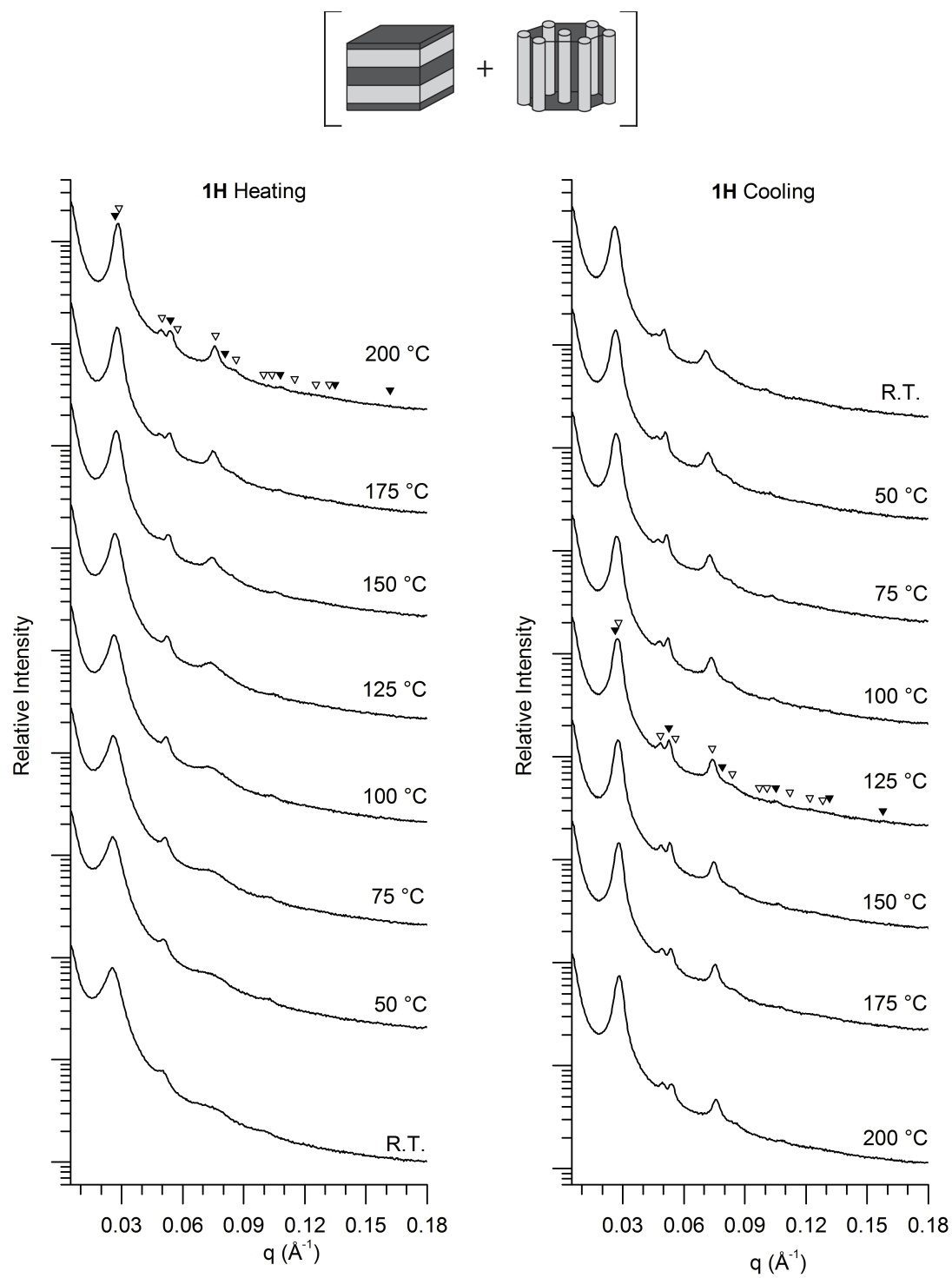


Figure 8-S17. Temperature dependent SAXS data for BCP 1H, $f_{\text{DOD}} = 0.66$.

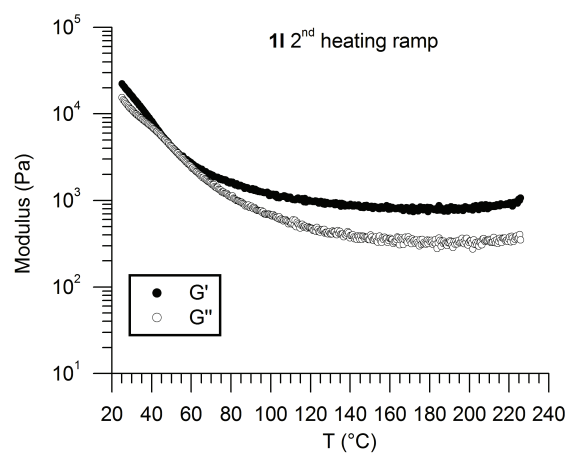
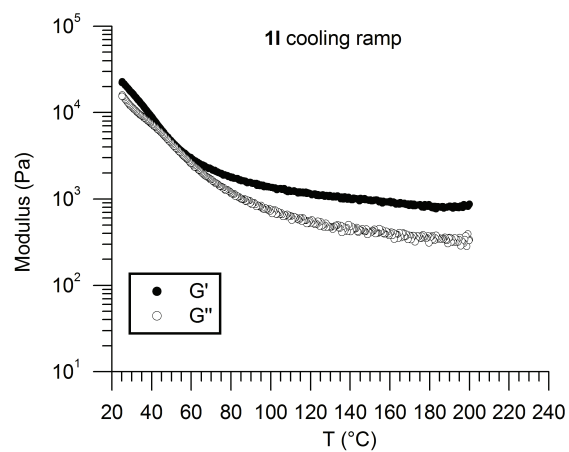
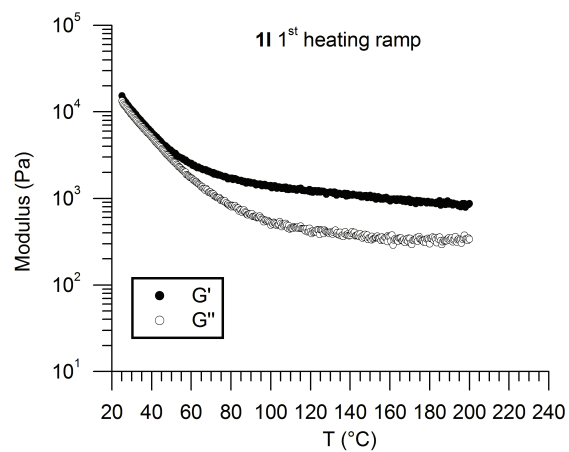


Figure 8-S18. Temperature ramps of BCP 1I, $f_{DOD} = 0.64$ at $1\text{ }^\circ\text{C min}^{-1}$, 1 rad s^{-1} and 7 % strain.

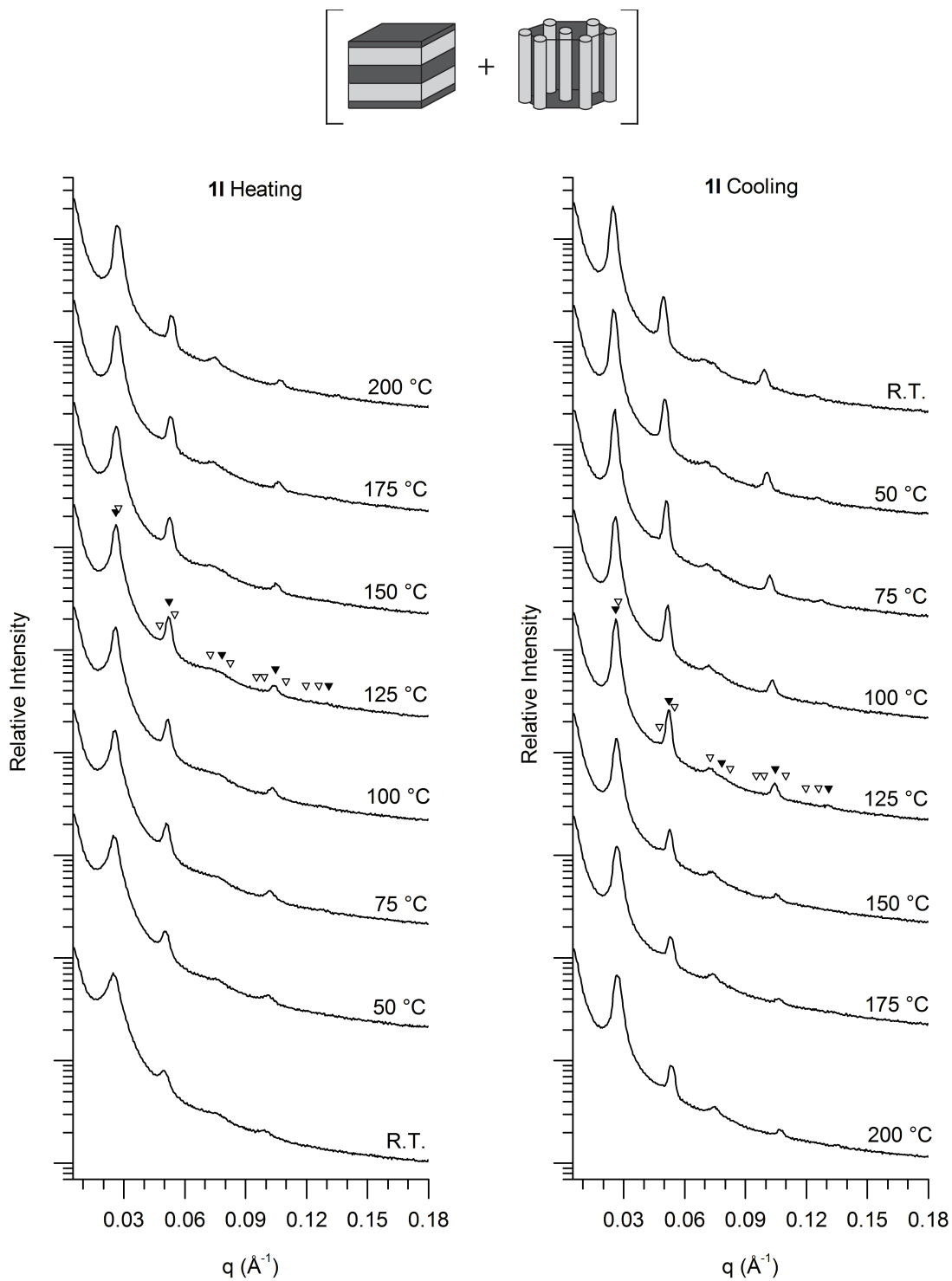


Figure 8-S19. Temperature dependent SAXS data for BCP II, $f_{\text{DOD}} = 0.64$.

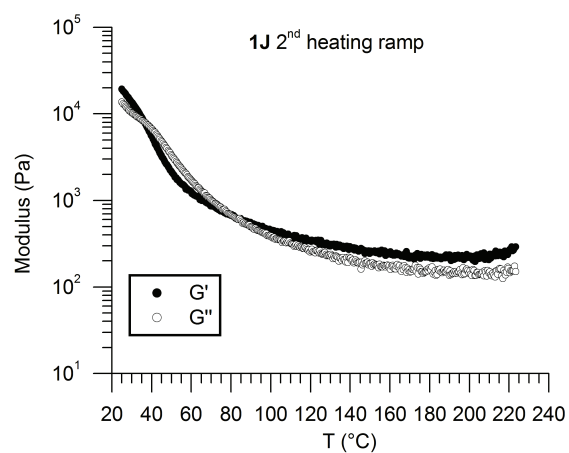
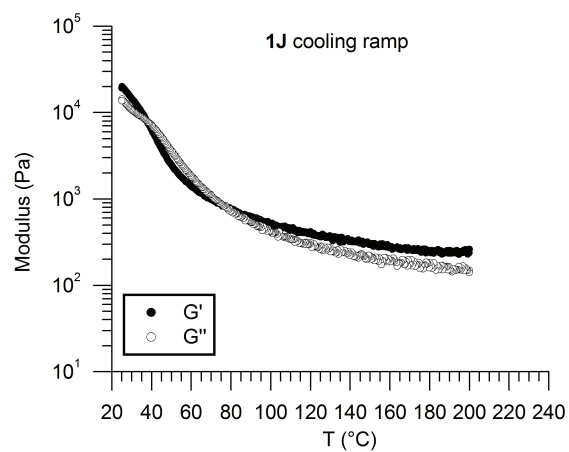
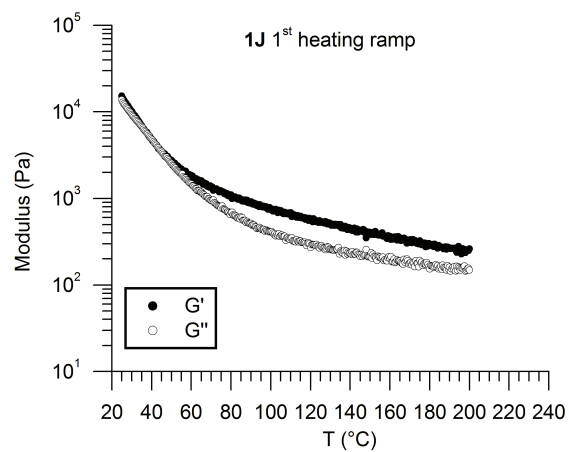


Figure 8-S20. Temperature ramps of BCP 1J, $f_{DOD} = 0.62$ at $1\text{ }^{\circ}\text{C min}^{-1}$, 1 rad s^{-1} and 8 % strain.

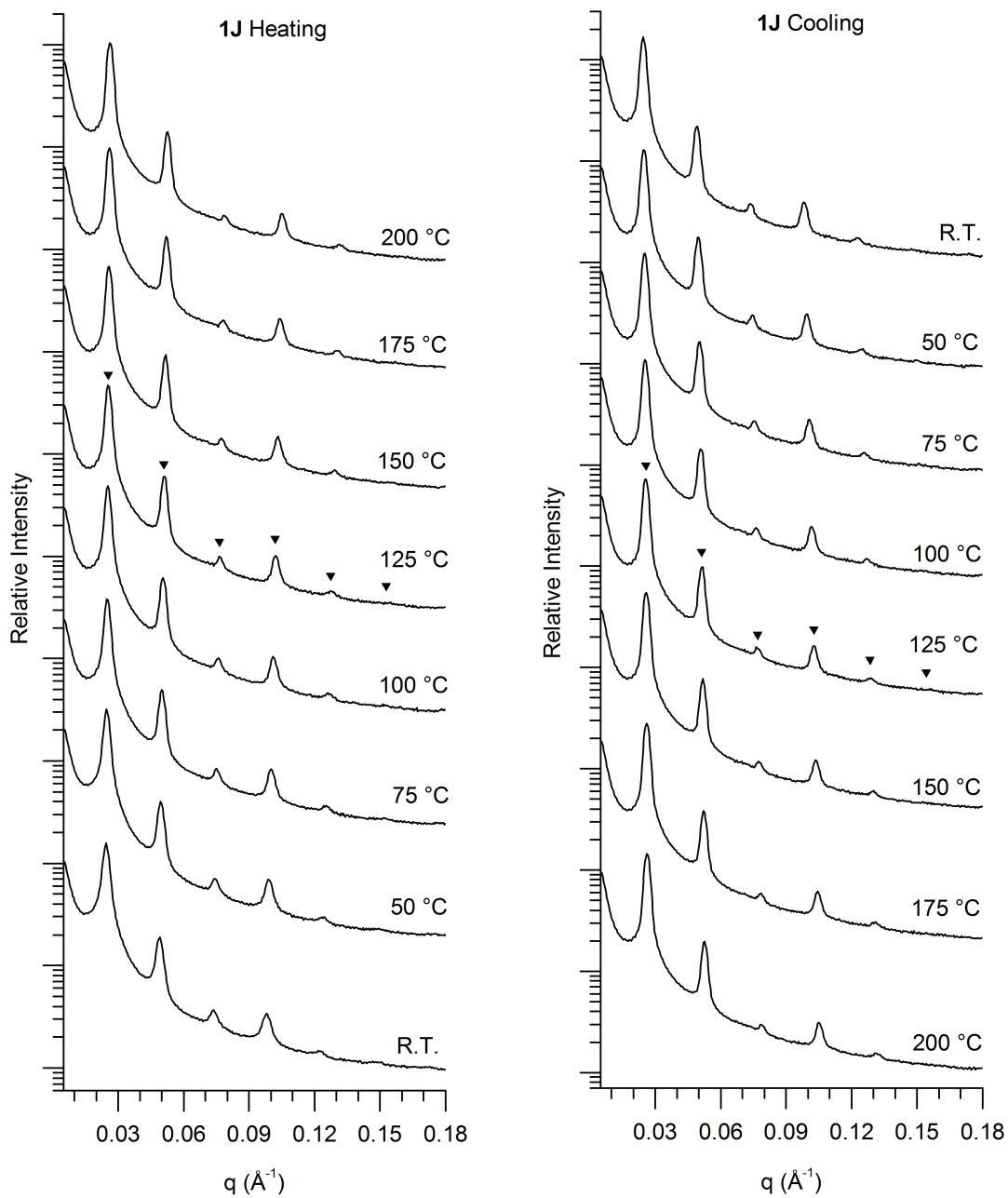
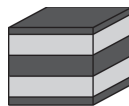


Figure 8-S21. Temperature dependent SAXS data for BCP 1J, $f_{\text{DOD}} = 0.62$.

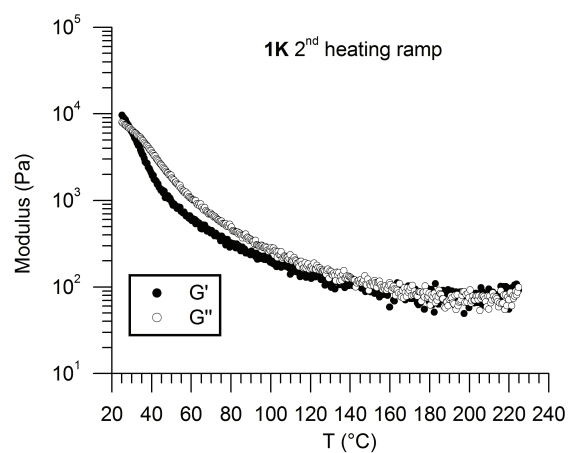
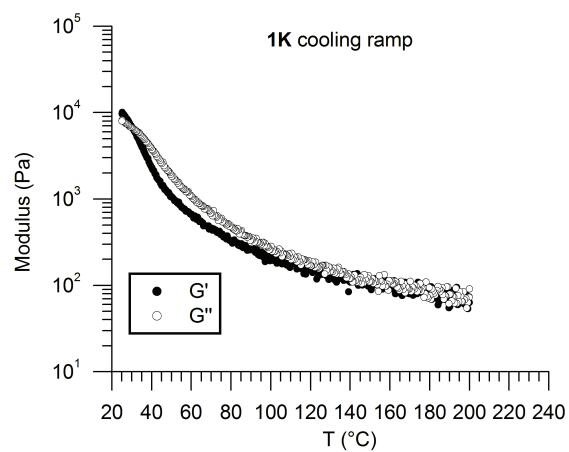
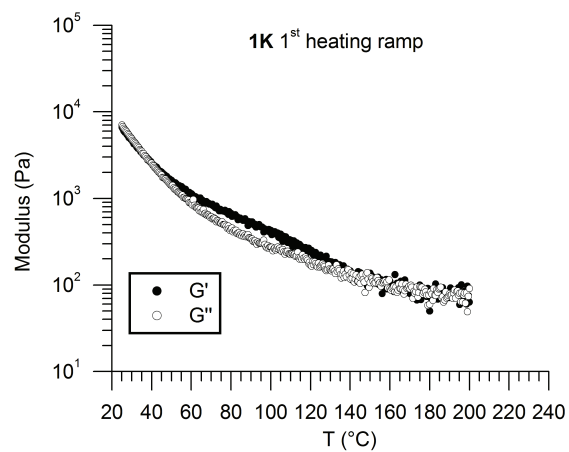


Figure 8-S22. Temperature ramps of BCP 1K, $f_{DOD} = 0.61$ at $1\text{ }^{\circ}\text{C min}^{-1}$, 1 rad s^{-1} and 7 % strain.

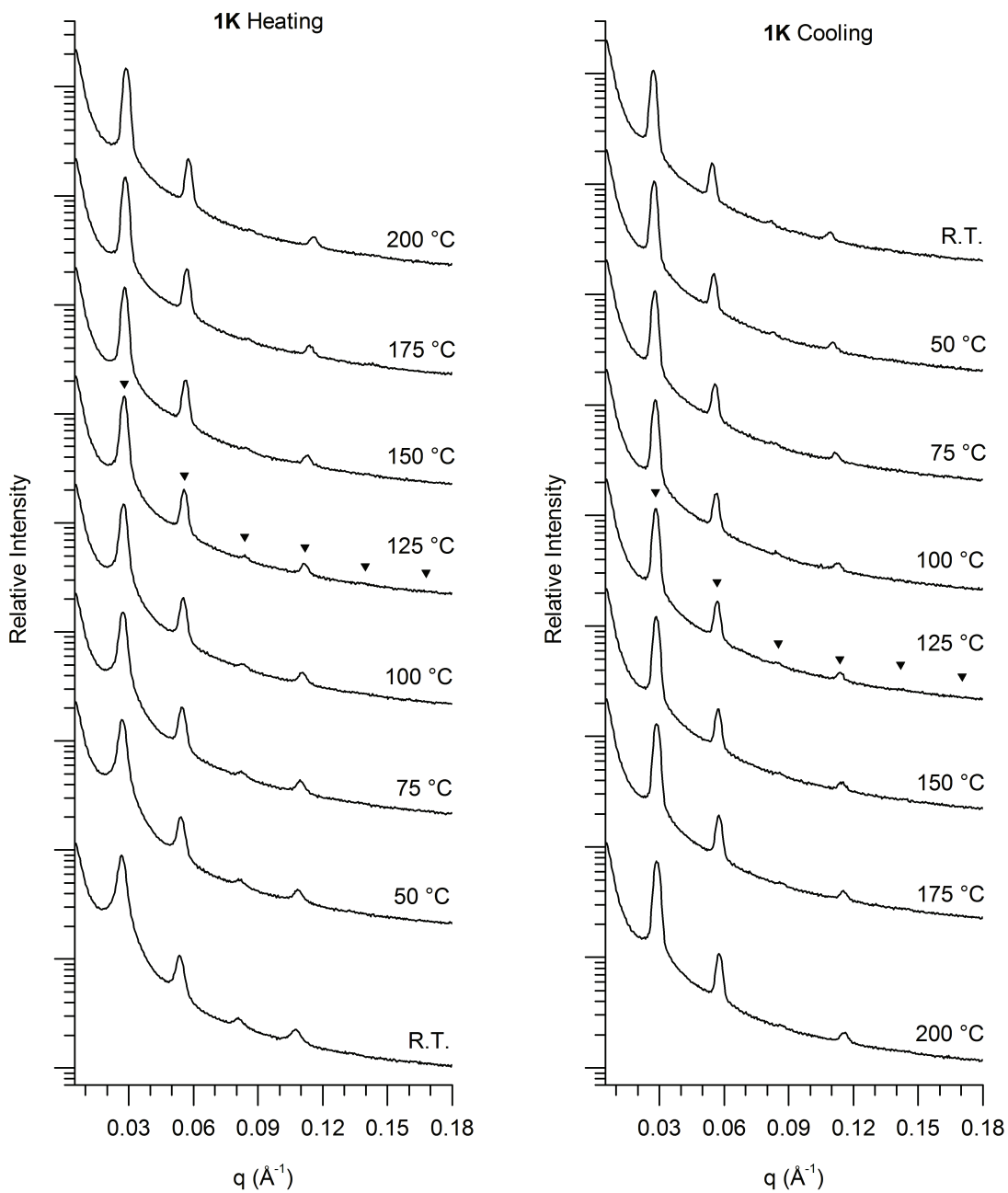
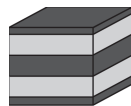


Figure 8-S23. Temperature dependent SAXS data for BCP 1K, $f_{\text{DOD}} = 0.61$.

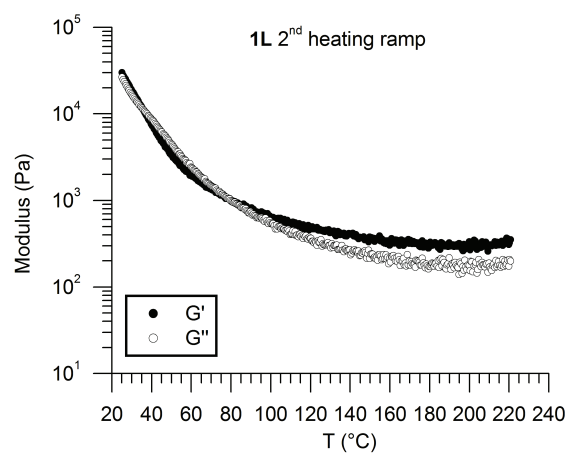
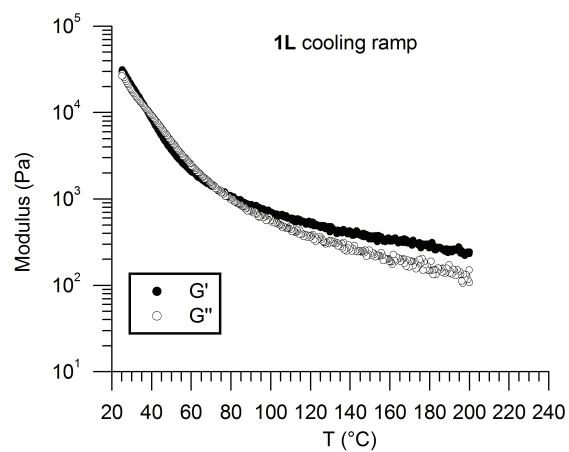
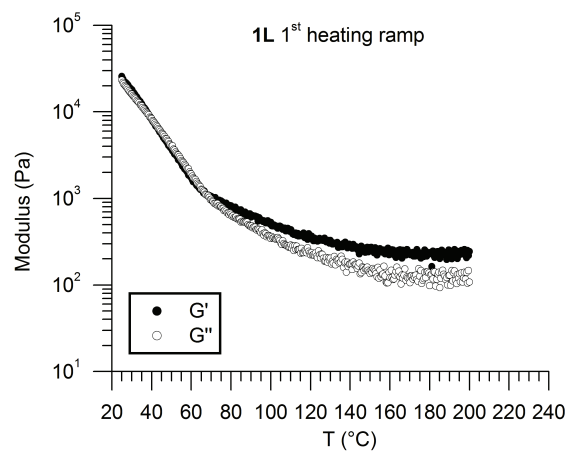


Figure 8-S24. Temperature ramps of BCP 1L, $f_{DOD} = 0.54$ at $1\text{ }^{\circ}\text{C min}^{-1}$, 1 rad s^{-1} and 6 % strain.

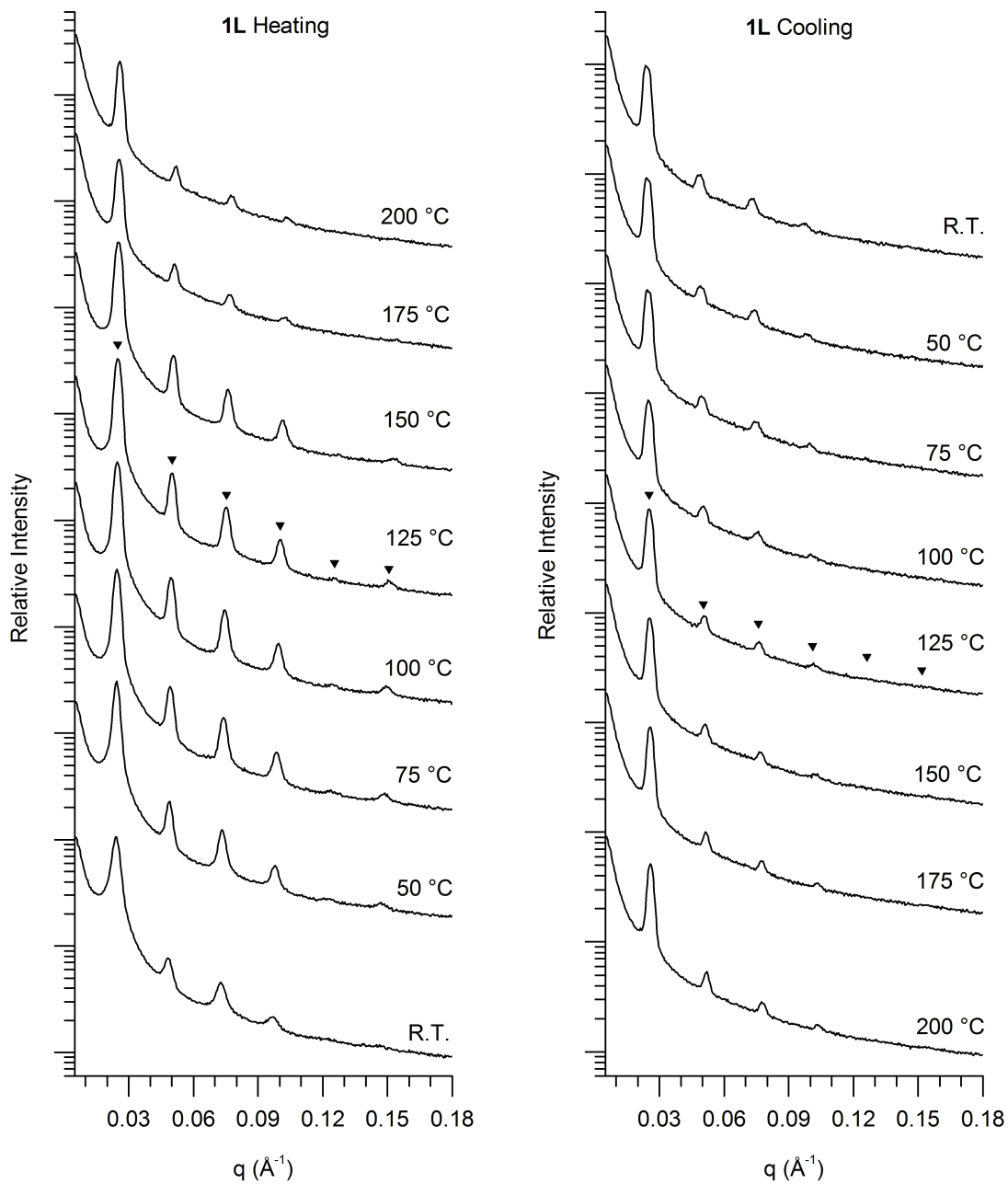
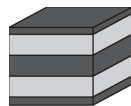


Figure 8-S25. Temperature dependent SAXS data for BCP 1L, $f_{\text{DOD}} = 0.54$.

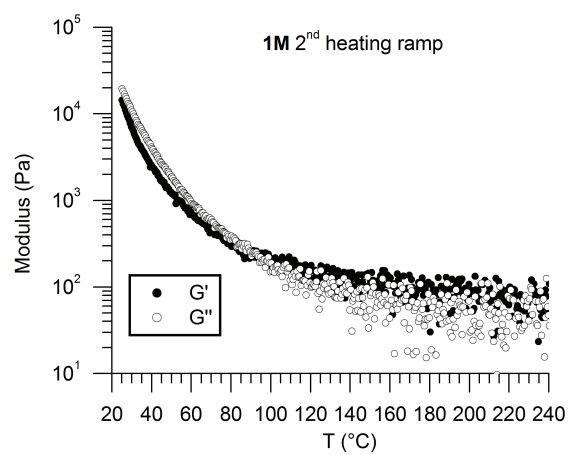
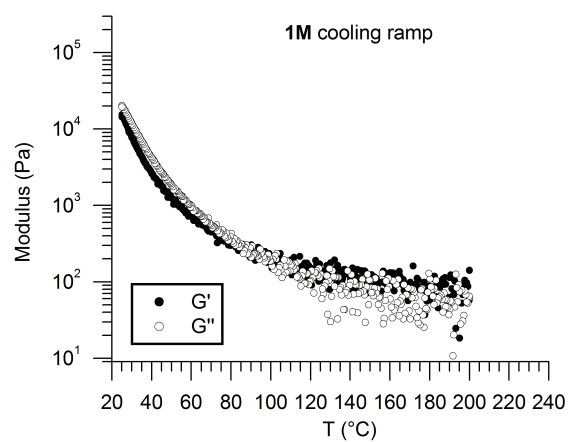
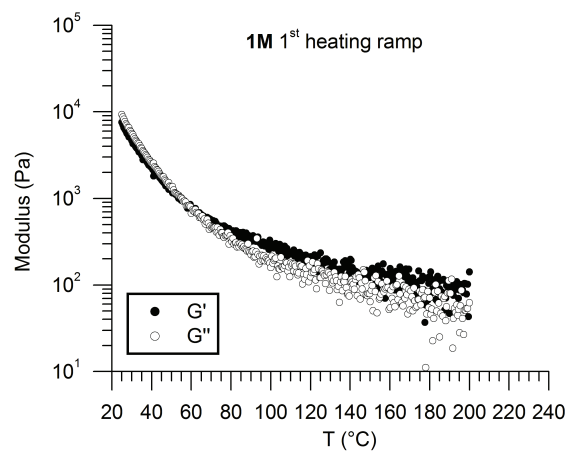


Figure 8–S26. Temperature ramps of BCP 1M, $f_{\text{DOD}} = 0.50_4$ at $1\text{ }^\circ\text{C min}^{-1}$, 1 rad s^{-1} and 2.5 % strain.

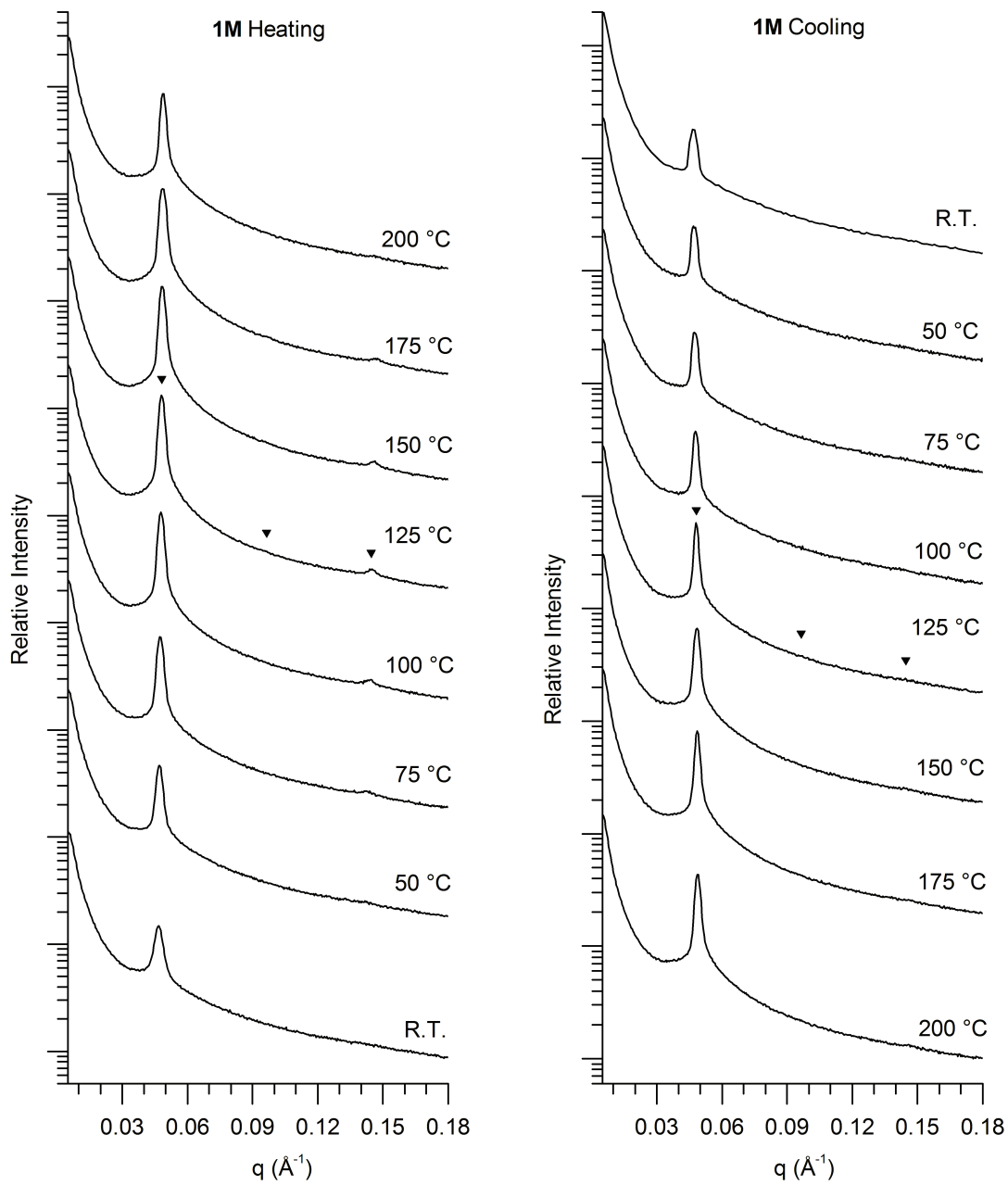
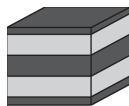


Figure 8-S27. Temperature dependent SAXS data for BCP IM, $f_{\text{DOD}} = 0.50_4$.

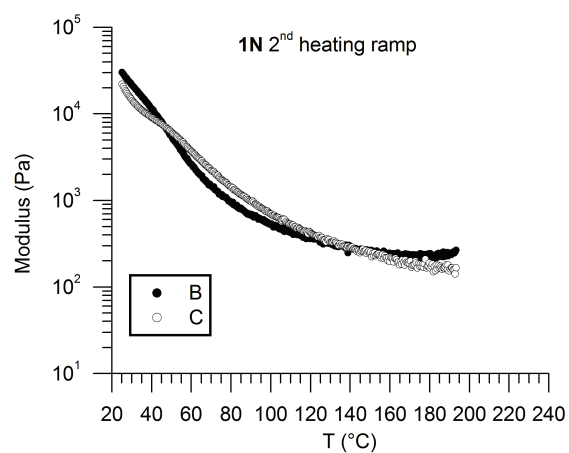
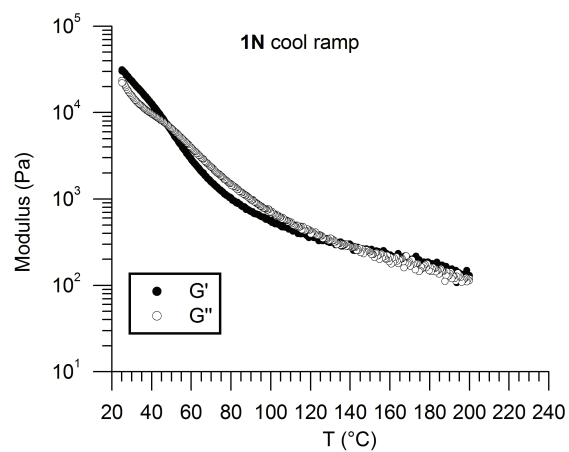
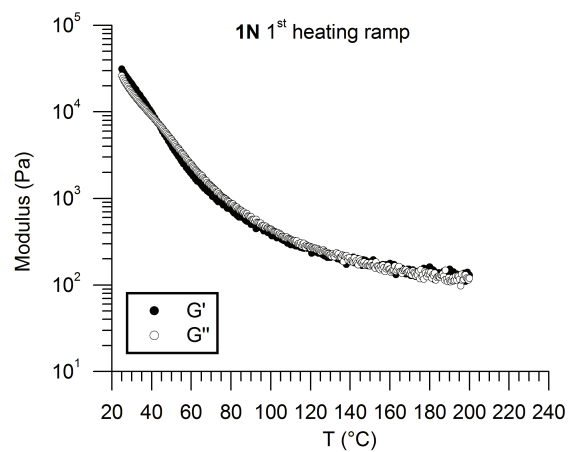


Figure 8-S28. Temperature ramps of BCP 1N, $f_{\text{DOD}} = 0.50_0$ at $1\text{ }^\circ\text{C min}^{-1}$, 1 rad s^{-1} and 7 % strain.

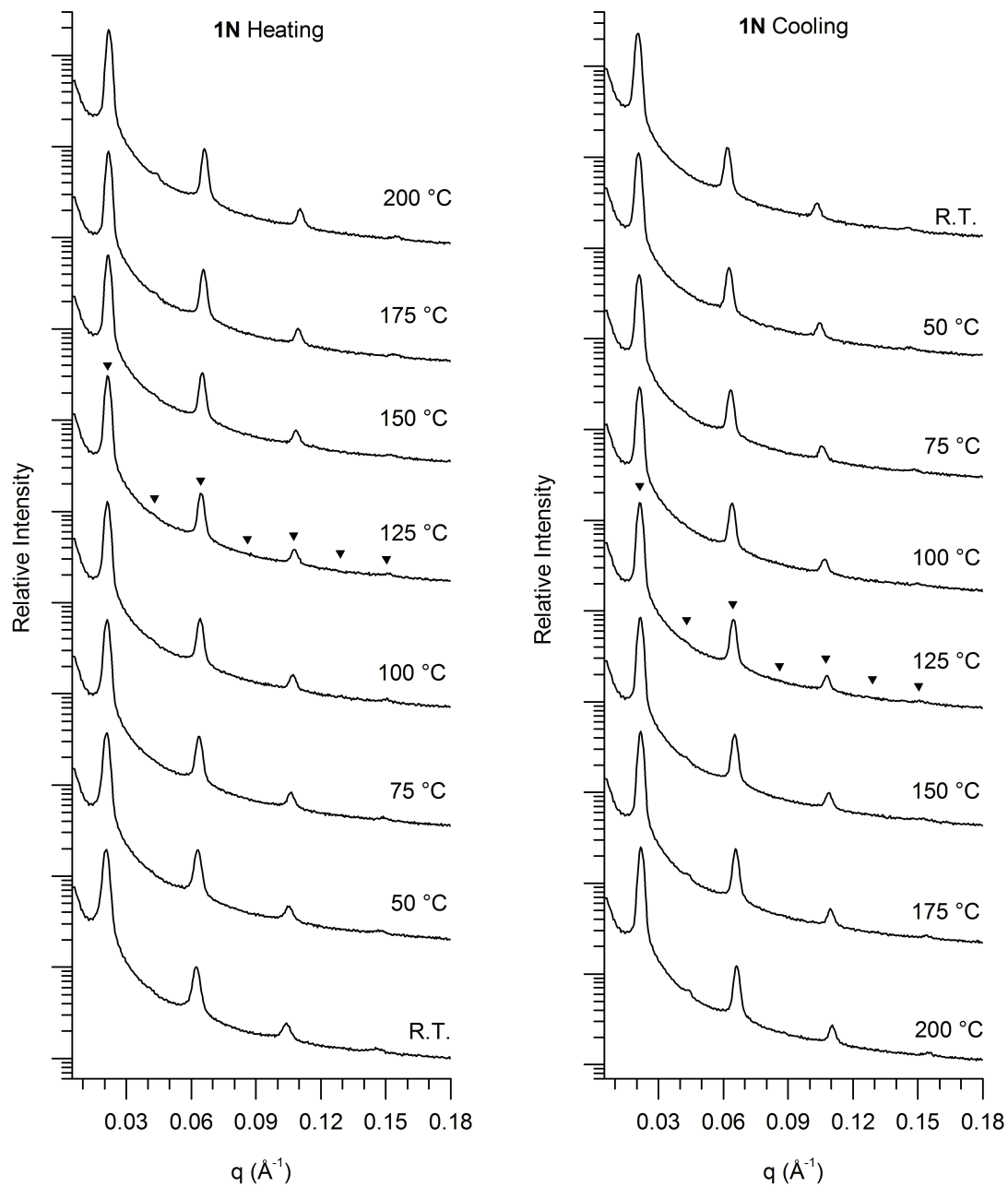
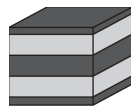


Figure 8-S29. Temperature dependent SAXS data for BCP 1N, $f_{\text{DOD}} = 0.50_0$.

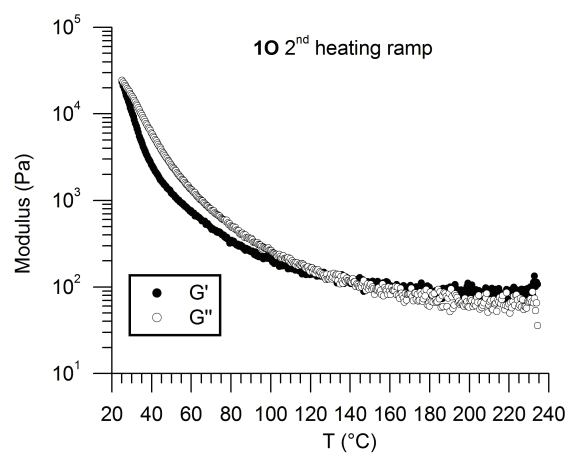
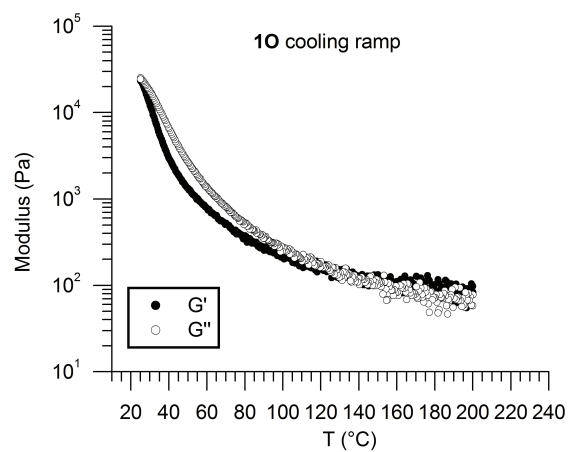
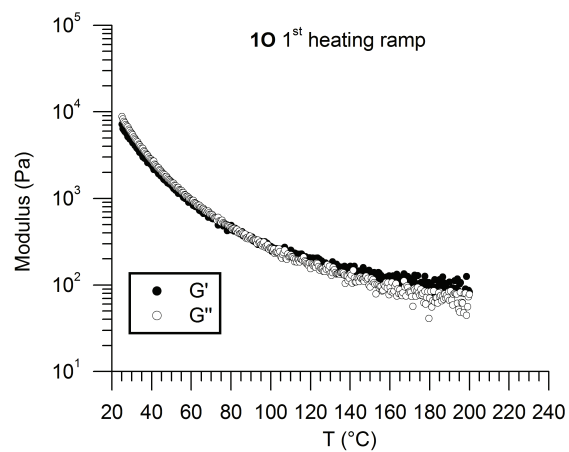


Figure 8-S30. Temperature ramps of BCP 1O, $f_{DOD} = 0.49$ at $1\text{ }^\circ\text{C min}^{-1}$, 1 rad s^{-1} and 7 % strain.

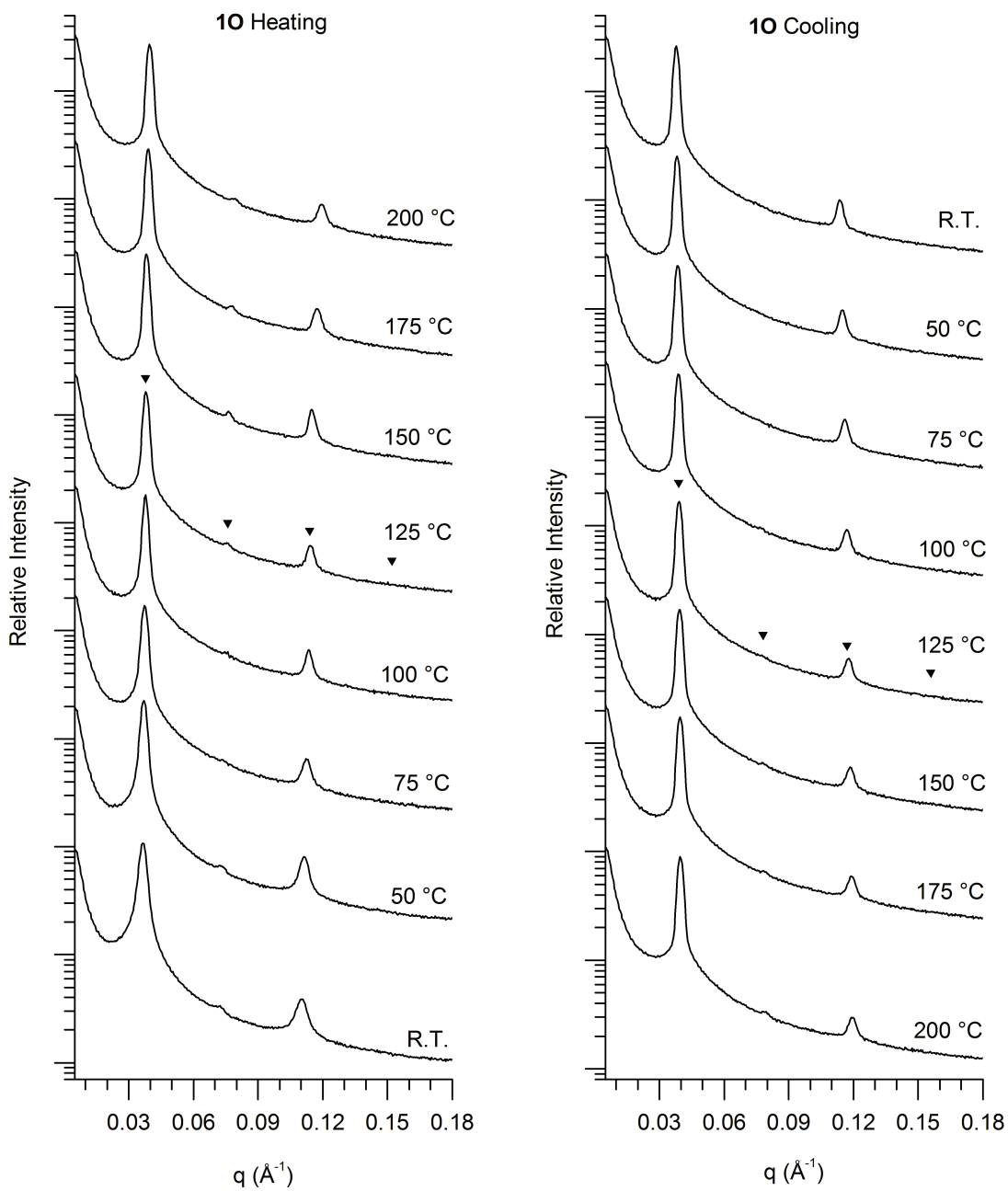
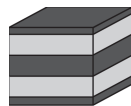


Figure 8-S31. Temperature dependent SAXS data for BCP 10, $f_{\text{DOD}} = 0.49$.

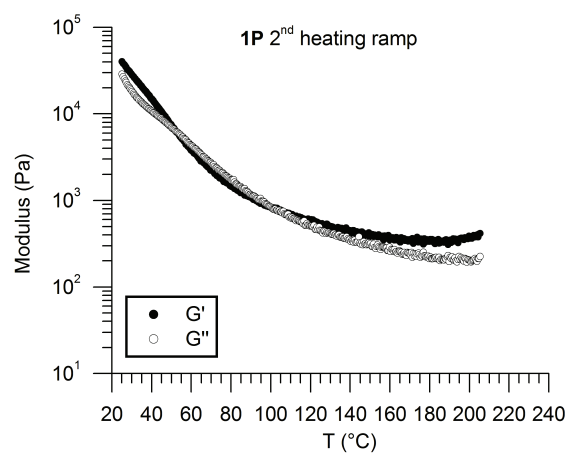
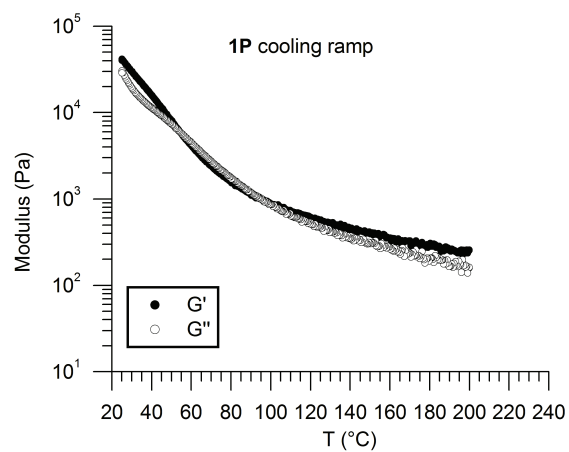
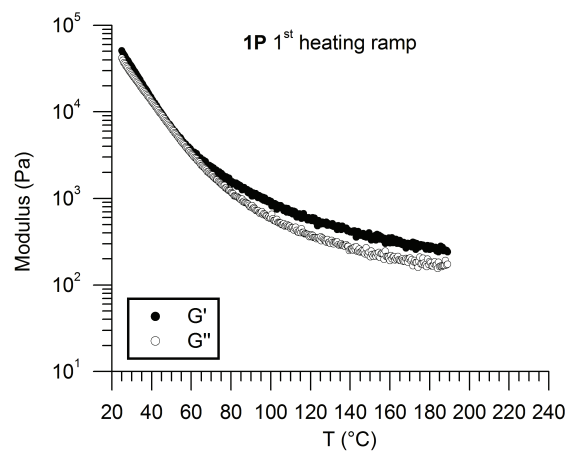


Figure 8-S32. Temperature ramps of BCP 1P, $f_{\text{DOD}} = 0.42$ at $1\text{ }^{\circ}\text{C min}^{-1}$, 1 rad s^{-1} and 8 % strain.

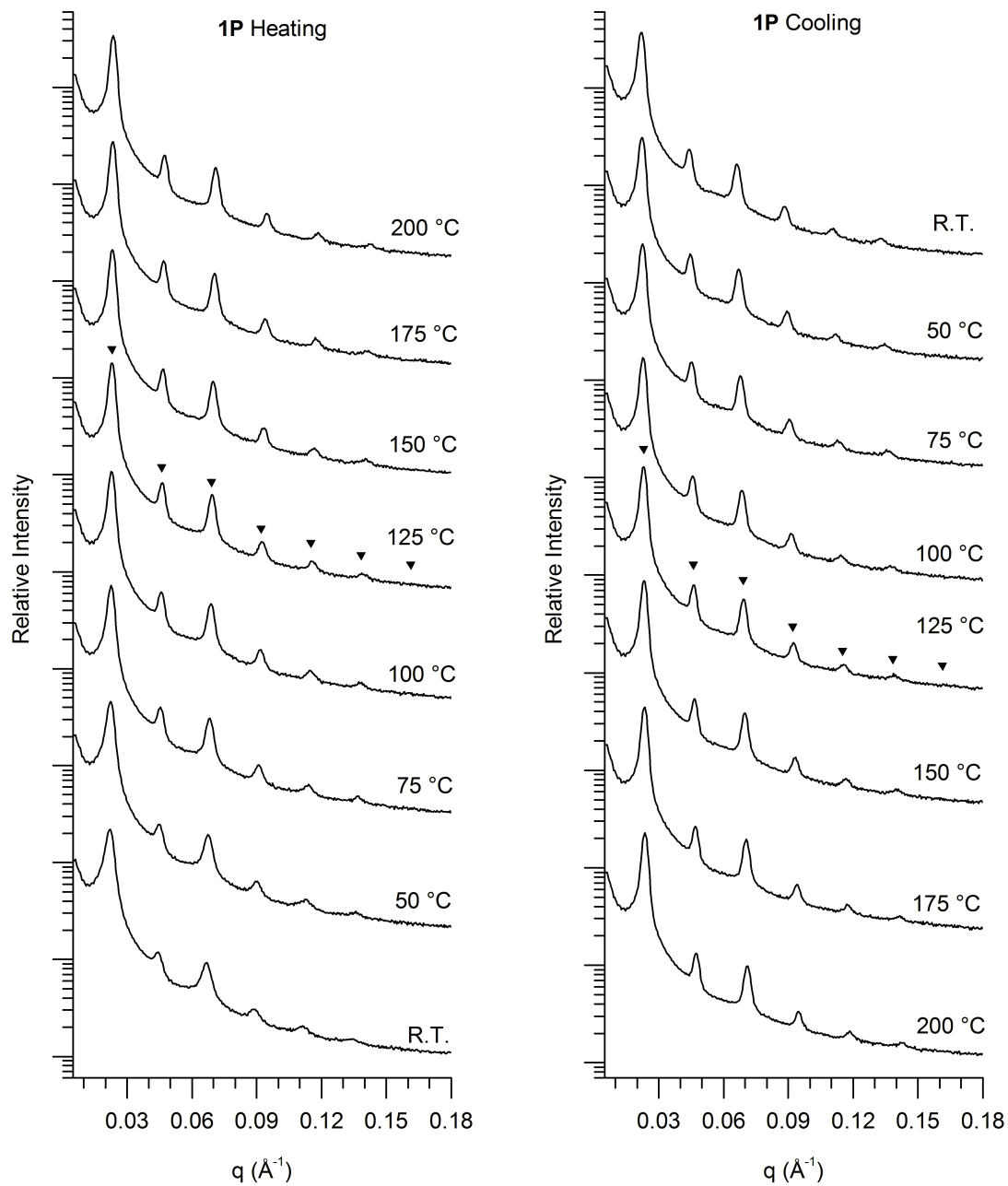
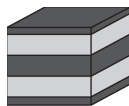


Figure 8-S33. Temperature dependent SAXS data for BCP 1P, $f_{\text{DOD}} = 0.42$.

APPENDIX I — SUPPLEMENTARY INFORMATION — NETWORK FORMATION IN AN ORTHOGONALLY SELF-ASSEMBLING SYSTEM

Materials

3,5-Bis((3S)-3,7-dimethyloctylcarbamoyl)benzoic acid (**9**) was synthesized according to literature.¹ 6-((((6-Isopropyl-4-oxo-1,4-dihydro-2-pyrimidinyl)amino)-carbonylamino) hexylcarbamate (**10**) and 6-((((6-methyl-4-oxo-1,4-dihydro-2-pyrimidinyl)amino)carbonylamino) hexylcarbamate (**13**) were purchased from SyMO-Chem BV. Kraton mono hydroxy (Kraton-OH) was purchased from Kraton Polymer Research (L-1203, $M_w = 3500$ g/mol, $PDI = 1.03$). All other reagents were purchased from Aldrich or Acros Organics and used as received unless otherwise specified. All solvents were purchased from Biosolve. Deuterated solvents were purchased from Cambridge Isotopes Laboratories. All reactions were run in flame-dried glassware under an argon atmosphere.

Instrumentation and Methods

CD and UV spectra were recorded on a Jasco J-815 CD spectrometer equipped with a Jasco PTC-348 WI temperature controller. Experiments were conducted using spectroscopic grade methylcyclohexane as the solvent. Cells with an optical path length of 0.1 cm or 1.0 cm were applied (for $\sim 10^{-4}$ M or $\sim 10^{-6}$ M solutions). The molar ellipticity is calculated as: $\Delta\epsilon = CD\text{-effect}/(32980 \times c \times l)$ where c is the concentration in mol/L and l = the optical path length in cm. Films of **1** and **2** were prepared by making solutions of **1** and **2** in chloroform (50 mg/mL, $C_{\text{BTA}} = 4 \times 10^{-3}$ M) and spin-coating a volume of 0.5 mL on 0.40 cm² quartz slides at 800 rpm for two minutes. The film thickness was determined by introducing scratches on the polymer surfaces, followed by measuring the difference in height using AFM (by Asylum Research, tapping mode). The ternary blend of **3/2/1** in a mol ratio of 42.5/42.5/15 was prepared by making a solution of **3** (100 mg) + **2** (100 mg) + **1** (50 mg) in dichloromethane (2 mL). The solvent was slowly evaporated by exposure to air. Subsequently, the polymer blend was annealed at 35 °C *in vacuo* for 2 h. Variable temperature CD measurements on the spin-coated films were performed by mounting

the Linkam THMS 600 heating device into the CD apparatus, which allowed heating up to 250 °C. ¹H-NMR and ¹³C-NMR spectra were recorded on a Varian Gemini 400 MHz NMR (400 MHz for ¹H-NMR and 100 MHz for ¹³C-NMR). Proton chemical shifts are reported in ppm downfield from tetramethylsilane (TMS). Carbon chemical shifts are reported downfield from TMS using the resonance of the deuterated solvent as the internal standard. IR spectra were recorded on a Perkin Elmer 1600 FT-IR. Variable temperature IR spectra were recorded on an Excalibur FTS 3000 MX FT-IR from Biorad. POM measurements were performed using a Jenaval polarisation microscope equipped with a Linkam THMS 600 heating device, with crossed polarisers. The thermal transitions were determined with DSC using a TA Q2000 under a nitrogen atmosphere with heating and cooling rates of 40 K min⁻¹. GPC measurements were performed on a Resi Pore column with chloroform as the eluent (flow = 1 mL/min) and employing a PDA ($\lambda = 254$ nm) as the detector. The molecular weights were determined using a polystyrene calibration method.

A thin film of **1** was cast on glass substrates (cleaned by sonicating in chloroform for 15 min and dried for 1 h at 40 °C *in vacuo*) from dilute solutions in CHCl₃ (1 mg/ml). The final film thickness was *ca.* 500 nm. This value is larger than the intrinsic pattern period observed in the materials, which ensures that the morphology is not driven by the assembly on the substrate. The films were annealed at 30 °C *in vacuo* for 18 h before AFM observation. All the AFM images were recorded with a Nanoscope IV microscope from Veeco Inc. (Santa Barbara, California) in the Tapping Mode (25 °C, in air). Microfabricated cantilevers were used with a resonance frequency of 300 kHz spring constant of 40 Nm⁻¹. The working frequency was chosen slightly below the resonance frequency to be sure to be in the repulsive regime. The instrument measured simultaneously height and phase cartography. Images of different areas of each sample were recorded. For image analysis, the Nanoscope image processing software was used.

Rheological melt experiments were run on a TA Instruments Advanced Rheometric Expansion System (ARES) rheometer. Samples were roughly formed as discs (2/3 blend had

*α-3-*t*-Butyldimethylsiloxy-1-propyl-ω-hydroxy-polybutadiene* (TBDMS-PB-OH) (4) 3-*t*-Butyldimethylsiloxy-1-propyllithium (9.37 mL, 0.5 M) was added to a cooled reactor (10 °C) containing 650 mL of cyclohexane and 1.88 mL THF (5:1 eq THF-Li ion). Purified 1,3-butadiene monomer (15.3 g, 18 h) was then added slowly over a period of 30 min to the reactor at a slight initial positive pressure of argon (1 psi). During the monomer addition, the temperature of the reactor was allowed to slowly warm to room temperature. Upon complete monomer addition, the reactor temperature was raised to 30 °C. A large excess of ethylene oxide (9.5 g, 1 h) was added to the reactor as an end-capping agent (Note: if the newly formed alkoxide chain-ends are not quenched within about 1 h, significant deprotection of the TBDMS initiator will occur). After purging the reactor of excess ethylene oxide, the terminal alkoxide was quenched with wet methanol (20 mL, 200:1 MeOH-H₂O). The protected initiator polymer solution was reduced in volume by half *in vacuo*, washed (2x) with 100 mL deionized water, and precipitated from cold (-20 °C) 4/1 MeOH/EtOH (2.5 L). The product was dissolved in benzene and freeze-dried *in vacuo* (25 °C, 48 h). A sticky, clear, viscous liquid was recovered. Yield: 14.9 g, 97%. GPC (polystyrene standards): $M_n = 11.4$ kg/mol, $PDI = 1.03$. ¹H-NMR (400 MHz, CDCl₃, δ): 5.2–5.9 (b, -CH₂-CH=CH-CH₂- and CH₂=CH-CH-), 4.7–5.1 (b, CH₂=CH-), 3.5–3.7 (m, 2H, -Si-O-CH₂- and t, 2H, -CH₂-OH), 1.7–2.3 (b, -CH₂-CH=CH-CH₂- and CH₂=CH-CH-), 1.0–1.7 (b, CH₂=CH-C(R)H-CH₂-), 0.8–0.9 (s, 9H (CH₃)₃-Si(CH₃)₂-O-), 0 (s, 6H, (CH₃)₃-Si(CH₃)₂-O-). M_n (calcd. from ¹H-NMR integrations) = 5403 g mol⁻¹. 1,2 content = 57%.

*α-3-*t*-Butyldimethylsiloxy-1-propyl-ω-phthalimide-polybutadiene*

(TBDMS-PB-Phthalimide) (5). TBDMS-PB-OH (4) (0.5 g, 0.093 mmol) was dissolved in 5 mL THF. Then, triphenylphosphine (36 mg, 0.14 mmol) and phthalimide (20 mg, 0.14 mmol) were added. The solution was cooled with an ice bath. Diisopropyl azodicarboxylate (DIAD) (28 mg, 0.14 mmol) was dissolved in 2 mL THF and added dropwise to the cooled solution. The mixture was stirred for 48 h. The resulting clear yellow solution was concentrated and precipitated twice in methanol. The product was obtained as a viscous, sticky oil in a 95% yield. ¹H-NMR (400 MHz, CDCl₃, δ): 7.87 (m, 2H, Ar-H), 7.72 (m, 2H, Ar-H), 5.2–5.9 (b, -CH₂-

$CH=CH-CH_2-$ and $CH_2=CH-CH-$), 4.7–5.1 (b, $CH_2=CH-$), 3.71 (t, 2H, CH_2-CH_2-N), 3.6 (m, 2H, $-Si-O-CH_2$), 1.7–2.3 (b, $-CH_2-CH=CH-CH_2-$ and $CH_2=CH-CH-$), 1.0–1.7 (b, $CH_2=CH-C(R)H-CH_2-$), 0.8–0.9 (s, 9H, $(CH_3)_3-Si(CH_3)_2-O-$), 0 (s, 6H, $(CH_3)_3-Si(CH_3)_2-O-$).

*α -3-*t*-Butyldimethylsiloxy-1-propyl- ω -amino-polybutadiene*

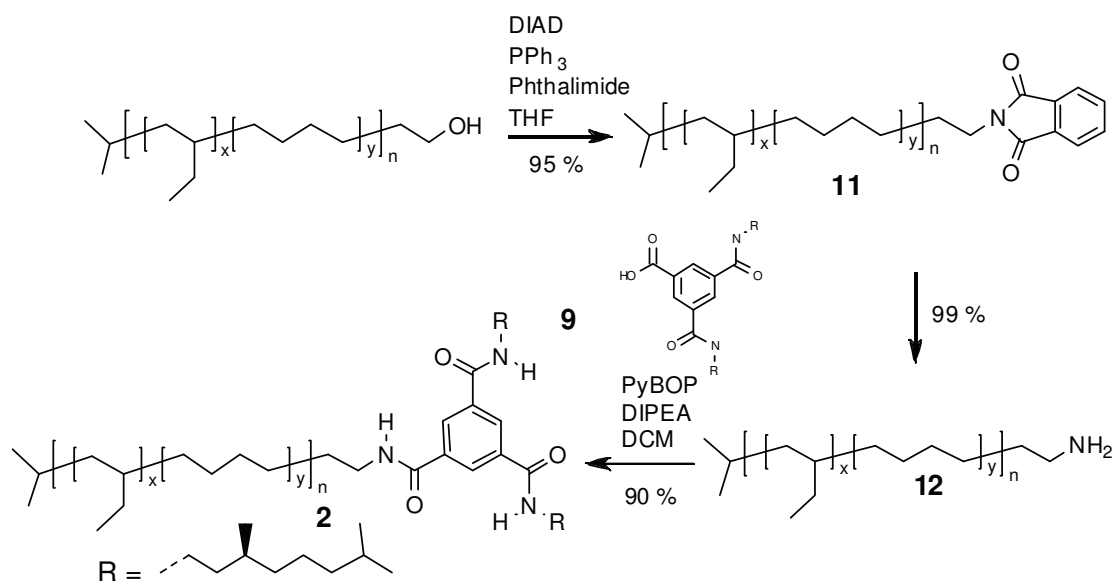
(TBDMS-PB-NH₂) (6). TBDMS-PB-phthalimide (5) (0.45 g, 0.08 mmol) was dissolved in 20 mL THF. After the addition of hydrazine monohydrate (100 mg, 2 mmol), the solution was stirred under reflux for 48 h. THF was removed *in vacuo*. Subsequently, 50 mL of chloroform was added. The organic phase was washed with NaOH (2 x 50 mL) and with brine (50 mL), respectively. After removal of chloroform *in vacuo* TBDMS-PB-NH₂ was obtained as a sticky oil in a 99% yield. ¹H-NMR (400 MHz, CDCl₃, δ): 5.2–5.9 (b, $-CH_2-CH=CH-CH_2-$ and $CH_2=CH-CH-$), 4.7–5.1 (b, $CH_2=CH-$), 3.6 (m, 2H, $-Si-O-CH_2$), 2.65 (t, 2H, $CH_2-CH_2-NH_2$), 1.7–2.3 (b, $-CH_2-CH=CH-CH_2-$ and $CH_2=CH-CH-$), 1.0–1.7 (b, $CH_2=CH-C(R)H-CH_2-$), 0.8–0.9 (s, 9H, $(CH_3)_3-Si(CH_3)_2-O-$), 0 (s, 6H, $(CH_3)_3-Si(CH_3)_2-O-$).

*α -3-*t*-Butyldimethylsiloxy-1-propyl- ω -BTA-polybutadiene*

(TBDMS-PB-BTA) (7). TBDMS-PB-NH₂ (0.41 g, 0.076 mmol) and 3,5-bis((3*S*)-3,7-dimethyloctylcarbonyl)benzoic acid (9) (40 mg, 0.084 mmol) were dissolved in 10 mL dry dichloromethane. Benzotriazol-1-yl-oxytripyrrolidinophosphonium hexafluorophosphate (PyBOP) (63 mg, 0.12 mmol) and *N,N*-diisopropylethylamine (DIPEA) (15.5 mg, 0.12 mmol) were added to the solution. The solution was stirred for 12 h at room temperature. Dichloromethane was removed *in vacuo*. Subsequently, 50 mL of chloroform was added. The originating precipitates were removed by filtration. The solution was concentrated *in vacuo* and precipitated in methanol (three times). The product was obtained as a sticky oil in a 95% yield. ¹H-NMR (400 MHz, CDCl₃, δ): 8.4 (s, 3H, Ar-H), 6.4 (t, 3H, NHC=O), 5.2–5.9 (b, $-CH_2-CH=CH-CH_2-$ and $CH_2=CH-CH-$), 4.7–5.1 (b, $CH_2=CH-$), 3.6 (m, $-Si-O-CH_2$), 3.48 (t, 6H, $CH_2-NHC=O$), 1.7–2.3 (b, $-CH_2-CH=CH-CH_2-$ and $CH_2=CH-CH-$), 1.0–1.7 (b, $CH_2=CH-C(R)H-CH_2-$), 0.8–0.9 (s, 9H, $(CH_3)_3-Si(CH_3)_2-O-$), 0 (s, $(CH_3)_3-Si(CH_3)_2-O-$).

α -Hydroxy-1-propyl- ω -BTA-polyethylenebutylene (BTA-PEB-OH) (**8**). TBDMS-PB-BTA (**7**) (650 mg, 0.12 mmol) was dissolved in 30 mL of toluene. *p*-Toluenesulfonyl hydrazide (*p*TSH) (5.28 g, 28 mmol) and tripropylamine (TPA) (2.03 g, 14 mmol) were added to the solution. The solution was stirred for 18 h at reflux temperature. The solution was concentrated *in vacuo* and subsequently precipitated in methanol (three times). The product was obtained as a sticky oil in a 90% yield. GPC (Polystyrene standards): $M_n = 12.0$ kg/mol, $M_w = 12.3$ kg/mol, $PDI = 1.03$. $^1\text{H-NMR}$ (400 MHz, CDCl_3 , δ): 8.4 (s, 3H, Ar-H), 6.4 (t, 3H, NHC=O), 3.68 (t, CH_2OH), 3.48 (t, 6H, $\text{CH}_2\text{-NHC=O}$), 1.7–0.8 (alkyl).

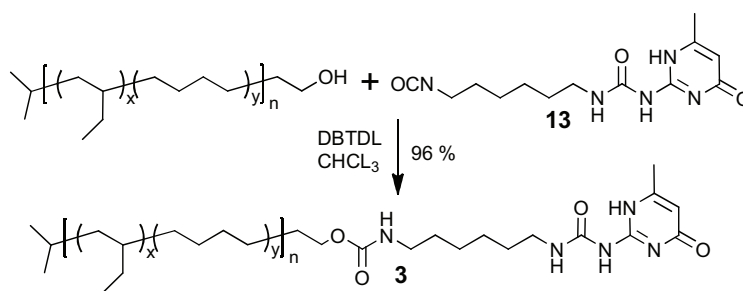
α -UPy-1-propyl-UT- ω -BTA-polyethylenebutylene (**1**) (BTA-PEB-UPy). BTA-PEB-OH (**8**) (0.5 g, 0.083 mmol) was dissolved in 15 mL chloroform. *N*-(6-Isocyanatohexyl)-*N'*-(6-isopropyl-4-oxo-1,4-dihydro-2-pyrimidinyl)urea (**8**) (30 mg, 0.092 mmol) was added to the reaction mixture. One drop of DBTDL was added as a catalyst and stirred for 12 h at 90 °C. Silicagel (2 gram) was added and after 3 h the mixture was diluted with 50 mL chloroform. Subsequently, the silicagel was removed by filtration. After evaporation of the solvent *in vacuo* the product was obtained as a yellowish solid. Compound **2** was purified by precipitation in methanol. Yield = 0.42 gram, 82%. GPC (Polystyrene standards): $M_n = 12.7$ kg/mol, $M_w = 13.0$ kg/mol, $PDI = 1.03$. $^1\text{H-NMR}$ (400Mhz, CDCl_3 , δ): 13.30 (s, 1H, NH, UPy), 11.91 (s, 1H, NH, UPy), 10.13 (s, 1H, NH, UPy), 8.36 (s, 3H, ArH), 6.67 (m, 3H, NH, BTA), 5.86 (s, 1H, C=CH), 4.85 (s, 1H, NH(C=O)O), 4.05 (t, 2H, NHOCO- CH_2), 3.46 (t, 6H, NHCH_2 , BTA), 3.24 (t, 2H, CH_2OCONH), 3.18 (t, 2H, $\text{CH}_2\text{-NH-CO-NH}$), 2.57 (m, 1H, $(\text{CH}_2)_2\text{CH}$, UPy), 1.66–1.19 (alkyl). $^{13}\text{C-NMR}$ (100 MHz, CDCl_3 , δ): 173.5, 165.5, 157.6, 156.7, 154.8, 135.2, 127.9, 103.8, 64.9, 40.7, 39.7, 39.2, 39.1, 39.0, 38.9, 38.5, 38.4, 37.9, 37.1, 36.8, 36.6, 36.1, 36.0, 34.3, 33.6, 33.5, 33.4, 33.2, 32.9, 31.6, 30.7, 30.6, 30.2, 29.7, 29.3, 29.1, 27.9, 26.7, 26.6, 26.4, 26.1, 24.6, 22.7, 22.5, 20.4, 19.5, 10.8, 10.6, 10.4, 10.2.



Kraton-NH₂ (**12**). *Kraton-OH* (0.5 g, 0.14 mmol) was dissolved in 10 mL THF. Then triphenylphosphine (39.6 mg, 0.154 mmol) and phthalimide (22 mg, 0.154 mmol) were added. The solution was cooled with an ice bath. DIAD (30.8 mg, 0.154 mmol) was dissolved in 2 mL THF and added drop wise to the cooled solution. The mixture was stirred for 48 h. The resulting clear yellow solution was concentrated and precipitated twice in methanol. The product was obtained as a viscous, sticky oil in a 95% yield. ¹H-NMR (400 MHz, CDCl₃, δ): 7.87 (m, 2H, Ar-H), 7.72 (m, 2H, Ar-H), 3.71 (t, 2H, CH₂-CH₂-N), 1.7-0.8 (alkyl). *Kraton-phthalimide* (**11**) was dissolved in 20 mL THF. After the addition of hydrazine monohydrate (150 mg, 3 mmol), the solution was stirred under reflux for 48 h. THF was removed *in vacuo*. Subsequently 50 mL of chloroform was added. The organic phase was washed with NaOH (2 x 50 mL) and with brine (50 mL), respectively. After removal of chloroform *in vacuo* *Kraton-NH₂* was obtained as a sticky oil in a 99% yield. ¹H-NMR (400 MHz, CDCl₃, δ): 2.65 (t, 2H, -CH₂-NH₂) 1.7-0.8 (alkyl).

Kraton-BTA (**2**). *Kraton-NH₂* (**12**) (0.46 g, 0.13 mmol) and 3,5-bis((3*S*)-3,7-dimethyloctylcarbamoyl)benzoic acid (**9**) (69 mg, 0.145 mmol) were dissolved in 10 mL dry dichloromethane.

PyBOP (101.4 mg, 0.195 mmol) and DIPEA (25.3 mg, 0.195 mmol) were added to the solution. The solution was stirred for 12 h at room temperature. Dichloromethane was removed *in vacuo*. Subsequently, 50 mL of chloroform was added. The originating precipitates were removed by filtration. The solution was concentrated *in vacuo* and precipitated in methanol (three times). The product was obtained as a sticky oil in a 95% yield. GPC (Polystyrene standards): $M_n = 7.6$ kg/mol, $M_w = 7.8$ kg/mol, $PDI = 1.03$. $^1\text{H-NMR}$ (400 MHz, CDCl_3 , δ): 8.38 (s, 3H, Ar-H), 6.49 (t, 3H, NHC=O), 3.50 (t, 6H, $\text{CH}_2\text{-NHC=O}$), 1.7–0.8 (alkyl). $^{13}\text{C-NMR}$ (100 MHz, CDCl_3 , δ): 165.4, 136.8, 127.7, 40.2, 39.2, 38.8, 38.4, 37.9, 36.8, 36.1, 34.4, 33.5, 33.2, 31.8, 30.7, 30.3, 29.7, 29.5, 29.3, 27.0, 26.8, 26.6, 26.5, 26.3, 26.2, 26.1, 25.8, 25.0, 22.7, 14.2, 10.9, 10.6, 10.7.



Kraton-UPy (**3**). *Kraton-OH* (2.0 g, 0.57 mmol) was dissolved in 50 mL chloroform. *N*-(6-Isocyanatohexyl)-*N'*-(6-methyl-4-oxo-1,4-dihydro-2-pyrimidinyl)urea (**13**) (183 mg, 0.629 mmol) was added to the reaction mixture. One drop of DBTDL was added as a catalyst and stirred for 18 h at 90 °C. Silicagel was added and after 5 h the mixture was diluted with 150 mL chloroform. Subsequently, the silicagel was removed by filtration. The solution was concentrated *in vacuo* and subsequently precipitated in methanol (three times). The product was obtained as a sticky oil. Yield = 2.0 gram, 96%. GPC (Polystyrene standards): $M_n = 7.9$ kg/mol, $M_w = 8.1$ kg/mol, $PDI = 1.03$. $^1\text{H-NMR}$ (400 MHz, CDCl_3 , δ): 13.30 (s, 1H, NH, UPy), 11.91 (s, 1H, NH, UPy), 10.13 (s, 1H, NH, UPy), 5.86 (s, 1H, C=CH), 4.85 (s, 1H, NH(C=O)O), 4.05 (t, 2H, NHOCO- CH_2), 3.68 (t, 2H, CH_2OH), 3.24 (t, 2H, CH_2OCONH), 3.18 (t, 2H, $\text{CH}_2\text{-NH-}$

CO-NH), 2.2 (s, 3H, CH₃, UPy), 1.7–0.8 (alkyl). ¹³C-NMR (100 MHz, CDCl₃, δ): 168.2, 158.2, 157.3, 156.8, 130.6, 38.9, 38.4, 37.9, 36.7, 36.1, 34.4, 33.4, 33.2, 30.7, 30.2, 29.7, 29.5, 26.8, 26.8, 26.4, 26.1, 26.0, 25.9, 19.2, 11.4, 10.9, 10.7, 10.6.

UV measurements of 1 in MCH

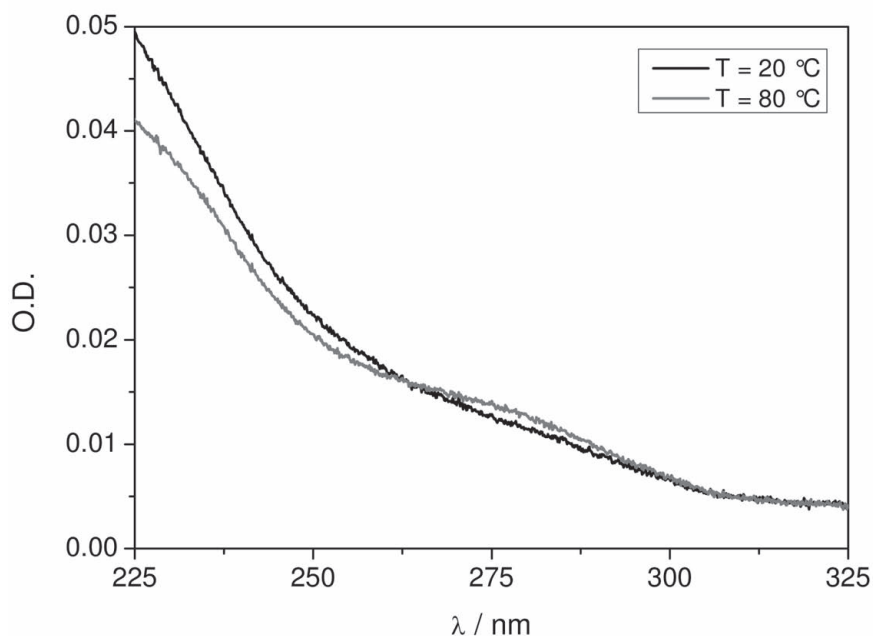


Figure AI-S1: UV spectroscopy measurements of **1** at 20 and 80 °C in MCH ($c = 1.25 \times 10^{-6} \text{ mol L}^{-1}$, $l = 1.0 \text{ cm}$).

The spectra at 80 °C show a shoulder at 275 nm indicative for the loss of quadruple hydrogen bonding between the Upy groups. This indicates that the Upys are dimerized at 20 °C. The molar ellipticity $\Delta\epsilon$ in **1** (CD-effect = -10 mdeg, $\Delta\epsilon = -6 \text{ L/mol.cm}$) is significantly lower than that of **2** (CD-effect = -58 mdeg, $\Delta\epsilon = -35 \text{ L/mol.cm}$) (Figure 2B in the main text). We rationalise this difference by the fact that the UPy groups of **1** are dimerized at this concentration as verified by UV spectroscopy measurements. As a result, the dimerization of the UPy groups

leads to an increase of the virtual molecular weight of the spacer attached to the BTA unit. The association constant K of a supramolecular motif is affected by the molecular weight of the polymer backbone to which it is connected, presumably as a result of the steric crowding that the polymer imposes.² Hence, we attribute the differences in $\Delta\varepsilon$ between **1** and **2** to a reduction of the association constant K upon increasing the molecular weight of the side chain.

Variable temperature CD measurements on films of 1 and 2

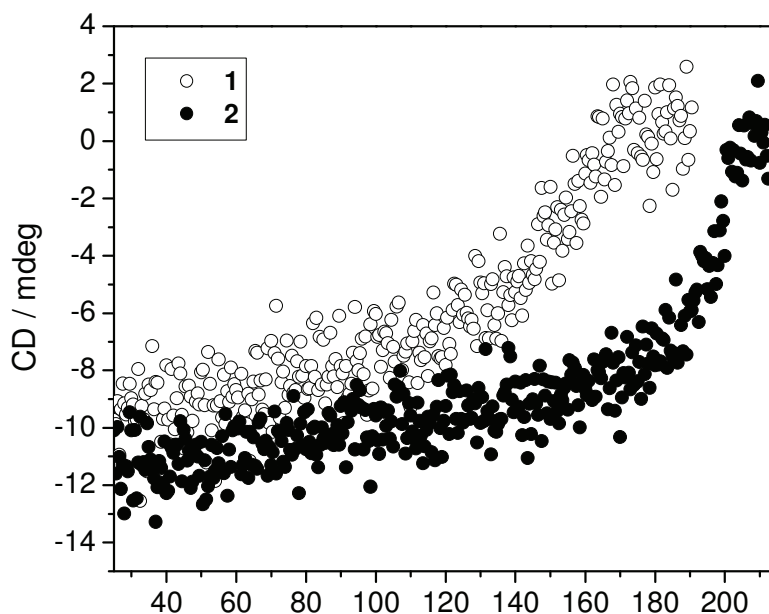


Figure AI-S2 CD cooling curve of **2** (open circles) and **3** (closed circles) measured at $\lambda = 223$ nm. The film thickness is 340 nm for **1** and 260 nm for **2**.

The films were prepared by spin-coating a CHCl_3 solution ($c_{\text{BTA}} = 4 \times 10^{-3}$ M) on a quartz plate. The film thickness was determined by introducing scratches on the polymer surfaces, followed by measuring the difference in height using AFM (by Asylum Research, tapping mode).

DSC trace of Upy-urethane-pEB-urethane-Upy

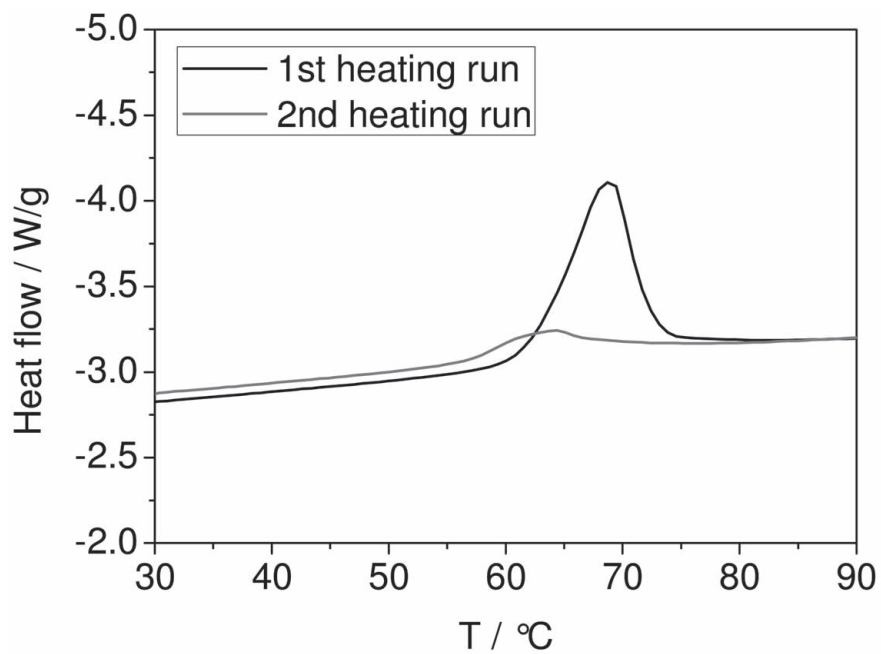


Figure AI-S3 DSC trace of Upy-urethane-pEB-urethane-Upy (BisUpy-urethane-pEB).

The DSC traces of the first and second heating run of BisUPy-urethane-pEB are given.³ In the first heating run: $T_m = 69^\circ\text{C}$ $\Delta H = 6.65$ J/g and in the second heating run $T_m = 62^\circ\text{C}$ $\Delta H = 1.98$ J/g. Heating and cooling rates were 10 K min^{-1} .

VT-IR of polymer 1

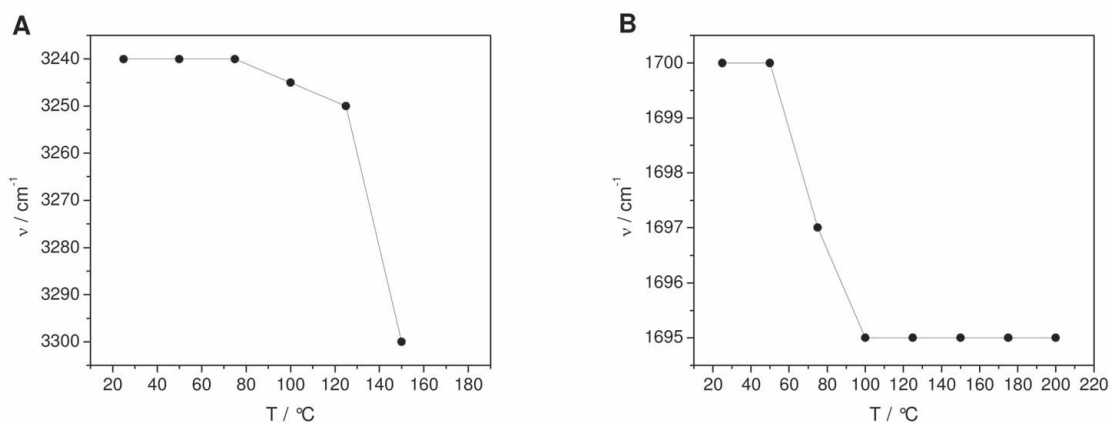


Figure AI-S4 VT-IR of **1**. A) The position of the N-H stretch vibration is plotted versus temperature. B) The position of the UPy isocytosine C=O vibration is plotted versus temperature.

Dynamic frequency dependence of blends 2/3 and 1/2/3

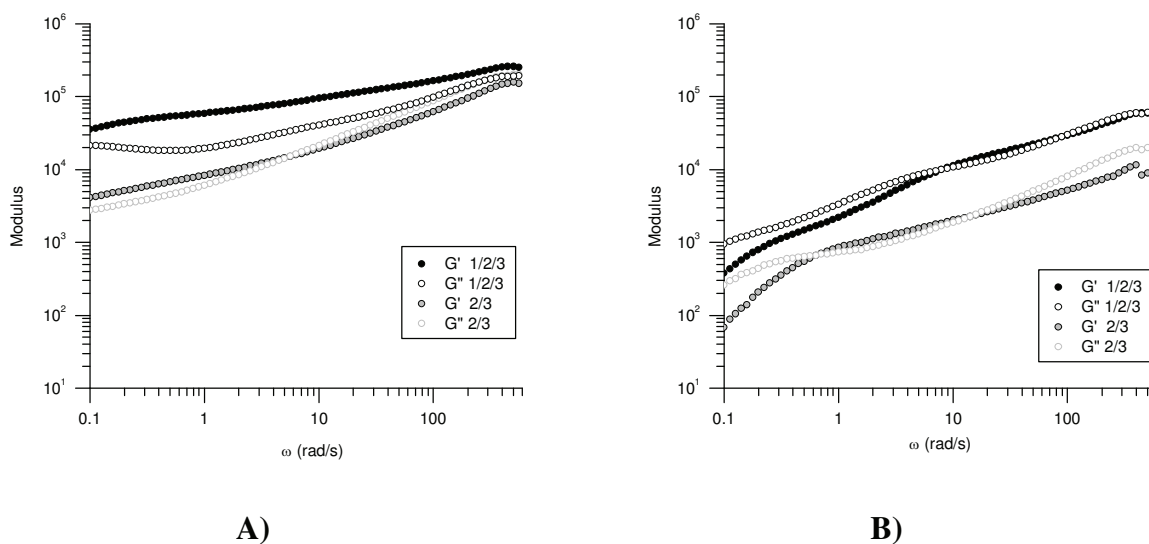
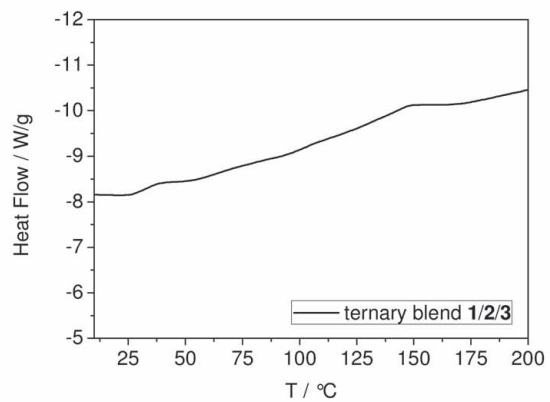
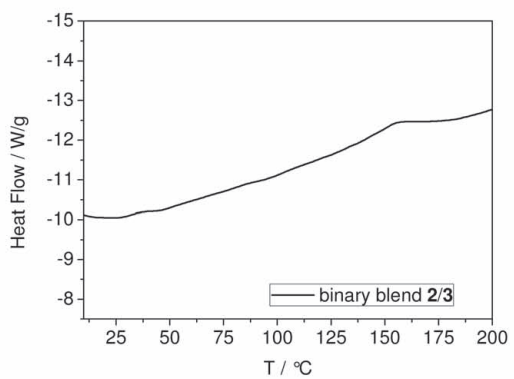
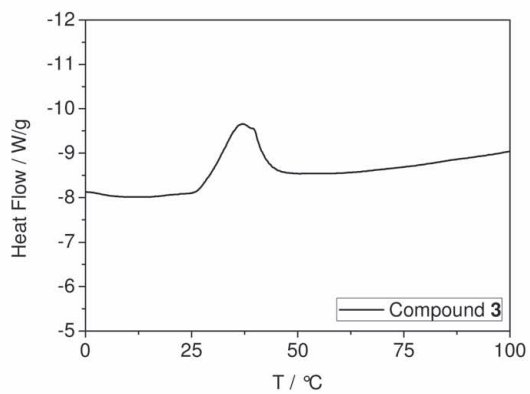
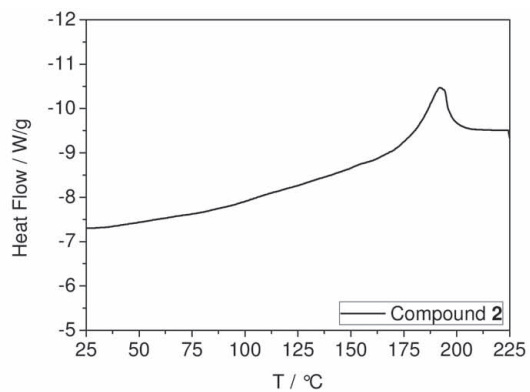
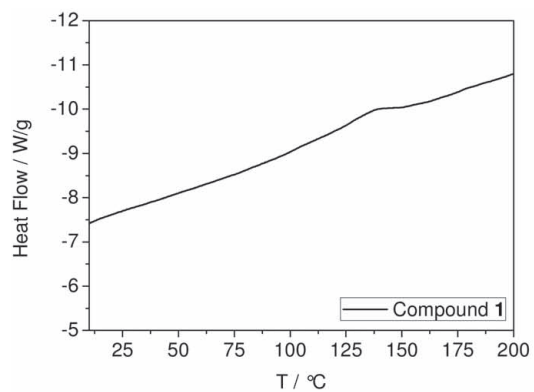


Figure AI-S5. Dynamic frequency dependence of blends **2/3** and **1/2/3** at A) 25 °C and 10% strain and B) at 60 °C and 10% strain.

The dynamic frequency dependence at 25 and 60 °C on blends of **2/3** and **1/2/3** was measured with a strain of 10%. The **2/3** blend displays a frequency response similar to what is expected for concentrated polymer liquids, that is a steady decrease in modulus until approaching terminal flow where the loss modulus crosses over and above the storage modulus. In contrast, sample **1/2/3** exhibits elastomeric properties at 25 °C, where there is a region of near plateau in the storage modulus coupled with an elastic recovery of the loss modulus at low frequencies. The loss modulus also tracks below the storage modulus, which is expected for rubber-like materials. Upon heating sample **1/2/3** to 60 °C, the elastic response is no longer present in the frequency dependence, instead the material behaves similarly to sample **2/3** where there is a steady decrease in modulus approaching terminal flow. The absence of elastomeric properties above the phase transition at 39 °C is attributed to the loss of lateral hydrogen bonds between the UPy-urethane groups, and is consistent with behavior expected for the disappearance of physical cross-links in the system.

DSC Traces of Compounds 1,2,3 and blends 2/3 and 1/2/3



References for Appendix I Supplementary Information

1. Roosma, J. R.; Mes, T.; Leclere, P. E. L. G.; Palmans, A. R. A.; Meijer, E. W. *J. Am. Chem. Soc.* **2008**, *130*, 1120–1121.
2. Ilhan, F.; Gray M.; Rotello V. M., *Macromolecules*, **2001**, *34*, 2597–2601; Chen, S. B.; Bertrand, A.; Chang, X. J.; Alcouffe, P.; Ladaviere, C.; Gerard, J. F.; Lortie, F.; Bernard, J. *Macromolecules* **2010**, *43*, 5981–5988.
3. Kautz, H.; van Beek, D. J. M.; Sijbesma, R. P.; Meijer, E. W., *Macromolecules* **2006**, *39*, 4265–4267.